# Modeling technique for the efficient design of microwave bandpass filters

Matthias Caenepeel

UNIVERSITE DE NICE-SOPHIA ANTIPOLIS

# ECOLE DOCTORALE STIC

**SCIENCES ET TECHNOLOGIES DE L'INFORMATION ET DE LA COMMUNICATION**

# T H E S E

pour l'obtention du grade de

## Docteur en Sciences

de l'Université de Nice-Sophia Antipolis

présentée et soutenue par

AUTEUR *Matthias CAENEPEEL*

## Modeling technique for the efficient design of microwave bandpass filters

Thèse dirigée par *Yves ROLAIN et Martine Olivi*

soutenue le *19 Octobre 2016*

**Jury :**

| | | |
|---|---|---|
| G. Macciarella | Professeur | Rapporteur |
| A. Alvarez-Melcón | Professeur | Rapporteur |
| A. Pérrigaud | Ingénieur de recherche | Examinateur |
| F. Ferranti | Professeur | Examinateur |
| A. Hubin | Professeur | Examinateur |
| R. Vounck | Professeur | Examinateur |
| Y. Rolain | Professeur | Directeur de thèse |
| M. Olivi | Chargée de recherche | Directeur de thèse |
| F. Seyfert | Chargé de recherche | Co-directeur de thèse |

Vrije Universiteit Brussel (VUB)
Faculty of engineering (IR)
Department of fundamental electricity and instrumentation (ELEC)

INRIA (Université Nice Sophia Antipolis)
Team APICS: Analysis and problems of inverse type in control and signal processing

# MODELING TECHNIQUES FOR THE EFFICIENT DESIGN OF MICROWAVE BANDPASS FILTERS

Thesis submitted in fulfilment of the requirements for the award of the degree of Doctor in Engineering Sciences (Doctor in de ingenieurswetenschappen) by

Matthias Caenepeel

October 2016

Advisors: Prof. dr. ir. Yves Rolain
Chargée de recherche Martine Olivi
Chargé de recherche Fabien Seyfert

## Members of the jury

Prof. dr. ir. **Yves Rolain** (advisor)
Vrije Universiteit Brussel

Chargée de recherche **Martine Olivi** (advisor)
INRIA

Chargé de recherche **Fabien Seyfert** (advisor)
INRIA

Prof. dr. ir. **Annick Hubin** (chairman)
Vrije Universiteit Brussel

Prof. dr. **Roger Vounckx** (vice-chairman)
Vrije Universiteit Brussel

Prof. dr. ir. **Alejandro Alvarez-Melcón** (rapporteur)
Universidad Politécnica De Cartagena, Spain

Prof. dr. ir. **Giuseppe Macchiarella** (rapporteur)
Politecnico di Milano, Italy

Prof. dr. ir. **Francesco Ferranti** (secretary)
Vrije Universiteit Brussel

dr. ir. **Aurélien Périgaud**
XLIM, France

# Acknowledgements

During the last four years I've had the opportunity to do a joint PhD between the ELEC department of the VUB and the APICS team of INRIA Sophia-Antipolis. This experience broadened my vision on science, engineering and life in general. I want to thank all of the people that made this possible and supported me during this unforgettable experience.

First of all I would like to thank Yves Rolain, Martine Olivi and Fabien Seyfert for their guidance and for giving me the opportunity to do this PhD.

Yves, first of all I would like to thank you for believing in me as a PhD candidate. By pushing me out of my comfort zone, you have helped me to develop several skills. Your enthusiastic way of teaching has taught me the importance of a well-structured yet vivid presentation. I also want to thank you for correcting my writings. Although the result of these corrections was not always pleasant, it has drastically improved my writing skills. Finally I would like to thank you for the all the interesting discussions we had during the last five years, not only on technical subjects but also on other topics. I am proud to say that I have been one of your PhD students.

Martine, first of all thank you for helping me set up this joint PhD. I also highly appreciated your patience when you were explaining me various mathematical concepts and helping me with proofs. I would also like to thank you for always thoroughly reading my writings. Your eye for detail is truly remarkable. Finally I want to thank you for always helping me to put things into perspective when I thought everything was going in the wrong direction.

Fabien, thank you for all of the hours you have invested in discussing about and explaining me the coupling matrix theory. Thank you for the late evenings you spent with me at INRIA and for the Skype meetings to figure out the errors in my work. Although I lacked the energy to figure out an important error at the end

of my thesis, I am really glad you have pushed me to do so. Moreover you have convinced me that scientific results are more important than writing astronomic amounts of papers. Your view on life, critical attitude towards results and sense of humor have truly inspired me.

Next, I would like to thank Annick Hubin, Roger Vounckx, Francesco Ferranti, Aurélien Périgaud, Giuseppe Macchiarella and Alejandro Alvarez-Melcón for being a member of the jury of my thesis. Your comments, questions and expertise allowed me to drastically improve the quality of this work.

Also I would like to thank both of the research teams APICS and ELEC for providing a pleasant environment and all the necessary means to be able to do my research. I would especially like to thank Ann Pintelon, Johan Pattyn, Stéphanie Sorres and Sven Reyniers for all of their administrative and technical support.

During my PhD I have also learned the value of collegiality and friendship. I was very lucky to share an office with Hannes, Adam and Egon at ELEC.

Hannes, you are a true friend to whom I can talk about literally every aspect of my life. Thank you for all the support, advice and good times we had. I strongly value your opinion. Your view on things has helped me clear my mind several times. Moreover our trip the USA was one of the best experiences of my life. I am really going to miss seeing you on a daily basis.

Adam, working on a project or traveling together with you always has brought us closer as friends. Thank you for solving all those questions I was struggling with. I truly hope that our professional paths will cross again in the future. But for now I wish you all the best as a new member of the APICS team.

Egon, I am glad that we did not only share an office but that we also worked together on the ping-pong tower project. You are one of the most helpful people I know. I would specifically like to thank you for all of the times you helped me with computer related issues.

I would also like to thank Maral and Evi for working together with me on microwave filters. Maral, due to the topic of your master thesis, you pushed this work in the direction of the coupling matrix theory. This would not have been the same work if it wasn't for you.

I would also like to thank Francesco and Krishnan for working with me on incorporating metamodels in filter design. Francesco, I thank you for sharing your expertise with me. It was a real pleasure to work with you.

I would also like to thank Piet, Ebrahim, Dries, John, Anna, Maarten, Jan, Alexander, Cedric, Koen, Philippe, Rik, Gerd and Leo for being such nice colleagues. Thank you for all of the nice chats and laughter during several lunches, coffee breaks and beer Fridays. I would specifically like to thank Piet for all the extra good times he offered me during our daily lifting sessions.

I would also like to thank Glenn and Philemon for living with me during the first two years of this PhD. Thanks for all whisky tastings, balcony discussions and crazy times we had in our little palace.

I was very lucky to be part of such warm and pleasant research group at INRIA.

Dmitry, although I called you Vladimir during my first week at INRIA, I will always remember your name. Your presence made my visits to APICS even more pleasant. I am also very proud to be a part of the Porco Rosso team: Christos, Stephano, Konstaninos and Dmitry. I would like to thank you all for your support, good times and nice food we had together. And a special thanks for the moral support when my computer crashed while I was writing this thesis. I would also like to thank David for all the discussions about our works in order to improve them both. Finally I also want to thank Juliette, Sylvain and Laurent for the warm welcoming every time I visited.

At the VUB in general, I have always been surrounded by lovely people: Hannes, Philemon, Glenn, Maarten, Adam, Lara, Petey, Ken, Jens, Hans, Simen and Aushim. Thank you for all the parties, concerts and crazy nights we had together. May more of these good times follow in the future!

Another very important person during me PhD is my brother, Free. Having a beer or a run together always gave me the right energy to push me further into my research or putting things into perspective when I was having a hard time. Thank you for your support and I hope I am able to do the same for you.

There are no words to express my love and gratitude towards Evy. Thank you for always being there for me. I highly appreciate your open mind towards my long stays in France. I would also like to thank you for your contributions to the visual aspects of my work in general. Without you, the layout of this thesis would simply have been ugly. Finally I want to thank you for your patience, especially during the last days of the writing period. Evy, thank you for all of the help, support, freedom and love you have been given me during this PhD.

Finally I want to thank my parents for all of the opportunities and the beautiful youth they have given me. Papa, sending me to the VUB is one of the best things that ever happened to me. Mama, it is impossible to list up all of the amazing things you have done for me over the last 27 years.

Therefore I would like to dedicate this work to my parents.

Matthias Caenepeel
Antibes and Brussels, October 2016

# Abstract

The design of microwave bandpass filter generally requires optimization or fine-tuning of the physical design parameters in order to meet the electrical specifications given by a frequency template. In this thesis we develop models to assist the designer in the time-efficient physical design of the distributed element microwave filters. The aim is to incorporate these models in different computer-aided design (CAD) methods. By a time-efficient design, we mean a design that requires a low number of electromagnetic (EM) simulations. The EM-simulations typically represent the most time-consuming step during the optimization process. We propose different modeling approaches for the frequency response behavior of the filter. The first approach models the coupling matrix as a function of the physical design parameters and the second approach models the scattering ($S$-) parameters, again as a function of the physical parameters.

In the first part of the text we focus on the design of narrow-band microwave bandpass filters implemented in a microstrip technology. The design of such filters is often based on the coupling matrix theory. It models the distributed element microwave filter by a lumped element circuit consisting of coupled $LC$-resonators that resonate in the vicinity of its center frequency. The behavior of these coupled resonator circuits is represented by a coupling matrix. The first step of the design process synthesizes a coupling matrix (golden goal) realizing a filter function that fulfills the frequency specifications. Next this coupling matrix is physically implemented by correctly dimensioning the design parameters of the actual microwave filter. Over the last few years several computer-aided tuning (CAT) methods have been developed to optimize the physical design parameters. These tuning methods often extract a coupling matrix from the filters $S$-parameters and compare it to the golden goal. The extraction of the coupling matrix is critical, especially in the case of coupling topologies that allow multiple solutions.

Therefore we have developed a coupling matrix extraction procedure that identifies the physically implemented coupling matrix. Moreover we introduce a novel CAT technique based on an efficient estimation of the Jacobian of the function relating the design parameters to the (physical) coupling parameters. The estimation of the Jacobian uses adjoint sensitivity analysis , which drastically reduces the number of required EM-simulations. This novel technique has been applied to design examples having multiple-solution coupling topologies.

In the second part of the thesis we propose an alternative modeling approach which is a based on the concept of a *metamodel*. The idea is that the metamodel is numerically much cheaper to evaluate than the original simulation model while keeping an acceptable accuracy. First we use the metamodel approach to efficiently generate initial values for the filters' physical design parameters. Next we will use metamodels to optimize the $S$-parameters. The use of metamodels reduces the time required to optimize the filters heavily. Moreover metamodels can be used to optimize for different design scenarios.

# Contents

## List of symbols

### LATIN LOWER CASE

| | |
|---|---|
| $a_i$ | transmitted power wave at port $i$ |
| $b_i$ | reflected power wave at port $i$ |
| $c$ | phase velocity in free space ( $c \approx 3 \times 10^8 \frac{\mathrm{m}}{\mathrm{s}}$) |
| $f$ | frequency |
| $f_c$ | center frequency in the bandpass domain |
| $f_{res}$ | resonance frequency |
| $j$ | unit imaginary number , $j^2 = -1$ |
| $k_s$ | filter selectivity |
| $k_X$ | bandpass inter-resonator coupling coefficient |
| $k_B$ | mixed bandpass coupling coefficient |
| $k_E$ | electric bandpass coupling coefficient |
| $k_M$ | magnetic bandpass coupling coefficient |
| $h$ | thickness of the dielectric substrate of a microstrip structure |
| $l$ | physical length of a transmission line |
| $n_F$ | number of simulated frequencies |
| $n_{fz}$ | number of transmission zeros located at a finite frequency |
| $n_g$ | number of physical design parameters |
| $n_S$ | number of solutions to the coupling matrix reconfiguration problem |
| $s$ | Laplace variable, $s = \sigma + j\omega$ |
| $t$ | thickness of metal strip of a microstrip structure |

### LATIN UPPER CASE

| | |
|---|---|
| $\boldsymbol{A}_{LP}$ | nodal admittance matrix in the lowpass domain |
| $\boldsymbol{A}_{BP}$ | nodal admittance matrix in the bandpass |
| $\boldsymbol{A}_Y$ | system matrix of the admittance matrix $\boldsymbol{Y}$ |
| $\boldsymbol{B}_Y$ | input matrix of the admittance matrix $\boldsymbol{Y}$ |
| $\boldsymbol{C}_Y$ | output matrix of the admittance matrix $\boldsymbol{Y}$ |

| | |
|---|---|
| $\boldsymbol{D}_Y$ | direct transmission matrix of the admittance matrix $\boldsymbol{Y}$ |
| $BW$ | absolute bandwidth |
| $C_a$ | per unit capacitance for air |
| $C_d$ | per unit capacitance for a dielectric |
| $E(s)$ | common denominator polynomial |
| $F(s)$ | numerator polynomial of $S_{11}(s)$ |
| $FBW$ | fractional or relative bandwidth |
| $G_L$ | reference admittance at the load |
| $G_S$ | reference admittance at the source |
| $\boldsymbol{I}_n$ | identity matrix of size $n \times n$ |
| $\boldsymbol{J}$ | Jacobian matrix of the function that maps the geometrical parameters to the coupling parameters |
| $J$ | $J$-inverter |
| $K_N$ | filter function of order $N$ |
| $L_A$ | insertion loss |
| $L_R$ | return loss |
| $M_{vv}$ | lowpass self-coupling of resonator $v$ |
| $\boldsymbol{M}_{arr}$ | arrow form coupling matrix |
| $N$ | McMillan degree |
| $\boldsymbol{P}$ | similarity transformation |
| $P(s)$ | numerator polynomial of $S_{21}(s)$ |
| $Q_c$ | conductor quality factor |
| $Q_d$ | dielectric quality factor |
| $Q_e$ | external quality factor |
| $Q_r$ | radiation quality factor |
| $Q_u$ | unloaded quality factor of a resonator |
| $Q_r$ | radiation quality factor |
| $RL$ | minimal return loss in the passband |
| $\boldsymbol{S}$ | scattering matrix |
| $\boldsymbol{S}_C$ | scattering matrix with de-embedded access lines |
| $\boldsymbol{S}_{Sim}$ | simulated scattering matrix |
| $\boldsymbol{S}_{rat}$ | rational scattering matrix |
| $\boldsymbol{T}$ | coupling topology matrix |
| $W$ | width of metal strip of a microstrip structure |
| $\boldsymbol{Y}$ | admittance matrix |
| $Z_c$ | characteristic impedance |
| $Z_L$ | reference impedance at the load |
| $Z_S$ | reference impedance at the source |

GREEK CASE

| | |
|---|---|
| $\alpha$ | attenuation constant |
| $\beta$ | lossless propagation constant |
| $\alpha_{kk}$ | delay introduced by the access line at port $k$ |
| $\varepsilon_r$ | relative permittivity |
| $\varepsilon_{re}$ | effective dielectric constant |
| $\gamma$ | propagation constant |
| $\lambda_0$ | wavelength in free space |
| $\lambda_g$ | guided wavelength |
| $\tan\delta$ | loss tangent of a dielectric substrate |
| $\tau$ | group delay |
| $\theta$ | electrical length |
| $\omega$ | normalized angular lowpass frequency |
| $\Omega$ | angular bandpass frequency |
| $\Omega_k$ | resonance frequency of resonator $k$ in the lowpass domain |
| $\Omega_c$ | center frequency in the lowpass domain |

ABBREVIATIONS

| | |
|---|---|
| AFS | adaptive frequency sampling |
| BP | bandpass |
| CAT | computer-aided tuning |
| CQ | cascaded quadruplet |
| CT | cascaded triplet |
| dB | decibels ($20\log_{10}$) |
| EM | electromagnetic |
| FIR | frequency invariant reactance |
| FRF | frequency response function |
| I/O | input/output |
| LP | lowpass |
| LSE | least square estimation |
| MAE | mean absolute error |
| MoM | method of moments |
| PCB | printed circuit board |
| SOLR | square open loop resonator |
| SQ | single quadruplet |
| TEM | transverse electromagnetic |
| TZ | transmission zero |
| VF | vector fitting |

# 1 Introduction

Microwave filters are indispensable building blocks in modern telecommunication systems. They are designed to pass electromagnetic signals within certain frequency bands, while attenuating signals whose spectral content lies outside of these frequency bands. Over the last years the frequency spectrum has become more and more crowded, which automatically led to more stringent filter specifications. These specifications consist of a frequency template, which specifies the frequency bands that should be attenuated and passed. Several techniques have been developed to design a wide variety of microwave filters in various technologies such as: waveguide, dielectric resonator and planar technologies such as microstrip filters. The literature helps filter designers to select the most convenient type of filter to meet the design requirements [Levy 02; Levy 84]. Besides the electrical specifications of the filter, that are grouped in the frequency template, there are several aspects that must be taken into account such as minimization of the mass and volume, manufacturing cost, development time and power handling capability [Snyd 07; Kuds 92]. All these aspects influence both the choice of the implementation technology and of the topology of the filter to be designed. In this work we focus on the electrical specifications of the filters. The most common design approach which is also used here, can roughly be divided into three design stages [Matt 64]:

1. The first stage approximates or estimates a filter function that fulfills the electrical specifications.

2. The second stage synthesizes an equivalent lumped-element network that realizes the filter function.

3. The third stage transforms this network into the actual microwave filter by correctly dimensioning the physical (design) parameters of the filter.

In this thesis we focus on the last stage of the design approach. We develop models to assist the designer in the time-efficient physical design of the distributed element microwave filters. The aim is to incorporate these models in different computer-aided design (CAD) methods. By a time-efficient design, we mean a design that requires a low number of electromagnetic (EM) simulations. The EM-simulations typically represent the most time-consuming step during the last design stage. We propose different modeling approaches for the frequency response behavior of the filter. The first approach models the coupling matrix (which is introduced later) as a function of the physical design parameters and the second approach models the scattering ($S$-) parameters, again as a function of the physical parameters.

In the first part of the text we focus on the design of narrow-band microwave bandpass filters implemented in a microstrip technology. The design of such filters is often based on the coupling matrix theory. It models the distributed element microwave filter by a lumped element circuit consisting of coupled $LC$-resonators that resonate in the vicinity of its center frequency [Hong 01]. The behavior of these coupled resonator circuits is represented by a coupling matrix [Came 99; Atia 71]. This matrix contains the electromagnetic couplings between the different resonators in the filter. The way these resonators are coupled, is called the coupling topology. The concept of the coupling matrix was first introduced in the early 1970s by Atia and Williams to design a dual-mode symmetric waveguide filter [Atia 71; Atia 72; Atia 74]. One of its main advantages is that it can be easily linked to the physical design parameters of the actual filter [Came 07b].

Chapter 2 explains the concepts of the coupling matrix based design approach that will be used in the rest of the text: the generation of a rational filter function and the synthesis of a coupling matrix which represents the equivalent lumped-element network. In order to translate the coupling matrix into the actual microwave filter, it is necessary to transform the coupling matrix into a coupling topology that is adapted to the selected filter structure. This process is often referred to as the reconfiguration of the coupling matrix. The reconfiguration problem is a complex problem and for some coupling topologies there are multiple solutions. Topologies with multiple solutions are called non-canonical topologies. Several methods have been developed to tackle the reconfiguration problem: some of them are optimization-based [Amar 00b; Atia 98] and for some other topologies analytical techniques exist [Tami 05]. The most general approach uses Groebner basis and homothopy techniques to solve the reconfiguration problem

[Came 07a]. This is also the approach used here. The second stage of the design process thus yields a coupling matrix with a suitable coupling topology. This matrix is often referred to as the golden goal or the target coupling matrix.

The third stage of the design process is to dimension the physical filter such that the coupling matrix of the actual filter is as close as possible to the target matrix. This step is called the physical implementation. It often starts with the generation of initial values for the design parameters, which are then further optimized to meet the specifications.

Chapter 3 proposes a method to generate initial values for the physical parameters. Although the method is general for various technologies, we use microstrip filters to illustrate it. Therefore the chapter first summarizes the most important characteristics of microstrip transmission lines that are used in the remainder of the text. We also discuss the use of the full-wave EM field solvers that are used to simulate the filters, which are ADS Momentum [ADS 14] and CST Microwave Studio [CST 15]. We briefly describe the properties of both EM-solvers and the simulation settings used in this work.

The initial dimensioning divides the filter into building blocks consisting of individual resonators or pairs of resonators. Next, it dimensions these blocks separately and finally merges them to obtain the complete filter. Therefore it is sometimes referred to as the 'divide and conquer strategy' [Came 07b]. The dimensioning of each individual block uses design curves. These are look-up tables that relate the physical parameters to the coupling parameters [Pugl 00; Pugl 01]. We explain how the design curves are generated using simulated $S$-parameters. This approach yields relatively good initial values for the design. Nevertheless an optimization or tuning phase is often required to ensure that the filter meets the specifications.

In the literature several optimization methods are available to tune microwave filters based on various cost functions [Swan 07a; Band 94b; Arnd 04; Koza 02]. For the coupling matrix based designs, we follow an approach which compares the golden goal to the coupling matrix of the physical filter as is done in [Lamp 04; Koza 06]. A very important step in this approach is the extraction of the physical coupling matrix. This can be a tedious task especially in the case of coupling topologies supporting multiple solutions.

Chapter 4 presents a method to extract the coupling matrix starting from the simulated (or measured) $S$-parameters of the filter. It first estimates a rational common denominator matrix for the $S$-parameters. Next it, synthesizes a

coupling matrix starting from this rational approximation using the techniques explained in Chapter 2. In general the coupling topology of this matrix does not correspond to the physically implemented coupling topology. Moreover, the extracted matrix contains parasitic couplings, which are not present in the golden goal. In the case of non-canonical topologies, the process extracts all possible solutions taking into account the presence of parasitics. This extraction procedures gives rise to the following question: *Which of these solutions corresponds to the physically implemented one?* Answering this is very important for the tuning of the filter. Using a non-physical solution may lead to wrong adjustments of the design parameters, hereby destroying the whole tuning procedure. The answer is however not always obvious and extra information about the physical structure of the filter is indispensable.

Chapter 5 presents a novel identification method to determine the physically implemented coupling matrix in the case of cascaded trisection (CT) and cascaded quadruplet (CQ) topologies. These topologies are often used, since they yield very selective filter responses [Yang 99; Hong 99; Hong 01]. The identification method basically links specific parts of the coupling matrix to specific parts of the physical structure. To establish this link, several EM-simulations are required. The number of required EM-simulations depends of the complexity of the structure. The usefulness of the identification method is illustrated on the tuning of an $8^{th}$ order CQ filter. The tuning is a *manual* and requires a relatively large number of EM-simulations. In order to automate the tuning procedure and minimize the number of EM-simulations, we propose another approach based on adjoint sensitivity analysis.

Chapter 6 presents a novel computer-aided tuning (CAT) procedure for coupled resonator microwave bandpass filters. The method is based on the estimation of the Jacobian of the relation between the geometrical design parameters of the filter and the physically implemented coupling parameters. The Jacobian is estimated by combining the adjoint sensitivity of the $S$-parameters with respect to the coupling parameters on the one hand and the adjoint sensitivity of the $S$-parameters with respect to the physical filter design parameters on the other hand. Lately, commercial EM-simulators such as CST Microwave Studio [CST 15] provide the adjoint sensitivities of the $S$-parameters with respect to the geometrical or substrate parameters of the filter without drastically increasing the simulation time. As a consequence, one EM-simulation suffices to estimate the Jacobian. In the case of coupling topologies with multiple solutions, the Jacobian is estimated for each solution separately and a criterion

is presented to determine the physical solution amongst the candidates. The Jacobian provides a lot of useful information for the tuning procedure and we will see that this drastically lowers the number of EM-simulations required to tune the filter.

In the second part of the thesis we propose an alternative modeling approach which is a based on the concept of a *metamodel*. A metamodel is defined in the literature as: *an approximation of the Input/Output (I/O) function that is defined by the underlying simulation model* [Klei 08]. The word *meta* implies that we are actually modeling a (simulation) model. The idea is that the model is cheaper to evaluate than the original simulation model while keeping an acceptable accuracy. In this work we consider the physical design parameters as the input parameters of the metamodel. First we use the metamodel approach to efficiently generate the design curves introduced in Chapter 3 to generate initial values. In this context the output parameters of the metamodel are the coupling parameters of the individual building blocks. Next we will use this approach to optimize the $S$-parameters. The output in this case are $S$-parameters and the inputs are the design parameters and the frequency. In this context we will use the term *scalable or parametric macromodel*, rather than metamodel as this is more commonly used in the literature [Triv 09; Ferr 11; Ferr 12].

Chapter 7 introduces a metamodel approach to automatically generate multi-dimensional design curves for the initial dimensioning of coupled-resonator filters. This approach has some advantages: it requires very little user interaction and adaptive sampling methods [Wang 07] limit the amount of EM-simulations needed to generate the curve. Design curves can hence cheaply be generated and used for the initial dimensioning for multiple design scenarios. The curves yield initial values and an optimization is generally still required.

Chapter 8 introduces a CAD method based on scalable macromodels to model the $S$-parameters as a function of the physical design parameters within a well defined, user selected range of values. Similarly as in Chapter 7, adaptive sampling methods are used to limit the number of required EM-simulations [Chem 14a]. The fact that the scalable macromodel is numerically cheap to evaluate, reduces the time required to optimize the filters heavily. Moreover if the ranges of the design parameters are chosen broad enough, the macromodel can be used to optimize different design scenarios. Remember that broader ranges come however at the cost of longer generation times for the model. The CAD method is applied to a state-of-the art dual-band microstrip filer.

# PART I

## Coupling Matrix Approach

# 2
# Narrow-band Bandpass Filter Design based on Coupling Matrix Theory

This chapter introduces the coupling matrix theory. This theory assumes that in the vicinity of its center frequency, the distributed element microwave filter behaves as a lumped-element circuit consisting of coupled $LC$-resonators The lumped-equivalent can be represented by a coupling matrix. In this chapter we explain the synthesis of a coupling matrix for which the corresponding filter response fulfills the specifications; moreover we introduce important concepts that are related to the design methodology. Section 2.2 introduces the scattering parameters. Section 2.3 introduces the pseudo-elliptical or general Chebyshev filter functions, which are the filter functions we focus on in this work. Section 2.4 discusses the behavior of the equivalent lumped-element network used to model the filter in bandpass domain. Section 2.5 explains how the circuit is transformed to the lowpass domain. Section 2.6 shows how a coupling matrix can be constructed starting from the lowpass equivalent circuit. We show the relation between the coupling matrix representation and the state-space representation of the $Y$-parameters. In Section 2.7 we use this relation to directly synthesize the coupling matrix starting from the filter function. Finally Section 2.8 discusses how the coupling matrix can be reconfigured obtain a coupling topology that can be physically realized.

## 2.1 Introduction

The design of the microwave filters considered in this work relies on the coupling matrix theory. This design methodology assumes that in the vicinity of its center frequency, the distributed element microwave filter behaves as a lumped-element circuit consisting of coupled $LC$-resonators [Came 07b; Hong 01]. This equivalence holds in the frequency band of interest due to the limited relative bandwidth of the microwave filter. The behavior of these coupled resonator circuits can also be represented by a coupling matrix. One of the main advantages

of the coupling matrix representation is that it can easily be linked to a physical circuit topology that is capable to realize the actual filter. This chapter discusses how such a coupling matrix can be synthesized to ensure that the given design specifications, called the template of the filter, can be met. Moreover, it introduces some important concepts that are related to the design methodology and are used intensively in the remainder of this text. The physical implementation of the filters on the other hand is discussed in Chapter 3.

The electrical (design) specifications of a filter are often expressed by a frequency template or spectral mask on the scattering ($S$-) parameters introduced in Section 2.2. The design therefore typically starts by the approximation phase where a filter function is either estimated or obtained from a table to ensure that the corresponding $S$-parameters obey the frequency template. In order to reduce the complexity, the specifications are transformed to the normalized lowpass domain. In this work, we focus on the class of pseudo-elliptical or general Chebyshev filter functions [Came 82], which is introduced in Section 2.3. This class of filter functions has some interesting characteristics such as an equiripple behavior in the passband and the fact that its response can be asymmetrical with respect to the center frequency. The aim of this design methodology is to synthesize a coupling matrix that realizes the chosen the filter function. There are 2 ways to do this [Came 07b]:

- The first way starts with the synthesis of a lumped-element network that realizes the requested filter function. Next, it constructs a coupling matrix starting from the circuit element values of the network.
- The second way synthesizes a coupling matrix directly from the filter function, without the need for the circuit representation.

In this work we follow the second way, which avoids the synthesis of the lumped-element circuit. The coupling matrix represents an equivalent lumped-element circuit used to model the filter behavior in the vicinity of the center frequency. Section 2.4 introduces the equivalent lumped-element circuit in the bandpass domain. Section 2.5 explains how the network is transformed to the lowpass domain. Moreover it introduces the frequency invariant reactance (FIR) element, which has a purely imaginary admittance that does not depend on the frequency. Due to the FIR element the resonators resonate at frequencies different from the center frequency of the filter. Such filters are called asynchronously tuned filters. The FIR element is needed to realize frequency responses that are asymmetric with respect to the center frequency. Section 2.6 shows how a coupling matrix

can be constructed starting from the equivalent circuit. This section also introduces an alternative way to represent the filters frequency response namely the admittance or ($Y$-) parameter representation. We show the relation between the coupling matrix representation and the state-space representation of the $Y$-parameters. In Section 2.7 we use this relation to directly synthesize the coupling matrix starting from the filter function. The link between the coupling matrix and the state-space representation also shows that the coupling matrix is not unique. Applying an orthogonal similarity transformation to the coupling matrix preserves the filter frequency response, while it changes the coupling matrix topology (the way how resonators are coupled to each other). The coupling matrix synthesis generally results in a full coupling matrix [Came 99; Seyf 07]. It is possible to transform the full coupling matrix to a canonical form such as the arrow or the folded form. In this work we use the arrow form. Although this is a canonical form [Seyf 98] (up to sign changes), it is not always practical (and sometimes impossible) to implement it physically. Similarity transformations allow to reconfigure the coupling matrix (change the coupling topology) such that it becomes more practical to implement. Section 2.8 discusses how the coupling matrix can be reconfigured to obtain a coupling topology that can be physically realized. There are however limitations: not every filter response can be implemented by any coupling topology. The link between the filter response and the coupling topology is also discussed in this section.

## 2.2 Rational Form of the Scattering Parameters

### 2.2.1 THE SCATTERING MATRIX $\boldsymbol{S}$

We represent the filter by a two-port network as is shown in Figure 2.1, where $v_1$, $v_2$ and $i_1$, $i_2$ are the port voltages and port currents at port 1 and 2 respectively, $Z_S$ and $Z_L$ are the reference impedances at port 1 and 2 respectively and $e_S$ and $e_L$ is the source voltages at port 1 and 2 respectively. If we assume that the reference impedances are real-valued, the transmitted and reflected powerwaves at port 1 and 2 respectively are defined by [Kuro 65; Mark 92]:

$$a_1 = \frac{v_1 + Z_S i_1}{2\sqrt{Z_S}} \qquad b_1 = \frac{v_1 - Z_S i_1}{2\sqrt{Z_S}} \tag{2.1}$$

$$a_2 = \frac{v_2 + Z_L i_2}{2\sqrt{Z_L}} \qquad b_2 = \frac{v_2 - Z_L i_2}{2\sqrt{Z_L}} \tag{2.2}$$

The scattering ($S$-) parameters relate the power waves at the two ports:

$$S_{11} = \left.\frac{b_1}{a_1}\right|_{a_2=0} \qquad S_{12} = \left.\frac{b_1}{a_2}\right|_{a_1=0} \tag{2.3}$$

$$S_{21} = \left.\frac{b_2}{a_1}\right|_{a_2=0} \qquad S_{22} = \left.\frac{b_2}{a_2}\right|_{a_1=0} \tag{2.4}$$

where $a_1 = 0$ when $e_L \neq 0$, $e_S = 0$ and $a_2 = 0$ when $e_S \neq 0$, $e_L = 0$ imply a perfect match at port 1 and 2 respectively. Since the two-port system is linear time-invariant, the $S$-parameters are also frequency dependent. $S_{11}$ and $S_{22}$ are called the reflection coefficients and $S_{12}$ and $S_{21}$ the transmission coefficients. The $S$-parameters can also be grouped in the scattering ($S$-) matrix $\boldsymbol{S}$:

$$\begin{bmatrix} b_1 \\ b_2 \end{bmatrix} = \begin{bmatrix} S_{11} & S_{12} \\ S_{21} & S_{22} \end{bmatrix} \begin{bmatrix} a_1 \\ a_2 \end{bmatrix} \tag{2.5}$$

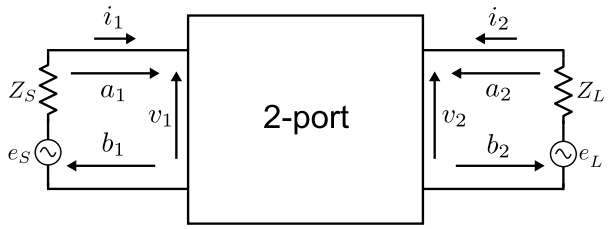


**Figure 2.1** The two-port representation of the filter.

Remark that when the two-port is excited by a current source (Figure 2.2) where $G_S$ and $G_L$ are the reference admittances and $i_S$ is the source current, the waves become

$$a_1 = \frac{G_S v_1 + i_1}{2\sqrt{G_S}} \qquad b_1 = \frac{G_S v_1 - i_1}{2\sqrt{G_S}} \tag{2.6}$$

$$a_2 = \frac{G_L v_2 + i_2}{2\sqrt{G_L}} \qquad b_2 = \frac{G_L v_2 - i_2}{2\sqrt{G_L}} \tag{2.7}$$

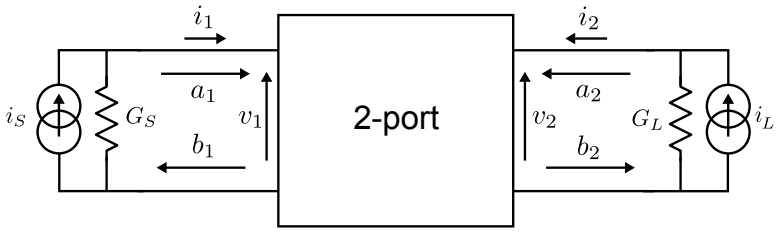


**Figure 2.2** The two-port representation of the filter excited by a current source.

### 2.2.2 *ABCD*-PARAMETERS

Sometimes it is convenient to represent the two-port by means of a cascadable formalism, to obtain that a tandem connection boils down to a matrix product. This is done using the *ABCD*-parameters or *ABCD*-matrix, which relate the current and voltage at port 2 to the current and voltage at port 1 in the following way [Poza 98]:

$$\begin{bmatrix} v_1 \\ i_1 \end{bmatrix} = \begin{bmatrix} A & B \\ C & D \end{bmatrix} \begin{bmatrix} v_2 \\ -i_2 \end{bmatrix} \tag{2.8}$$

where

$$A = \left.\frac{v_1}{v_2}\right|_{i_2=0} \qquad B = \left.\frac{v_1}{i_2}\right|_{v_2=0} \tag{2.9}$$

$$C = \left.\frac{i_1}{v_2}\right|_{i_2=0} \qquad D = -\left.\frac{i_1}{i_2}\right|_{v_2=0} \tag{2.10}$$

This representation is used to describe the behavior of $J$-inverters introduced in Section 2.4.

### 2.2.3 FILTER SPECIFICATIONS

The design of a bandpass filter starts with frequency dependent specifications given on the amplitude and sometimes phase of the scattering parameters $S_{11}$ and $S_{21}$. A template imposes a maximum amount of reflection in the passband and a minimum amount of attenuation in the stopbands (Figure 2.3). There, $\Omega$ is the angular frequency in the bandpass domain. In the remainder of this work, we will call the angular frequency just frequency for the ease of the reader and the notation. The passband is defined by the lower and upper corner frequency $\Omega_1$ and $\Omega_2$. The absolute bandwidth of the filter is $BW = \Omega_2 - \Omega_1$. The center frequency of the filter is defined by $\Omega_0 = \frac{\Omega_2+\Omega_1}{2}$. The fractional bandwidth is then defined by $FBW = \frac{\Omega_2-\Omega_1}{\Omega_0}$. A microwave bandpass filter is considered to be a narrow-band filter when its $FBW$ is less than 10 % [Swan 07b]. The lower and the upper stopbands of the filter begin at frequencies $\Omega_{s1}$ and $\Omega_{s2}$ respectively. The selectivity of the filter is defined by $k_s = \frac{\Omega_2-\Omega_1}{\Omega_{s2}-\Omega_{s1}}$(in the case the response of the filter is symmetrical with respect to $\Omega_0$). The selectivity is a measure of the steepness of the response in the transition zone located between the passband and stopband. The more selective the filter becomes, the steeper the response has to be in the transition area. For lossless filters $S_{21}$ and $S_{11}$ are related to each other due to the conservation of energy:

$$|S_{11}|^2 + |S_{21}|^2 = 1 \tag{2.11}$$

This implies that a specification on $|S_{11}|$ in the passband automatically puts a specification on $|S_{21}|$ and vice versa.

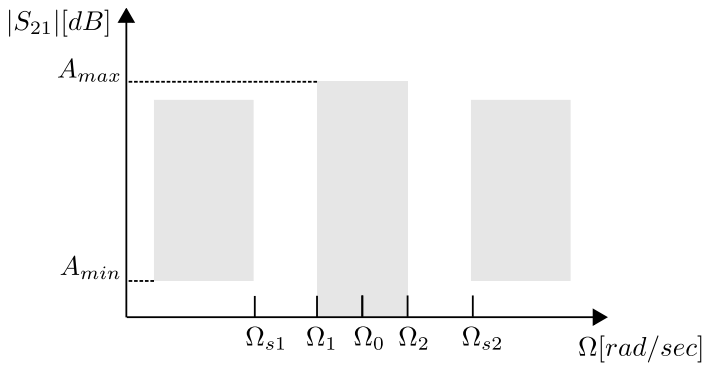


**Figure 2.3** The template imposes specifications on $|S_{21}|$. $|S_{21}|$ needs to be above $A_{max}$ for frequencies between $\Omega_1$ and $\Omega_2$ (passband) and below $A_{min}$ for frequencies below $\Omega_{s1}$ and above $\Omega_{s2}$ (stopbands).

The specifications are also often given on the insertion loss $L_A$ between port 2 and 1 and the return loss $L_R$ at port 1 which are expressed in decibel (dB) and defined by [Came 07b]:

$$\begin{aligned} L_A(\Omega) &= -20\log|S_{21}(\Omega)| \\ L_R(\Omega) &= -20\log|S_{11}(\Omega)| \end{aligned} \tag{2.12}$$

### 2.2.4 RATIONALITY OF THE $S$-PARAMETERS

The idea of designing a filter is to synthesize a rational $S$-matrix that can be realized and whose frequency dependent $S$-parameters fulfill the specifications. In order to reduce the complexity of the design, the specifications are first transformed to the lowpass domain. This halves the degree of the polynomials of the rational $S$-matrix [Poza 98]. Before we discuss the properties of the rational scattering matrix (in the lowpass domain), we introduce some notation:

- $s = \sigma + j\omega$ is the Laplace variable and $j^2 = -1$. We denote the real part of a complex number $s$ as $\mathrm{Re}(s)$ and the imaginary part as $\mathrm{Im}(s)$.
- The para-conjugate polynomial $p^*(s)$ of the polynomial $p(s) = \Sigma_{k=0}^{N} a_k s^k$ (where the $a_k$ are complex numbers) is defined by

$$p^*(s) = \sum_{k=0}^{n} \overline{a_k}(-s)^k \tag{2.13}$$

  where $\overline{a_k}$ is the complex conjugate of $a_k$. Remark that when the polynomials are evaluated on the imaginary axis ($s = j\omega$), $p^*(j\omega) = \overline{p(j\omega)}$.

- If $\boldsymbol{A}$ is a matrix, we denote its transpose as $\boldsymbol{A}^t$ and its Hermitian transpose as $\boldsymbol{A}^H = \overline{\boldsymbol{A}^t}$.

When a filter is passive and loss-less, the corresponding $S$-matrix describing the filter response verifies [Ande 73]:

$$\boldsymbol{S}(j\omega)\boldsymbol{S}^H(j\omega) = \boldsymbol{I}_2 \tag{2.14}$$

$$\boldsymbol{I}_2 - \boldsymbol{S}(s)\boldsymbol{S}^H(s) \geq 0 \text{ , for } \sigma \geq 0 \text{ (in the left half plane)} \tag{2.15}$$

where $\boldsymbol{I}_2$ is the $2 \times 2$ identity matrix and the operator $\geq$ is to be taken in the semi-positive definite matrix sense.

It can be shown that a $2\times2$, rational, loss-less and reciprocal matrix of McMillan degree $N$ (Section 2.7.2), which goes to the identity matrix at infinity, can always be written in the Belevitch form [Bele 68; Seyf 07]:

$$\boldsymbol{S}(s) = \frac{1}{E(s)} \begin{bmatrix} F(s) & P(s) \\ P(s) & (-1)^N F^*(s) \end{bmatrix} \tag{2.16}$$

where $F$ is monic (highest coefficient equal to 1) and has degree $N$. $P$ is of degree $n_{fz} < N$, where $n_{fz}$ is the number of transmission zeros at finite frequencies. The fact that $\boldsymbol{S}$ goes to the identity matrix at infinity implies that $n_{fz} < N$ and that $E$ is also monic. Because $\boldsymbol{S}$ is reciprocal, we have that $P = (-1)^{N+1} P^*$ (para-conjugated) . Therefore the zeros of $P$ must lie symmetrically with respect to the imaginary axis in the Laplace plane [Bele 68; Came 07b]. Since the $S$-parameters are stable, $E$ must have all of its roots in the left half-plane (Hurwitz polynomial). $E$ can be expressed as a function of $F$ and $P$ using the conservation of energy (2.11):

$$F(s)F^*(s) + P(s)P^*(s) = E(s)E^*(s) \tag{2.17}$$

Hence, $\boldsymbol{S}$ is fully characterized by the two numerator polynomials $F$ and $P$. If the roots of $F$ and $P$ are known, (2.17) allows to determine the roots of $EE^*$. Since $E$ is a Hurwitz polynomial, the roots of $EE^*$ that lie in the left half-plane are the roots of $E$. The squared modulus of the transmission coefficient $|S_{21}|^2$ can also be expressed as a function of $F$ and $P$:

$$|S_{21}|^2 = \frac{PP^*}{EE^*} = \frac{1}{1 + \frac{FF^*}{PP^*}} = \frac{1}{1 + |\frac{F}{P}|^2} \tag{2.18}$$

The function $K_N = \frac{F}{P}$ is called the filter function. To fulfill the specifications on the $S$-parameters, a suitable rational filter function is chosen and its numerator and denominator are derived. Different classes of predefined filter functions exist such as Chebyshev, elliptic and Butterworth filter functions. In this work we will focus on the general class of Chebyshev filter functions, also called the pseudo-elliptical filter function [Came 82] as introduced below.

## 2.3 The Pseudo-elliptical Filter Function

The pseudo-elliptical filter function is also called the general Chebyshev filter function because of its equiripple behavior in the passband. All of its reflection zeros lie on the imaginary axis in the passband [Came 82]. This class of filter functions also allows to place transmission zeros at finite frequencies, as long as they come in symmetric pairs with respect to the imaginary axis (paraconjugated character of $P$). This is convenient to realize characteristics that are asymmetrical with respect to $\omega = 0$, when the zeros are placed on the imaginary axis in an asymmetric way. This type of characteristic is what we we want to realize in this thesis. The zeros are chosen in such a way that the template specifications are met. The number of transmission zeros $n_{fz}$ which can be placed by the type of filters considered in this work is maximally $N-2$ for a filter of order $N$. This is a direct consequence of the 'shortest path rule' (Theorem 1) which is explained in Section 2.8.

The transmission zeros can also be complex (not purely imaginary). This improves the phase and group delay response of the filter at the cost of a decreased attenuation in the stopband [Came 07b].

### 2.3.1 SYNTHESIS OF THE FILTER FUNCTION

The pseudo-elliptical filter function has the form [Came 82]:

$$K_N(\omega) = \frac{F_1(\omega)}{P_1(\omega)} = \cosh[\sum_{k=1}^{N} \cosh^{-1}(x_k(\omega))] \tag{2.19}$$

$x_k$ is a function of the frequency variable $\omega$ and is given by:

$$x_k = \frac{\omega - \frac{1}{\omega_k}}{1 - \frac{\omega}{\omega_k}} \tag{2.20}$$

where $\omega_k$ is a prescribed transmission zero located at a finite frequency ($s_k = j\omega_k$) or a zero at an infinite frequency ($\omega_k = \pm\infty$). Remark that $K_N$ is a function of $\omega$ (not of $j\omega$).

When all of the transmission zeros are placed at an infinite frequency, the filter function becomes the classical Chebyshev filter function:

$$K_N(\omega)\Big|_{\omega_k \to \infty, \forall k \in \{1,\ldots,N\}} = \cosh[N \cosh^{-1}(\omega))] \tag{2.21}$$

As explained in Section 2.2, $S_{11}$ and $S_{21}$ can be written as

$$S_{11}(\omega) = \frac{F_1(\omega)}{E_1(\omega)} \qquad \text{and} \qquad S_{21}(\omega) = \frac{P_1(\omega)}{\varepsilon E_1(\omega)}$$

where the polynomials are monic. Note that $F_1$, $P_1$ and $E_1$ are functions of $\omega$. $\varepsilon$ is a constant whose value is related to the minimal return loss $RL$ (expressed in dB) in the passband as follows:

$$\varepsilon = (10^{\frac{RL}{10}} - 1)^{-\frac{1}{2}} \left| \frac{P_1(1)}{F_1(1)} \right| \tag{2.22}$$

where $\frac{P_1}{F_1}$ is evaluated at the edge of the passband $\omega = 1$. The return loss is linked to $S_{11}$ by (2.12). The minimum return loss $RL$ is the inverse of the amplitude of the maximum reflection in the passband (2.12). Since the passband is equiripple, the amplitude of the reflection becomes maximal at its edges. Therefore $P_1$ and $F_1$ are evaluated in $\omega = 1$ in (2.22).

Since the transmission zeros of $P_1$ (the poles of $K_N$) are prescribed, the computation of the coefficients of $P_1$ is straightforward. Different recursion relations are formed in the literature to determine the coefficients of $F_1$ [Amar 00b; Came 82]. The recursion relations are not repeated here. To obtain the coefficients of $F$, $P$ and $E$, the coefficient of $\omega^k$ must be divided by $j^k$ to obtain the coefficient for $s^k$.

### 2.3.2 EXAMPLES

This section discusses two examples to clarify what was explained above: an asymmetrical and symmetrical filter function are selected. We denote a filter in the lowpass domain of order $N$ having $n_{fz}$ finite transmission zeros as a $(N, n_{fz})$ filter.

#### Asymmetric (6,2) Pseudo-Elliptic Filter

The first example is a filter function of order 6 with 2 prescribed finite transmission at $\omega = 1.3$ and $\omega = 1.8$. The equiripple return loss in the passband is $RL = 22$ dB, which corresponds to $\varepsilon = 4.4777$. Figure 2.4 shows the magnitude of the corresponding transmission and reflection coefficients. Figure 2.5 shows the corresponding transfer zeros, reflection zeros and poles. The coefficients of

the polynomials are complex.

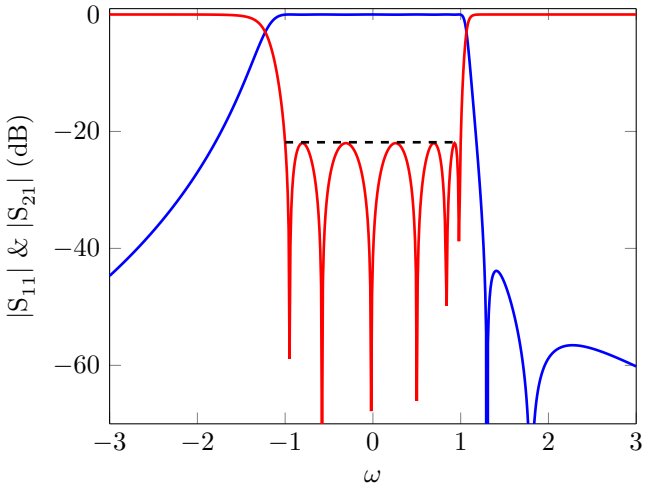


**Figure 2.4** Magnitude of $S_{11}$ (—) and $S_{21}$ (—) of (6-2) asymmetric pseudo-elliptical filter in the lowpass domain, with $RL = 22$ dB and finite transmission zeros at $\omega = 1.3$ and $\omega = 1.8$.

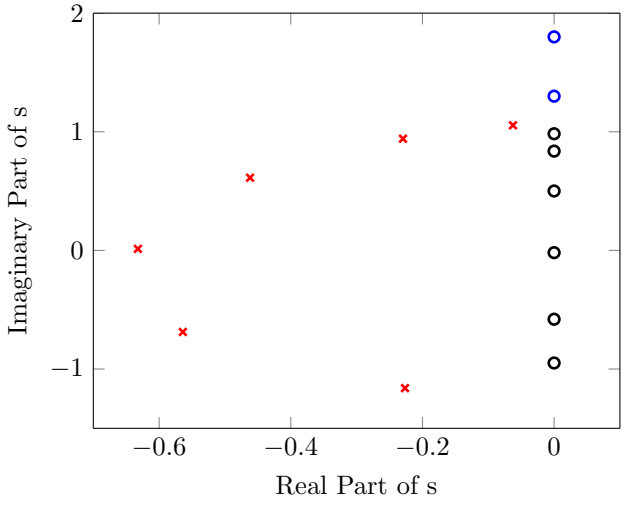


**Figure 2.5** Pole-zero map of the transmission and reflection coefficients for a (6-2) asymmetric pseudo-elliptical filter in the lowpass domain. The transmission zeros are shown in blue (o), the reflection zeros in black (o) and the poles in red (x).

Symmetric (8,4) Pseudo-Elliptic Filter

The second example is a filter function of order 8 with 4 prescribed finite transmission at $\omega = \pm 1.2$ and $\omega = \pm 1.5$. The equiripple return loss in the band is $RL = 20$ dB, which corresponds to $\varepsilon = 19.1338$. The zeros of both $P(s)$ and $F(s)$ lie on the imaginary axis symmetrically with respect to the real axis (Figure 2.7). Figure 2.6 shows the magnitude of the corresponding transmission and reflection coefficients. The coefficients of the polynomials are real.

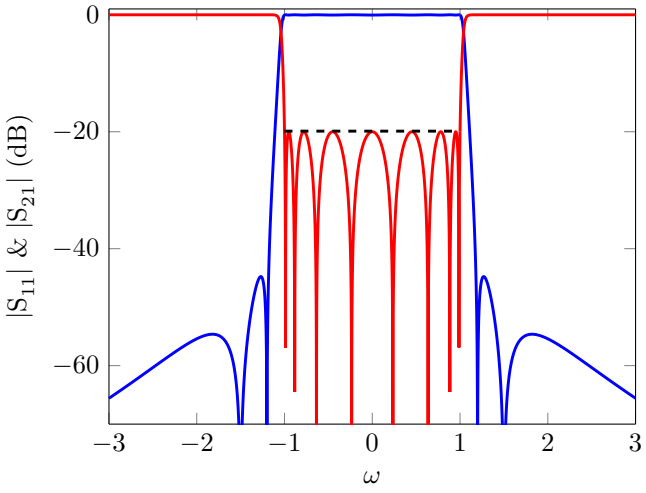


**Figure 2.6** Magnitude of $S_{11}$ (—) and $S_{21}$ (—) of (8-4) symmetric pseudo-elliptical filter in the lowpass domain, with $RL = 20$ (- - -) dB and finite transmission zeros at $\omega = \pm 1.2$ and $\omega = \pm 1.5$.

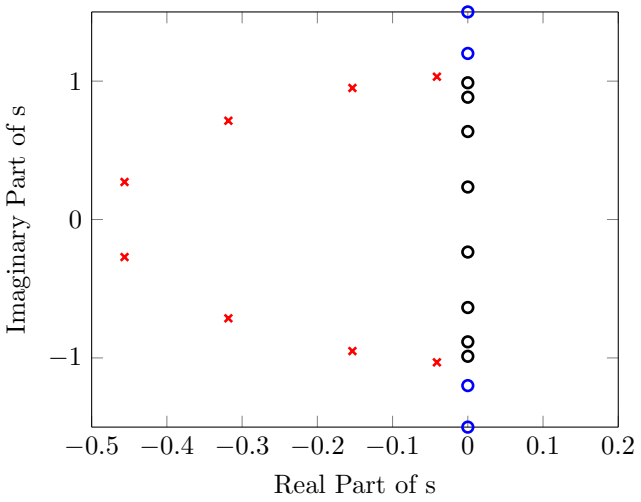


**Figure 2.7** Pole-zero map of the transmission and reflection coefficients for a (8-4) symmetric pseudo-elliptical filter in the lowpass domain. The transmission zeros are shown in blue (o), the reflection zeros in black (o) and the poles in red (x).

## 2.4 Equivalent Lumped Bandpass Network

In the vicinity of its center frequency $\Omega_0$, the behavior of an $N^{th}$ order narrowband bandpass microwave filter can be modeled using an equivalent network that consists of $N$ parallel $LC$ resonators (Figure 2.8) [Came 07b; Hong 01; Matt 64]. Each resonator $k$ consists of a shunt inductor $L'_k$ in parallel with a capacitor $C'_k$ and conductance $G'_k$ (in the case of losses). The resonators are coupled to each other through mutual capacitances $C'_{lk} = C'_{kl}$. The behavior of the mutual capacitance is described using an $ABCD$-matrix formalism (Section 2.2.2). It relates the current $i_1$ flowing in the inverter at port 1 and the voltage $u_1$ presented at port 1 to the current $i_2$ flowing in the inverter at port 2 and the voltage $u_2$ presented at port 2:

$$\begin{bmatrix} u_1 \\ i_1 \end{bmatrix} = \begin{bmatrix} 0 & \frac{1}{j\Omega C'_{12}} \\ j\Omega C'_{12} & 0 \end{bmatrix} \begin{bmatrix} u_2 \\ -i_2 \end{bmatrix} \tag{2.23}$$

An equivalent circuit of the mutual capacitance is shown in Figure 2.9 [Mont 48].

In the case of asynchronously tuned filters, the resonant frequency of the individual resonators $\Omega_k = \frac{1}{\sqrt{L'_k C'_k}}$ does not correspond to $\Omega_0$ for all resonators. The first resonator is coupled to the source by a mutual capacitance $C'_{S1}$. Similarly,

the $Nth$ resonator is coupled to the load by a mutual capacitance $C'_{NL}$. In the case of a lossless filters, all of the conductances are zero ($G'_1 = \ldots = G'_N = 0$). Applying Kirchoff's Current Law in every node yields the following result:

$$\begin{bmatrix} i_S \\ 0 \\ 0 \\ \vdots \\ 0 \\ 0 \end{bmatrix} = \boldsymbol{A}_{BP} \begin{bmatrix} U_S \\ U_1 \\ U_2 \\ \vdots \\ U_N \\ U_L \end{bmatrix} \tag{2.24}$$

where

$$\boldsymbol{A}_{BP} = \begin{bmatrix} G_S & j\Omega C'_{S1} & 0 & \ldots & 0 & 0 \\ j\Omega C'_{S1} & Y'_1 & j\Omega C'_{12} & \ldots & j\Omega C'_{1N} & 0 \\ 0 & j\Omega C'_{12} & Y'_2 & \ldots & j\Omega C'_{2N} & 0 \\ \vdots & \vdots & & \ddots & & \vdots \\ 0 & j\Omega C'_{1N} & j\Omega C'_{2N} & \ldots & Y'_N & j\Omega C'_{LN} \\ 0 & 0 & 0 & \ldots & j\Omega C'_{LN} & G_L \end{bmatrix} \tag{2.25}$$

with

$$Y'_k = j\Omega C'_k + \frac{1}{j\Omega L'_k} + G'_k \tag{2.26}$$

The network shown in Figure 2.8 models the filter in the bandpass domain ($\Omega$). Since the rational $S$-matrix is synthesized in the normalized lowpass domain ($\omega$), we need to also transform the network to the lowpass domain.

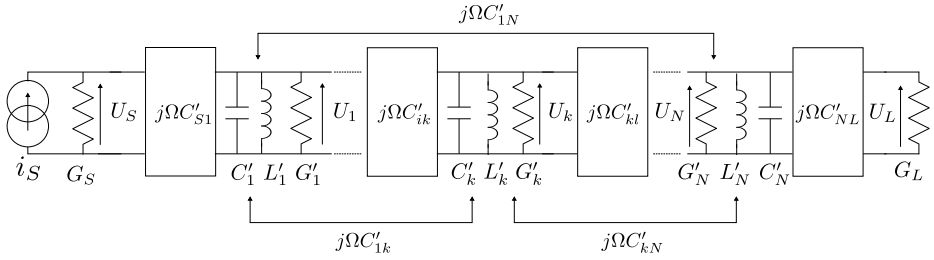


**Figure 2.8** Equivalent lumped-element bandpass network of the microwave filter in the vicinity of $\Omega_0$.

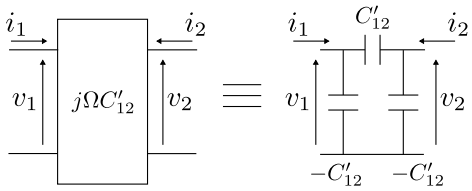


**Figure 2.9** Equivalent circuit of mutual capacitive coupling $C'_{12}$.

## 2.5 Equivalent Lumped Lowpass Network

### 2.5.1 LINEARIZATION AROUND $\Omega_0$

In order to obtain an equivalent lowpass network, the behavior of the bandpass network is first linearized over the frequency around $\Omega_0$. Next, the frequency is scaled and shifted to transform the passband to [-1,1]. The linearization relies on the hypothesis that the actual microwave filter is sufficiently narrow-band to allow for an accurate linearization. Since the bandpass network only models the behavior of the filter in the vicinity of $\Omega_0$, we may assume that $\frac{\Omega-\Omega_0}{\Omega_0} << 1$ allowing us to linearize $\frac{1}{\Omega}$ as:

$$\begin{aligned}\frac{1}{\Omega} &= \frac{1}{\Omega_0(1+\frac{(\Omega-\Omega_0)}{\Omega_0})} \\ &\approx \frac{1}{\Omega_0}(1-\frac{(\Omega-\Omega_0)}{\Omega_0}) \\ &= \frac{2}{\Omega_0}-\frac{\Omega}{\Omega_0^2}\end{aligned} \tag{2.27}$$

Using (2.27) the admittance $Y'_k$ of the $k^{th}$ resonator (2.31) is approximated as:

$$G'_k + j\Omega C'_k + \frac{1}{j\Omega L'_k} \approx G'_k + j\Omega(C'_k + \frac{1}{L'_k\Omega_0^2}) - j\frac{2}{L'_k\Omega_0} \tag{2.28}$$

The term $-j\frac{2}{L'_k\Omega_0}$ does not depend on the frequency. Its corresponding circuit element is called a frequency-invariant reactive (FIR) element [Came 07b]. This hypothetical element is needed to model the frequency offset between the resonance frequency $\Omega_k$ of the filter and the center frequency $\Omega_0$ of the filter in the case of an asynchronously tuned $k^{th}$ resonator. Based on the narrow-

band hypothesis, the coupling between resonators is seen to become frequency independent too:

$$j\Omega C'_{kl} \approx j\Omega_0 C'_{kl} = jC_{kl} \tag{2.29}$$

Shifting and scaling the frequency $\Omega$, transforms $\Omega$ to the lowpass frequency $\omega$ such that the pass-band of the filter corresponds to the frequency range $\omega \in [-1, 1]$. To this end we define $\omega$ as follows:

$$\omega = \frac{2}{\Omega_2 - \Omega_1}(\Omega - \Omega_0) = \frac{2}{BW}(\Omega - \Omega_0) \tag{2.30}$$

Using (2.30) we can now express the impedance under the linearized approximation (2.28) as a function of $\omega$:

$$G'_k + j\omega\frac{BW}{2\Omega_0}(C'_k\Omega_0 + \frac{1}{L'_k\Omega_0}) + j(C'_k\Omega_0 - \frac{1}{L'_k\Omega_0}) = G_k + j\omega C_k + jB_k \tag{2.31}$$

where

$$\begin{aligned} G_k &= G'_k \\ C_k &= \frac{FBW}{2}(C'_k\Omega_0 + \frac{1}{L'_k\Omega_0}) \\ B_k &= (C'_k\Omega_0 - \frac{1}{L'_k\Omega_0}) \end{aligned} \tag{2.32}$$

Note that because $G_k$ is frequency invariant, it remains unchanged under the transformation. Also note that when $\frac{1}{\sqrt{L'_k C'_k}} = \Omega_0$, there is no frequency offset with respect to $\Omega_0$ and thus $B_k = 0$. Applying Kirchoff's Current Law in every node of the network of Figure 2.10 yields the following result:

$$\begin{bmatrix} i_S \\ 0 \\ 0 \\ \vdots \\ 0 \\ 0 \end{bmatrix} = \boldsymbol{A}_{LP} \begin{bmatrix} U_S \\ U_1 \\ U_2 \\ \vdots \\ U_N \\ U_L \end{bmatrix} \tag{2.33}$$

where

$$\boldsymbol{A}_{LP} = \begin{bmatrix} G_S & jC_{S1} & 0 & \dots & 0 & 0 \\ jC_{S1} & Y_1 & jC_{12} & \dots & jC_{1N} & 0 \\ 0 & jC_{12} & Y_2 & \dots & jC_{2N} & 0 \\ \vdots & \vdots & & \ddots & & \vdots \\ 0 & jC_{1N} & jC_{2N} & \dots & Y_N & jC_{LN} \\ 0 & 0 & 0 & \dots & jC_{LN} & G_L \end{bmatrix} \tag{2.34}$$

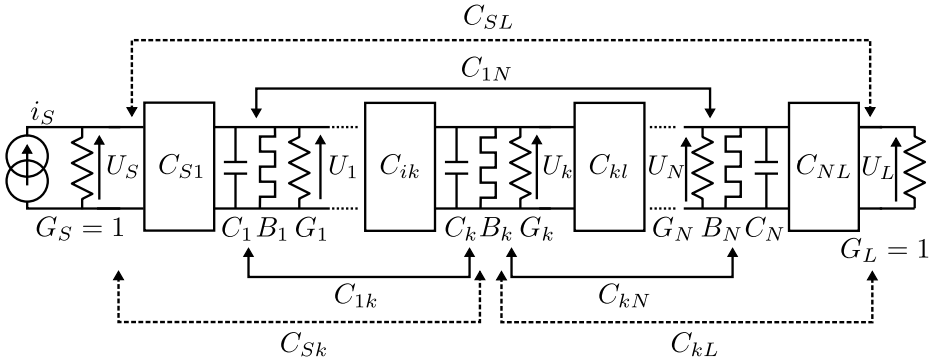


**Figure 2.10** Equivalent lumped-element lowpass network of the microwave filter in the normalized lowpass domain $\omega$. The dashed arrows model the possible presence of source-to-resonator $C_{Sk}$, load-to-resonator $C_{kL}$ and direct source-to-load $C_{SL}$ coupling.

Equations (2.33) and (2.34) describe the behavior of the equivalent lumped-element network in the normalized lowpass domain $\omega$ as is shown in Figure 2.10.

The frequency independent coupling $jC_{kl}$, behaves as admittance or $J$- inverter [Hong 01]. This behavior is described by an $ABCD$-matrix which relates the current $i_1$ flowing in the inverter at port 1 and the voltage $u_1$ presented at port 1 to the current $i_2$ flowing in the inverter at port 2 and the voltage $u_2$ present at port 2 (Figure 2.11):

$$\begin{bmatrix} u_1 \\ i_1 \end{bmatrix} = \begin{bmatrix} 0 & \pm\frac{1}{jJ} \\ \mp jJ & 0 \end{bmatrix} \begin{bmatrix} u_2 \\ -i_2 \end{bmatrix} \tag{2.35}$$

When an admittance inverter $J$ is terminated in an impedance $Y_2$ at one port, one sees an admittance $Z_1 = \frac{J^2}{Y_1}$ when looking from the other port [Matt 64] (Figure 2.12). This last property is used to normalize the source and load admittance $G_S$ and $G_L$ to one by choosing $M_{S1} = \sqrt{G_S}$ and $M_{LN} = \sqrt{G_L}$.

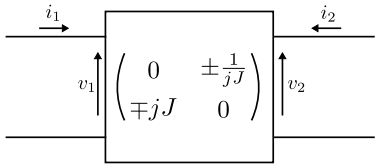


**Figure 2.11** Behavior of an admittance or $J-$ inverter.

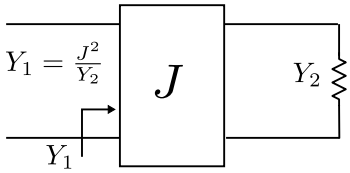


**Figure 2.12** Admittance $Y_1 = \frac{J^2}{Y_2}$ seen from port 1, when a $J$-inverter is terminated in $Y_2$.

In some microwave filters however, the source is not only coupled to the first resonator but also to other resonators (source-to-resonator $k$ coupling). Similarly, the load can be coupled to other resonators than the $N^{th}$ resonator (load-to-resonator $k$ coupling). It is even possible that there is a direct coupling between the source and the load. In that case the matrix $\boldsymbol{A}_{LP}$ (2.34) becomes:

$$\boldsymbol{A}_{LP,SL} = \begin{bmatrix} G_S & jC_{S1} & jC_{S2} & \dots & jC_{SN} & jC_{SL} \\ jC_{S1} & Y_1 & jC_{12} & \dots & jC_{1N} & jC_{L1} \\ jC_{S2} & jC_{12} & Y_2 & \dots & jC_{2N} & jC_{L2} \\ \vdots & \vdots & & \ddots & & \vdots \\ jC_{SN} & jC_{1N} & jC_{2N} & \dots & Y_N & jC_{LN} \\ jC_{SL} & jC_{L1} & jC_{L2} & \dots & jC_{LN} & G_L \end{bmatrix} \tag{2.36}$$

Although we do not synthesize coupling structures for a source-to-resonator $k$ and load-to-resonator $k$ coupling, such couplings can be present in the actual mi-

crowave filter. We already mention them here as they will prove to be important in the remainder of the text.

### 2.5.2 DISCUSSION OF THE EQUIVALENT NETWORK BEHAVIOR

Due to the linearization of the term $\frac{1}{\Omega}$ (2.27) the order of the equivalent lowpass network is halved (2.28) with respect to the bandpass filter. For the bandpass lumped-element network (and thus for the actual microwave filter) the resonant frequency of each resonator is double namely $\Omega_k$ and $-\Omega_k$. This is no longer the case for the equivalent lowpass network. The introduction of the FIR element $B_k$ accounts for the difference in resonant frequency of the $LC$-resonators in the bandpass domain and the filter center frequency $\Omega_0$.

Section 2.6 introduces the coupling matrix representation of the lumped-element circuit. This representation will be used here to implement the microwave filter. Techniques exist to synthesize a lumped-element network from the polynomials $F$,$P$ and $E$ [Bele 68]. The synthesis techniques are not discussed in this work, as we will synthesize the coupling matrix directly from $F$,$P$ and $E$ instead and will hereby avoid the synthesis of the network all together.

### 2.5.3 LINK TO THE CLASSICAL BANDPASS-TO-LOWPASS TRANSFORMATION

In classical network synthesis a different bandpass-to-lowpass frequency transformation is often used to go from the bandpass to the lowpass domain:

$$\omega = \frac{1}{FBW}\left(\frac{\Omega}{\Omega_0} - \frac{\Omega_0}{\Omega}\right) \tag{2.37}$$

The advantage of the classical bandpass-to-lowpass transformation is that it transforms all lowpass circuit elements to bandpass resonators resonating at $\Omega_0$, which is the case for all the symmetrical responses. In microwave filters having asymmetrical responses, the resonators are not synchronously tuned. The transformation given by (2.37) also yields the equivalent lumped lowpass network presented in Section 2.5 if FIR elements are included in the bandpass domain to model the offset between individual resonant frequency of resonator and the center frequency of the filter [Came 07b]. Note that the classical transformation transforms the positive (around $\Omega_0$) and negative (around $-\Omega_0$) bandpass image to the lowpass domain. The linearization as is used here only takes the positive bandpass behavior around $\Omega_0$ into account. Both transformations result in a lowpass prototype that has half the order of the original bandpass filter.

## 2.6 Coupling Matrix Representation

This section introduces the coupling matrix representation of coupled-resonator filters. One of the benefits is that matrix operations such as an inversion or a similarity transformation can be applied to the coupling matrix directly resorting to network transformations. These operations simplify both the analysis and the synthesis of the microwave filter.

Moreover the coupling matrix elements can easily be linked to the elements in the microwave filter, which simplifies the diagnosis as well as the tuning.

We discuss next how the coupling matrix can be derived from the lowpass lumped-element circuit. This coupling matrix used here is referred to as the $N+2$ coupling matrix, as it also contains source-to-resonator $k$ coupling, load-to-resonator $k$ coupling and source-to-load coupling [Came 03]. At the end of this section we introduce the admittance ($Y$-) parameters and use them to discuss the relation between the coupling matrix and the state-space representation based on the $Y$-parameters. In Section 2.7 we use this relation to synthesize the coupling matrix from $F$,$P$ and $E$.

### 2.6.1 THE $N+2$ COUPLING MATRIX

Dividing row $k \in \{2,\ldots,N\}$ by $\sqrt{C_{k-1}}$ and dividing column $l \in \{2,\ldots,N\}$ by $\sqrt{C_{l-1}}$ normalizes the set of equations given in (2.33) and (2.34). The normalized matrix $\boldsymbol{A}_{LP}$ becomes:

$$
\begin{aligned}
\boldsymbol{A} &= \begin{bmatrix}
1 & j\frac{C_{S1}}{\sqrt{C_1}} & 0 & \dots & 0 & 0 \\
j\frac{L_{S1}}{\sqrt{C_1}} & j\omega + j\frac{B_1}{C_1} + \frac{G_1}{C_1} & j\frac{C_{12}}{\sqrt{C_1 C_2}} & \dots & \frac{C_{1N}}{\sqrt{C_1 C_N}} & 0 \\
0 & j\frac{C_{12}}{\sqrt{C_1 C_2}} & j\omega + j\frac{B_2}{C_2} + \frac{G_2}{C_2} & \dots & j\frac{C_{2N}}{\sqrt{C_2 C_N}} & 0 \\
\vdots & \vdots & & \ddots & & \vdots \\
0 & j\frac{C_{1N}}{\sqrt{C_1 C_N}} & j\frac{C_{2N}}{\sqrt{C_2 C_N}} & \dots & j\omega + j\frac{B_N}{C_N} + \frac{G_N}{C_N} & j\frac{C_{LN}}{\sqrt{C_N}} \\
0 & 0 & 0 & \dots & j\frac{C_{LN}}{\sqrt{C_N}} & 1
\end{bmatrix} \\
&= \begin{bmatrix}
1 & jM_{S1} & 0 & \dots & 0 & 0 \\
jM_{S1} & j\omega + jM_{11} + \frac{G_1}{C_1} & jM_{12} & \dots & jM_{1N} & 0 \\
0 & jM_{12} & j\omega + jM_{22} + \frac{G_2}{C_2} & \dots & jM_{2N} & 0 \\
\vdots & \vdots & & \ddots & & \vdots \\
0 & jM_{1N} & jM_{2N} & \dots & j\omega + jM_{NN} + \frac{G_N}{C_N} & jM_{LN} \\
0 & 0 & 0 & \dots & jM_{LN} & 1
\end{bmatrix} \\
&= \boldsymbol{M} + \boldsymbol{G} + j\omega\tilde{\boldsymbol{I}}_{\boldsymbol{N+2}}
\end{aligned}
\tag{2.38}
$$

Herein, the matrix $\boldsymbol{M}$ is called the $N+2$ coupling matrix, which is obtained as:

$$
\boldsymbol{M} = \begin{bmatrix}
1 & jM_{S1} & 0 & \dots & 0 & 0 \\
jM_{S1} & jM_{11} & jM_{12} & \dots & jM_{1N} & 0 \\
0 & jM_{12} & jM_{22} & \dots & jM_{2N} & 0 \\
\vdots & \vdots & & \ddots & & \vdots \\
0 & jM_{1N} & jM_{2N} & \dots & jM_{NN} & jM_{LN} \\
0 & 0 & 0 & \dots & jM_{LN} & 1
\end{bmatrix}
\tag{2.39}
$$

The inner part of $\boldsymbol{M}$ containing rows $k \in \{2, \dots, N+1\}$ and columns $l \in \{2, \dots, N+1\}$) describes the inter-resonator coupling and is defined as the $N \times N$ coupling matrix. The diagonal elements $M_{kk}$ define the self-couplings. A coupling $M_{k(k+1)}$ is called a sequential coupling and a coupling $M_{lk}$ ($k \neq l+1$,resonator $l$ and $k$ are not adjacent) is called a cross-coupling.

The matrix $\boldsymbol{G}$ contained in (2.38) is a diagonal matrix of size $(N+2) \times (N+2)$ where the diagonal elements are $\frac{G_k}{C_k}$ and the first and last elements of the diagonal are 0. Writing $G_k$ and $C_k$ as a function of the bandpass equivalent elements yields (2.32)):

$$\frac{G_k}{C_k} = \frac{1}{Q_k}\frac{1}{FBW} \tag{2.40}$$

These elements can be interpreted as the inverse of the quality factor $Q_k$ of the $k^{th}$ $LC$ resonator of the bandpass equivalent if the non-diagonal coupling elements are purely imaginary [Came 07b]. The matrix $\tilde{\boldsymbol{I}}_{\boldsymbol{N+2}}$ is an identity matrix of size $(N+2)\times(N+2)$ where the first and last elements of the diagonal are 0. Figure 2.13 shows the equivalent network that is represented by the matrix $\boldsymbol{A}$.

To denormalize the bandwidth of the coupling matrix, it suffices to multiply the inter-resonator couplings $M_{kl}$ and frequency offsets $M_{kk}$ by $FBW$ and the source-to-resonator and load-to-resonator coupling by $\sqrt{FBW}$ (2.32).

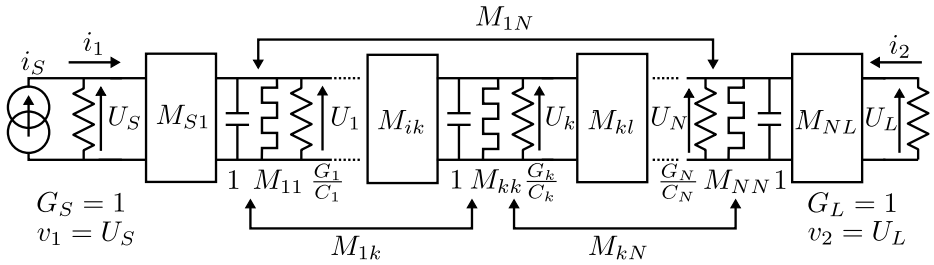


**Figure 2.13** Equivalent lumped-element lowpass network of the microwave filter that is represented by the matrix $\boldsymbol{A}$

### 2.6.2 $S$-PARAMETERS AS A FUNCTION OF $\boldsymbol{A}$

It is possible to express the $S$-parameters as a function of $\boldsymbol{A}^{-1}$. Multiplying both sides of (2.33) by $\boldsymbol{A}^{-1}$ yields:

$$\boldsymbol{A}^{-1}\begin{bmatrix} i_S \\ 0 \\ 0 \\ \vdots \\ 0 \\ 0 \end{bmatrix} = \begin{bmatrix} U_S \\ U_1 \\ U_2 \\ \vdots \\ U_N \\ U_L \end{bmatrix} \tag{2.41}$$

Which allows to write:

$$\begin{aligned} U_S &= [\boldsymbol{A}^{-1}]_{1,1} i_S \\ U_L &= [\boldsymbol{A}^{-1}]_{N+2,1} i_S \end{aligned} \tag{2.42}$$

where $[\boldsymbol{A}]_{k,l}$ denotes element $(k,l)$ of the matrix $\boldsymbol{A}$. Since $G_S = G_L = 1$, we also have that (Figure 2.13):

$$\begin{aligned} i_1 &= i_S - U_S \\ i_2 &= -v_2 = -U_L \end{aligned} \tag{2.43}$$

Using the definitions for the $S$-parameters for a normalized impedance ($Z_S = Z_L = 1$) ((2.4)) we write:

$$\begin{aligned} S_{11} &= \frac{v_1 - i_1}{v_1 + i_1} = \frac{U_S - i_1}{i_S} \\ &= \frac{U_S - (i_S - U_S)}{i_S} \\ &= \frac{i_S(2[\boldsymbol{A}^{-1}]_{1,1} - 1)}{i_S} \\ &= 2[\boldsymbol{A}^{-1}]_{1,1} - 1 \end{aligned} \tag{2.44}$$

$$\begin{aligned} S_{21} &= \frac{v_2 - i_2}{v_1 + i_1} = \frac{U_L - i_2}{i_S} \\ &= \frac{2U_L}{i_S} \\ &= \frac{i_S(2[\boldsymbol{A}^{-1}]_{N+2,1})}{i_S} \\ &= 2[\boldsymbol{A}^{-1}]_{N+2,1} \end{aligned} \tag{2.45}$$

To calculate $S_{12}$ and $S_{22}$ as a function of the elements of $\boldsymbol{A}^{-1}$, an ideal current source providing current $i_L$ in parallel with a normalized conductance $G_L = 1$ must be presented at port 2 and port 1 must be terminated in a normalized conductance $G_S = 1$. This yields:

$$\begin{aligned} i_1 &= -v_1 = -U_S \\ i_2 &= i_L - U_L \end{aligned} \tag{2.46}$$

$$\begin{aligned} S_{22} &= \frac{v_2 - i_2}{v_2 + i_2} = \frac{U_L - i_2}{i_L} \\ &= \frac{i_L(2[\boldsymbol{A}^{-1}]_{N+2,N+2} - 1)}{i_L} \\ &= 2[\boldsymbol{A}^{-1}]_{N+2,N+2} - 1 \end{aligned} \tag{2.47}$$

$$\begin{aligned} S_{12} &= \frac{v_1 - i_1}{v_2 + i_2} = \frac{U_S - i_2}{i_L} \\ &= \frac{i_L(2[\boldsymbol{A}^{-1}]_{1,N+2})}{i_L} \\ &= 2[\boldsymbol{A}^{-1}]_{1,N+2} \end{aligned} \tag{2.48}$$

Expressions (2.44), (2.45), (2.47) and (2.48) will be used to calculate the sensitivity of the $S$-parameters with respect to the the elements of the coupling matrix $\boldsymbol{M}$ (2.39).

### 2.6.3 LINK TO THE STATE-SPACE REPRESENTATION

#### The Admittance Matrix $\boldsymbol{Y}$

When the filter is represented by a linear time-invariant two-port network (Figure 2.1), the admittance ($Y$-) parameters relate the input port voltage $v_1$ and output port voltage $v_2$ to the input port current $i_1$ and output port current $i_2$ [Poza 98]:

$$Y_{11} = \left.\frac{i_1}{v_1}\right|_{v_2=0} \qquad Y_{12} = \left.\frac{i_1}{v_2}\right|_{v_1=0} \tag{2.49}$$

$$Y_{21} = \left.\frac{i_2}{v_1}\right|_{v_2=0} \qquad Y_{22} = \left.\frac{i_2}{v_2}\right|_{v_1=0} \tag{2.50}$$

The $Y$-parameters can also be grouped in the admittance matrix $\boldsymbol{Y}$:

$$\begin{bmatrix} i_1 \\ i_2 \end{bmatrix} = \begin{bmatrix} Y_{11} & Y_{12} \\ Y_{21} & Y_{22} \end{bmatrix} \begin{bmatrix} v_1 \\ v_2 \end{bmatrix} = \boldsymbol{Y} \begin{bmatrix} v_1 \\ v_2 \end{bmatrix} \tag{2.51}$$

Note that the $\boldsymbol{Y}$-matrix models the behavior of the filter as a function of frequency. An equivalent representation of the dynamics contained in the $Y$-parameters is contained in the state-space representation.

STATE-SPACE REPRESENTATION OF THE EQUIVALENT LOWPASS NETWORK
The state-space representation [Kail 80] of the $Y$-parameter matrix is:

$$\begin{aligned} \dot{\boldsymbol{x}}(t) &= \boldsymbol{A}_Y \boldsymbol{x}(t) + \boldsymbol{B}_Y \begin{bmatrix} v_1(t) \\ v_2(t) \end{bmatrix} \\ \begin{bmatrix} i_1(t) \\ i_2(t) \end{bmatrix} &= \boldsymbol{C}_Y \boldsymbol{x}(t) + \boldsymbol{D}_Y \begin{bmatrix} v_1(t) \\ v_2(t) \end{bmatrix} \end{aligned} \tag{2.52}$$

with

- $\boldsymbol{x}$ : a vector of size $N \times 1$ containing the states of the system, also called the state-vector
- $\dot{\boldsymbol{x}}$ : the time derivative of the state-vector of size $N \times 1$
- $\boldsymbol{A}_Y$ : the system matrix of size $N \times N$
- $\boldsymbol{B}_Y$ : the input matrix of size $N \times 2$
- $\boldsymbol{C}_Y$ : the output matrix of size $2 \times N$
- $\boldsymbol{D}_Y$ : the direct transmission matrix of size $2 \times 2$

We now determine the state-space representation of the system starting from the $Y$-parameters of the low-pass equivalent network. We consider the general case where every resonator is coupled to the source and the load and there is a direct source to load coupling. We consider the $N$ rows $k \in \{2, \ldots, N+1\}$ of $\boldsymbol{A_{LP,SL}}$ ((2.36)) and write (2.33) in the time-domain. Next, we group the derivative of $[U_1, \ldots, U_N]^t$ on the left hand side (LHS) and we split up the contributions of $[U_1, \ldots, U_N]^t$ and $[U_S, U_L]^t$ on the right hand side (RHS) of the resulting expression as follows:

$$\begin{bmatrix} \frac{dU_1(t)}{dt} \\ \frac{dU_2(t)}{dt} \\ \vdots \\ \frac{dU_N(t)}{dt} \end{bmatrix} = \begin{bmatrix} -\frac{G_1+jB_1}{C_1} & -\frac{jC_{12}}{C_1} & \cdots & -\frac{jC_{1N}}{C_1} \\ -\frac{jC_{12}}{C_2} & -\frac{G_2+jB_2}{C_2} & \cdots & -\frac{jC_{2N}}{C_2} \\ \vdots & \vdots & \ddots & \vdots \\ -\frac{jC_{1N}}{C_N} & -\frac{jC_{2N}}{C_2} & \cdots & -\frac{G_N+jB_N}{C_N} \end{bmatrix} \begin{bmatrix} U_1(t) \\ U_2(t) \\ \vdots \\ U_N(t) \end{bmatrix} + \begin{bmatrix} -j\frac{C_{S1}}{C_1} & -j\frac{C_{L1}}{C_1} \\ -j\frac{C_{S2}}{C_2} & -j\frac{C_{L2}}{C_2} \\ \vdots & \vdots \\ -j\frac{C_{SN}}{C_N} & -j\frac{C_{LN}}{C_N} \end{bmatrix} \begin{bmatrix} U_S \\ U_L \end{bmatrix} \tag{2.53}$$

The first and last row of $\boldsymbol{A_{LP,SL}}$ ((2.36)) allow to determine $i_1$ and $i_2$. Since $i_1 = i_S - G_S U_S$ and $i_2 = i_L - G_L U_L$, we write:

$$\begin{bmatrix} i_1 \\ i_2 \end{bmatrix} = \begin{bmatrix} jC_{S1} & jC_{S2} & \cdots & jC_{SN} \\ jC_{L1} & jC_{L2} & \cdots & jC_{LN} \end{bmatrix} \begin{bmatrix} U_1(t) \\ U_2(t) \\ \vdots \\ U_N(t) \end{bmatrix} + \begin{bmatrix} 0 & jC_{SL} \\ jC_{SL} & 0 \end{bmatrix} \begin{bmatrix} U_S \\ U_L \end{bmatrix} \tag{2.54}$$

Equations (2.53) and (2.54) are a state-space representation of the admittance parameters of the lowpass equivalent network. The states in this case are the voltages $\boldsymbol{U} = [U_1, \ldots, U_N]^t$. This state-vector $\boldsymbol{U}$ however can be transformed to another state-vector $\boldsymbol{x} = \boldsymbol{P}\boldsymbol{U}$, where $\boldsymbol{P}$ is an invertible matrix of size $N \times N$. Applying the transformation $\boldsymbol{P}$ to a state-space representation yields:

$$\begin{aligned} \boldsymbol{x}_P &= \boldsymbol{P}\boldsymbol{x} \\ \boldsymbol{A}_{PY} &= \boldsymbol{P}\boldsymbol{A}_Y\boldsymbol{P}^{-1} \\ \boldsymbol{B}_{PY} &= \boldsymbol{P}\boldsymbol{B}_Y \\ \boldsymbol{C}_{PY} &= \boldsymbol{C}_Y\boldsymbol{P}^{-1} \end{aligned} \tag{2.55}$$

Assume that we choose $\boldsymbol{P}$ such that the state-vector $\boldsymbol{U}$ is transformed to obtain a system matrix that is symmetric and an input matrix that becomes the transpose of the output matrix. To this end, we choose $\boldsymbol{P}$ as:

$$\boldsymbol{P} = \begin{bmatrix} j\sqrt{C_1} & 0 & \dots & 0 \\ 0 & j\sqrt{C_2} & \dots & 0 \\ \vdots & & \ddots & \vdots \\ 0 & \dots & 0 & j\sqrt{C_N} \end{bmatrix} \tag{2.56}$$

Applying the transformation $\boldsymbol{P}$ to (2.53) and (2.54) yields:

$$\begin{aligned} \dot{\boldsymbol{x}} &= \begin{bmatrix} -\frac{G_1+jB_1}{C_1} & -\frac{jC_{12}}{\sqrt{C_1C_2}} & \dots & -\frac{jC_{1N}}{\sqrt{C_1C_N}} \\ -\frac{jC_{12}}{\sqrt{C_1C_2}} & -\frac{G_2+jB_2}{C_2} & \dots & -\frac{jC_{2N}}{\sqrt{C_2C_N}} \\ \vdots & \vdots & \ddots & \vdots \\ -\frac{jC_{1N}}{\sqrt{C_1C_N}} & -\frac{jC_{2N}}{\sqrt{C_2C_N}} & \dots & -\frac{G_N+jB_N}{C_N} \end{bmatrix} \boldsymbol{x} + \begin{bmatrix} \frac{C_{S1}}{\sqrt{C_1}} & \frac{C_{L1}}{\sqrt{C_1}} \\ \frac{C_{S2}}{\sqrt{C_2}} & \frac{C_{L2}}{\sqrt{C_2}} \\ \vdots & \vdots \\ \frac{C_{SN}}{\sqrt{C_N}} & \frac{C_{LN}}{\sqrt{C_N}} \end{bmatrix} \begin{bmatrix} v_1 \\ v_2 \end{bmatrix} \\ \begin{bmatrix} i_1 \\ i_2 \end{bmatrix} &= \begin{bmatrix} \frac{C_{S1}}{\sqrt{C_1}} & \frac{C_{S2}}{\sqrt{C_2}} & \dots & \frac{C_{SN}}{\sqrt{C_N}} \\ \frac{C_{L1}}{\sqrt{C_1}} & \frac{C_{L2}}{\sqrt{C_2}} & \dots & \frac{C_{LN}}{\sqrt{C_N}} \end{bmatrix} \boldsymbol{x} + \begin{bmatrix} 0 & jC_{SL} \\ jC_{SL} & 0 \end{bmatrix} \begin{bmatrix} v_1 \\ v_2 \end{bmatrix} \end{aligned} \tag{2.57}$$

Using the notation introduced in Section 2.6.1 we write (2.57) as:

$$\begin{aligned} \dot{\boldsymbol{x}} &= \begin{bmatrix} -jM_{11} - \frac{G_1}{C_1} & -jM_{12} & \dots & -jM_{1N} \\ -jM_{12} & -jM_{22} - \frac{G_2}{C_2} & \dots & -jM_{2N} \\ \vdots & \vdots & \ddots & \vdots \\ -jM_{1N} & -jM_{2N} & \dots & -jM_{NN} - \frac{G_N}{C_N} \end{bmatrix} \boldsymbol{x} \\ &\quad + \begin{bmatrix} M_{S1} & M_{L1} \\ M_{S2} & M_{L2} \\ \vdots & \vdots \\ M_{SN} & M_{LN} \end{bmatrix} \begin{bmatrix} v_1 \\ v_2 \end{bmatrix} \\ \begin{bmatrix} i_1 \\ i_2 \end{bmatrix} &= \begin{bmatrix} M_{S1} & M_{S2} & \dots & M_{SN} \\ M_{L1} & M_{L2} & \dots & M_{LN} \end{bmatrix} \boldsymbol{x} + \begin{bmatrix} 0 & jC_{SL} \\ jC_{SL} & 0 \end{bmatrix} \begin{bmatrix} v_1 \\ v_2 \end{bmatrix} \end{aligned} \tag{2.58}$$

Where $\boldsymbol{x} = \boldsymbol{PU}$. In the case of a lossless filter, where only the first resonator is coupled to the source and the last resonator is coupled to the load the state-space representation of (2.58) becomes:

$$\dot{\boldsymbol{x}} = \begin{bmatrix} -jM_{11} & -jM_{12} & \dots & -jM_{1N} \\ -jM_{12} & -jM_{22} & \dots & -jM_{2N} \\ \vdots & \vdots & \ddots & \vdots \\ -jM_{1N} & -jM_{2N} & \dots & -jM_{NN} \end{bmatrix} \boldsymbol{x} + \begin{bmatrix} M_{S1} & 0 \\ 0 & 0 \\ \vdots & \vdots \\ 0 & M_{LN} \end{bmatrix} \begin{bmatrix} v_1 \\ v_2 \end{bmatrix} \tag{2.59}$$
$$\begin{bmatrix} i_1 \\ i_2 \end{bmatrix} = \begin{bmatrix} M_{S1} & 0 & \dots & 0 \\ 0 & 0 & \dots & M_{LN} \end{bmatrix} \boldsymbol{x}$$

(2.59) shows that if the system matrix is symmetrical and the input matrix is the transpose of the output matrix, the system matrix $\boldsymbol{A}_{PY}$ is equal to the $N \times N$ coupling matrix with a negative sign. Moreover the input $\boldsymbol{B}_{PY}$ and output $\boldsymbol{C}_{PY}$ matrix contain the source-to-resonator couplings and load-to-resonator couplings. The direct transmission matrix $\boldsymbol{D}_Y$ only exist in the case of a direct source-to-load coupling. Note that applying a similarity transformation to the coupling matrix preserves the frequency response while it changes the coupling matrix. This means that the coupling matrix is not unique representation and thus several equivalent coupling matrices exist that realize the same filter.

Transforming (2.58) back to the frequency domain and eliminating the state-vector allows to write the $Y$-parameters as a function of the state-space matrices:

$$\boldsymbol{Y}(s) = \boldsymbol{C}_Y(s\boldsymbol{I}_N - \boldsymbol{A}_Y)^{-1}\boldsymbol{B}_Y + \boldsymbol{D}_Y \tag{2.60}$$

Herein, $(\boldsymbol{A}_Y, \boldsymbol{B}_Y, \boldsymbol{C}_Y, \boldsymbol{D}_Y)$ is also called a realization of $\boldsymbol{Y}$.

## 2.7 Synthesis of the Coupling Matrix

This section explains how to perform the synthesis of a coupling matrix starting from the polynomials $F$,$P$ and $E$ found in Section 2.3. First we transform the $S$-matrix to the $Y$-matrix using the Cayley transformation. Next we construct a minimal realization of the $Y$-matrix using Gilbert's method [Gilb 63]. Finally, we transform the obtained realization to a canonical form. In this case we choose the arrow form [Seyf 98]. The obtained system matrix corresponds to the canonical arrow form coupling matrix up to a sign change (2.59).

### 2.7.1 CAYLEY TRANSFORMATION AND PROPERTIES OF $\boldsymbol{Y}$

The scattering matrix $\boldsymbol{S}$ is transformed to the admittance matrix $\boldsymbol{Y}$ using the Cayley transformation:

$$\boldsymbol{Y} = (\boldsymbol{I}_2 - \boldsymbol{S})(\boldsymbol{I}_2 + \boldsymbol{S})^{-1} \tag{2.61}$$

Applying the transformation to (2.16) yields $\boldsymbol{Y}$ as a function of $F$,$P$ and $E$:

$$\begin{aligned}\boldsymbol{Y} &= \frac{\begin{bmatrix} E - F + (-1)^{N+1}(E^* - F^*) & -2P \\ -2P & E + F + (-1)^{N+1}(E^* + F^*) \end{bmatrix}}{E + F + (-1)^N(F^* + E^*)} \\ &= \frac{1}{q}\begin{bmatrix} n_{11} & n_{12} \\ n_{12} & n_{22} \end{bmatrix}\end{aligned} \tag{2.62}$$

Note that since $F$ and $E$ are monic, the numerators of $Y_{11}$ and $Y_{22}$ are of degree $N-1$. The admittance matrix has a common denominator:

$$q = E + F + (-1)^N(F^* + E^*) \tag{2.63}$$

Since the filter is passive and loss-less the corresponding $Y$-matrix verifies the conditions [Ande 73]:

$$\boldsymbol{Y}(j\omega) + \boldsymbol{Y}^H(j\omega) = 0 \tag{2.64}$$

$$\boldsymbol{Y}(s) + \boldsymbol{Y}^H(s) \geq 0 \text{ , for } \mathrm{Re}(s) = \sigma \geq 0 \tag{2.65}$$

Note that these relations express the same properties as (2.14) and (2.15). Due to the analytic continuation of $\boldsymbol{Y}$ (2.64) implies:

$$\boldsymbol{Y}(s) = -\boldsymbol{Y}^*(s) \tag{2.66}$$

This means that the poles of $\boldsymbol{Y}$ must be symmetrical with respect to the imaginary axis. If $s_i$ is a pole of $\boldsymbol{Y}$, by (2.66) we have that:

$$q(s_i) = 0 \Rightarrow q^*(s_i) = 0 \tag{2.67}$$

Using the definition of the para-conjugation we can write:

$$q^*(s_i) = \overline{q(-\overline{s_i})} = 0 \tag{2.68}$$

which yields:

$$\overline{q(-\overline{s_i})} = 0 \Rightarrow q(-\overline{s_i}) = 0 \tag{2.69}$$

(2.69) shows that if $s_i$ is a pole of $\boldsymbol{Y}$, $-\overline{s_i}$ is also a pole of $\boldsymbol{Y}$ and therefore the poles must lie symmetrically with respect to the imaginary axis.

Due to (2.65) the real part of $\boldsymbol{Y}$ is a semi-positive matrix of $s$ when the real part of $s$ is equal or greater than zero. This implies that the real part of the diagonal elements of $\boldsymbol{Y}$, $Y_{11}$ and $Y_{22}$ is non-negative when evaluated for $s$ in the right half plane. We will use this property to show that the poles are purely imaginary, simple and that their residues are non-negative.

In the vicinity of a pole $s_i$ of multiplicity $n$ of $Y_{11}(s)$ (the rationale is similar for $Y_{22}$), we have that:

$$Y_{11}(s)\ \frac{R}{(s-s_i)^n} = \frac{re^{j\phi}}{(s-s_i)^n}\ \text{, for } s \to s_i \tag{2.70}$$

where $R \in \mathbb{C}$. Assume that $Y_{11}$ has a pole $s_i$ in the right half plane. On a circle with a center $s_i$ and a radius $\rho$ ($s = s_i + \rho e^{j\theta}$), we can write:

$$Y_{11}(s) \approx \frac{re^{j\phi}}{\rho e^{jn\theta}} = \frac{r}{\rho} e^{j(\phi - n\theta)} \tag{2.71}$$

The real part of (2.71) is:

$$\mathrm{Re}(Y_{11}(s)) = \frac{r}{\rho} cos(\phi - n\theta) \tag{2.72}$$

If we run over a circle around a pole in the right half plane ($\theta : 0 \to 2\pi$), the sign of $\mathrm{Re}(Y_{11}(s))$ changes $n$ times. This is in contradiction with the fact that $\mathrm{Re}(Y_{11}(s)) \geq 0$ for $\sigma \geq 0$, thus $\boldsymbol{Y}$ has no poles in the right half plane. In

combination with the fact that the poles must lie symmetrically with respect to the imaginary axis, this yields that the poles must lie on the imaginary axis.

If we now run over the part of a circle around an imaginary pole $j\omega_i$ that lies in the right half plane ($\theta : -\frac{\pi}{2} \to \frac{\pi}{2}$), the sign of $\mathrm{Re}(Y_{11}(s))$ does not change if and only if $n = 1$ and $\phi = 0$. This shows that the multiplicity of $j\omega_i$ is 1. Moreover since $R = re^{j\phi} = r$ is the residue of the pole, this shows that the residue is real and positive.

Since the poles are simple and purely imaginary, $\boldsymbol{Y}$ admits the following partial expansion :

$$\boldsymbol{Y} = \sum_{k=1}^{N} \frac{\boldsymbol{R}_{(k)}}{s - j\omega_k} = \sum_{k=1}^{N} \frac{\begin{bmatrix} r_{11}^{(k)} & r_{12}^{(k)} \\ r_{21}^{(k)} & r_{22}^{(k)} \end{bmatrix}}{s - j\omega_k} \tag{2.73}$$

Substituting (2.73) in (2.66) yields:

$$-\sum_{k=1}^{N} \frac{\boldsymbol{R}_{(k)}}{s - j\omega_k} = \sum_{k=1}^{N} \frac{\boldsymbol{R}_{(k)}^H}{-s + j\omega_k} \tag{2.74}$$

Thus we have that $\boldsymbol{R}_{(k)} = \boldsymbol{R}_{(k)}^H$. Since $\boldsymbol{R}_{(k)}$ is symmetrical, we also have that $\boldsymbol{R}_{(k)} = \boldsymbol{R}_{(k)}^t$ and therefore $\boldsymbol{R}_{(k)}$ is a real symmetric matrix.

Substituting (2.73) in (2.65) yields:

$$\boldsymbol{Y} + \boldsymbol{Y}^H = \sum_{k=1}^{N} \boldsymbol{R}_{(k)} \left(\frac{1}{s - j\omega_k} + \frac{1}{\overline{s} + j\omega_k}\right) = \sum_{k=1}^{N} \boldsymbol{R}_{(k)} \frac{2\,\mathrm{Re}(s)}{|s - j\omega_k|^2} \tag{2.75}$$

Since $\boldsymbol{Y} + \boldsymbol{Y}^H$ is semi-positive definite matrix for $\sigma \geq 0$, we have $\forall x \in \mathbb{C}^2$:

$$x^H(\boldsymbol{Y} + \boldsymbol{Y}^H)x = \sum_{k=1}^{N} x^H \boldsymbol{R}_{(k)} x \frac{2\sigma}{|s - j\omega_k|^2} \geq 0 \tag{2.76}$$

(2.76) is only true if $x^H \boldsymbol{R}_{(k)} x \geq 0$ and therefore $\boldsymbol{R}_{(k)}$ is also a semi-positive definite matrix.

Writing $Y_{21} = Y_{12}$ in its pole-residue form yields:

$$Y_{21}(s) = \sum_{k=1}^{N} \frac{r_{21}^{(k)}}{s - j\omega_k} = \frac{\sum_{k=1}^{N} r_{21}^{(k)} \prod_{i=1, i\neq k}^{N} (s - j\omega_i)}{\prod_{i=k}^{N} s - j\omega_k} \tag{2.77}$$

(2.77) shows that the coefficient corresponding to $s^{N-1}$ of the numerator is $\sum_{k=1}^{N} r_{21}^{(k)}$. Since $n_{fz} < N-1$, this coefficient must be zero:

$$\sum_{k=1}^{N} r_{21}^{(k)} = 0 \tag{2.78}$$

It is shown in classical realization theory that if a transfer function $\boldsymbol{Y}$ has simple poles and thus admits an expansion as (2.73), the residues verify ([Kail 80],p.349):

$$\sum_{k=1}^{N} rank(\boldsymbol{R}_{(k)}) = N \tag{2.79}$$

This is equivalent to:

$$\forall k, rank(\boldsymbol{R}_{(k)}) = 1 \Rightarrow det(\boldsymbol{R}_{(k)}) = 0 \tag{2.80}$$

Summary of the Obtained Properties of $\boldsymbol{Y}$

The admittance matrix $\boldsymbol{Y}(s)$ of a filter can be obtained by transforming $\boldsymbol{S}(s)$ using the Cayley transform ((2.61)). In the case of a passive and loss-less filter with maximally $N-2$ finite transmission zeros, $\boldsymbol{Y}(s)$ admits a partial fraction expansion of the form (2.73), where the residues:

$$\boldsymbol{R}_{(k)} = \begin{bmatrix} r_{11}^{(k)} & r_{12}^{(k)} \\ r_{12}^{(k)} & r_{22}^{(k)} \end{bmatrix} \tag{2.81}$$

verify the following properties:

$$\begin{cases} r_{11}^{(k)}, r_{22}^{(k)}, r_{12}^{(k)} \in \mathbb{R} \\ r_{11}^{(k)} \geq 0 \text{ and } r_{22}^{(k)} \geq 0 \\ r_{11}^{(k)} r_{22}^{(k)} - (r_{12}^{(k)})^2 = 0 \\ \sum_{k=1}^{N} r_{12}^{(k)} = 0 \end{cases} \tag{2.82}$$

### 2.7.2 MINIMAL REALIZATION OF $\boldsymbol{Y}$

If $\boldsymbol{Y}$ is a proper rational matrix, then it admits a realization. In this section we construct a realization of $\boldsymbol{Y}(s)$, $(\boldsymbol{A}_Y, \boldsymbol{B}_Y, \boldsymbol{C}_Y, \boldsymbol{D}_Y)$ that verifies $\boldsymbol{A}_Y = \boldsymbol{A}_Y^t$ and $\boldsymbol{B}_Y = \boldsymbol{C}_Y^t$. Moreover the size of $\boldsymbol{A}_Y$ is equal to $N \times N$.

The degree of a realization $(\boldsymbol{A}_Y, \boldsymbol{B}_Y, \boldsymbol{C}_Y, \boldsymbol{D}_Y)$ is defined as the size of the matrix $\boldsymbol{A}_Y$. We define the *McMillan degree* as the minimum of the degree of all possible realizations of $\boldsymbol{Y}$. If $(\boldsymbol{A}_Y, \boldsymbol{B}_Y, \boldsymbol{C}_Y, \boldsymbol{D}_Y)$ is a realization of $\boldsymbol{Y}$ it is minimal if and only if its degree is equal to the McMillan degree of $\boldsymbol{Y}$ [Kail 80].

If $(\boldsymbol{A}_{(1)}, \boldsymbol{B}_{(1)}, \boldsymbol{C}_{(1)}, \boldsymbol{D}_{(1)})$ and $(\boldsymbol{A}_{(2)}, \boldsymbol{B}_{(2)}, \boldsymbol{C}_{(2)}, \boldsymbol{D}_{(2)})$ are two minimal realizations of the same proper rational matrix, there exists a unique invertible matrix $P$ such that:

$$\begin{cases} \boldsymbol{A}_{(2)} = P^{-1}\boldsymbol{A}_{(1)}P \\ \boldsymbol{B}_{(2)} = P^{-1}\boldsymbol{B}_{(1)} \\ \boldsymbol{C}_{(2)} = \boldsymbol{C}_{(1)}P \\ \boldsymbol{D}_{(2)} = \boldsymbol{D}_{(1)} \end{cases} \tag{2.83}$$

This means that once we find a minimal realization we can transform it to any other minimal realization. In the case where a rational matrix has simple poles, Gilbert's realization is a minimal realization for which the system matrix is diagonal. We now apply Gilbert's method [Gilb 63] to the admittance matrix $\boldsymbol{Y}$ found in (2.62).

Section 2.7.1 shows that $\boldsymbol{Y}$ admits the following expansion:

$$\boldsymbol{Y} = \sum_{k=1}^{N} \frac{\boldsymbol{R}_{(k)}}{s - j\omega_k} = \sum_{k=1}^{N} \frac{\begin{bmatrix} r_{11}^{(k)} & r_{12}^{(k)} \\ r_{21}^{(k)} & r_{22}^{(k)} \end{bmatrix}}{s - j\omega_k} \tag{2.84}$$

where

$$r_{11}^{(k)} r_{22}^{(k)} - (r_{12}^{(k)})^2 = 0 \tag{2.85}$$

This means that $\boldsymbol{R}_k$ can be written as

$$\boldsymbol{R}_k = \boldsymbol{C}_k \boldsymbol{B}_k = \begin{bmatrix} \frac{r_{12}^{(k)}}{\sqrt{r_{22}^{(k)}}} \\ \sqrt{r_{22}^{(k)}} \end{bmatrix} \begin{bmatrix} \frac{r_{12}^{(k)}}{\sqrt{r_{22}^{(k)}}} & \sqrt{r_{22}^{(k)}} \end{bmatrix} \tag{2.86}$$

Remark that $\boldsymbol{C}_k = \boldsymbol{B}_k^t$. If we now write $\boldsymbol{C}_d$ and $\boldsymbol{B}_d$ as the concatenation of $\boldsymbol{C}_k$ and $\boldsymbol{B}_k$ respectively, we can rewrite $\boldsymbol{Y}$ ((2.84)) as:

$$\begin{aligned} \boldsymbol{Y} &= \begin{bmatrix} \frac{r_{12}^{(1)}}{\sqrt{r_{22}^{(1)}}} & \frac{r_{12}^{(2)}}{\sqrt{r_{22}^{(2)}}} & \cdots & \frac{r_{12}^{(N)}}{\sqrt{r_{22}^{(N)}}} \\ \sqrt{r_{22}^{(1)}} & \sqrt{r_{22}^{(2)}} & \cdots & \sqrt{r_{22}^{(N)}} \end{bmatrix} \begin{bmatrix} j\omega_1 & 0 & \dots & 0 \\ 0 & j\omega_2 & \dots & 0 \\ \vdots & \ddots & & \vdots \\ 0 & \dots & 0 & j\omega_N \end{bmatrix} \begin{bmatrix} \frac{r_{12}^{(1)}}{\sqrt{r_{22}^{(1)}}} & \sqrt{r_{22}^{(1)}} \\ \frac{r_{12}^{(2)}}{\sqrt{r_{22}^{(2)}}} & \sqrt{r_{22}^{(2)}} \\ \vdots & \vdots \\ \frac{r_{12}^{(N)}}{\sqrt{r_{22}^{(N)}}} & \sqrt{r_{22}^{(N)}} \end{bmatrix} \\ &= \boldsymbol{C}_d (s\boldsymbol{I}_N - \boldsymbol{A}_d)^{-1} \boldsymbol{B}_d \end{aligned} \tag{2.87}$$

The corresponding $N+2$ coupling matrix is (2.59):

$$\boldsymbol{M}_d = \begin{bmatrix} 1 & j\frac{r_{12}^{(1)}}{\sqrt{r_{22}^{(1)}}} & j\frac{r_{12}^{(2)}}{\sqrt{r_{22}^{(2)}}} & \dots & j\frac{r_{12}^{(N)}}{\sqrt{r_{22}^{(N)}}} & 0 \\ j\frac{r_{12}^{(1)}}{\sqrt{r_{22}^{(1)}}} & -j\omega_1 & 0 & \dots & 0 & j\sqrt{r_{22}^{(1)}} \\ j\frac{r_{12}^{(2)}}{\sqrt{r_{22}^{(2)}}} & 0 & -j\omega_2 & \dots & 0 & j\sqrt{r_{22}^{(2)}} \\ \vdots & \vdots & & \ddots & & \vdots \\ j\frac{r_{12}^{(N)}}{\sqrt{r_{22}^{(N)}}} & 0 & 0 & \dots & -j\omega_N & j\sqrt{r_{22}^{(N)}} \\ 0 & j\sqrt{r_{22}^{(1)}} & j\sqrt{r_{22}^{(2)}} & \dots & j\sqrt{r_{22}^{(N)}} & 1 \end{bmatrix} \tag{2.88}$$

The coupling matrix $\boldsymbol{M}_d$ is better known as the transversal $N+2$ coupling matrix and (2.88) is the same as the relation found in [Came 03]. Remark that $\boldsymbol{M}_d$ is not unique. If the ordering of the poles changes, $\boldsymbol{M}_d$ changes as well without affecting $\boldsymbol{Y}$.

Finally note that due to (2.78) and (2.85), we have that:

$$\boldsymbol{C}_d\boldsymbol{B}_d = \boldsymbol{B}_d^t\boldsymbol{B}_d = \begin{bmatrix} \sum_{k=1}^{N} r_{11}^{(k)} & 0 \\ 0 & \sum_{k=1}^{N} r_{22}^{(k)} \end{bmatrix} \tag{2.89}$$

which also shows that the columns of $\boldsymbol{B}_d$ are orthogonal and their norms are equal to $\sum_{k=1}^{N} r_{11}^{(k)}$ and $\sum_{k=1}^{N} r_{22}^{(k)}$ respectively.

### 2.7.3 ARROW FORM OF THE $N \times N$ COUPLING MATRIX

It can be shown that if a matrix $\boldsymbol{A}_r$ is a real symmetric matrix of size $N \times N$, there exists an orthogonal transformation $\boldsymbol{P}_f$ ($\boldsymbol{P}_f = \boldsymbol{P}_f^t$) such that $\boldsymbol{P}_f^{-1}\boldsymbol{A}_r\boldsymbol{P}_f = \boldsymbol{A}_f$ has the arrow form [Seyf 98]:

$$\boldsymbol{A}_f = \begin{bmatrix} * & * & (0) & * \\ * & \ddots & \ddots & \vdots \\ (0) & \ddots & \ddots & * \\ * & \dots & * & * \end{bmatrix} \tag{2.90}$$

Where all the entries of $\boldsymbol{A}_f$ must be zero except for those on the diagonal, the first upper-diagonal, the first lower-diagonal, and those in the last row and column. If all of the elements lower-diagonal are non zero the transformation $\boldsymbol{P}_f$ is unique up to sign changes, meaning that $\boldsymbol{A}_f$ is unique up to sign changes and thus is a canonical form [Seyf 07]. The first and the last column of the transformation matrix $\boldsymbol{P}_f$ are chosen to be the normalized first and last column of $\boldsymbol{B}_d$. The vectors are normalized by dividing each element by the 2-norm of the vector. Applying transformation $\boldsymbol{P}_f$ to the Gilbert realization $(\boldsymbol{A}_d, \boldsymbol{B}_d, \boldsymbol{C}_d)$ yields a canonical realization $(\boldsymbol{A}_f, \boldsymbol{B}_f, \boldsymbol{C}_f)$ where

$$\boldsymbol{B}_f = \boldsymbol{C}_f^t = \begin{bmatrix} \sum_{k=1}^{N} r_{11}^{(k)} & 0 \\ 0 & 0 \\ \vdots & \vdots \\ 0 & \sum_{k=1}^{N} r_{22}^{(k)} \end{bmatrix} \tag{2.91}$$

Remark that other canonical forms exist such as the folded form [Came 99].

## 2.8 Reconfiguration of the Coupling Matrix

Section 2.7 explains how to synthesize a coupling matrix in the arrow form starting from $F$,$P$ and $E$. Although this form is canonical it is not always possible to implement it physically, due to its associated coupling topology. The coupling topology of the filter describes the way that the resonators are coupled to each other. To make this structure more easy to interpret, we represent the coupling topology by a coupling graph (Figure 2.14) in this work. In the case of the arrow form all adjacent resonators are coupled to each other and every resonator is coupled to the last resonator. In a planar technology such as a microstrip technology it is not always practically possible to obtain such an implementation. Therefore the coupling matrix is usually transformed by similarity transformation to obtain a more practical coupling topology. There are however limitations: it is impossible to implement an arbitrary filter function in an arbitrary coupling topology. In this section we list up the conditions that are necessary to ensure that a certain filter function is compatible with a specific coupling topology.

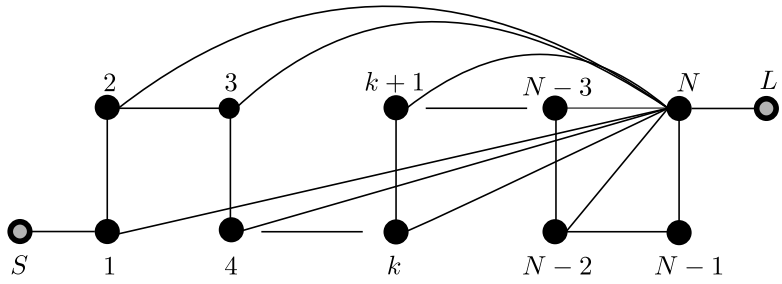


**Figure 2.14** Coupling graph of the arrow form coupling topology. A black node represents a resonator, the gray nodes represent the source and the load and a full line represents a coupling. For the arrow form all sequential resonators are coupled and each resonator is coupled to the last resonator. When a self-coupling is non zero the resonator is presented by a full black node, otherwise by a white node.

### 2.8.1 SHORTEST PATH RULE

For a given topology, define $l$ to be the shortest path length (= number of connections) between the source and the load in a coupling graph (Figure 2.14). Physically, $l$ is the number of couplings present between the load and the source.

**Theorem 1** (Shortest Path Rule)**.** *The maximum number of finite transmission zeros accommodated by the coupling topology containing $N$ resonators and having a shortest path length $l$ between the source and the load is $N + 1 - l$.*

The proof of the shortest path rule is given in [Amar 99].

The shortest path rule allows to evaluate the number of finite transmission zeros accommodated by a specific coupling topology. When a coupling topology contains a direct source-to-load coupling $M_{SL}$, the smallest number of connections between the source and the load is 1. Thus the shortest path length is 1 ($l = 1$). In that case the number of finite transmission zeros accommodated by the coupling topology is $N$.

In this work we do not synthesize coupling topologies with a direct source-to-load coupling. In the case of no direct source-to-load coupling, the shortest possible path between the source and the load in a coupling topology consists of 3 connections. This occurs when there is a coupling between the input and the output resonator. In that case the shortest path consists of one source-to-resonator coupling $M_{S1}$, one inter-resonator coupling $M_{1N}$ and one load-to-resonator coupling $M_{NL}$, which makes that the shortest path length is 3. Therefore the maximal number of finite transmission zeros accommodated by the filters in this work is $N - 2$.

### 2.8.2 COMPATIBILITY BETWEEN THE FILTER RESPONSE AND THE COUPLING TOPOLOGY

Two filter responses are said to be part of the same class of filter responses if they have the same order $N$, the same number of finite transmission zeros $n_{fz}$ and their frequency responses are both symmetrical or both asymmetrical with respect to the center frequency [Seyf 07]. $N$, $n_{fz}$ and the fact whether the response is symmetrical or asymmetrical sets the number of degrees of freedom that can be used in the filter response. We call this number the dimension of the class. For a filter response it is possible to determine the number of real independent parameters that define $P$ and $F$. This number is exactly the number of degrees of freedom that can be used in the filter response. We now determine the dimensions of the general class of symmetric and asymmetric filter responses having an order $N$ and $n_{fz}$ finite transmission zeros.

For an asymmetric filter response of order $N$ having $n_{fz}$ finite transmission zeros we can choose $N$ complex reflection zeros (yielding $N$ complex coefficients of $F$ and thus $2N$ independent parameters). Due to its para-conjugated nature the coefficients of $P$ alternate between purely real and purely imaginary numbers. Since there are $n_{fz}$ finite transmission zeros, $P$ has $n_{fz} + 1$ independent real coefficients only. Therefore, the dimension of the general class of asymmetric filter characteristics of order $N$ having $n_{fz}$ finite transmission zeros is $2N +$

$n_{fz} + 1$.

For symmetric filter response characteristics, the coefficients of $F$ must be real. Therefore, $F$ has $N$ independent real coefficients. Since the transmission zeros are also symmetric with respect to the center frequency, $P$ is an even polynomial and thus $n_{fz}$ is even as well resulting in $\frac{n_{fz}}{2}$ degrees of freedom. The dimension of the class of symmetric filter responses of order $N$ having $n_{fz}$ finite transmission zeros therefore is $N + \frac{n_{fz}}{2} + 1$.

In order for a coupling topology to accommodate for a class of filter responses, the number of independent coupling parameters of the coupling topology must at least be equal to the dimension of the filter responses. If these numbers are equal, the realization problem has a finite number of solutions this includes the possibility that no solution exists [Seyf 07].

### Compatibility between Class of Responses and the Arrow Form Topology

The arrow form topology (Figure 2.14) has $N$ self-couplings $M_{kk}$, $N-1$ sequential couplings $M_{k(k+1)}$ $(k \neq N)$, $N-2$ cross-couplings between each resonator and resonator $N$ and two input and output couplings. This results in $3N-1$ coupling parameters in total. Since the first resonator is coupled to the last resonator and there is no direct source-to-load coupling, the shortest path rule says that there can be $N-2$ finite transmission zeros. The dimension of the class of asymmetric filter responses of order $N$, having $N-2$ transmission zeros is also $2N + N - 2 + 1 = 3N - 1$. If the shortest path enlarges by eliminating couplings to resonator $N$, the number of admissible finite transmission zeros decreases. If we eliminate all couplings $M_{kN}$, the shortest path becomes $N-1$ and thus we have no more finite transmission zeros. This corresponds to the classical Chebyshev response, where only sequential couplings are present.

It is shown [Bell 82] that coupling topologies where $M_{kl} = 0$ if $k + l$ is even, are symmetric. In the case of the arrow form, this means that all self-couplings $M_{kk}$ and every second cross-coupling to the last resonator become zero. If $N$ is even this means that each element $M_{kN}$ is zero if $k$ is even, yielding $\frac{N-2}{2}$ non-zero cross-coupling. The number of non-zero elements in the arrow form is $N - 1 + \frac{N-2}{2} + 2$, which corresponds to the dimension of the class of $(N, N-2)$ symmetric filter responses. In the case where $N$ is odd, each element $M_{kN}$ is zero if $k$ is odd. This means that the shortest path is enlarged by one, yielding only $N-3$ transmission zeros (which is consistent with the fact the zeros are located symmetrically with respect to the center frequency). The number of non-zero

elements in this case is $N-1+\frac{N-3}{2}+2$, which corresponds to the dimension of the class of $(N, N-3)$ symmetric filter responses (where $N$ is odd).

Finally note that a coupling topology is said to be canonical for a class of filter responses if it is unique and has exactly the same number of independent parameters as the dimension of the class [Seyf 07].

### 2.8.3 RECONFIGURATION TO A GENERAL COUPLING TOPOLOGY

In this work we focus on the class of topologies made of cascaded triplets and quadruplets. For this coupling topologies, the compatibility condition given in Section 2.8.2 is sufficient to guarantee the existence of a solution of the realization problem. In the case of cascaded triplet and quadruplet topologies multiple solutions exist. Reconfiguring a coupling matrix to a desired coupling topology is also called coupling matrix reduction, since the process eliminates certain couplings. Various approaches, based on optimization have been proposed to solve the reduction problem [Atia 98; Amar 00b]. The main drawback of these methods is that they do not necessarily yield all the possible solutions. Therefore a procedure that is based on Groebner basis and homotopy techniques has been developed. This method solves the underlying non-linear set of equations to yield all of the possible solutions for all of the relevant topologies [Came 07a; Came 05]. This technique has been implemented in the Matlab toolbox DEDALE-HF [Seyf 00], which we use to reconfigure the coupling matrix here.

### 2.8.4 EXAMPLE: CASCADED QUADRUPLET TOPOLOGY

In this example we first synthesize an arrow form coupling matrix for the symmetric (8,4) pseudo-elliptic filter given in Section 2.3.2. Next we reconfigure it to the a topology consisting of 2 cascaded quadruplet sections as is shown in Figure 2.15.

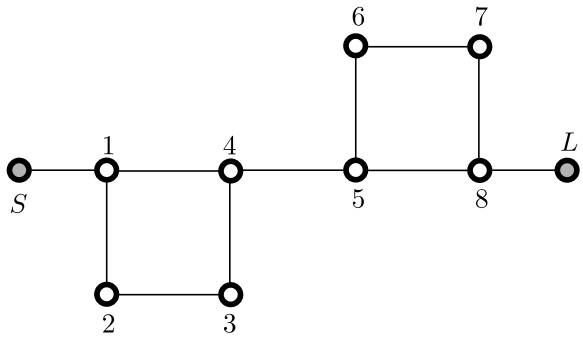


**Figure 2.15** Coupling graph of a topology consisting of 2 cascaded quadruplet sections. A quadruplet consist of 4 sequential couplings and 1 cross-coupling between the first and last resonator of the quadruplet. Note that the resonators are represented by white nodes, because all of the self-coupling are zero.

A quadruplet consist of 4 sequential couplings and 1 cross-coupling between the first and last resonator of the quadruplet. The corresponding arrow form is ($N \times N$ coupling matrix):

$$\begin{bmatrix} 0 & -0.8112 & 0 & 0 & 0 & 0 & 0 & 0 \\ -0.8112 & 0 & -0.5824 & 0 & 0 & 0 & 0 & 0 \\ 0 & -0.5824 & 0 & -0.5402 & 0 & 0 & 0 & -0.0571 \\ 0 & 0 & -0.5402 & 0 & -0.5597 & 0 & 0 & 0 \\ 0 & 0 & 0 & -0.5597 & 0 & -0.3576 & 0 & 0.4684 \\ 0 & 0 & 0 & 0 & -0.3576 & 0 & -0.8761 & 0 \\ 0 & 0 & 0 & 0 & 0 & -0.8761 & 0 & -0.6599 \\ 0 & 0 & -0.0571 & 0 & 0.4684 & 0 & -0.6599 & 0 \end{bmatrix}$$

and $M_{S1} = M_{NL} = 0.9844$. Remark that the length of the shortest path is 5 ($M_{S1} \rightarrow M_{14} \rightarrow M_{45} \rightarrow M_{58} \rightarrow M_{8N}$) which yields indeed $8 + 1 - 5 = 4$ finite transmission zeros. The number of non-zero elements $7 + 2 + 2 = 11$, which corresponds to the dimension of the $(8, 4)$ symmetrical class of responses. Using DEDALE-HF to reconfigure the coupling matrix to obtain the cascaded

quadruplet topology yields 2 possible solutions:

$$\begin{bmatrix} 0 & 0.7425 & 0 & -0.3269 & 0 & 0 & 0 & 0 \\ 0.7425 & 0 & 0.7917 & 0 & 0 & 0 & 0 & 0 \\ 0 & 0.7917 & 0 & 0.4522 & 0 & 0 & 0 & 0 \\ -0.3269 & 0 & 0.4522 & 0 & 0.5265 & 0 & 0 & 0 \\ 0 & 0 & 0 & 0.5265 & 0 & 0.5116 & 0 & -0.1567 \\ 0 & 0 & 0 & 0 & 0.5116 & 0 & 0.6852 & 0 \\ 0 & 0 & 0 & 0 & 0 & 0.6852 & 0 & 0.7960 \\ 0 & 0 & 0 & 0 & -0.1567 & 0 & 0.7960 & 0 \end{bmatrix}$$

and

$$\begin{bmatrix} 0 & 0.7960 & 0 & -0.1567 & 0 & 0 & 0 & 0 \\ 0.7960 & 0 & 0.6852 & 0 & 0 & 0 & 0 & 0 \\ 0 & 0.6852 & 0 & 0.5116 & 0 & 0 & 0 & 0 \\ -0.1567 & 0 & 0.5116 & 0 & 0.5265 & 0 & 0 & 0 \\ 0 & 0 & 0 & 0.5265 & 0 & 0.4522 & 0 & -0.3269 \\ 0 & 0 & 0 & 0 & 0.4522 & 0 & 0.7917 & 0 \\ 0 & 0 & 0 & 0 & 0 & 0.7917 & 0 & 0.7425 \\ 0 & 0 & 0 & 0 & -0.3269 & 0 & 0.7425 & 0 \end{bmatrix}$$

The fact that there are 2 solutions can be interpreted as follows; each quadruplet creates a pair of transmission zeros that is symmetric with respect to the center frequency. There are 2 ways of doing this. In the first solution the first quadruplet creates the (-1.2,1.2) pair and the second one the (-1.5,1.5) pair. For the other solution it is the other way around, the pairs are inverted.

# 3 Physical Implementation of the Coupling Matrix in Microstrip Technology

This chapter introduces a method to obtain initial values for the physical parameters of the actual microwave filter that is to be realized. The idea is to select the physical dimensions of the filter such that coupling matrix of the actual filter is close to the ideal or target coupling matrix. The dimensioning method described in this chapter first divides the filter into building blocks. It dimensions these blocks separately and finally merges them to obtain the complete filter. This method is applicable to a general physical realization, but in this work we focus on microstrip filters.

This chapter first introduces the microstrip transmission line structure. Section 3.2 summarizes some important characteristics of the microstrip line. Section 3.3 introduces the half-wavelength or $\frac{\lambda}{2}$ resonators, that are used to realize the filters. Full wave electromagnetic (EM) field solvers are intensively used to investigate the behavior of coupled-resonator structures and to design the filters. Section 3.4 discusses the use of the EM-solvers and their simulation settings. Section 3.5 explains the dimensioning method for microstrip resonators in detail. Finally Section 3.6 applies the method to design a fourth order quadruplet square-open-loop resonator (SOLR) filter.

## 3.1 Introduction

In this chapter we explain how to obtain initial values for the physical parameters of the actual microwave filter obtained from the design before. To physically implement the coupling matrix obtained in Chapter 2, the layout of the microwave resonators is selected to correspond to the coupling topology. Moreover the resonators are dimensioned to have the desired frequency offset with respect to the center frequency of the prototype filter and the input/output and inter-resonator

distance is selected to approximate the ideal coupling as closely as possible. The dimensioning method described in this chapter divides the filter into building blocks consisting of individual or pairs of resonators. Next, it dimensions these blocks separately and finally merges them to obtain the complete filter. Therefore it is sometimes referred to as the 'divide and conquer strategy' [Came 07b]. The building blocks used to represent coupled resonator filters are typically the input/output resonator and sections consisting of 2 coupled resonators. The dimensioning of each individual block uses so called design curves, which relate the physical parameters to the coupling parameters [Pugl 00; Pugl 01].

This dimensioning method has been applied to several types of physical coupled resonator filters such as waveguide filters, dielectric resonator filters, superconducting filters and microstrip filters [Hong 01; Came 07b]. In this work we use microstrip filters.

For convenience of the reader and to clarify the notation, we first introduce the microstrip transmission line structure [Fook 90; Gupt 79]. Section 3.2 summarizes some important characteristics of the microstrip line used in the remainder of the text such as the characteristic impedance and the effective dielectric constant. Section 3.2.1 gives more details about the loss mechanisms present in microstrip lines. Since the microstrip filters are often placed in a metal box, Section 3.2.2 discusses the effect of metallic housing on the properties of the microstrip structure.

Section 3.2.3 focuses on the electromagnetic coupling that occurs between 2 microstrip lines. This effect is used to physically implement the inter-resonator coupling. Section 3.3 introduces the half-wavelength or $\frac{\lambda}{2}$ resonators [Matt 64], which are used in this work. Various types of $\frac{\lambda}{2}$ resonators can be found in the literature such as hairpin and square-open-loop resonators (SOLR) [Hong 96].

In the remainder of this work EM field solvers are intensively used to investigate the behavior of coupled-resonator structures and to design the filters. Two different EM-solvers are used: ADS Momentum [ADS 14] and CST Microwave Studio [CST 15]. Section 3.4 discusses shortly the properties of both EM-solvers and describes the simulation settings as were used in this work. These setting have proven to be very important to obtain accurate, repeatable simulations.

Section 3.5 explains the generation of the design. It is based on a lumped equivalent model of the microwave building blocks. This model allows to relate the $S$-parameters of the block to the coupling parameter. This relationship is then used to extract the coupling parameter of such a building block starting

from the simulated $S$-parameters.

To obtain a design curve for a block, the physical parameters are varied in the region of interest and in a number of well-chosen values the corresponding microwave structure is simulated. For each value the coupling parameters is extracted. Linking these coupling parameters to the physical design parameters eventually yields the design curves [Swan 07b].

Section 3.5 illustrates this for the inter-resonator coupling between square-open-loop resonators and for the input and output coupling realized by a SOLR with tapped feeding line [Hong 01].

Section 3.6 uses the design curves to obtain initial dimensions for a forth order quadruplet square-open-loop resonator (SOLR) filter [Hong 96].

## 3.2 Microstrip Structure

A microstrip structure consists of a metal strip of width $W$ and thickness $t$ (conducting line) lying on a dielectric substrate of thickness $h$ batched by a conducting ground plane (Figure 3.1 and Figure 3.2). The relative permittivity of the substrate is $\varepsilon_r$. The inhomogeneity of the medium (air-dielectric) around the line can be described as a shift of $\varepsilon_r$, $\varepsilon_{re}$ which is called the effective dielectric constant [Fook 90]. Due to the air-dielectric interface, the waves are no longer perfectly transverse but also have a longitudinal component [Gupt 79]. Therefore the microstrip line does not support a transverse electromagnetic (TEM) propagation mode. However, when the wavelengths are significantly smaller than $W$ and $h$, the transverse components are dominant resulting in quasi-TEM propagation. For practical frequencies, the waves are considered to be TEM. This is called the quasi-TEM approximation. Figure 3.2 shows the distribution of the electric and magnetic field in the cross-section of microstrip line. In what follows we will briefly discuss how some important characteristics of microstrip line can be analyzed and synthesized as a function of the geometrical and substrate parameters. Note that we assume that the substrate is loss-less and the metal is a perfect conductor.

Several analysis methods exist to determine the characteristic impedance $Z_c$ and effective dielectric constant $\varepsilon_{re}$ as a function of the substrate material properties $\varepsilon_r$ and the dimensions $W$, $h$ and $t$ of the microstrip line. As the analysis used here neglects the presence of the longitudinal components of the waves (quasi-TEM approximation), these methods are referred to as the quasi-static analysis [Gupt 79]. A more rigorous full-wave analysis methods exist that take into

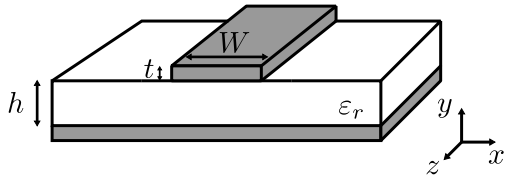


**Figure 3.1** Configuration of a microstrip line.

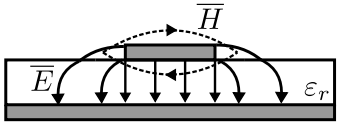


**Figure 3.2** Cross section of a microstrip line and the quasi-TEM field distribution.

account the non-TEM nature [Gupt 79]. The microstrip filters used in this work operate at frequencies for which the quasi-TEM approximation holds. The quasi-static analysis expresses the characteristics of the microstrip line as:

$$\varepsilon_{re} = \frac{C_d}{C_a} \tag{3.1}$$

$$Z_c = \frac{1}{c\sqrt{C_a C_d}} \tag{3.2}$$

where $C_d$ is the per unit capacitance when the dielectric is present, $C_a$ is the per unit capacitance when the dielectric is replaced by air and $c$ is the phase velocity of the wave in free space ( $c \approx 3 \times 10^8 \frac{\mathrm{m}}{\mathrm{s}}$). For very thin strip lines ($t \to 0$), empirical formulae exist that express $Z_c$ and $\varepsilon_{re}$ as a function $\frac{W}{h}$ and $\varepsilon_r$ [Hamm 80]. Formulae taking into account the finite thickness of the strip also exist [Bahl 77]. The effect of the strip thickness on $Z_c$ and $\varepsilon_{re}$ is however small for small values of $\frac{t}{h}$ which is the case for the PCB based filters that are considered in this text. The guided wavelength of a quasi-TEM wave in a microstrip line for a frequency $f$ is:

$$\lambda_g = \frac{\lambda_0}{\sqrt{\varepsilon_{re}}} \tag{3.3}$$

where $\lambda_0 = \frac{c}{f}$ is the wavelength in free space. The associated propagation constant and phase velocity are:

$$\beta = \frac{2\pi}{\lambda_g} \tag{3.4}$$

$$v_p = \frac{\Omega}{\beta} \tag{3.5}$$

where $\Omega = 2\pi f$. The electrical length $\theta$ of a microstrip line is defined as:

$$\theta = \beta l \tag{3.6}$$

where $l$ is the physical length of the line. These characteristics are important to dimension the half-wavelength resonators.

### 3.2.1 LOSSES IN MICROSTRIP STRUCTURES

Microstrip losses are mainly caused by 2 loss mechanisms: conductor loss and substrate loss [Gupt 79]. For lossy microstrip lines, the propagation constant $\gamma = \alpha + j\beta$ is a complex number. The real part of this constant $\alpha$ is called the attenuation constant and the imaginary part corresponds to $\beta$ (3.4). The attenuation constant is the sum of the attenuation constant of each loss mechanism and it is usually expressed in dB per unit length [Puce 68; Denl 80]. The conductor loss attenuation is due to the skin-effect and the dielectric attenuation can be calculated using the loss tangent ($\tan\delta$) of the dielectric substrate. Because the microstrip line is a semi-open structure, there are also radiation losses. These losses depend on the shape of the microstrip structure and are due to microstrip discontinuities such as corners, bends and variation line widths [Denl 80].

### 3.2.2 HOUSING EFFECTS

Microstrip filters are often enclosed by a metallic housing. The presence of the housing affects the values of $\varepsilon_{re}$ and $Z_c$. The effect of the housing decreases with the distance between the sides of the enclosing box and the microstrip structure. As a rule of thumb the effect can be neglected when the side walls are at a distance of $5h$ and the conducting top at a distance $8h$ of the microstrip filter [Hong 01], where $h$ is the height of the dielectric substrate.

### 3.2.3 COUPLED MICROSTRIP LINES

When 2 microstrip lines of width $W$ are at a distance $d$ from each other, proximity coupling occurs through the fringe fields [Garg 79]. A coupled line structure

supports 2 quasi-TEM coupling modes (Figure 3.3). When the voltages on each line have the same signs, the even mode is excited and there is an electric wall at the symmetry plane (Figure 3.3a). When the voltages have opposite sign, the odd mode is excited and there is a magnetic wall at the symmetry plane (Figure 3.3b).

In general the 2 modes occur at the same time [Hong 01]. However the corresponding characteristic impedance and effective dielectric constant slightly differ for the 2 modes. Expressions for the even and odd mode characteristic impedances and effective dielectric constants can be found in [Garg 79; Kirs 84]. This coupling mechanism is used to implement the coupling between the microwave resonators. In Section 3.5 we discuss the relation between the geometrical parameters of the coupled resonator structure (for example the distance between resonators) and the inter-resonator coupling.

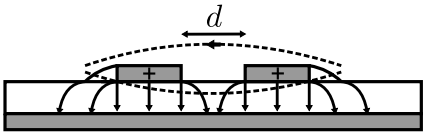


**(a)** Field distribution for the even quasi-TEM mode.

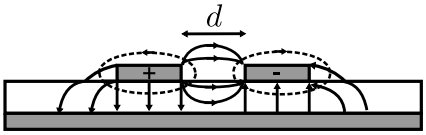


**(b)** Field distribution for the odd quasi-TEM mode.

**Figure 3.3** Cross section of 2 coupled microstrip lines of equal width separated by a distance $d$.

## 3.3 Half-Wavelength ($\frac{\lambda}{2}$) Resonators

There are various ways to construct microwave resonators using microstrip structures. In this work we use transmission line resonators whith electrical length $\theta = \pi$. This corresponds to a physical length which is equal to half of the guided wavelength at the corresponding resonant frequency $f_{res}$ (3.6) [Matt 64; Poza 98; Hong 01]. Therefore such a resonator is also called a $\frac{\lambda}{2}$ resonator. In the vicinity of $f_{res}$, such a resonator behaves equivalently to a parallel $LC$-resonator [Matt 64]. This equivalence however only holds at $f_{res}$ and in a small neighborhood set by the steepness of the resonators. Remember that, unlike lumped $LC$-resonators, $\frac{\lambda}{2}$ resonators resonate at all integer multiples of $f_{res}$. A well-known example of a half-wavelength resonator is the open ended simple

microstrip line resonator of length $\frac{\lambda_g}{2}$, which is used to implement parallel-coupled half-wavelength resonator filters [Cohn 58]. Note that the length of these resonators is not exactly $\frac{\lambda_g}{2}$ due to the presence of fringing fields and length correction empirical formulas exist and are used to compensate this effect. In order to reduce the occupied surface or implement multi-coupled resonator topologies, variations of the simple line $\frac{\lambda}{2}$ resonator were introduced such as the hairpin resonator (Figure 3.4a) [Cris 72] and the square-open-loop resonator (SOLR) (Figure 3.4b) [Hong 96]. We will use the SOLR $\frac{\lambda}{2}$ resonator to realize the resonators in our filters.

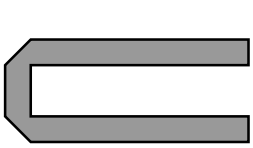

**(a)** Topview of a $\frac{\lambda}{2}$ hairpin resonator.

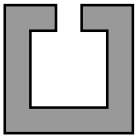

**(b)** Top view of a $\frac{\lambda}{2}$ square-open-loop resonator (SOLR).

**Figure 3.4** Variations of the simple line $\frac{\lambda}{2}$ resonator.

### 3.3.1 UNLOADED QUALITY FACTOR

Generally the design of the microwave filters is based on loss-less prototype networks. In some cases predistortion allows to take the losses of the resonator into account [Came 07b]. To apply predistortion the unloaded quality factor of the resonators needs to be known. The unloaded quality factor of resonator $Q_u$ is defined as [Belo 75]:

$$Q_u = \omega \frac{(\text{average energy stored in resonator})}{(\text{average power lost in resonator})} \tag{3.7}$$

The unloaded quality factor of a microstrip resonator is again mainly determined by 3 loss mechanisms: conductor loss, dielectric loss and radiation loss. The total quality factor is given by [Belo 75; Gopi 81; Hong 01]:

$$\frac{1}{Q_u} = \frac{1}{Q_c} + \frac{1}{Q_d} + \frac{1}{Q_r} \tag{3.8}$$

where $Q_c$ is the conductor quality factor which is inversely proportional to the skin effect, $Q_d$ is the dielectric quality factor which is inversely proportional to $\tan\delta$, $Q_r$ is the radiation quality factor. The latter is defined as the resonant

frequency times the ratio between the average energy stored in the resonator over the average power that is radiated [Hong 01]. Formulas exist in the literature to determine these quality factors separately [Belo 75; Gopi 81; Hong 01]. In this work however the effect of the losses is predicted using full-wave EM-simulators and considered at the end of the design procedure only. When a resonator is coupled to an external load with an admittance $G_e$, the load also affects the quality factor of the resonator. This is expressed by means of the external quality factor [Hong 01; Macc 08]:

$$Q_e = \frac{\Omega_0 C}{G_e} \tag{3.9}$$

where $\Omega_0 C$ is the susceptance slope parameter of the resonator.

## 3.4 Electromagnetic (EM-) Simulators

Although the quasi-static analysis methods yield accurate expressions for some important characteristics of the more simple microstrip structures, full-wave analysis methods are indispensable to predict the behavior of more complex microstrip structures such as hairpin resonators. In what follows, we use EM software tools to simulate the $S$-parameters of various structures such as individual resonators, coupled resonators and complete filters. In this work we use 2 different EM-simulators: ADS Momentum [ADS 14] and CST Microwave Studio [CST 15].

### 3.4.1 ADS MOMENTUM

ADS Momentum is a 3D planar electromagnetic solver , which means the dielectric must be layered (sometimes it is referred to as a 2.5D solver). This solver uses the Method of Moments (MoM) [Harr 96] in the frequency domain to simulate microstrip structures. An important simulation setting is the mesh density to obtain accurate results. In this work we choose a mesh density of 60 cells per wavelength of the highest simulated frequency. Although it is possible to use the the adaptive frequency setting, we usually simulate the structures for an equidistant frequency grid instead (unless specified differently). We simulate all the filter structures under the assumption that the ground plane is infinite. This assumption implies that the groundplane of the fabricated filter must be large enough (more than 5 times $h$ larger than the edge of the circuit). The ports are calibrated in 50 Ω and the waves appear as perfect TEM waves at the ports. These ports are called TML calibrated ports.

### 3.4.2 CST MICROWAVE STUDIO

The Frequency Domain Solver of CST Microwave Studio is a full 3D electromagnetic solver. In this work we have selected a tetrahedral mesh and the general purpose solver mode. The solver then calculates the underlying equation for one single frequency at a time and repeats this for a number of adaptively chosen frequencies. For each frequency the solution is calculated by an iterative solver (a solution comprises the field distribution and $S$-parameters). The full spectrum in the frequency range of interest is then derived from the simulated frequencies [CST 15]. CST adaptively changes the mesh until the difference between the $S$-parameters of a previous mesh setting and the current mesh setting is lower than a threshold $\Delta S$. In this work this threshold is chosen to be $\Delta S = 0.01$ and the adaptive meshing is performed at the center frequency of the filter. The ports are waveguide ports and the $S$-parameters are normalized to the 50 $\Omega$ reference. The size of the waveguide port is determined using a CST built-in macro called *Calculate port extension coefficient*.

This type of solver includes the effects of the presence of a metallic housing. One of the major advantages of CST Microwave Studio is its ability to compute the sensitivity of the $S$-parameters with respect to geometrical parameters such as the distance between resonators. This feature is intensively used in the novel tuning method introduced in Chapter 5.

## 3.5 Generation of the Design Curves

To generate initial values for the physical design parameters of the microstrip filter, the filter is first divided into building blocks. The design curves relate the physical dimensions of these building blocks to the corresponding coupling parameters. The building blocks of coupled-resonator filters are sections of 2 coupled resonators and the input/output resonator which is a coupled feeding structure. The coupled resonator block is used to implement the inter-resonator couplings $M_{kl}$. The input/output one describes the source-to-resonator coupling $M_{S1}$ and load-to-resonator coupling $M_{LN}$ (introduced in Section 2.6). The self-couplings $M_{kk}$ represent frequency offsets between the individual resonant frequency of the resonator and the center frequency and are therefore implemented by adjusting the physical length of the $\frac{\lambda}{2}$ resonator.

In order to dimension the individual building blocks design curves are generated by extracting the coupling parameter from the $S$-parameters of the individual building blocks. This extraction procedure is based on a lumped-equivalent

model of the microwave resonator structures. The simplified model allows one to express the coupling coefficient as a function of certain features of the $S$-parameters. To generate the design curves the physical parameters are varied within a well-chosen region and for each set of physical dimensions the $S$-parameters are simulated [Swan 07b]. This region must be chosen such that the desired coupling values fall within it. From the simulated $S$-parameters the corresponding coupling coefficient is extracted.

Section 3.5.1 introduces the lumped-equivalent model used for 2 coupled resonators in some detail. It also explains how the inter-resonator coupling is extracted from the amplitude response of the transmission coefficient $|S_{21}|$. The extraction procedure is illustrated on three different SOLR coupling structures. Section 3.5.2 introduces the lumped equivalent model used for a single resonator coupled to a feeding structure. Next it explains how the input/output coupling is extracted from the group delay of the reflection coefficient $S_{11}$. The extraction procedure is illustrated on a single SOLR which is fed using a tapped-line [Wong 79]. The design curves obtained in this section are used next in Section 3.6 to dimension a SOLR filter structure.

Note that it is also possible to generate the curves using measured $S$-parameters. Moreover it is clear that the curves only provide initial values for the physical parameters, since they isolate the different building blocks and rely on an approximation of the behavior of the structure. The curves do not take into account the effect of the presence of other resonators on the coupling between 2 adjacent ones. The use of lumped equivalent models also assumes that the coupling is frequency independent, which is only valid in a narrow-band around the resonant frequency of the resonators. Finally, note that the design curves describe the behavior of the coupling between the resonators in the bandpass domain, while the couplings in the coupling matrix are normalized in the lowpass domain. To de-normalize them, the inter-resonator coupling must be multiplied by $FBW$ and the input/output coupling by $\sqrt{FBW}$ (Section 2.6).

### 3.5.1 INTER-RESONATOR COUPLING

The coupling coefficient $k$ between 2 coupled microwave resonators expresses the ratio of energy coupled between the resonators and the total energy that is present in the resonators [Hong 00]. The coupling between microstrip resonators occurs through the fringing fields (Section 3.2.3). There are 2 different possible coupling mechanisms namely the electric coupling through the electric fields and similarly the magnetic coupling through the magnetic fields. Usually both types

of coupling occur at the same time. When the electric coupling is dominant, it is usually referred to as an electric coupling and vice-versa for the magnetic coupling. When both fields have a similar influence, the coupling is called a mixed coupling.

In [Hong 01] an equivalent $LC$ model is proposed for each type of coupling. It is concluded that the expressions of the coupling coefficient $k_X$ are the same for each circuit. $k_X$ can be expressed as a function of the 2 frequencies at which peaks appear in the magnitude of the response $|S_{21}|$ (Figure 3.7). These frequencies are called the peak frequencies in the remainder of the text. In this work we use the most general equivalent model, that contains both the electric and the magnetic coupling and where the resonators are asynchronously tuned. Figure 3.5 shows the equivalent circuit: resonator 1 that is formed by $C_1 - C_m$ and $L_1 - L_m$ resonates at $\Omega_{01} = \frac{1}{\sqrt{L_1 C_1}}$ and resonator 2 formed by $C_2 - C_m$ and $L_2 - L_m$ at $\Omega_{02} = \frac{1}{\sqrt{L_2 C_2}}$. The electric coupling is modeled through the mutual capacitance $C_m$ and the magnetic coupling through the mutual inductance $L_m$. Remark that the model shown in Figure 3.5 is simplified by subtracting the mutual capacitance from $C_1$ and $C_2$ and similarly by subtracting the mutual inductance from $L_1$ and $L_2$. The coupling coefficient between the resonators can be expressed in terms of the peak frequencies and resonant frequencies of the resonators [Hong 00]:

$$k_X = \pm \frac{1}{2} \left( \frac{\Omega_{02}}{\Omega_{01}} + \frac{\Omega_{01}}{\Omega_{02}} \right) \sqrt{\left( \frac{\Omega_2^2 - \Omega_1^2}{\Omega_2^2 + \Omega_1^2} \right)^2 - \left( \frac{\Omega_{02}^2 - \Omega_{01}^2}{\Omega_{02}^2 + \Omega_{01}^2} \right)^2} \tag{3.10}$$

where $\Omega_{01}$ and $\Omega_{02}$ are the resonant frequencies of the individual resonators and $\Omega_1$ and $\Omega_2$ are the two peak frequencies of the coupled-resonator circuit. In the case of synchronously tuned resonators ($\Omega_{01} = \Omega_{02}$) (3.10) becomes:

$$k_X = \pm \frac{\Omega_2^2 - \Omega_1^2}{\Omega_2^2 + \Omega_1^2} = \pm \frac{f_{p2}^2 - f_{p1}^2}{f_{p2}^2 + f_{p1}^2} \tag{3.11}$$

where $f_{p1} = 2\pi\Omega_1$ and $f_{p2} = 2\pi\Omega_2$ are called the peak frequencies. The derivation of this formulas can be found in [Hong 00].

The sign of the coupling is dependent on the physical coupling structure of the microwave structure. A positive sign enhances the stored energy where a negative sign reduces the stored energy in a resonator [Hong 00]. This means the magnetic and electric couplings have the same effect if they have the same sign or an opposite effect if they have an opposite sign. The sign of the coupling can

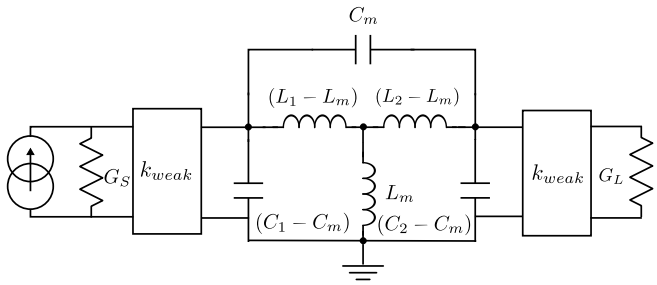


**Figure 3.5** General asynchronously tuned coupled LC-resonator network. The resonance frequencies of the resonators are $\Omega_{01} = \frac{1}{\sqrt{L_1 C_1}}$ and $\Omega_{02} = \frac{1}{\sqrt{L_2 C_2}}$. The electrical coupling is modeled by a mutual capacitance $C_m$ and the magnetic coupling by a mutual inductance $L_m$. $k_{weak}$ represents the input/output coupling.

be determined using the phase response of $S_{21}$. If the phase of $S_{21}$ increases for frequencies lower than the peak frequencies and decreases for higher frequencies, the coupling has a positive sign. If the phase decreases for frequencies lower then the peak frequencies and increases for higher frequencies, then the sign is negative (Section 3.5.1).

At the peak frequencies, peaks appear in the magnitude of the transmission coefficient $|S_{21}|$ of the coupled-resonator structure when they are loosely coupled to the input and output. Figure 3.7 shows the typical behavior of $|S_{21}|$ of two loosely coupled synchronously tuned resonators. To have loosely input/output coupling, the null between the peaks should be lower -40 dB [Swan 07b]. We now generate inter-resonator coupling design curves for SOLRs, which we use in Section 3.6 to dimension a forth order quadruplet filter.

An alternative approach to obtain the inter-resonator coupling coefficients is to use the eigenmode solver [Came 07b]. Note that not all simulators have an eigenmode solver. CST Microwave Studio [CST 15] has an eigenmode solver, but ADS Momentum [ADS 14] does not.

Note that the the derivation of the coupling coefficient expressions assuming lumped elements (capacitors and inductors) is not exactly congruent with the synthesis assumptions, where we have assumed ideal frequency-invariant inverters. Therefore Figure 3.5 is suitable for the analysis of the structures but not for the synthesis. Under the narrow band approximation the synthesized coupling coefficients only differ slightly from the frequency dependent coupling coefficients.

SOLR Coupling Structures

There are different possible ways to position SOLRs with respect to each other (Figure 3.6). The way they are positioned and the distance $d$ between them determines the nature (the sign) and the strength of the coupling. At resonance, the SOLR has its maximum electric field density around the gap and its maximum magnetic field density at the opposite side of the resonator [Hong 96]. Therefore the electric coupling mechanism is dominant when the sides with the gaps are facing each other (Figure 3.6a). Similarly the magnetic coupling mechanism is dominant when the sides with gaps are oriented away from each other(Figure 3.6b). When both resonators are oriented as in Figure 3.6c both coupling mechanisms have similar effects and therefore this coupling is referred to as mixed coupling.

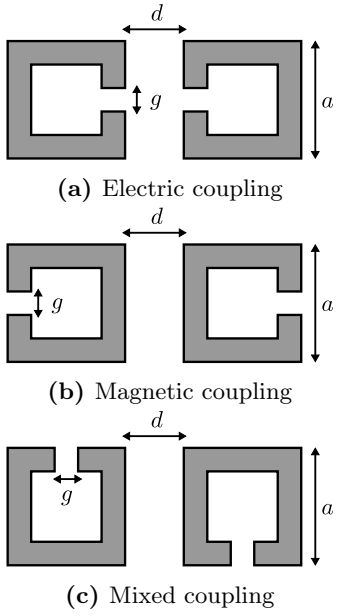


**(a)** Electric coupling

**(b)** Magnetic coupling

**(c)** Mixed coupling

**Figure 3.6** Different coupled SOLR structures.

Since the coupling is a proximity effect, the distance between the resonator $d$ affects the inter-resonator coupling most. Therefore this parameter is varied to generate the design curves.

The resonators in this example are realized on a RO4360 substrate having a thickness $t = 1.27$ mm and $\varepsilon_r = 6.15$. The parameters $a = 19.9$ mm and $g = 1.5$ mm are designed such that the resonators resonate at 1 GHz. Figure 3.7 shows the magnitude of $S_{21}$ for a structure where the magnetic coupling is dominant

(blue curve), the electrical coupling is dominant (red curve) and where a mixed coupling (green curve) is present for an inter-resonator distance $d = 1.8$ mm.

- Magnetic coupling: The peak frequencies are $f_{p1} = 0.98$ GHz and $f_{p2} = 1.024$ GHz. Filling these values in in (3.11) yields a coupling value of $k_M = 0.0439$.
- Electric coupling: The peak frequencies are $f_{p1} = 0.993$ GHz and $f_{p2} = 1.009$ GHz and thus $k_E = 0.016$. This indicates that the electric coupling is weaker than the magnetic one.
- Mixed coupling: The peak frequencies are $f_{p1} = 0.986$ GHz and $f_{p2} = 1.016$ GHz and thus $k_B = 0.03$ which is in between the electric and magnetic coupling value.

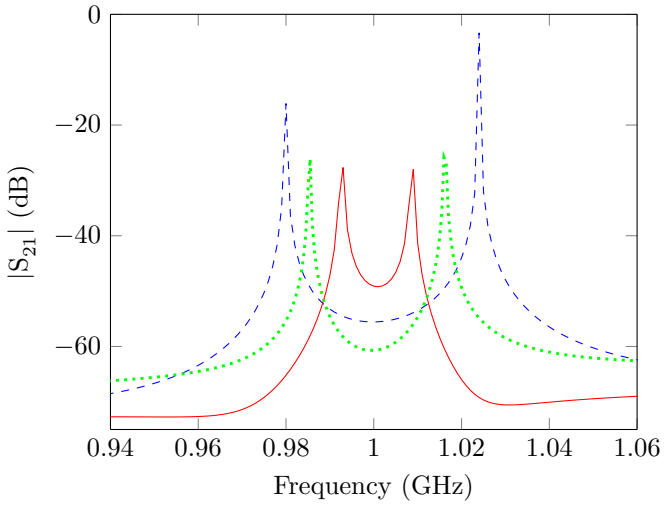


**Figure 3.7** Magnitude of $S_{21}$ for SOLR coupled resonator structures: magnetic coupling (- - -), electric coupling (—) and mixed coupling (. . .) for $a = 19.9$ mm, $g = 1.5$ mm and $d = 1.8$ mm

Figure 3.8 shows that phase responses of the magnetic and mixed coupling structures behave similarly and have an opposite curvature with respect to the phase behavior of the electric coupling. This indicates that the signs of the electric coupling is opposite to that of the mixed and magnetic coupling.

To generate the design curves, the parameter $d$ is varied over an interval [1:0.1:2.5] mm. As we will see in Section 3.6, this interval is chosen such that the desired

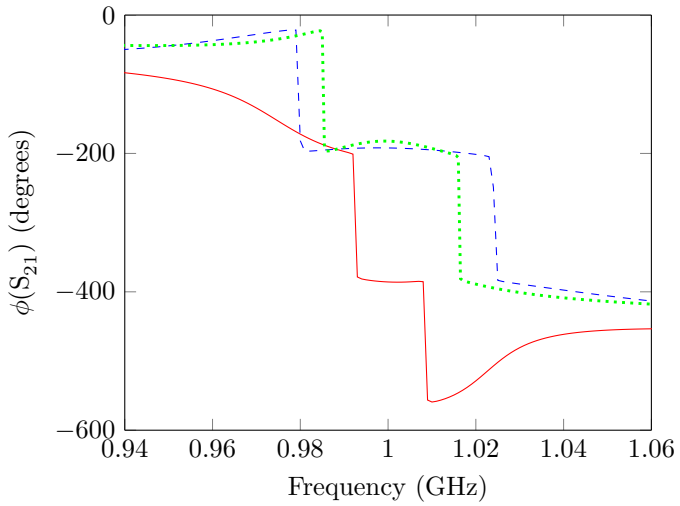


**Figure 3.8** Phase of $S_{21}$ for SOLR coupled resonator structures: magnetic coupling (- - -), electric coupling (—) and mixed coupling (. . .) for $a = 19.9$ mm, $g = 1.5$ mm and $d = 1.8$ mm.

coupling values are within this interval. Each structure is simulated for an equidistant frequency grid [0.94:0.001:1.06] GHz using ADS Momentum. The frequency grid is chosen fine enough in order to capture the peak frequencies. Figure 3.9 shows the resulting design curves for each coupling structure. The curves show that the magnetic coupling ($k_M$) is stronger than the electrical one ($k_E$). Since the mixed coupling $k_B$ is a result of both coupling mechanism it does end up between the others.

### 3.5.2 INPUT/OUTPUT COUPLING

The equivalent model for a single input or output resonator coupled to a source (external load) consists of a $J$-inverter that is cascaded with a parallel $LC$-resonator. The $J$-inverter models the (assumed frequency invariant) source-to-resonator coupling $C_{S1}$ ($C_{LN}$) (Figure 3.10). Remark that this model corresponds to the input/output coupling circuit that is used in the lumped equivalent circuit of the filter in the bandpass domain (Figure 2.8). We now show how the value of the input coupling is extracted from the group delay of the reflection coefficient $\tau_{S_{11}}$. In the literature the input or output coupling is often expressed by the external quality factor $Q_e$ and [Hong 01] derives the relation between $Q_e$ and $\tau_{S_{11}}$. Here we derive the relation between the input (or output) coupling and $\tau_{S_{11}}$. Moreover we show the link between the input (or output) coupling

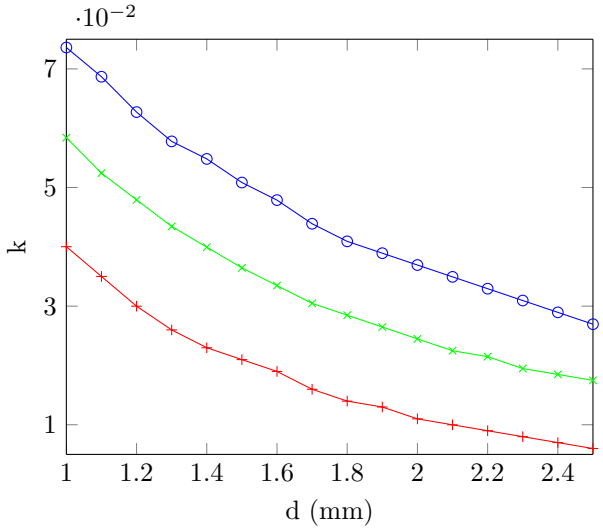


**Figure 3.9** Desgin curves relating the inter-resonator coupling $k_E$ for the electric coupling (+), $k_M$ for the magnetic coupling (o) and $k_B$ for the mixed coupling (x) to the design parameter $d$.

and $Q_e$.

The input reflection coefficient is written as a function of the impedance of the source $Z_S = \frac{1}{G_S}$ and the input impedance $Z_{IN}$ of the filter seen from the source [Poza 98]:

$$S_{11} = \frac{Z_{IN} - Z_S}{Z_{IN} + Z_S} \tag{3.12}$$

where $Z_{IN} = \frac{1}{Y_{IN}}$. To determine $Y_{IN}$, we obtain $Y_1$ first. If $Y_1$ is the admittance of the parallel $LC$ resonator (Figure 3.10) and given the resonant frequency $\Omega_0 = \frac{1}{\sqrt{C'_1 L'_1}}$ we obtain $Y_{IN}$ by transformation through the $J$-inverter $C_{S1}$:

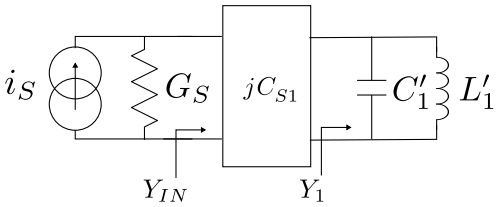


**Figure 3.10** Lumped-equivalent circuit for a single input/output resonator coupled to the a non-ideal source with admittance $G_S$.

$$Y_{IN} = \frac{C_{S1}^2}{Y_1} \Rightarrow Z_{IN} = j\frac{C_1'\Omega_0}{C_{S1}^2}(\frac{\Omega}{\Omega_0} - \frac{\Omega_0}{\Omega}) \tag{3.13}$$

If we write $\Omega = \Omega_0 + \Delta\Omega$ for a frequency that is assumed to lie in the vicinity of resonance $\Omega \approx \Omega_0$, we approximate $(\frac{\Omega}{\Omega_0} - \frac{\Omega_0}{\Omega})$ as:

$$\begin{aligned} \frac{\Omega}{\Omega_0} - \frac{\Omega_0}{\Omega} &= \frac{(\Omega + \Omega_0)(\Omega - \Omega_0)}{\Omega\Omega_0} \\ &\approx \frac{2\Omega\Delta\Omega}{\Omega\Omega_0} = \frac{2\Delta\Omega}{\Omega_0} \end{aligned} \tag{3.14}$$

If we now introduce (3.13) in (3.12) using the approximation in (3.14), we obtain:

$$\begin{aligned} S_{11} &= \frac{G_S Z_{IN} - 1}{G_S Z_{IN} + 1} \\ &= \frac{j\frac{\Omega_0 C_1' G_S}{C_{S1}^2}\frac{\Delta\Omega}{\Omega_0} - 1}{j\frac{\Omega_0 C_1' G_S}{C_{S1}^2}\frac{\Delta\Omega}{\Omega_0} + 1} \\ &= \frac{jX - 1}{jX + 1} = \frac{1 - X^2}{1 + X^2} - j\frac{2X}{1 + X^2} \end{aligned} \tag{3.15}$$

where $X = \frac{C_1' G_S \Delta\Omega}{C_{S1}^2}$. The phase of $S_{11}$ is

$$\phi(S_{11}) = \arctan\frac{-2X}{1 - X^2} \tag{3.16}$$

The group delay $\tau$ is defined as [Poza 98]:

$$\tau = -\frac{d\phi}{d\Omega} \tag{3.17}$$

We now calculate $\tau_{S_{11}}(\Omega_0)$ by deriving (3.16) and evaluating it in $\Omega_0$. First we derive (3.16):

$$\begin{aligned}\tau_{S_{11}} &= -\frac{1}{1+\frac{(-2X)^2}{(1-X^2)^2}}\frac{-2(1-X^2)-2X(-2X)}{(1-X^2)^2}\frac{G_S C_1'}{C_{S1}^2} \\ &= \frac{(1-X^2)^2}{(1+X^2)^2}\frac{-2(1+X^2)}{(1-X^2)^2}\frac{G_S C_1'}{C_{S1}^2} \\ &= \frac{1}{(1+X^2)^2}\frac{2G_S C_1'}{C_{S1}^2}\end{aligned} \tag{3.18}$$

Since $X(\Omega_0) = 0$, we have that:

$$\tau_{S_{11}}(\Omega_0) = \frac{2G_S C_1'}{C_{S1}^2} \tag{3.19}$$

Using (2.38) we have that $M_{S1} = \frac{C_{S1}}{\sqrt{G_S C_1}}$ is the input-coupling in the lowpass domain, where $C_1 = \frac{FBW\Omega_0}{2}C_1'$ (2.32). Filling this in (3.19) yields:

$$M_{S1}^{'2} = M_{S1}^2 FBW = \frac{4}{\Omega_0 \tau_{S_{11}}(\Omega_0)} \tag{3.20}$$

where we define $M_{S1}' = \frac{C_{S1}}{\sqrt{G_S \Omega_0 C_1'}}$ as the input coupling in the bandpass domain. Equation (3.20) shows again that to de-normalize the input (output) coupling it must be multiplied by $\sqrt{FBW}$. Note that in the literature the input/output coupling is often expressed using the external quality factor $Q_{EXT}$ [Macc 08]. In the case when a resonator $l$ is coupled to an external load $G_0$ through a J-inverter $J_{0l}$, the external quality factor is defined as

$$Q_{EXT,l} = \frac{b_l G_0}{J_{0l}^2} \tag{3.21}$$

where $b_l$ is the susceptance slope parameter of the admittance $Y_l$ of the resonator:

$$b_l = \frac{1}{2}\frac{\partial \operatorname{Im}(Y_l)}{\partial \Omega}\bigg|_{\Omega=\Omega_0} \tag{3.22}$$

In the case of the input parallel $LC$-resonator, $b_l = b_1 = \Omega_0 C_1'$. If we now assume that $G_0 = G_S$ and $J_{0l} = C_{S1}$ we have:

$$Q_{EXT,1} = \frac{\Omega_0 C_1^{'} G_S}{C_{S1}^2} = M_{S1}^{'2} = \frac{1}{M_{S1}^{'2}} = \frac{\Omega_0 \tau_{S_{11}}(\Omega_0)}{4} \tag{3.23}$$

Expression (3.23) corresponds to the expression found in [Hong 01; Swan 07b] to extract the quality factor starting from the group delay $\tau_{S_{11}}$.

We now apply the extraction method to generate design curves for a SOLR which is fed using a tapped-line.

### Tapped-line Feed SOLR example

A SOLR is usually fed using a tapped-line feeding structure, where the position of the center of the feed line with respect to the center of the resonators labeled $t$ mainly affects the input coupling [Wong 79] (Figure 3.11). The width of the feeding line $W_{feed}$ is chosen such that the characteristic impedance of the line corresponds to the impedance of the source (or the load), which in this case is 50 Ω. The corresponding width of the feed line in the example as used earlier is $W_{feed} = 1.48$ mm. The derivative of the phase of $S_{11}$ with respect to the frequency is approximated by the forward numerical differentiation $\frac{\Delta\phi}{\Delta\omega} = \frac{\phi_2 - \phi_1}{\omega_2 - \omega_1}$. The structures are simulated for the same frequency range as before, which is [0.94:0.001:1.06] GHz again using ADS Momentum for values of $t$ within the interval [7.45:0.01:9.45] mm. These values are chosen to make sure that the desired input (and output) coupling are within this interval. Figure 3.12 shows $\tau_{S_{11}}$ for $a = 19.9$ mm, $g = 1.5$ mm and $t = 7.95$ mm. $\tau_{S_{11}}(\Omega_0)$ is 12.7 ns and $\Omega_0 = 2\pi 10^9 \frac{\text{rad}}{s}$, which makes that $M'_{S1} = 0.224$. Figure 3.13 shows $M'_{S1}$ as a function of $t$, the coupling between the source and the resonator increases when $t$ increases, which is expected and is in line with field density and the impedance along the resonator.

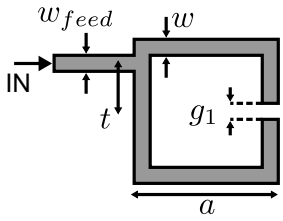


**Figure 3.11** Top-view of the layout of a single SOLR fed using a tapped-line feeding structure. $t$ denotes the distance between the center of the feed line and the center of the resonator.

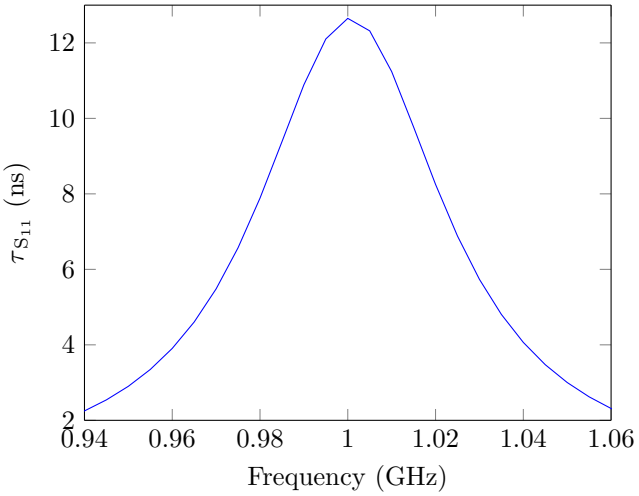


**Figure 3.12** $\tau_{S_{11}}$ as a function of frequency for a tapped SOLR structure with $a = 19.9$ mm, $g = 1.5$ mm and $t = 7.95$ mm.

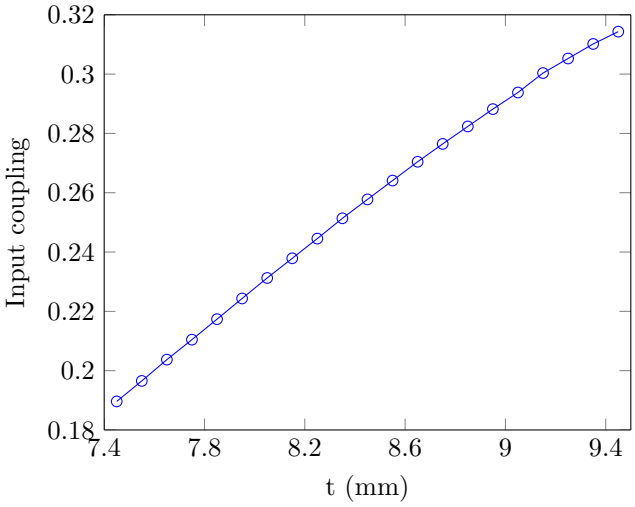


**Figure 3.13** Input/output coupling for a tapped SOLR structure with $a = 19.9$ mm, $g = 1.5$ mm and $t$ in the interval [7.45:0.01:9.45] mm.

## 3.6 Initial Dimensioning of a Single Quadruplet SOLR Filter

In this section we use the design curves generated in Section 3.5.1 to dimension a fourth order SOLR quadruplet filter. The filter is designed to have a center frequency $f_c = 1$ GHz, a $FBW = 0.05$ and a $RL = -20$ dB and 2 finite TZs at $\omega = \pm 1.4$. We first synthesize the ideal coupling matrix in the lowpass domain

using the techniques described in Chapter 2. The ideal $N+2$ coupling matrix is called $M_{id}$ and is shown below:

$$M_{id} = \begin{bmatrix} 0 & 1.0123 & 0 & 0 & 0 & 0 \\ 1.0123 & 0 & 0.7787 & 0 & -0.4286 & 0 \\ 0 & 0.7787 & 0 & 0.8612 & 0 & 0 \\ 0 & 0 & 0.8612 & 0 & 0.7787 & 0 \\ 0 & -0.4286 & 0 & 0.7787 & 0 & 1.0123 \\ 0 & 0 & 0 & 0 & 1.0123 & 0 \end{bmatrix}$$

To implement the coupling matrix, it must be de-normalized. Hence, the inter-resonator coupling must be multiplied by $FBW$ and the input/output couplings by $\sqrt{FBW}$ yielding:

$$M_{denorm} = \begin{bmatrix} 0 & 0.2263 & 0 & 0 & 0 & 0 \\ 0.2263 & 0 & 0.0389 & 0 & -0.0214 & 0 \\ 0 & 0.0389 & 0 & 0.0431 & 0 & 0 \\ 0 & 0 & 0.0431 & 0 & 0.0389 & 0 \\ 0 & -0.0214 & 0 & 0.0389 & 0 & 0.2263 \\ 0 & 0 & 0 & 0 & 0.2263 & 0 \end{bmatrix} \tag{3.24}$$

In the ideal coupling matrix, the inter-resonator coupling $M_{14}$ has an opposite sign to that of the sequential couplings. Therefore we implement $M_{14}$ using the electric coupling structure shown in Figure 3.6a. Moreover the couplings $M_{12} = M_{34}$. To impose this equality we then implement these couplings using a mixed coupling structure (Figure 3.6c). Finally we implement $M_{24}$ using the magnetic coupling structure (Figure 3.6b). Figure 3.14 shows the top-view of the physical layout of the filter. Table 3.1 contains the initial geometrical dimensions obtained using the design curves. Figure 3.15 shows the magnitude responses in the bandpass domain for the filter with the initial dimensions. Figure 3.16 compares the simulated response to the ideal one obtained from the coupling matrix $M_{id}$.

Clearly, the filter response is reasonably close to the ideal one, however there is still an offset and room for improvement. The TZs have a frequency offset and quality factor shift with respect to the ideal ones, the bandwidth is slightly larger than the ideal one and not all of the reflection zeros appear. It is not surprising that response does not perfectly match the ideal response, as the design curves

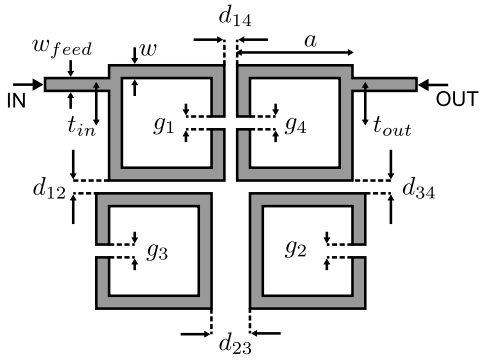


**Figure 3.14** Top-view of the layout of a fourth order SOLR quadruplet filter.

| Physical design parameter | Initial value (mm) |
|---|---|
| $w_{feed}$ | 1.48 |
| $t_{in} = t_{out}$ | 7.95 |
| $g_1 = g_2 = g_3 = g_4$ | 1.5 |
| $a$ | 19.9 |
| $w$ | 1 |
| $d_{12}$ | 1.45 |
| $d_{23}$ | 1.75 |
| $d_{34}$ | 1.45 |
| $d_{14}$ | 1.45 |

**Table 3.1** Initial values for the physical design parameters of the SOLR quadruplet filter.

are based on the approximation that does not take into account the effects of the loading of other resonators on the coupling parameters. Moreover parasitic couplings may be present in the actual microwave filter. To assess the difference in some more detail, knowledge about the implemented (actual) coupling matrix is helpful. It enables a designer to tune or optimize the geometrical parameters or at least helps to diagnose the source of the error on the implemented coupling parameters. In the next chapter we will explain how to extract the implemented coupling matrix starting from the simulated full-wave response. Later we use this extraction method to optimize the filter response.

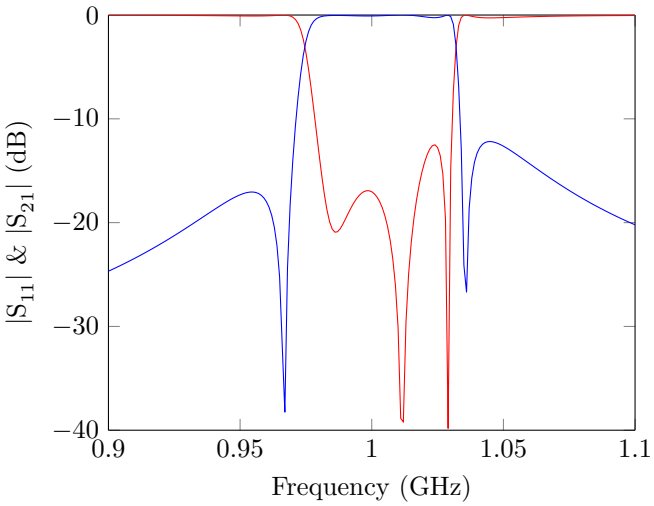


**Figure 3.15** $|S_{11}|$ (dB) (—) and $|S_{21}|$ (dB) (—) in the bandpass domain for the initial design obtained with the design curves.

## 3.7 Conclusion

This chapter explains a method to generate initial values for the design parameters of microwave filters. The method heavily uses design curves to dimension the filter. These design curves can be seen as look-up tables that relate physical parameters of the individual building blocks to their coupling parameters. Therefore these curves do not take into account the effect of other resonators present in the filter on the implemented coupling parameter. This makes that the filter must be optimized to meet the specifications. We have applied the initial dimensioning method to the design of fourth order SOLR filter and the example shows that indeed further tuning is required to meet the specifications.

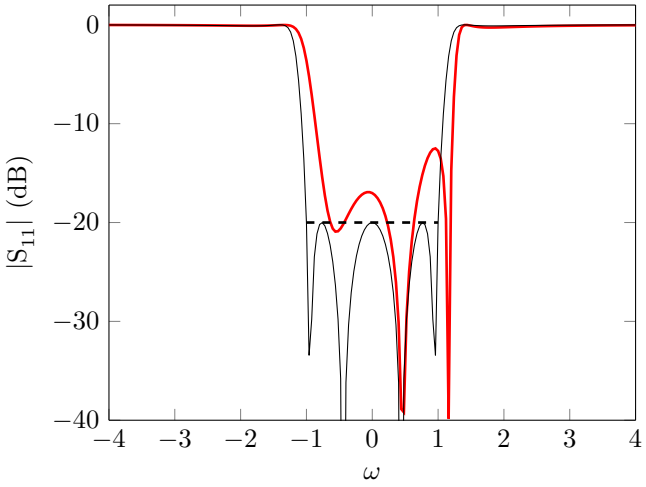


**(a)** $|S_{11}|$ (—) for the simulated filter and ideal response (—) and the specifications (- - -).

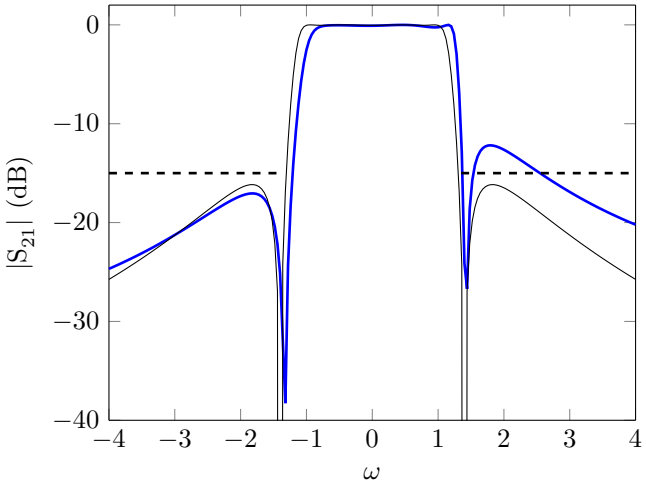


**(b)** $|S_{21}|$ (—) for the simulated filter and ideal response (—) and the specifications (- - -).

**Figure 3.16** Comparison between the ideal and simulated response.

# 4

# Extraction of the Coupling Matrix

This chapter presents a method to extract a coupling matrix starting from the simulated (or measured) $S$-parameters of the filter. The $S$-parameters are first transformed to the lowpass domain. The extraction method estimates a common denominator matrix of prescribed McMillan degree $N$ for the $S$-parameters of the filter in the lowpass domain after adjusting the reference plane. Next it synthesizes a coupling matrix in the arrow form. This coupling matrix is then reconfigured to match the implemented coupling topology. In the case of multiple solutions, all admissible solutions are determined. The extraction method has been implemented in the Matlab toolbox PRESTO-HF [Seyf 04], which we use to extract the arrow form coupling matrix starting from the simulated $S$-parameters of the filter. Since we are dealing with non-ideal (real) filters, the simulated data do not perfectly match the coupling matrix model. By a real filter, we mean the electromagnetic model of the filter, and not real in the sense that the filter is manufactured. This makes that the coupling matrix also contains parasitic couplings. At the end of this chapter we explain how parasitic couplings are handled and how this affects the reconfiguration of the coupling matrix. The coupling matrix extraction method is applied to a single and to a cascaded quadruplet filter.

## 4.1 Introduction

In filter design it is necessary to extract the arrow form coupling matrix starting from the simulated or measured $S$-parameters of the filter. Knowledge of the extracted coupling matrix allows a designer to diagnose problems if the implemented coupling matrix is too far a way from the ideal target coupling matrix. This ideal matrix is also called the golden goal. A designer can then correct or tune the physical dimensions of the filter to bring the coupling matrix closer to the target one. To be able to tune the physical dimensions of the filter using the

extracted coupling matrix, one must be sure to extract the coupling matrix that is physically implemented. As we have seen in Section 2.8.3 and Section 3.6, the implemented coupling topology does not always correspond to the arrow form. Moreover the implemented topology can have multiple mathematically equivalent solutions leading to a coupling matrix of the desired form. Another problem is the presence of parasitic couplings. These second order perturbation effects change the structure of the coupling matrix, hereby modifying the frequency response function (FRF) in a way that is not contained in the golden goal. In this chapter we explain how we extract the arrow form coupling matrix starting from simulated (or measured) $S$-parameters, to reconfigure it to the target coupling topology and to handle the presence of parasitic couplings. The procedure used to handle multiple solutions is discussed in the next chapter.

Over the last years several methods to extract the coupling matrix starting from the $S$-parameters have been developed in order to tune filters [Hars 01; Hars 02; Bila 99; Seyf 03; Garc 04; Lamp 04; Hu 13; Hu 14]. These extraction techniques can roughly be divided in 2 categories:

- Optimization-based methods optimize the coupling matrix parameters to fit the measured/simulated $S$-parameters in the lowpass domain [Hars 01; Hars 02]. These methods yield only one solution by construction. The solution strongly depends on the initial values for the coupling parameters that need to be specified by the user. Only one solution is obtained, even if there are multiple possibilities. Unfortunately, this one solution does not necessarily correspond to the physically implemented one. A comparison based on a coupling matrix that is inconsistent with the actual filter physical dimensions can propose incoherent corrections destroying the tuning procedure.

- Network-synthesis-based methods first identify the numerator polynomials of $S_{11}$ and $S_{21}$ [Garc 04; Lamp 04] or a rational matrix [Bila 99; Seyf 03; Hu 13; Hu 14] representing the measured/simulated $S$-parameters in the lowpass domain. Next the method synthesizes a coupling matrix starting from the identified polynomials or the rational form. In the case of coupling topologies having multiple solutions these methods do not specify which solution is synthesized.

Since we want to handle coupling topologies supporting multiple solutions, we use an extraction method of the second category. The rational approxima-

tion used in this work is described in [Seyf 03; Oliv 13] and is based on $H^2$-approximation [Marm 02]. This method mainly consists of 2 steps:

1. An analytical completion is obtained first to derive a stable and causal model of very high degree that fits the data.
2. A rational approximation is pursued next that identifies a stable rational matrix of an a-priori and imposed McMillan degree $N$.

The method also takes into account the influence of the presence of feeding or access lines on the filter response and automatically adjusts the reference plane. The method has been implemented in the Matlab toolbox PRESTO-HF [Seyf 04], which we will use intensively in the remainder of this work. Section 4.3 explains the principles used in the rational approximation method. The main benefit of this method is that it identifies a stable, causal, rational matrix of fixed MacMillan degree $N$, where $N$ corresponds to the order of the lowpass equivalent filter or the number of resonators present in the physical filter. As we have seen in Section 2.7.2, this is a necessary condition to be able to synthesize a minimal coupling matrix of size $(N+2)\times(N+2)$. We now briefly discuss the differences with the other methods of the second category.

The method described in [Garc 04] is called the Cauchy method. This method assumes that the Feldtkeller equation (2.17) is valid for the physical filter. The method first estimates the rational model for the ratio $\frac{S_{11}}{S_{21}}$. Next it identifies the numerator of this function as the reflection polynomial and the denominator as the numerator polynomial of the transmission function. Finally it constructs the common denominator of the rational $S$-matrix using the Feldtkeller equation. One of the drawbacks of this method is that it assumes that the filter is loss-less, which is not the case in practice. Therefore the method has been improved to handle lossy data by reformulating the total least-squares problem without imposing the lossless condition [Lamp 04]. Another approach [Macc 10] assumes that all of the resonators have the same unloaded quality factor $Q_u$. This method transforms the $S$-parameters to a predistorted frequency domain using the following frequency transformation:

$$\omega = \frac{1}{FBW}\left(\frac{1}{Q_u} + j\left(\frac{f}{f_c} - \frac{f_c}{f}\right)\right) \tag{4.1}$$

Next it applies the Cauchy method in the predistorted frequency domain, thereby avoiding all of the problems related to the synthesis of lossy networks such

as complex couplings. This method heavily relies on the assumption that the unloaded quality factor is known and equal for all resonators.

The method described in [Hu 13; Hu 14] estimates a rational matrix for the $Y$-parameters using the vector fitting (VF) algorithm [Gust 99; Gust 06]. The VF algorithm estimates a pole-residue form in least-squares sense on the data by iteratively re-locating the position of the poles. The benefit of the methods described above is that they are relatively simple to implement and yield accurate rational models.

The main drawback of the methods described in [Lamp 04; Hu 13; Hu 14] is the fact that the identified rational matrix is not imposed to have a McMillan degree $N$. This is a problem since the methods next synthesize a coupling matrix using the method described in [Came 03]. This method [Came 03] is equivalent to Gilbert's method [Gilb 63] and thus assumes that the rational matrix is of fixed McMillan degree $N$ (Section 2.7.2). Applying it to a rational form that is not of McMillan degree $N$, introduces an error and results in the estimation of a coupling matrix that does no longer represent the rational $S$-matrix. Since the method used here extracts a rational matrix of McMillan degree $N$, it can always be used to synthesize the transversal $N+2$ coupling matrix.

The transversal $N+2$ coupling matrix is first transformed to the canonical arrow form coupling topology. To enable one to transform the arrow form to the target coupling topology, both coupling matrices have to have the same number of non-zero elements as is discussed in Section 2.8.3. Since the filter is not ideal, this compatibility condition is generally not met. In section Section 4.5, we explain how to reduce the arrow form matrix (remove the parasitic couplings) such that it can be transformed to the target coupling topology. The transformation is done using the Matlab toolbox DEDALE-HF [Seyf 00]. In the case of multiple solutions, we determine all possible solutions. How to identify the physical solutions in this set of possibilities is discussed in the next chapter. Section 4.6 explains how the parasitic couplings are taken into account and how they should be interpreted. Finally the extraction method is applied to two examples: a single and a cascaded quadruplet filter.

A limitation of the proposed extraction technique is that the model order must be the same of the synthesized filter $N$. In the physical device the actual order is however higher, due to the frequency variation of the couplings, higher order mode resonances, etc. The effect of these inaccuracies can not be compensated by including spurious couplings, since this modifies only the number of zeros $n_{fz}$ as is explained in Section 2.8.

In what follows we first explain how the data is transformed to the lowpass domain, next the rational approximation and finally the synthesis of the coupling matrix having the desired coupling topology. Note that Section 4.3 can be seen as a summary of [Oliv 13] and [Seyf 03].

## 4.2 Bandpass-to-Lowpass Transformation

The simulated or measured frequencies are transformed to the lowpass domain using the following transformation:

$$\omega_i = \frac{2}{f_2 - f_1}(f_i - f_0) = \frac{2}{\Omega_0 FBW}(\Omega_i - \Omega_0) \tag{4.2}$$

where $f_i$ is a simulated frequency in the bandpass domain and $\omega_i$ is the corresponding normalized frequency in the lowpass domain and $\Omega$ is the bandpass angular frequency. $f_0$ is the center frequency and $f_1$ and $f_2$ are the cut-off frequencies of the passband specified by the frequency template. Since the center frequency $f_0$ and fractional bandwidth $FBW$ of the filter to be optimized are not necessarily equal to the ideal $f_0$ and $FBW$, the passband of the simulated $S$-parameters in the lowpass domain does not always lie between [-1,1]. Note that the transformation given in (4.2) is the same as the one used in Section 2.5 to transform the lumped-equivalent network to the lowpass domain (2.30).

## 4.3 Rational Approximation and Reference Plane Adjustment of the $S$-parameters

The extraction method identifies a mathematical model for the simulated $S$-parameters of the filter in the lowpass domain:

$$\boldsymbol{S}_{Sim}(j\omega_i) = \begin{bmatrix} S_{Sim_{11}}(j\omega_i) & S_{Sim_{12}}(j\omega_i) \\ S_{Sim_{21}}(j\omega_i) & S_{Sim_{22}}(j\omega_i) \end{bmatrix} \tag{4.3}$$

where $i \in \{1, \ldots, n_F\}$ and $n_F$ denotes the number of simulated frequencies. The mathematical model is denoted as $\boldsymbol{H}$ and has the following form:

$$\boldsymbol{H}(j\omega) = \frac{1}{q(j\omega)} \begin{bmatrix} e^{-j(\omega\alpha_{11}+\beta_{11})}p_{11}(j\omega) & e^{-j(\omega\frac{\alpha_{11}+\alpha_{22}}{2}+\frac{\beta_{11}+\beta_{22}}{2})}p_{12}(j\omega) \\ e^{-j(\omega\frac{\alpha_{11}+\alpha_{22}}{2}+\frac{\beta_{11}+\beta_{22}}{2})}p_{21}(j\omega) & e^{-j(\omega\alpha_{22}+\beta_{22})}p_{22}(j\omega) \end{bmatrix} \tag{4.4}$$

where $q$ is the common denominator polynomial of order $N$ and $p_{11}, p_{12}, p_{21}$ and $p_{22}$ are the numerator polynomials of order $N$. $\alpha_{11}$ and $\alpha_{22}$ are real-valued constants that model the delays introduced by the access (feeding) lines at input and output respectively. $\beta_{11}$ and $\beta_{22}$ are real-valued constants that model the frequency shift introduced by the bandpass-to-lowpass transformation (4.2). Note that (4.4) can also be written as:

$$\begin{bmatrix} e^{-j(\omega\alpha_{11}+\beta_{11})} & 0 \\ 0 & e^{-j(\omega\alpha_{22}+\beta_{22})} \end{bmatrix} \boldsymbol{S}_{rat}(j\omega) \begin{bmatrix} e^{-j(\omega\alpha_{11}+\beta_{11})} & 0 \\ 0 & e^{-j(\omega\alpha_{22}+\beta_{22})} \end{bmatrix} \quad (4.5)$$

where the first and last matrix model the access lines and the matrix $\boldsymbol{S}_{rat}(j\omega)$ models the filter. The coupling matrix is synthesized starting from the stable rational matrix $\boldsymbol{S}_{rat}$ of McMillan degree $N$:

$$\boldsymbol{S}_{rat}(j\omega_i) = \frac{1}{q(j\omega_i)} \begin{bmatrix} p_{11}(j\omega_i) & p_{12}(j\omega_i) \\ p_{21}(j\omega_i) & p_{22}(j\omega_i) \end{bmatrix} \quad (4.6)$$

To have a stable rational approximation of good quality, the algorithm requires that the $S$-parameters are known at each frequency ranging from $-\infty$ to $+\infty$ ($\forall\omega \in \mathbb{R}$). Therefore the identification method first computes a stable and causal model of high degree starting from the simulated $S$-parameters with the delays removed, this step is called the completion stage. This high degree model thus describes the behavior of the filter (without access lines) in the lowpass domain for all frequencies going from $-\infty$ to $+\infty$. Next the rational matrix (of much lower degree $N$) is estimated by rational $H^2$ approximation using the high degree model as an input [Oliv 13; Marm 02].

The method to identify the mathematical model given in (4.4) starting from simulated $S$-parameters of the filter in the lowpass domain consists of the following steps:

1. Completion:
    - Estimation of the delays $\alpha_{11}$ and $\alpha_{22}$.
    - Analytic completion of the simulated $S$-parameters with delays removed
    - Estimation of the frequency shifts $\beta_{11}$ and $\beta_{22}$.

2. Estimation of the rational matrix $\boldsymbol{S}_{rat}$ starting from the analytic completion.

### 4.3.1 DELAY ESTIMATION

The estimation of $\alpha_{11}$ and $\alpha_{22}$ relies on the hypothesis that the rational behavior in (4.4) for frequencies far from the passband are well approximated by the first few terms of their Taylor expansion at infinity [Seyf 03]. This boils down to assuming that the rational model of the filter behaves as a low degree polynomial in $\frac{1}{\omega}$ for frequencies far out the passband. To be able to estimate the delays, the filter must therefore be simulated over a broader frequency band than the passband of the filter. Consider only the simulated frequencies that are smaller than $-\omega_c$ and larger than $\omega_c$ with $|\omega_c| > 1$:

$$I = \{\omega_i, |\omega_i| \geq \omega_c\} \tag{4.7}$$

The value of $\alpha_{11}$ is found by minimizing the least-squares cost function $\psi$:

$$\psi(\alpha_l) = \min_{(a_0,a_1,\ldots,a_{n_m-1})\in\mathbb{C}^{(n_c-1)}} \sum_{\omega_i\in I} \left| \sum_{k=0}^{n_m-1} \frac{a_k}{\omega_i^k} - S_{Sim_{11}}(\omega_i) e^{j\omega_i\alpha_l} \right|^2 \tag{4.8}$$

For a fixed value of $\alpha_l$, $\psi(\alpha_l)$ is minimized in least-squares sense over the coefficients $(a_0, a_1, \ldots, a_{n_m-1}) \in \mathbb{C}^{(n_m-1)}$. Since the value of $\alpha_{11}$ corresponds to the physical delay, it is possible to determine boundaries for the interval in which $\alpha_{11}$ is located based on the geometry of the circuit. The function $\psi$ is exhaustively searched within this interval with a prescribed tolerance on $\alpha_l$. $\alpha_{11}$ is determined as the value for which $\psi$ is minimal within the interval.

To determine $\alpha_{22}$ we proceed in the same way using $S_{Sim_{22}}$ instead of $S_{Sim_{11}}$. Once $\alpha_{11}$ and $\alpha_{22}$ are estimated, we de-embed the delays of simulated $S$-parameters as follows:

$$\boldsymbol{S}_{Ca}(j\omega_i) = \begin{bmatrix} e^{j\omega_i\alpha_{11}} S_{Sim_{11}}(j\omega_i) & e^{j\omega_i\frac{\alpha_{11}+\alpha_{22}}{2}} S_{Sim_{12}}(j\omega_i) \\ e^{j\omega_i\frac{\alpha_{11}+\alpha_{22}}{2}} S_{Sim_{21}}(j\omega_i) & e^{j\omega_i\alpha_{22}} S_{Sim_{22}}(j\omega_i) \end{bmatrix} \tag{4.9}$$

### 4.3.2 ANALYTIC COMPLETION

The completion stage computes a stable and causal high degree order model $\boldsymbol{F}$ for the de-embedded $S$-parameters for all frequencies going from $-\infty$ to $+\infty$. The model is computed starting from the de-embedded $S$-parameters at the simulated frequencies in the lowpass domain. The frequency interval corresponding to the simulated frequency band is denoted as:

$$J = [\min(\omega_i), \max(\omega_i)] \tag{4.10}$$

where $\omega_i$ denotes a simulated frequency in the lowpass domain. For a value between 2 simulated frequencies $\boldsymbol{S}_{Ca}$ is computed by spline interpolation. We denote the complement of the interval $J$ as:

$$J_c = ]-\infty, \min(\omega_i)[ \cup ] \max(\omega_i), +\infty[ \tag{4.11}$$

We split the frequency span $-\infty \leq \omega \leq +\infty$ in the partition of $J$ and $J_c$. For frequencies in $J_c$, we model the $S$-parameters using a low degree polynomial $m_{kl}$ in $\frac{1}{\omega}$ using the same assumption as in Section 4.3.1. $S_{Ca_{kl}}(j\omega)$ (the elements of the matrix $\boldsymbol{S}_{Ca}$ labeled $k, l \in \{1, 2\}$) represents the function in $J$, while the polynomial $m_{kl}(j\omega)$ is used for frequencies in $J_c$. The complete function is labeled as $S_{Ca_{kl}}(j\omega) \wedge m_{kl}(j\omega)$. In order to determine $m_{kl}$ we use a cost function as in (4.8) to estimate the coefficients of $m_{kl}(j\omega)$, but we also take into account that $\boldsymbol{F}$ must be causal and stable. Since we want to obtain a stable, causal and rational model $\boldsymbol{S}_{rat}$, we first want to have a stable high-order model to prepare the rational approximation step.

For a rational model the stability and causality properties require that all the poles are finite and in the open left half plane. The latter is equivalent to the fact that the function is analytic in the closed right half plane and at infinity.

To properly handle these properties mathematically we embed the rational functions in a larger space of functions which are known to be analytic in the right half plane: the Hilbert space of analytic functions in the open right half plane. Their $L^2(d\mu(\omega))$-norm remains uniformly bounded on vertical lines [Seyf 03; Part 97] whenever $d\mu(\omega) = \frac{d\omega}{1+\omega^2}$. This space is a Hardy space of the right half plane and we denote it as $H^2_\mu$. The $L^2(d\mu(\omega))$-norm of a function $f$ is given by:

$$\| f \|^2 = \int_{-\infty}^{+\infty} \frac{|f(j\omega)|^2}{1+\omega^2} d\omega \tag{4.12}$$

We define $L_\mu^2$ as the space of all complex functions defined on the imaginary axis for which (4.12) is finite. $H_\mu^2$ can be viewed as a subspace of the space $L_\mu^2$. If we define $G_\mu^2$ as the orthogonal complement of $H_\mu^2$ in $L_\mu^2$ every function $f \in L_\mu^2$ can be written as the sum of a function in $H_\mu^2$ (the stable part) and a function in $G_\mu^2$ (the unstable part) [Seyf 03]. We denote $P_{H_\mu^2}(f)$ as the orthogonal projection of $f$ on $H_\mu^2$ and similarly $P_{G_\mu^2}(f)$ as the orthogonal projection of $f$ on $G_\mu^2$. This framework provides us with an interesting tool to estimate the stability and causality of a function.

The following minimization problem is solved to determine the polynomials $m_{kl}(j\omega)$ $(k, l \in \{1, 2\})$:

$$\min_{m_{kl}} \sum_{\omega_i \in I} \left| S_{Ca_{kl}}(j\omega_i) - m_{kl}\left(\frac{1}{j\omega_i}\right) \right|^2 \tag{4.13}$$

with

$$\begin{cases} m_{kl} \in \mathbb{C}^{n_m}[X] \\ \parallel P_{G_\mu^2}(S_{Ca_{kl}} \wedge m_{kl}) \parallel^2 \leq E_c \\ \forall \omega \in J_c, |m_{kl}|^2 \leq 1 \end{cases} \tag{4.14}$$

Herein $P_{G_\mu^2}(S_{Ca_{kl}} \wedge m_{kl})$ is the projection of the completed data on $G_\mu^2$ and represents the unstable part of the completed data. $\mathbb{C}^{n_c}[X]$ denotes the set of polynomials with complex coefficients whose degree is smaller or equal to $n_m$. $E_c$ is an upper bound on the norm of the unstable part of the completed data. The last expression in (4.14) is an upper bound on the magnitude of the completed data in $J_c$, which must be smaller than 1 for $\omega_i \in J_c$. This optimization problem has a unique solution unless the set of admissible solutions is empty, hence it is a convex problem [Seyf 03].

The completed $S$-matrix is given by:

$$\boldsymbol{S}_{Cb}(j\omega) = \begin{bmatrix} (S_{Ca_{11}} \wedge m_{11})(j\omega) & (S_{Ca_{12}} \wedge m_{12})(j\omega) \\ (S_{Ca_{21}} \wedge m_{21})(j\omega) & (S_{Ca_{22}} \wedge m_{22})(j\omega) \end{bmatrix} \tag{4.15}$$

Novel approach

In the latest version of PRESTO-HF [Seyf 04], the completion is performed simultaneously with the determination of the delay $\tau$. We associate a polynomial $p_\tau$ to a delay $\tau$ where $p_\tau$ is the minimizer of:

$$p_\tau = \arg\min_{p\in\mathcal{P}} \int_{-\infty}^{+\infty} \frac{|P_{G_\mu^2}(S_{Sim_{11}}(j\omega)e^{j\omega\tau} \wedge p(\frac{1}{j\omega}))|^2}{1+\omega^2} d\omega \tag{4.16}$$

where $\mathcal{P} = \{p \text{ is a polynomial in } j\omega;\ \deg p \leq n_c;\ \forall\omega \in J_c,\ |p|^2 \leq 1.$

Similarly to what is done Section 4.3.1 (4.16) is scanned for an a-priori defined number of values of $\tau$ within a range that is based on prior knowledge. The value of $\tau$ that results in the smallest discontinuity between the completion and the data in the interval $I$ (4.7), is chosen equal to the delay $\alpha_{11}$. To determine $\alpha_{22}$ we proceed in the same way using $S_{Sim_{22}}$ instead of $S_{Sim_{11}}$ in (4.16). The completion polynomials $p_{\alpha_{11}}$ and $p_{\alpha_{22}}$ are improved next using (4.13).

### 4.3.3 DETERMINATION OF THE FREQUENCY SHIFTS

The determination of the frequency shifts $\beta_{kl}$ $(k,l \in \{1,2\})$ is based on the observation that the behavior of the completed $S$-matrix $\boldsymbol{S}_{Cb}$ must be close to the behavior of the lumped equivalent lowpass network introduced in Section 2.5. At an infinite frequency the equivalent network behaves as an open ended circuit and therefore the $S$-matrix is equal to the identity matrix of size $2\times 2$ $\boldsymbol{I}_2$ at $\omega = +\infty$. The phase of the reflection factors $S_{kk}(j\omega)$ at both ports is thus 0 for the lumped equivalent lowpass network. We then determine $\beta_{11}$ and $\beta_{22}$ to be equal to the phase of $S_{Cb_{11}}$ and $S_{Cb_{22}}$ at $\omega = +\infty$ respectively:

$$\begin{aligned} \beta_{11} &= \arg(m_{11}(0)) \\ \beta_{22} &= \arg(m_{22}(0)) \end{aligned} \tag{4.17}$$

Note that the solutions $\beta_{11}$ and $\beta_{22}$ are determined up to $k\pi$ $(k \in \mathbb{Z})$. The software PRESTO-HF makes an arbitrary choice for the value of $k$. This choice can change the sign of the output coupling. It is thus possible to select the values of $\beta_{11}$ and $\beta_{22}$ by looking at the sign of the output coupling. The final completed $S$-matrix is given by:

$$\boldsymbol{S}_C(j\omega) = \begin{bmatrix} e^{j(\omega\alpha_{11}+\beta_{11})}S_{Sim_{11}} \wedge m_{11}(\frac{1}{\omega}) & e^{j(\omega\frac{\alpha_{11}+\alpha_{22}}{2}+\frac{\beta_{11}+\beta_{22}}{2})}S_{Sim_{12}} \wedge m_{12}(\frac{1}{\omega}) \\ e^{j(\omega\frac{\alpha_{11}+\alpha_{22}}{2}+\frac{\beta_{11}+\beta_{22}}{2})}S_{Sim_{21}} \wedge m_{21}(\frac{1}{\omega}) & e^{j(\omega_i\alpha_{22}+\beta_{22})}S_{Sim_{22}} \wedge m_{22}(\frac{1}{\omega}) \end{bmatrix} \tag{4.18}$$

The matrix $\boldsymbol{S}_C$ models the de-embedded behavior of the filter data for $-\infty \leq \omega \leq +\infty$. The projection of $\boldsymbol{S}_C$ on $H^2_\mu$ is $\boldsymbol{F}$. The matrix $\boldsymbol{F}$ is the starting point for the rational approximation $S_{rat}$.

### 4.3.4 DETERMINATION OF STABLE RATIONAL MATRIX OF MCMILLAN DEGREE $N$

Knowing the delays $\alpha_{ii}$, the frequency shifts $\beta_{ii}$ and the polynomials $m_{kl}$ that complete the $S$-parameters outside of the simulated frequency band, we can finally define the matrix $\boldsymbol{F}$:

$$\boldsymbol{F}(j\omega) = \begin{bmatrix} P_{H^2}(S_{C_{11}})(j\omega) & P_{H^2}(S_{C_{12}})(j\omega) \\ P_{H^2}(S_{C_{21}})(j\omega) & P_{H^2}(S_{C_{22}})(j\omega) \end{bmatrix} \tag{4.19}$$

The matrix $\boldsymbol{F}(j\omega)$ represents the stable part of the filter response with the influence of the access lines de-embedded for every lowpass frequency in the range from $-\infty$ to $+\infty$. The rational matrix $\boldsymbol{S}_{rat}(j\omega)$ is determined by minimizing the following least-squares approximation problem:

$$\min_{\boldsymbol{R}} \parallel \boldsymbol{F}(j\omega) - \boldsymbol{R}(j\omega) \parallel^2 = \sum_{k,l\in\{1,2\}} \parallel F_{kl}(j\omega) - R_{kl}(j\omega) \parallel^2 \tag{4.20}$$

where $\boldsymbol{R}(j\omega)$ is a stable rational matrix of McMillan degree $\leq N$. The minimizer of (4.20) is called $\boldsymbol{S}_{rat}(j\omega)$. The problem (4.20) is minimized using the software RARL2 [RARL] . Without going into detail, we mention that the algorithms implemented in RARL2 [RARL] are based on the following principles:

- The stable rational matrices of given McMillan degree can be nicely parametrized using Schur parameters.
- If $F_{kl} \notin H^2$, the unstable part of $F_{kl}$ can not be well approximated by a stable rational function $R_{kl}$.

More details can be found in [Oliv 13; Marm 02].

## 4.4 Synthesis of the Coupling Matrix in Arrow Form

The coupling matrix extraction yields a transversal $N+2$ coupling matrix starting from the rational matrix $\boldsymbol{S}_{rat}(j\omega)$ using Gilbert's method [Gilb 63] (Section 2.7.2). Next, this matrix is transformed to its canonical arrow form $\boldsymbol{M}^0_{arr}$ (Section 2.7.3). The rational approximation method imposes the causality, the

stability and the McMillan degree $N$ of $\boldsymbol{S}_{rat}(j\omega)$. The latter is a necessary condition to obtain a state-space system matrix of size $N \times N$ (Section 2.7.2) as is required here.

The rational approximation does not impose the order of $p_{21}(j\omega)$ and therefore it normally identifies $N$ finite transmission zeros. This implies that a direct source-to-load coupling is to be present in the extracted $N+2$ coupling matrix. This can be shown using the shortest path rule that is explained in Section 2.8.1.

The corresponding rational $Y$-parameters hence do not fulfill (2.78), as the number of transmission zeros exceeds $N-2$. (2.78) is a necessary condition to obtain a matrix $\boldsymbol{B}_f$ where only elements $(1,1)$ and $(N,2)$ are non-zero as is explained in (2.91). These elements represent the source-to-resonator 1 and load-to-resonator $N$ coupling respectively. When the number of transmission zeros exceeds $N-1$, the elements $(1,2)$ and $(N,1)$ of $\boldsymbol{B}_f$ are also non-zero. The elements $(1,2)$ and $(N,1)$ represent the load-to-resonator 1 and source-to-resonator $N$ coupling respectively.

The fact that the number of transmission zeros exceeds $N-2$, also results in a non-zero arrow form where the main diagonal, first upper diagonal and last column are obtained as is explained in Section 2.8.2. This implies that the presence of more inter-resonator couplings in the simulated filter than in the ideal coupling topology. These couplings can be interpreted as parasitic or unwanted couplings. The non-zero diagonal elements can be interpreted as frequency offsets between the resonant frequency of the individual resonators and the center frequency of the filter.

Note that the simulated filter is not necessarily lossless. In the case of a lossy structure the elements of the coupling matrix are complex rather than purely imaginary. The real part of the diagonal elements can be interpreted as the quality factor of the resonators (Section 2.6.1). Although synthesis methods exist that take into account lossy couplings [Mira 08], we do not take them into account here neither during the synthesis or the tuning of the filter.

The extraction method yields a complex-valued arrow form coupling matrix $\boldsymbol{M}^0_{arr}$ where the diagonal, first upper diagonal and last column are non-zero. This is not in line with the arrow form obtained from the golden goal and therefore additional steps are needed to bring the 2 representations as closely together as possible in order to be able to reconfigure the extracted matrix to the coupling topology of the golden goal.

## 4.5 Reconfiguration of the Extracted Arrow Form Matrix

The extracted arrow form $\boldsymbol{M}^0_{arr}$ is in general not compatible with the ideal coupling topology of the prototype filter, since its number of non-zero elements exceeds the number of degrees of freedom that can be accommodated by the target topology (Section 2.8.2). As seen in Section 4.4, this is due to the presence of parasitic couplings.

Some of these couplings can be seen as second order effects that influence the filter only marginally, but unfortunately some others must be treated as first order effects with a significant impact. In what follows we describe the coupling topology of a filter by means of a matrix $\boldsymbol{T}$ whose elements are 1 if the corresponding coupling is present in the topology and are 0 otherwise. As is explained in Section 2.8.2 a full arrow form is not always compatible with any topology $\boldsymbol{T}$. We denote the arrow form that is compatible with a topology $\boldsymbol{T}$ as $\boldsymbol{M}^{\boldsymbol{T}}_{arr}$. In order to obtain a compatible arrow form, certain elements of the extracted arrow form matrix $\boldsymbol{M}^0_{arr}$ must be forced to zero, yielding a reduced arrow form $\boldsymbol{M}^{\boldsymbol{T}}_{arr}$ of the initial coupling matrix $\boldsymbol{M}^0_{arr}$. We denote the ideal coupling topology of the golden goal as $\boldsymbol{T}_{id}$. We explain in the next section that the coupling topology of the real filter denoted as $\boldsymbol{T}_{struct}$ does not necessarily correspond to $\boldsymbol{T}_{id}$.

### Reduction of $\boldsymbol{M}^0_{arr}$ to $\boldsymbol{M}^{\boldsymbol{T}}_{arr}$

To be able to reduce the complete arrow form $\boldsymbol{M}_{arr}$ to the reduced one that is compatible with the selected physical filter structure $\boldsymbol{M}^{\boldsymbol{T}}_{arr}$, we need to assume that the implemented coupling topology is sufficiently close to the ideal topology $\boldsymbol{T}_{id}$. This assumption implies that the elements that are set to zero during the reduction of the arrow form are small with respect to the elements that are kept. In other words, we assume that the parasitic inter-resonator couplings are second order effects. In practice we observe that the parasitic couplings are at least an order of magnitude lower than the desired couplings.

For topologies supporting asymmetrical responses the matrix $\boldsymbol{M}^0_{arr}$ is reduced to an arrow form $\boldsymbol{M}^{\boldsymbol{T}_{id}}_{arr}$ by simply eliminating the undesired parasitic couplings in $\boldsymbol{M}^0_{arr}$. In practice this corresponds to eliminating elements in the last row and column $\boldsymbol{M}^0_{arr}$ as is explained in Section 2.8.2. Physically, this eliminates the couplings that are present in the real filter, but not in the ideal coupling topology.

For topologies supporting symmetrical responses, the diagonal of $\boldsymbol{T}_{id}$ is zero and the diagonal of the corresponding arrow form is to be zero as well. Since the real physical filter is never perfectly tuned, its response is not ideally symmetrical

with respect to the center frequency. This asymmetry is mainly due to the presence of self-couplings. Unlike the inter-resonator parasitic couplings, these self-coupling can not be treated as a second order effects. Therefore they have to remain present in the reduced arrow form as well. We do not eliminate the diagonal elements of $\boldsymbol{M}_{arr}^{0}$ by bluntly setting them to zero. We reduce $\boldsymbol{M}_{arr}^{0}$ to an arrow form compatible with the coupling topology closest to the ideal coupling topology that accommodates asymmetric responses instead. This makes that the coupling topology $\boldsymbol{T}_{struct}$ to which the coupling matrix is reconfigured does not correspond to $\boldsymbol{T}_{id}$ in this case. This is different in the case for topologies supporting asymmetrical responses. The choice of the coupling topology $\boldsymbol{T}_{struct}$ heavily depends on the topology $\boldsymbol{T}_{id}$. In the examples considered in this work, we see that $\boldsymbol{T}_{struct}$ has a non-zero diagonal and some extra cross-couplings with respect to $\boldsymbol{T}_{id}$. We illustrate this for a cascaded quadruplet filter in Section 4.8. Note that the number of non-zero couplings grows from $N+\frac{n_{f2}}{2}+1$ to $2N+n_{fz}+1$ as is explained in Section 2.8.2.

Reconfiguration of $\boldsymbol{M}_{arr}^{\boldsymbol{T}}$

Once $\boldsymbol{M}_{arr}^{\boldsymbol{T}}$ is determined, we calculate all the similarity transformation matrices $\boldsymbol{P}_i$ that reconfigure $\boldsymbol{M}_{arr}^{\boldsymbol{T}}$ to the desired coupling topology $\boldsymbol{T}$. These similarity transformations are obtained using the software DEDALE-HF [Seyf 00]. Note that $n_S$ multiple solutions might exist for certain coupling topologies. ($n_S$ denotes the number of solutions) For such topologies every possible solution (every possible transformation $\boldsymbol{P}_i$ ($i \in \{1,\ldots,n_S\}$)) is determined. Once every $\boldsymbol{P}_i$ is determined, they are applied to the originally extracted arrow form coupling matrix $\boldsymbol{M}_{arr}^{0}$. We apply the transformation to $\boldsymbol{M}_{arr}^{0}$ rather than $\boldsymbol{M}_{arr}^{T}$, to take into account the second order parasitic couplings. This process yields $n_S$ extracted coupling matrices $\boldsymbol{M}_{P_i}$ ($i \in \{1,\ldots,n_S\}$). Note that these matrices still contain non-zero elements in their last column (and last row) that are not present in the ideal topology. This step thus re-introduces the parasitic couplings that were eliminated to obtain $\boldsymbol{M}_{arr}^{T}$.

## 4.6 Dealing with Parasitic Couplings

As is explained in Section 2.8.3, the matrices $\boldsymbol{M}_{P_i}$ ($i \in \{1,\ldots,n_S\}$) contain non-zero elements resulting in couplings that are not present in the ideal coupling topology. These non-zero elements are located in the last column and row of $\boldsymbol{M}_{P_i}$ and are therefore not necessarily located at the place where they are physically expected. These elements can be interpreted as follows: they model the part of the filter response that can not be explained (modeled) by the coupling matrix

model of the ideal coupling topology. They do not only model the effect of the parasitic couplings, but can also account for the fact that the physical coupling is not frequency independent while this is assumed in the coupling matrix model.

In order to have a more physical distribution of the parasitic couplings, we can approximate the compensated simulations $\boldsymbol{S}_C(j\omega)$ at the simulated lowpass frequencies by a coupling matrix that contains non-zero elements only at positions where the parasitic couplings are expected to be present from a physical point of view. The initial matrix that is used to start this optimization method is the matrix $\boldsymbol{M}_{P_i}$ in which the extra elements in the last row and column are removed. We denote this matrix as $\boldsymbol{M}_{par,0}$ . Eliminating elements in the last row and column, will for sure deteriorate the approximation. The idea is to add the parasitic couplings in the matrix to improve the approximation. Therefore the optimization method minimizes the 2-norm of the difference between the compensated $S$-matrix and the response created by the coupling matrix. For each $S$-parameter the method calculates the 2-norm of the difference between $S_{C_{kl}}(j\omega)$ and the response created by $\boldsymbol{M}_{par,h}$ (where $h$ denotes the iteration in the optimization method):

$$c_{kl} = \sqrt{\sum_{f=1}^{n_f} |S_{C_{kl}}(\omega_f) - S_{kl}^{\boldsymbol{M}_{par,h}}(\omega_f))|^2} \tag{4.21}$$

where $k, l \in \{1, 2\}$, $n_f$ is the number of simulated frequencies and $S_{kl}^{\boldsymbol{M}_{par,h}}$ is the response corresponding to the coupling matrix $\boldsymbol{M}_{par,h}$.

The least-squares cost function that is minimized is the 2-norm of the total difference:

$$c = \sqrt{\sum_{k=1}^{2}\sum_{l=1}^{2} c_{kl}^2} \tag{4.22}$$

and is to be minimized over the non-zero elements in the coupling matrix $\boldsymbol{M}_{par,h}$. The minimizer is calculated using the Matlab function *fminunc*, which searches the minimum for an unconstrained multi-variable scalar function. The drawback of this method is that it heavily depends of its initial values and that the algorithm might converge to a local minimum of unpredictable quality if the initial value is poor. In Section 4.8 we apply this optimization method to redistribute the parasitic couplings in cascaded quadruplet topology.

## 4.7 Example: Single Quadruplet (SQ) Filter

We now apply the coupling matrix extraction method to the single quadruplet square open-loop resonator filter introduced in Section 3.6. The prescribed McMillan degree of the lowpass filter is 4. The filter is simulated for [0.9:0.001:1] GHz. The ideal center frequency and fractional bandwidth for which the filter is designed, are $f_c = 1$ GHz and $FBW = 0.05$ respectively. The corresponding lowpass frequency grid is calculated to be [-4:0.04:4]. The extracted values for the delays and the frequency shifts are grouped in the matrices $\boldsymbol{\alpha}$ and $\boldsymbol{\beta}$ respectively:

$$\boldsymbol{\alpha} = \begin{bmatrix} 0.0580 & 0.0585 \\ 0.0585 & 0.059 \end{bmatrix} \qquad \boldsymbol{\beta} = \begin{bmatrix} -2.8491 & 0.3158 \\ 0.3158 & -2.8494 \end{bmatrix} \tag{4.23}$$

Figure 4.1 compares the simulated response $S_{Sim_{11}}$ to the completed data $S_{C_{11}}$ and the rational approximation $S_{Rat_{11}}$ and $S_{Sim_{21}}$ to $S_{C_{21}}$ and $S_{Rat_{21}}$ for the simulated frequencies in the lowpass domain. It can be observed that there is a difference in phase between $S_{Sim_{11}}$ and $S_{C_{11}}$ and between $S_{Sim_{21}}$ and $S_{C_{21}}$, due to the de-embedding of the access lines. Figure 4.2a compares the magnitude of to $|S_{C_{11}}|$ and $|S_{Rat_{11}}|$ and shows the magnitude of the approximation error $|S_{Rat_{11}} - S_{C_{11}}|$. Figure 4.2b compares the magnitude of to $|S_{C_{21}}|$ and $|S_{Rat_{21}}|$ and shows the magnitude of the approximation error $|S_{Rat_{21}} - S_{C_{21}}|$. Both figures show that $\boldsymbol{S}_{rat}$ approximates the data well, especially in the passband. Figure 4.3 shows the results given by PRESTO-HF. The red curve is the completed data $\boldsymbol{S}_C$. The number $r$ expresses the ratio between the norm of the unstable part of the data ($P_{G^2}(S_{C_{kl}})$, $k, l \in \{1, 2\}$) and the norm of the (unprojected) data ($S_{C_{kl}}$), $k, l \in \{1, 2\}$). It is clear that the unstable part is much smaller than the stable part: $r \leq 0.53\%$ for each $S$-parameter, which clearly indicates that the assumption that the filter is a stable device holds. The blue curve is the rational approximation $\boldsymbol{S}_{rat}$. The number *err* expresses $L^2$-norm of the relative error and *err.sup* the $L^\infty$-norm of the relative error. The rational approximations have very low relative errors which implies that the model fits the data well. This is also expected since the physical filter is narrow-banded and the number of resonators present is equal to the chosen McMillan degree, namely 4. This indicates that the behavior of the physical filter can be modeled well using a lumped-equivalent network.

Figure 4.4 shows the pole-zero map of $S_{rat_{21}}$, there are 4 transmission zeros. 2 of them are almost purely imaginary, which is expected from the ideal coupling

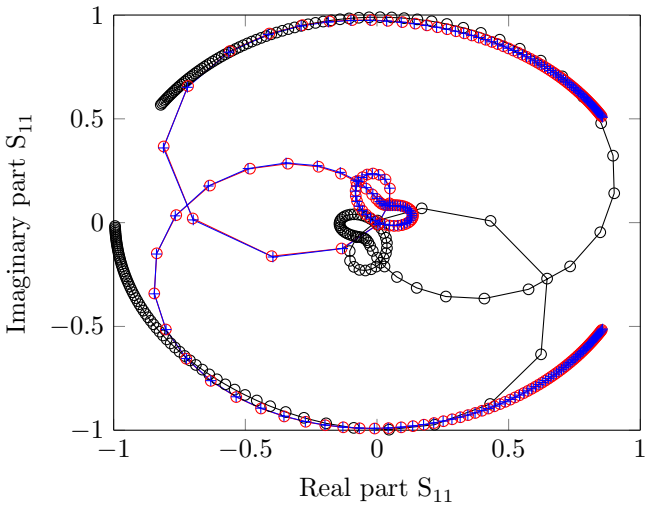


**(a)** Nyquist diagram for $S_{Sim_{11}}$ (–o), $S_{C_{11}}$ (–o) and $S_{Rat_{11}}$ (–+).

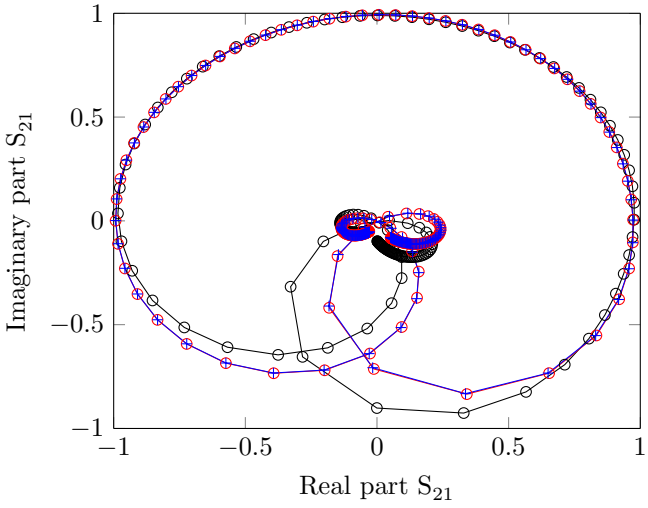


**(b)** Nyquist diagram for $S_{Sim_{21}}$ (–o), $S_{C_{21}}$ (–o) and $S_{Rat_{21}}$ (–+).

**Figure 4.1** Comparison between the simulations, analytic completion and rational approximation for $S_{11}$ and $S_{21}$.

topology. While the other 2 are complex and relatively far from the passband, which makes that the direct source-to-load coupling is not that strong as we will see in the extracted coupling matrix. Note that there are 2 poles that do not lie in the passband, which is consistent with the fact that the bandwidth of the physical filter is broader than the desired bandwidth.

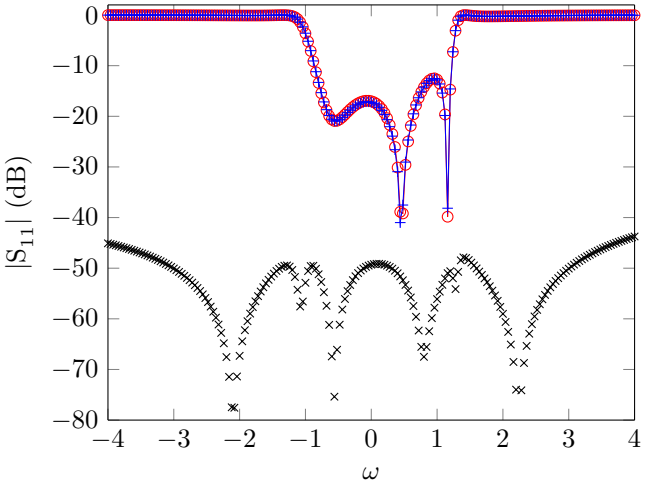


**(a)** Magnitude of $|S_{C_{11}}|$ (–o), $|S_{Rat_{11}}|$ (–+) and the approximation error (x).

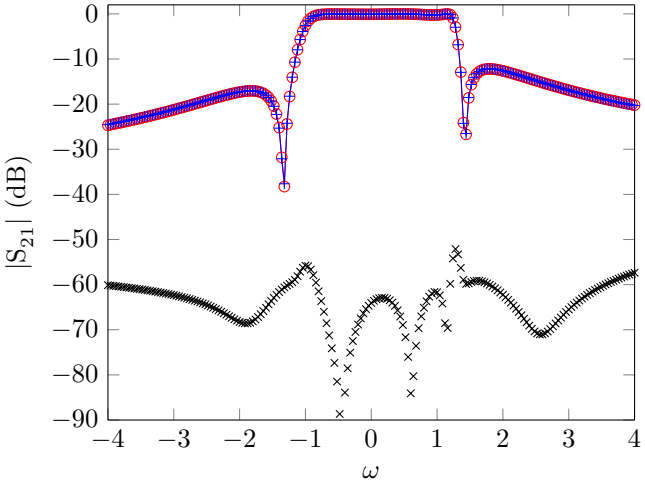


**(b)** Magnitude of $|S_{C_{21}}|$ (–o), $|S_{Rat_{21}}|$ (–+) and the approximation error (x).

**Figure 4.2** Comparison between the magnitude of the analytic completion and rational approximation for $S_{11}$ and $S_{21}$ and the error of the approximation.

Figure 4.5 compares the coupling graphs of the ideal SQ filter and the coupling graph of the extracted arrow form $\boldsymbol{M}^0_{arr}$.

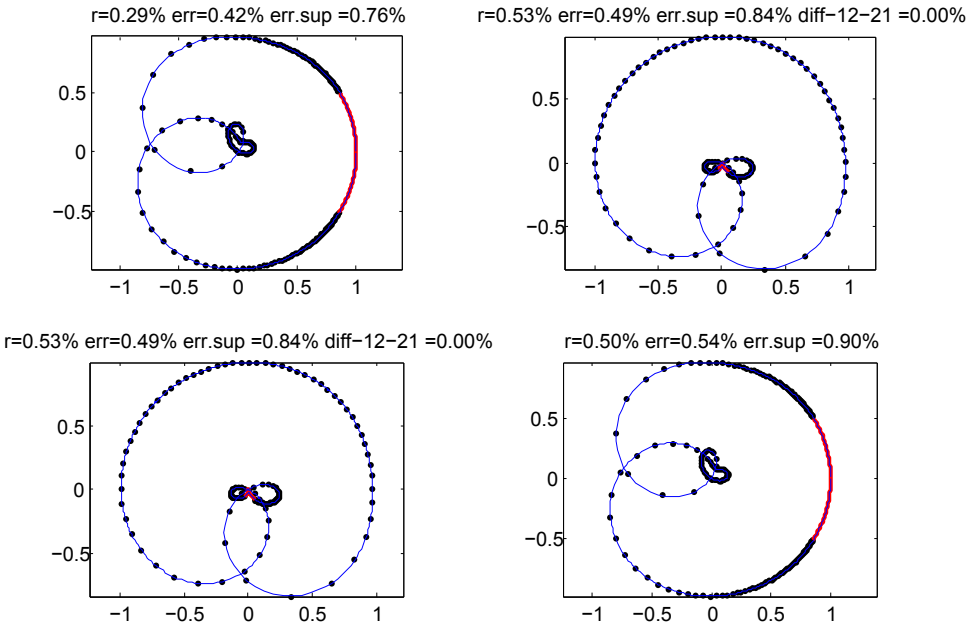


**Figure 4.3** The black dots are the simulated $S$-parameters in the lowpass domain for which the delays and frequency shifts are compensated. The red curve (—) is the completed data $\boldsymbol{S}_C$. The number $r$ expresses the ratio between the norm of the unstable part of the data ($P_{G^2}(S_{C_{kl}})$, $k,l \in \{1,2\}$) and the norm of the data ($S_{C_{kl}}$), $k,l \in \{1,2\}$). The blue curve (—) is the rational approximation $\boldsymbol{S}_{rat}$. The number *err* expresses $L^2$-norm of the relative error and *err.sup* the $L^\infty$-norm of the relative error.

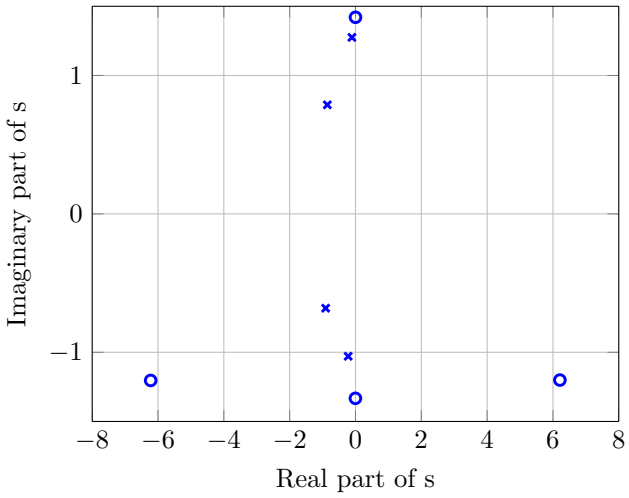


**Figure 4.4** Pole-zero map of $S_{rat_{21}}$, there are 4 transmission zeros (o) of which 2 are relatively far from the filter passband. The poles all lie in the passband (x).

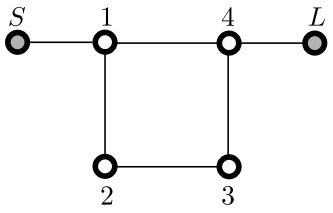


**(a)** Coupling graph of the ideal quadruplet filter.

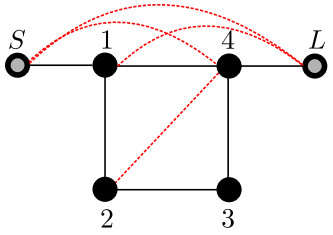


**(b)** Coupling graph of the extracted arrow form $\boldsymbol{M}^0_{arr}$.

**Figure 4.5** Coupling graph of the ideal coupling topology of single quadruplet filter and of the extracted arrow form $\boldsymbol{M}^0_{arr}$. There are 4 extra couplings (- - -) in the extracted coupling topology.

The imaginary part of the extracted arrow form matrix is:

$$\mathrm{Im}(\boldsymbol{M}^0_{arr}) = \begin{bmatrix} 0 & \mathbf{1.0228} & 0 & 0 & 0.0131 & 0.0115 \\ \mathbf{1.0228} & 0.0266 & \mathbf{0.7715} & 0 & \mathbf{-0.4555} & -0.0131 \\ 0 & \mathbf{0.7715} & -0.0097 & \mathbf{0.8366} & 0.1845 & 0 \\ 0 & 0 & \mathbf{0.8366} & -0.4123 & \mathbf{0.7501} & 0 \\ 0.0131 & \mathbf{-0.4555} & 0.1845 & \mathbf{0.7501} & 0.0266 & \mathbf{-1.0240} \\ 0.0115 & -0.0131 & 0 & 0 & \mathbf{-1.0240} & 0 \end{bmatrix} \tag{4.24}$$

Clearly, the extracted coupling matrix contains more non-zero elements than the ideal coupling matrix given by (3.24) (Figure 4.5). In this particular case the arrow form topology is very close to the ideal topology of the single quadruplet. Note that the elements in bold font correspond to the non-zero elements of the ideal topology. Therefore it is unnecessary to reconfigure $\boldsymbol{M}^0_{arr}$. Also note that in the case of a single quadruplet filter, there is only one solution to the coupling matrix reconfiguration problem.

As discussed in Section 4.4, the extracted coupling matrix contains a source-to-load coupling $M_{SL} = 0.0115$, a source-to-resonator $N$ coupling $M_{SN} = 0.0131$ and load-to-resonator 1 coupling $M_{L1} = -0.0131$. These couplings are 2 orders of magnitude lower than the input and output coupling $M_{S1} = 1.0228$ and $M_{LN} = -1.0240$, which confirms that these additional terms are second order effects. Also remark that $M_{LN}$ has a negative sign. This is due to the choice of $\beta_{21}$ as is discussed in Section 4.3.3. From a physical point of view $M_{LN}$ should have the same sign as $M_{S1}$. It is possible to redo the extraction procedure with a different choice for $\beta_{21}$. In this case we did not have to do this, because this choice does not affect the values of the coupling parameters.

Another notable difference is the presence of the self-couplings, which also explains why the center frequency of the passband of the filter does not exactly coincide with 1 GHz of the prototype filter (as can be seen in Figure 3.16). Finally there is $M_{24}$ which models the presence of a parasitic coupling. Although $M_{24}$ is smaller than the other inter-resonator couplings, it is still of the same order of magnitude indicating that the presence of the parasitic couplings is not negligible. From a physical point of view there is no reason to assume the presence of coupling $M_{24}$ and the absence of the coupling $M_{13}$. It is possible to re-optimize the coupling matrix to redistribute the parasitic couplings in a more

physical way. In this case one could argue that $M_{24}$ should be equal to $M_{13}$ due to the geometric symmetry that is present in the structure. This is easily imposed by applying the following similarity transformation:

$$\boldsymbol{P} = \begin{bmatrix} 1 & 0 & 0 & 0 & 0 & 0 \\ 0 & 1 & 0 & 0 & 0 & 0 \\ 0 & 0 & \cos\theta & -\sin\theta & 0 & 0 \\ 0 & 0 & \sin\theta & \cos\theta & 0 & 0 \\ 0 & 0 & 0 & 0 & 1 & 0 \\ 0 & 0 & 0 & 0 & 0 & 1 \end{bmatrix} \tag{4.25}$$

where $\theta$ is:

$$\theta = \arctan \frac{M_{24}}{M_{34} + M_{12}} \tag{4.26}$$

Applying $\boldsymbol{P}$ to $\boldsymbol{M}^0_{arr}$ yields:

$$\mathrm{Im}(\boldsymbol{P}\boldsymbol{M}^{\boldsymbol{0}}_{\boldsymbol{arr}}\boldsymbol{P}^t) = \begin{bmatrix} 0 & 1.0228 & 0 & 0 & 0.0131 & 0.0115 \\ 1.0228 & 0.0266 & 0.7659 & 0.0929 & -0.4555 & -0.0131 \\ 0 & 0.7659 & -0.2155 & 0.8366 & 0.0929 & 0 \\ 0 & 0.0929 & 0.8366 & -0.2065 & 0.7668 & 0 \\ 0.0131 & -0.4555 & 0.0929 & 0.7668 & 0.0266 & -1.0240 \\ 0.0115 & -0.0131 & 0 & 0 & -1.0240 & 0 \end{bmatrix} \tag{4.27}$$

Note that due to the transformation now $M_{13} = M_{24} = 0.0929$ which is more or less half of $M_{24}$ of (4.24). Another important consequence is that $M_{22} \approx M_{33}$ (which is also physically expected). It is however important to remember that from a mathematical point of view it is impossible to uniquely identify the parasitics and more information is needed if one wants to do so.

Finally note that extracted matrix also has a real part which is equal to:

$$\mathrm{Re}(\boldsymbol{M}^0_{arr}) =$$

$$\begin{bmatrix} 0 & -0.0001 & 0 & 0 & -0.0002 & -0.0016 \\ -0.0001 & 0.0024 & 0.0009 & 0 & 0.0004 & 0.0002 \\ 0 & 0.0009 & -0.0007 & 0.0014 & 0.0005 & 0 \\ 0 & 0 & 0.0014 & -0.0004 & 0.0008 & 0 \\ -0.0002 & -0.0004 & 0.0005 & 0.0008 & 0.0023 & 0.0001 \\ -0.0016 & 0.0002 & 0 & 0 & 0.0001 & -0.0004 \end{bmatrix} \tag{4.28}$$

Although the filter is simulated for a loss-less substrate and a perfect conductor, Momentum takes into account the radiation effects. These losses are however small and can be neglected, as it is seen that the real part is 3 orders of magnitude smaller than the imaginary part.

## 4.8 Example: Cascaded Quadruplet (CQ) Filter

For the second example, we apply the extraction method to the design of an 8-pole cascaded quadruplet (CQ) filter consisting of SOLR resonators (Figure 4.6). The filter is implemented in a RT/duroid substrate with a relative dielectric constant $\varepsilon_r = 10.2$ and a thickness $t = 1.27$ mm. The filter is designed to have a center frequency $f_c = 1$ GHz, a $FBW = 0.06$ and a $RL = -23$ dB and 2 pairs of finite TZs at $\omega = \pm 1.2$ and $\omega = \pm 1.6$. We first synthesize the ideal coupling matrix in the lowpass domain using the techniques described in Chapter 2. DEDALE-HF [Seyf 00] yields 2 possible solutions for this case, among which one is chosen. Table 4.1 contains the ideal lowpass coupling parameters. Since this topology accommodates a symmetric response, the self-coupling is zero. The initial values for this design are generated using the design curves presented in [Hong 96]. Table 4.2 contains the initial geometric dimensions.

| $M_{S1} = M_{8L}$ | $M_{12}$ | $M_{23}$ | $M_{34}$ | $M_{14}$ |
|---|---|---|---|---|
| 1.0416 | 0.8478 | 0.6896 | 0.5217 | -0.1463 |
| $M_{45}$ | $M_{56}$ | $M_{67}$ | $M_{78}$ | $M_{58}$ |
| 0.5328 | 0.4424 | 0.8218 | 0.7769 | -0.3694 |

**Table 4.1** Ideal lowpass coupling parameters for the 8-pole cascaded quadruplet filter.

Figure 4.7 compares the magnitude $|S_{11}|$ and $|S_{21}|$ of the rational approximation and the simulation. Figure 4.8 also shows the approximation error for the simulated frequencies. The error is acceptable in the pass band of the filter for

| Physical parameter | Value (mm) | Physical parameter | Value (mm) |
|---|---|---|---|
| $w_{feed}$ | 1 | $d_{34}$ | 1.77 |
| $t_{in} = t_{out}$ | 5.73 | $d_{14}$ | 2.27 |
| $g_1 = \ldots = g_8$ | 1.5 | $d_{45}$ | 2.2 |
| $a$ | 16.25 | $d_{56}$ | 1.96 |
| $w$ | 1 | $d_{67}$ | 1.53 |
| $d_{12}$ | 1.22 | $d_{78}$ | 1.32 |
| $d_{23}$ | 1.8 | $d_{58}$ | 1.56 |

**Table 4.2** Initial values for the physical design parameters of the SOLR CQ filter.

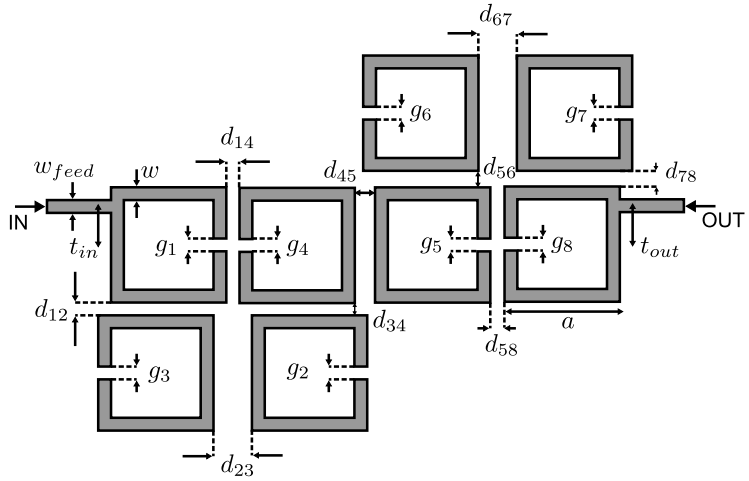


**Figure 4.6** Top-view of the layout of a eighth order SOLR cascaded quadruplet filter.

both $S_{11}$ and $S_{21}$.

Note however that the error has the same order of magnitude around the TZs. This is however expected since $|S_{21}|$ becomes very small in that region. The extracted arrow form $\boldsymbol{M}^0_{arr}$ contains 25 non-zero elements where the ideal coupling matrix contains 11 non-zero elements. The imaginary part of the $(N \times N)$ arrow form coupling matrix is:

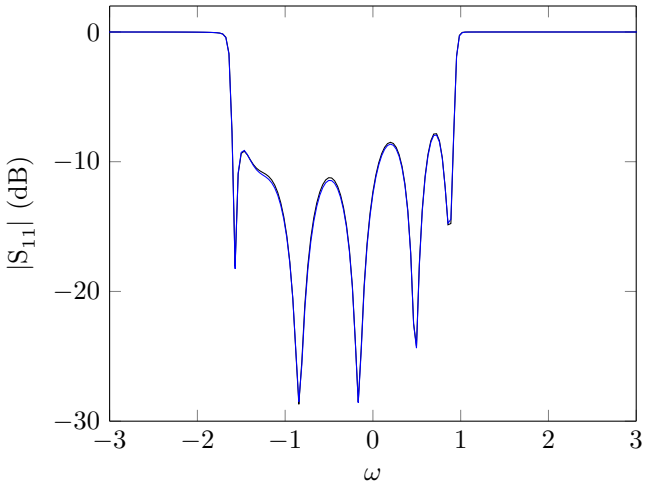


**(a)** $|S_{11}|$ (—) for the simulated filter and rational approximation (—).

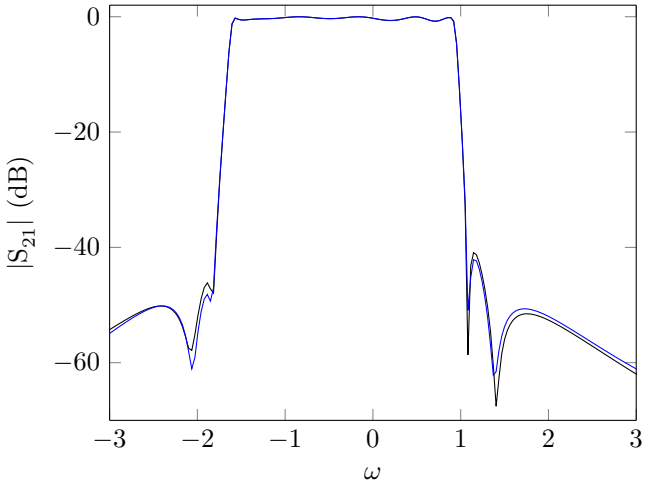


**(b)** $|S_{21}|$ (—) for the simulated filter and rational approximation (—).

**Figure 4.7** Comparison between the simulated response and the rational approximation.

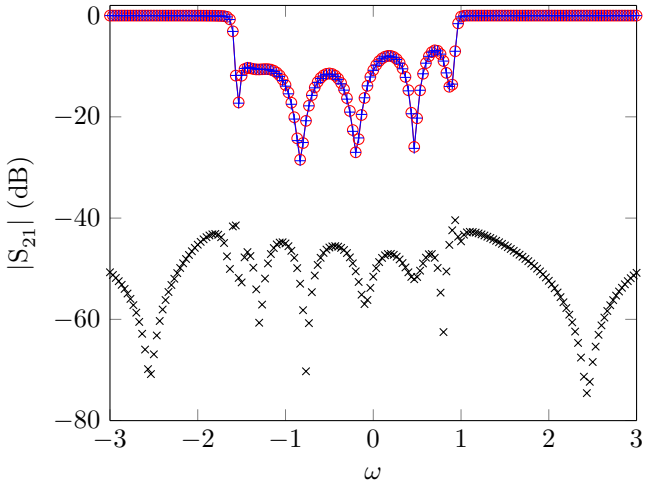


**(a)** Bode plot for $|S_{C_{11}}|$ (–o), $|S_{Rat_{11}}|$ (–+) and the approximation error (x).

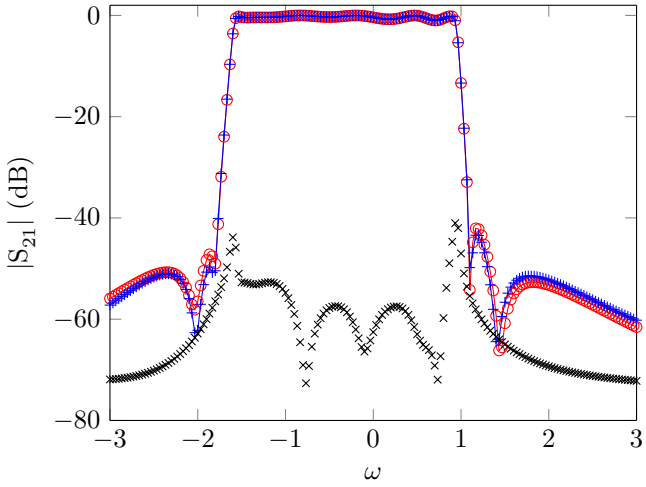


**(b)** Magnitude of $|S_{C_{21}}|$ (–o), $|S_{Rat_{21}}|$ (–+) and the approximation error (x).

**Figure 4.8** Comparison between the magnitude of the analytic completion and rational approximation for $|S_{11}|$ and $|S_{21}|$ and the error of the approximation.

$$\begin{bmatrix} 0.5780 & -0.9709 & 0 & 0 & 0 & 0 & 0 & -0.0016 \\ -0.9709 & 0.2995 & -0.7166 & 0 & 0 & 0 & 0 & -0.0041 \\ 0 & -0.7166 & 0.3176 & -0.6497 & 0 & 0 & 0 & -0.0822 \\ 0 & 0 & -0.6497 & 0.3416 & -0.7082 & 0 & 0 & 0.0175 \\ 0 & 0 & 0 & -0.7082 & 0.4180 & -0.4232 & 0 & 0.6026 \\ 0 & 0 & 0 & 0 & -0.4232 & 0.4936 & -1.0747 & 0.0986 \\ 0 & 0 & 0 & 0 & 0 & -1.0747 & 0.1211 & -0.7639 \\ -0.0016 & -0.0041 & -0.0822 & 0.0175 & 0.6026 & 0.0986 & -0.7639 & 0.5494 \end{bmatrix}$$

The source-to-resonator 1 coupling is 0.9941, the load-to-resonator $N$ coupling is 0.9920. The direct source-to-load coupling is only 0.0002, the source-to-resonator $N$ coupling is -0.0001 and the load-to-resonator coupling is -0.0001. These couplings are much smaller than the other non-zero couplings. Looking at the physical lay-out of the filter (Figure 4.6), this is expected since the load is well separated from the source. Figure 4.7a shows that there is a clear offset between the center frequency of the filter and the ideal center frequency. Moreover the response is asymmetric around $\omega = 0$. This is confirmed by the presence of the non-zero diagonal elements. In order to take this effect into account, the chosen target coupling topology is the one that supports asymmetric responses and is the closest to the ideal coupling topology. Figure 4.9 shows the extended coupling topology. Note that in each quadruplet an extra coupling is added. This coupling topology contains 21 non-zero couplings, which is the number that is needed to accommodate a $(8, 4)$ asymmetric response. There are 6 solutions to the reconfiguration problem and they are all calculated using DEDALE-HF. Table 4.3 contains the extracted coupling parameters for each solution. In Chapter 5 we will discuss how we can determine which solution corresponds to the physically implemented coupling matrix. Note that the input, output and the source-to-load couplings are not changed due to the transformations.

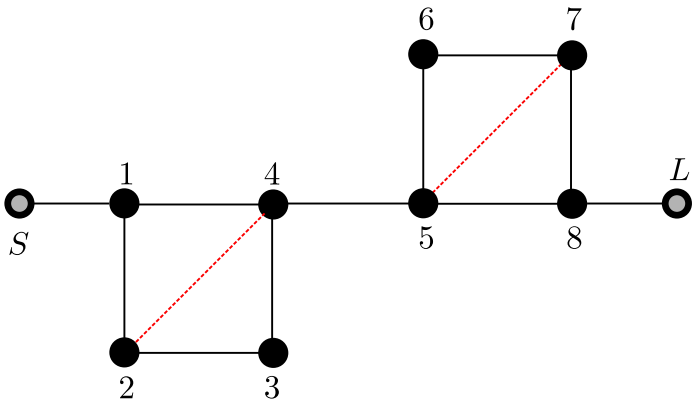


**Figure 4.9** Extended coupling topology for the cascaded quadruplet filter.

| Parameter | Sol. 1 | Sol. 2 | Sol. 3 | Sol. 4 | Sol. 5 | Sol. 6 |
|---|---|---|---|---|---|---|
| $M_{12}$ | 0.9467 | 0.8848 | 0.9073 | 0.9383 | 0.9296 | 0.9211 |
| $M_{23}$ | 0.8549 | 0.9655 | 0.9109 | 0.8618 | 0.2979 | 0.2628 |
| $M_{34}$ | 0.6169 | 0.5410 | 0.5438 | 0.6016 | 0.3585 | 0.3550 |
| $M_{14}$ | -0.2157 | -0.4001 | -0.3462 | -0.2496 | 0.2800 | 0.3067 |
| $M_{45}$ | 0.6656 | 0.6673 | 0.6674 | 0.6629 | 0.6750 | 0.6564 |
| $M_{56}$ | 0.5314 | 0.6215 | 0.6134 | 0.5282 | 0.3727 | 0.3405 |
| $M_{67}$ | 0.9410 | 0.8468 | 0.8577 | 0.8854 | 0.2555 | 0.2996 |
| $M_{78}$ | 0.8978 | 0.9581 | 0.9501 | 0.9193 | 0.9338 | 0.9396 |
| $M_{58}$ | -0.3973 | -0.2137 | -0.2468 | -0.3446 | 0.3025 | 0.2840 |
| $M_{11}$ | 0.5780 | 0.5780 | 0.5780 | 0.5780 | 0.5780 | 0.5780 |
| $M_{22}$ | 0.2656 | 0.3934 | 0.4313 | 0.2215 | -0.0383 | 0.6822 |
| $M_{33}$ | 0.4738 | 0.1397 | 0.0043 | 0.6173 | -0.7367 | 1.4598 |
| $M_{44}$ | 0.3833 | 0.3742 | 0.3655 | 0.3890 | 0.3598 | 0.2493 |
| $M_{55}$ | 0.3863 | 0.3733 | 0.3849 | 0.3702 | 0.2604 | 0.3524 |
| $M_{66}$ | 0.0267 | 0.3975 | 0.5316 | -0.0911 | 1.4411 | -0.7528 |
| $M_{77}$ | 0.4558 | 0.3133 | 0.2737 | 0.4845 | 0.7051 | 0.0006 |
| $M_{88}$ | 0.5494 | 0.5494 | 0.5494 | 0.5494 | 0.5494 | 0.5494 |
| $M_{24}$ | -0.0662 | 0.1190 | 0.1842 | -0.1363 | 0.5516 | -0.5663 |
| $M_{57}$ | 0.1388 | -0.0585 | -0.1243 | 0.1966 | -0.5496 | 0.5604 |

**Table 4.3** Extracted coupling parameters of the SOLR CQ filter for each possible solution of the extended coupling topology.

In this case the physically implemented $N \times N$ coupling matrix is $\boldsymbol{M}_{P_1}$:

$$\begin{bmatrix} 0.5780 & 0.9467 & 0 & -0.2157 & 0 & 0 & 0 & 0.0016 \\ 0.9467 & 0.2656 & 0.8549 & -0.0662 & 0 & 0 & 0 & -0.0040 \\ 0 & 0.8549 & 0.4738 & 0.6169 & 0 & 0 & 0 & 0 \\ -0.2157 & -0.0662 & 0.6169 & 0.3833 & 0.6656 & 0 & 0 & 0.0009 \\ 0 & 0 & 0 & 0.6656 & 0.3863 & 0.5314 & 0.1388 & -0.3973 \\ 0 & 0 & 0 & 0 & 0.5314 & 0.0267 & 0.9410 & 0 \\ 0 & 0 & 0 & 0 & 0.1388 & 0.9410 & 0.4558 & 0.8978 \\ 0.0016 & -0.0040 & 0 & 0.0009 & -0.3973 & 0 & 0.8978 & 0.5494 \end{bmatrix} \tag{4.29}$$

Note that the parasitic couplings are mainly modeled by elements $M_{24}$ and $M_{57}$. In the same way as in the case for the SQ filter, one could argue that extra couplings in each quadruplet should be equal: $M_{24} = M_{13}$ and $M_{57} = M_{46}$. A similar transformation as (4.25) allows also here to equalize the parasitic couplings in each quadruplet of matrix (4.29). From a physical point of view, one would also expect parasitic coupling between resonator 4 and 6 and between resonator 3 and 5. In order to redistribute the parasitic couplings, the parasitic couplings in the last row and column that are not present in the target topology are first eliminated in matrix (4.29). Next the matrix is transformed such that $M_{24} = M_{13}$ and $M_{57} = M_{68}$. This yields the matrix $\boldsymbol{M}_{par,0}$:

$$\begin{bmatrix} 0.5780 & 0.9458 & -0.0400 & -0.2157 & 0 & 0 & 0 & 0 \\ 0.9458 & 0.3382 & 0.8606 & -0.0400 & 0 & 0 & 0 & 0 \\ -0.0400 & 0.8606 & 0.4012 & 0.6192 & 0 & 0 & 0 & 0 \\ -0.2157 & -0.0400 & 0.6192 & 0.3833 & 0.6656 & 0 & 0 & 0 \\ 0 & 0 & 0 & 0.6656 & 0.3863 & 0.5423 & 0.0868 & -0.3973 \\ 0 & 0 & 0 & 0 & 0.5423 & 0.2118 & 0.9647 & 0.0868 \\ 0 & 0 & 0 & 0 & 0.0868 & 0.9647 & 0.2707 & 0.8936 \\ 0 & 0 & 0 & 0 & -0.3973 & 0.0868 & 0.8936 & 0.5494 \end{bmatrix} \tag{4.30}$$

This matrix is used as an initial guess for the optimization discussed in Section 4.6. For this matrix the value of the cost function is 0.0274. The optimization yields the matrix $\boldsymbol{M}_{par}$ given below:

$$\begin{bmatrix} 0.5791 & 0.9439 & -0.0431 & -0.2232 & 0 & 0 & 0 & 0 \\ 0.9439 & 0.3398 & 0.8657 & -0.0411 & 0 & 0 & 0 & 0 \\ -0.0431 & 0.8657 & 0.4040 & 0.6167 & -0.0011 & 0 & 0 & 0 \\ -0.2232 & -0.0411 & 0.6167 & 0.3894 & 0.6667 & 0.0001 & 0 & 0 \\ 0 & 0 & -0.0011 & 0.6667 & 0.3799 & 0.5462 & 0.0871 & -0.3869 \\ 0 & 0 & 0 & 0.0001 & 0.5462 & 0.2092 & 0.9581 & 0.0870 \\ 0 & 0 & 0 & 0 & 0.0871 & 0.9581 & 0.2683 & 0.8980 \\ 0 & 0 & 0 & 0 & -0.3869 & 0.0870 & 0.8980 & 0.5501 \end{bmatrix} \tag{4.31}$$

The cost function is 0.0128. Figure 4.10 compares the response obtained for the different coupling matrices ($\boldsymbol{M}_{P_1}$, $\boldsymbol{M}_{par,0}$, $\boldsymbol{M}_{par}$) to the one obtained with the compensated $S$-parameters. It is clear that a removal of the elements in the last row and column deteriorates the approximation. The optimization slightly improves the approximation as can be seen by the value of the cost function. It is important to note that the optimized coupling matrix depends heavily on the initial values and that the algorithm possibly converges to a local minimum. Moreover the example shows that the coupling parameters of interest are not heavily affected by the optimization.

## 4.9 Conclusion

In this chapter we have described a method to extract a coupling matrix whose corresponding response optimally approximates the simulated $S$-parameters and whose coupling topology is close to the coupling topology of the ideal prototype. Since the real filter contains parasitic inter-resonator couplings and in some cases unwanted self-couplings, we have proposed a strategy to handle them. In the case of topologies having multiple ($n_S$) solutions, we systematically determine all of these solutions using DEDALE-HF [Seyf 00]. In Section 4.7 and Section 4.8 we have treated a SQ and CQ filters respectively. In both cases the extracted coupling matrices approximate the simulated data very well. Moreover they give a good estimate of the first order and parasitic effects in the real filter. In the case of the CQ filter we find 6 possible solutions that are all equivalent from a mathematical point of view. In the next chapter we introduce a method that allows to determine which of these solutions corresponds to the filter that was physically implemented.

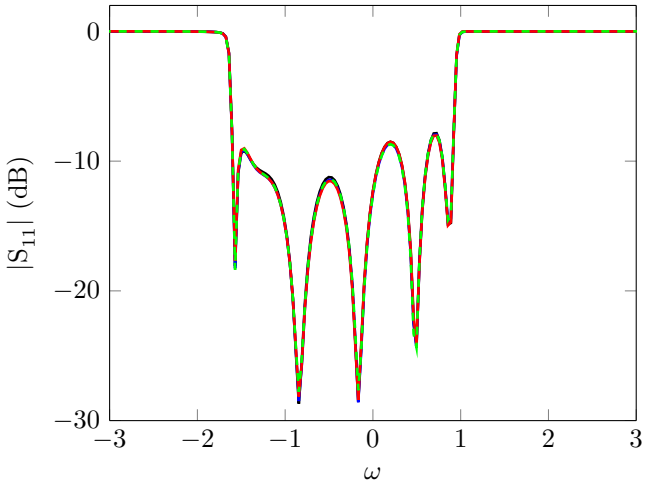


**(a)** $|S_{11}|$ (—) for the simulated filter, the response created by $\boldsymbol{M}_{P_1}$ (—), by $\boldsymbol{M}_{par,0}$ (- - -) and by $\boldsymbol{M}_{par}$ (—)

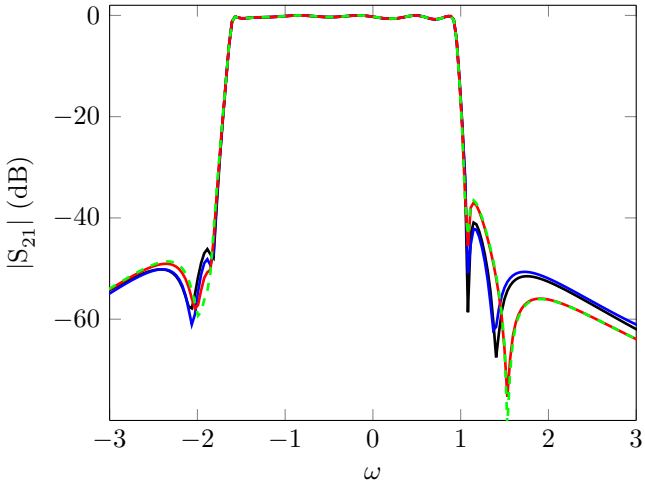


**(b)** $|S_{21}|$ (—) for the simulated filter, the response created by $\boldsymbol{M}_{P_1}$ (—), by $\boldsymbol{M}_{par,0}$ (- - -) and by $\boldsymbol{M}_{par}$ (—)

**Figure 4.10** Comparison between the simulated response and the response created by $\boldsymbol{M}_{P_1}$, $\boldsymbol{M}_{par,0}$ and $\boldsymbol{M}_{par}$. It is clear that the removal of the parasitic elements in the last column and row mainly affects the TZs.

# 5

# Dealing with Multiple Solutions: A Simulation Based Strategy

This chapter introduces a novel identification method to select the physically implemented coupling matrix in the case of cascaded trisection (CT) and cascaded quadruplet (CQ) topologies among all possible coupling matrices. Knowledge of the physically implemented coupling matrix enables a designer to adjust the filter dimensions to obtain a coupling matrix that is closer to the golden goal. In the case of CT and CQ filters, the reconfiguration problem has multiple solutions as discussed before. Selecting a non-physical solution may lead to wrong adjustments during the tuning procedure. The identification method consist of 2 phases: an initialization and a tracking phase. The initialization phase determines the physical coupling matrix for the initial design. Once the physical matrix of the initial design is known, we present a method to determine the physically implemented coupling matrix during the tuning procedure using the design curves introduced in Chapter 3. The method is based on the relation between the realized transmission zeros (TZs) and the geometry of the individual sections (triplets and quadruplets) of the filter. Section 5.2 analyzes the CT and CQ topologies in detail. Section 5.3 explains the identification method. Section 5.4 applies the method to tune a CQ filter. The work presented in this chapter has been published in [Caen 15a].

## 5.1 Introduction

In the literature there are several examples of microstrip CT and CQ filters using various types of resonators: [Hong 01] presents both CT and CQ filters using SOLR resonators. [Hong 99] uses SOLR resonators to implement CT filters, [Yang 99] combines $\frac{\lambda}{2}$ open line and hairpin line resonators.

The design methodologies presented in [Yang 99; Hong 99; Hong 01] are based on the divide-and-conquer strategy explained in Chapter 3. Therefore, they only yield initial values for the physical dimensions of the filters. In general tuning is

still required to meet the specifications. As discussed in Chapter 4, we propose to tune the filters by comparing the extracted coupling matrix to the golden goal. This comparison enables a designer to adjust the physical dimensions of the filter to obtain a coupling matrix that is closer to the golden goal. Several tuning methods based on this comparison have been developed in the literature [Hars 01; Garc 04; Koza 06]. Although these methods yield excellent results, they have an important limitation: they only handle topologies that have a unique solution to the reconfiguration problem.

In Chapter 4, we have seen that in the case of a CQ filter several solutions exist that correspond to the target coupling topology. In Section 5.2 we explain where these solutions come from and what their relation is to the finite TZs present in the response. From a mathematical point of view all these solutions are equivalent. However, during the tuning procedure it is important to compare the physically implemented solution to the golden goal. Selecting a non-physical solution instead may lead to wrong adjustments of the physical dimensions hereby destroying the whole tuning process. The identification method used to perform this selection is explained in Section 5.3. It consists of 2 phases: an initialization phase and a tracking phase. The initialization phase determines the physical coupling matrix for the initial design obtained using the design curves. This phase requires a number of extra simulations equal to the number of sections (quadruplets or trisections) that are present in the filter. Once the physical matrix of the initial design is known, it is possible to track the physical solution during the tuning procedure. This tracking is based on the knowledge of the design curves. To illustrate the usefullness of the method we use it to to tune the CQ filter introduced in Section 4.8.

## 5.2 Cascaded Trisection and Quadruplet Topologies

Cascaded trisection (CT) and cascaded quadruplet (CQ) topologies are typical examples of topologies supporting multiple solutions. These topologies consist of a cascade of sections, where each section corresponds to a quadruplet (Figure 5.1a) or a trisection (Figure 5.1b) of resonators. The coupling matrices associated to these topologies consist of blocks of non-zero elements. Such a block represents the couplings that are present within a section.

A quadruplet section (Figure 5.1a) creates a finite TZ pair which is symmetrically located with respect to the center frequency of the filter. Cascading quadruplets thus allows to realize filters that have several finite TZ pairs. The position of one TZ pair can be tuned by acting on the quadruplet that is responsible

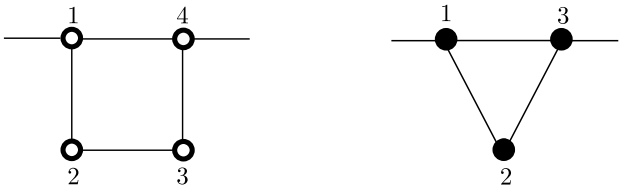


**(a)** Coupling graph of an ideal quadruplet section.

**(b)** Coupling graph of a trisection.

**Figure 5.1** Coupling graph of an (ideal) quadruplet and of a trisection.

for the realization of that pair. In the case that extra cross couplings and/or self-couplings are present in the quadruplet (for example between resonator 1 and 3), the quadruplet still creates 2 TZs, but their positions are no longer symmetrical with respect to the center frequency of the passband of the filter. In the examples discussed in Section 3.6 and Section 4.8 we observe indeed that the TZs of the implemented filter are not symmetrically located with respect to the center frequency of the filter because of the presence of parasitic cross-couplings and self-couplings in the quadruplet sections.

A trisection (sometimes called a triplet) consists of 3 sequentially coupled resonators and one extra cross-coupling between the first and the third resonator (Figure 5.1b). A trisection allows to place a single TZ at a finite frequency. Trisections hence allow to create filters with asymmetric responses. Similarly as for CQ filters, it is possible to tune the positions of the single TZs independently by acting on the corresponding trisections.

The link between the different sections of CT and CQ filters and the positions of the TZs and TZ pairs also explains the presence of more than 1 solution supported by the topology. We observe that the number of solutions corresponds to the number of ways that the independent TZs can be attributed to the different sections. We denote the number of possible solutions as $n_S$. Assume that there are $p$ different sections (trisections or quadruplets) in the filter and that a section $k$ creates $n_k$ independent TZs. The total number of independent TZs that can be attributed to the different sections is thus:

$$n_Z = \sum_{k=1}^{p} n_k \tag{5.1}$$

Using binomial coefficients we can calculate the number of possible ways to attribute the independent TZs to the different sections, which is then the number

of solutions $n_S$:

$$n_S = \binom{n_Z}{n_1} \dots \binom{n_Z - \sum_{l=1}^{k-1} n_l}{n_k} \dots \binom{n_Z - \sum_{l=1}^{p-1} n_l}{n_p} = \prod_{k=1}^{p} \binom{n_Z - \sum_{l=1}^{k-1} n_l}{n_k} \quad (5.2)$$

where $\binom{y}{x}$ denotes the binomial coefficient. $\binom{y}{x} = \frac{y!}{x!(y-x)!}$ should be read as $y$ *choose* $x$ since it expresses the number of ways $x$ elements can be chosen from a set of $y$ elements. Equation (5.2) can be interpreted as follows: the first section creates $n_1$ independent TZs and thus there are $\binom{n_Z}{n_1}$ ways to attribute the $n_1$ independent TZs to this section. Once these TZs have been attributed to the first section, there are only $n_Z - n_1$ independent TZs left to attribute. Thus there are $\binom{n_Z - n_1}{n_2}$ ways to attribute the remaining independent TZs to the second section. Repeating this reasoning for $p$ sections finally yields (5.2).

It is important to note that $n_Z$ is not necessarily equal to the total number of finite transmission zeros $n_{fz}$. For example, in the case of a CQ filter consisting of $p$ ideal quadruplets each quadruplet creates a symmetrical TZ pair and thus realizes only 1 independent TZ. Therefore $n_Z = p$, while $n_{fz} = 2p$. When the quadruplets are non-ideal each quadruplet creates 2 independent TZs and thus $n_Z = 2p = n_{fz}$.

### 5.2.1 EXAMPLE: CQ FILTER

Consider the two section CQ filter discussed in Section 4.8. The reconfiguration of the ideal coupling matrix yields 2 solutions. For the ideal coupling matrix each quadruplet creates 1 symmetrical finite TZ pair which results 1 independent finite TZ. Since the filter consists of 2 quadruplets, we have that $n_Z = 2$. If we fill this in in (5.2), we have that $n_S = \binom{2}{1}\binom{1}{1} = 2$ which corresponds to the number of solutions given by DEDALE-HF [Seyf 00]. For the physical filter the quadruplets are no longer ideal, since extra cross-couplings and self-couplings are present. These sections create 2 independent TZs. Therefore we have that $n_Z = 4$. If we fill this in (5.2), we find $n_S = \binom{4}{2}\binom{2}{2} = 6$, which corresponds to the number of solutions given by DEDALE-HF [Seyf 00]. This means that each of the six solutions describes a different attribution of the independent zeros to the different quadruplets.

In this example we have chosen to implement the ideal solution for which the first quadruplet creates the TZ pair at $\omega = \pm 1.6$ and the second quadruplet

creates the pair at $\omega = \pm 1.2$.

For the simulated filter, we observe 4 TZs, which we order and denote as follows: $z_k (k \in \{1, \ldots, 4\})$: $\omega_{z1} \approx -2.06$, $\omega_{z2} \approx -1.82$, $\omega_{z3} \approx 1.08$ and $\omega_{z4} \approx 1.4$. Table 4.3 lists the 6 possible solutions $\boldsymbol{M}_{P_i}$ $(i \in \{1, \ldots, 6\})$. It is now possible to verify for each solution which quadruplet is responsible for which TZs by calculating the $S$-parameters that correspond to one quadruplet (which is represented by a sub-matrix of the coupling matrix). We denote the first quadruplet as $\boldsymbol{Q1}$ and the second one as $\boldsymbol{Q2}$:

- $\boldsymbol{M}_{P_1}$: $\boldsymbol{Q1}$: $z_1$ and $z_4$, $\boldsymbol{Q2}$: $z_2$ and $z_3$
- $\boldsymbol{M}_{P_2}$: $\boldsymbol{Q1}$: $z_2$ and $z_3$, $\boldsymbol{Q2}$: $z_1$ and $z_4$
- $\boldsymbol{M}_{P_3}$: $\boldsymbol{Q1}$: $z_1$ and $z_3$, $\boldsymbol{Q2}$: $z_2$ and $z_4$
- $\boldsymbol{M}_{P_4}$: $\boldsymbol{Q1}$: $z_2$ and $z_4$, $\boldsymbol{Q2}$: $z_1$ and $z_3$
- $\boldsymbol{M}_{P_5}$: $\boldsymbol{Q1}$: $z_3$ and $z_4$, $\boldsymbol{Q2}$: $z_1$ and $z_2$
- $\boldsymbol{M}_{P_6}$ $\boldsymbol{Q1}$: $z_1$ and $z_2$, $\boldsymbol{Q2}$: $z_3$ and $z_4$

It is clear that when we interchange the quadruplets of $\boldsymbol{M}_{P_1}$, we obtain $\boldsymbol{M}_{P_2}$. This is also the case for $\boldsymbol{M}_{P_3}$ and $\boldsymbol{M}_{P_4}$ and for $\boldsymbol{M}_{P_5}$ and $\boldsymbol{M}_{P_6}$. The aim of the identification method introduced in this chapter is to determine the extracted coupling matrix which corresponds to the physically implemented coupling matrix $\boldsymbol{M}_{Phys}$. By the physically implemented coupling matrix, we mean the matrix for which the individual blocks create the TZs in the same way as the physical sections do. For example if physically the first quadruplet creates $z_1$ and $z_3$, we would say that $\boldsymbol{M}_{P_3}$ is the physically implemented coupling matrix $\boldsymbol{M}_{Phys}$. If we take a closer look at the solutions, we observe that for $\boldsymbol{M}_{P_5}$ and $\boldsymbol{M}_{P_6}$ the cross-couplings ($M_{14}$ and $M_{58}$) are non-negative. This means that $\boldsymbol{M}_{P_5}$ and $\boldsymbol{M}_{P_6}$ are not physical for the considered quadruplet filter, since the cross-coupling are implemented as electric couplings which have the opposite sign of the other couplings (Section 3.6).

To determine the physical solution $\boldsymbol{M}_{Phys}$ amongst the other 4 solutions, one could try to link the physical dimensions of the filter to the extracted couplings. In this case we have for example that $d_{14} > d_{58}$, which makes it likely that $|M_{14}| < |M_{58}|$. Therefore one would expect $\boldsymbol{M}_{P_1}$ or $\boldsymbol{M}_{P_4}$ to correspond to the physically implemented coupling matrix. It is however hard to discriminate between those 2 solutions since the frequency of $z_1$ is very close to that of $z_2$.

## 5.3 Identification of the Physically Implemented Coupling Matrix

This section explains the 2 phases of the identification method. The initialization phase determines the physical coupling matrix for the initial design. The idea behind the initialization is to first determine which of the sections (and thus the blocks in the coupling matrix) are responsible for which TZs by adjusting these sections separately. Once the physical matrix of the initial design $\boldsymbol{M}^0_{Phys}$ is determined, the method tracks the physical solution(s) for the filter adjusted during the tuning process by predicting the variations of the couplings. This prediction is carried out using the design curves discussed in Chapter 3.

### 5.3.1 INITIALIZATION PHASE

The initialization phase heavily uses of the fact that one section only acts on a specific set of TZs. This means that when we apply a variation to a physical design parameter within a certain section, the TZs created by the other sections remain unchanged. The blocks representing these sections must thus also remain unchanged under this variation. By comparing the blocks (sub-matrices) linked to the sections that should remain unchanged due to the applied variation in the set of possible solutions, it is possible to determine $\boldsymbol{M}_{Phys}$.

Consider a filter consisting of 2 sections having $n_S$ solutions to the reconfiguration problem. For the initial design values of the filter, the extraction procedure yields $n_S$ possible coupling matrices. Next we apply a variation to a physical parameter in the first section and we simulate the adapted structure. The extraction procedure yields $n_S$ new coupling matrices. Since the variation only acts on the first section, it only affects the TZs created by this section. Therefore the block representing the second section should remain unchanged. The elements of the block representing the second section are grouped in a new matrix (a sub-matrix of the $N \times N$ coupling matrix), which is denoted as $\boldsymbol{S}^x_v$. The index $x$ indicates the simulation ($x \in \{1, 2\}$) and $v$ indicates the index of the solution ($v \in \{1, \ldots, n_S\}$). We can now compare the matrices $\boldsymbol{S}^1_u$ and $\boldsymbol{S}^2_v$ by calculating the 2-norm of their difference:

$$\delta_{u,v} = \| \boldsymbol{S}^1_u - \boldsymbol{S}^2_v \|_2 \tag{5.3}$$

where ($u, v \in \{1, \ldots, n_S\}$). Comparing all of the possible combinations requires the calculation of $n_S^2$ 2-norms. The combination $(u, v)$ for which $\delta_{u,v}$ is minimal corresponds to the pair of solutions for which the second blocks remained maximally unaffected and thus to the pair of physically implemented coupling

matrices.

It is possible to generalize this rationale for cascaded coupling topologies having $p$ different sections. In the generalized version, we first apply physical variations to all sections but the last. This simulation allows to determine the solutions for which the last block remained unaffected. Next we apply physical variations in all sections but the second last and last section. This simulation allows to determine the solutions for which the last and second last block remained unaffected. We repeat this action $p-1$ times to determine the physically implemented coupling matrix.

### Initialization of the identification method for a CQ filter

We apply the initialization method to the initial design of the CQ filter discussed in Section 5.2.1. We change the value of the distance between resonator 1 and 4 from $d_{14} = 2.27$ mm to $d_{14} = 3$ mm and simulate the new filter. Figure 5.2 shows the effect of the parameter variation on $|S_{21}|$. It is clear that the variation of $d_{14}$ only affects the position of $z_1$ and $z_4$. Next we calculate all of the 36 values of $\delta_{u,v}$. The minimal value is $\delta_{1,1} = 0.1192$, which means that first solution $\boldsymbol{M}_{P_1}$ corresponds to $\boldsymbol{M}_{Phys}$. When the norms are sorted for increasing values, the second value $\delta_{6,6} = 0.1543$ is minimal. The maximal value is obtained for $\delta_{3,4} = 2.1292$.

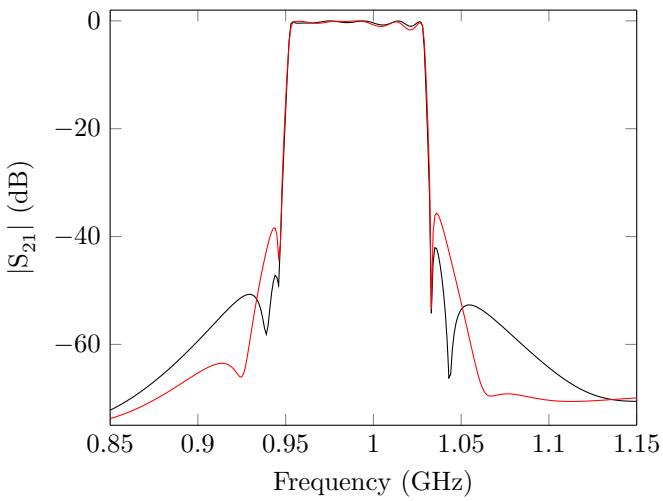


**Figure 5.2** $|S_{21}|$ for the initial dimension of the CQ filter (—) and after a variation of $d_{14} = 2.27$ mm $\rightarrow$ $d_{14} = 3$ mm (—).

### 5.3.2 TRACKING PHASE

The drawback of the initialization phase is that it requires $p-1$ extra EM-simulations. We want however to minimize the number of EM-simulations required to tune the filter, since they represent the most-time consuming action during the tuning procedure. Therefore we propose to use a different approach once the initial $\boldsymbol{M}^0_{Phys}$ has been determined. The tuning of a filter is an iterative process in which the physical dimensions are corrected at each iteration. In most cases the initial dimensions have been determined using design curves relating the couplings to one of the physical dimensions of the filter (Chapter 3). Although these curves do not take into account the effects of all the dimensions on the coupling parameters, they approximate the first order behavior of the inter-resonator coupling as a function of the dominant design parameter well. These curves thus allow to predict how the physical matrix $\boldsymbol{M}^m_{Phys}$ that will be found at iteration $m$ will vary in first order as a result of the corrected dimensions. Using the design curves and the knowledge of the corrected dimensions, we calculate a coupling matrix $\boldsymbol{M}^{m+1}_{Pred}$ that predicts the values of the coupling for iteration $m+1$ starting from the values obtained in iteration $m$. Next we compare the coupling matrices $\boldsymbol{M}^{m+1}_{P_i}$ $(i \in \{1,\ldots,n_S\})$ extracted at iteration $m+1$ to the prediction matrix $\boldsymbol{M}^{m+1}_{Pred}$ by calculating the 2-norm of the difference:

$$\delta_i^{m+1} = \| \boldsymbol{M}^{m+1}_{P_i} - \boldsymbol{M}^{m+1}_{Pred} \|_2 \tag{5.4}$$

where $i \in \{1,\ldots,n_S\}$. The solution $\boldsymbol{M}^{m+1}_{P_i}$ for which $\delta_i^{m+1}$ is minimal is considered to correspond to $\boldsymbol{M}^{m+1}_{Phys}$.

The design curves extracted in Section 3.5 act as look-up tables where the coupling for non-simulated values of the physical parameter are obtained by interpolation. To predict the effect of the variation of a geometrical parameter it is convenient to have an analytic expression for these curves. Since the coupling parameters behave smoothly in the region of interest and can be well approximated by quadratic polynomials [Amar 06], we estimate quadratic polynomials in least-square senses from the data in the look-up table. Note that since we only have curves for the inter-resonator couplings, we only take into account the imaginary part of the inter-resonator coupling to calculate $\delta_i^n$ (5.4).

#### Tracking $\boldsymbol{M}^m_{Phys}$ for a CQ filter

Based on the comparison between the extracted matrix $\boldsymbol{M}^0_{Phys}$ and the target coupling matrix, we adjust the dimensions of the initial filter. Figure 5.3 shows

$|S_{11}|$ and $|S_{21}|$ for the filter having adjusted dimensions. The dashed curves show the response for the initial design. Figure 5.4 shows the curves (and the least-square quadratic approximation) that are used to predict the effect of the corrected dimensions. The prediction matrix $\boldsymbol{M}^1_{Pred}$ is:

$$\begin{bmatrix} 0 & 0.8480 & 0 & -0.1741 & 0 & 0 & 0 & 0 \\ 0.8480 & 0 & 0.7684 & 0 & 0 & 0 & 0 & 0 \\ 0 & 0.7684 & 0 & 0.6023 & 0 & 0 & 0 & 0 \\ -0.1741 & 0 & 0.6023 & 0 & 0.6378 & 0 & 0 & 0 \\ 0 & 0 & 0 & 0.6378 & 0 & 0.5103 & 0 & -0.3834 \\ 0 & 0 & 0 & 0 & 0.5103 & 0 & 0.8868 & 0 \\ 0 & 0 & 0 & 0 & 0 & 0.8868 & 0 & 0.7564 \\ 0 & 0 & 0 & 0 & -0.3834 & 0 & 0.7564 & 0 \end{bmatrix} \tag{5.5}$$

Next we calculate the 6 differences between this prediction matrix and the physical solution for the initial design values $\boldsymbol{M}^0_{Phys}$ $\delta^1_i$ $(i \in \{1, \ldots, n_S\})$:

$$\begin{bmatrix} \delta^1_1 & \ldots & \delta^1_6 \end{bmatrix} = \\ \begin{bmatrix} 0.0144 & 0.1602 & 0.7724 & 0.7770 & 0.1819 & 0.2638 \end{bmatrix} \tag{5.6}$$

It is clear that the first element $\delta^1_1$ is minimal and thus $\boldsymbol{M}^1_{P_1} = \boldsymbol{M}^1_{Phys}$:

$$\begin{bmatrix} 0.5506 & 0.8509 & 0 & -0.1624 & 0 & 0 & 0 & 0.0025 \\ 0.8509 & 0.3164 & 0.7669 & -0.0375 & 0 & 0 & 0 & -0.0030 \\ 0 & 0.7669 & 0.4514 & 0.6016 & 0 & 0 & 0 & 0 \\ -0.1624 & -0.0375 & 0.6016 & 0.3927 & 0.6321 & 0 & 0 & 0.0006 \\ 0 & 0 & 0 & 0.6321 & 0.4082 & 0.5183 & 0.1024 & -0.3894 \\ 0 & 0 & 0 & 0 & 0.5183 & 0.1157 & 0.8937 & 0 \\ 0 & 0 & 0 & 0 & 0 & 0.8937 & 0.4796 & 0.7664 \\ 0 & 0 & 0 & 0 & -0.3894 & 0 & 0.7664 & 0.5136 \end{bmatrix} \tag{5.7}$$

Comparing the values of the matrix (5.5) to (5.7) shows that $\boldsymbol{M}^1_{Pred}$ predicts the coupling parameters well. Moreover Table 5.1 shows that the corresponding coupling matrix is closer to the target coupling matrix than $\boldsymbol{M}^0_{Phys}$. Looking

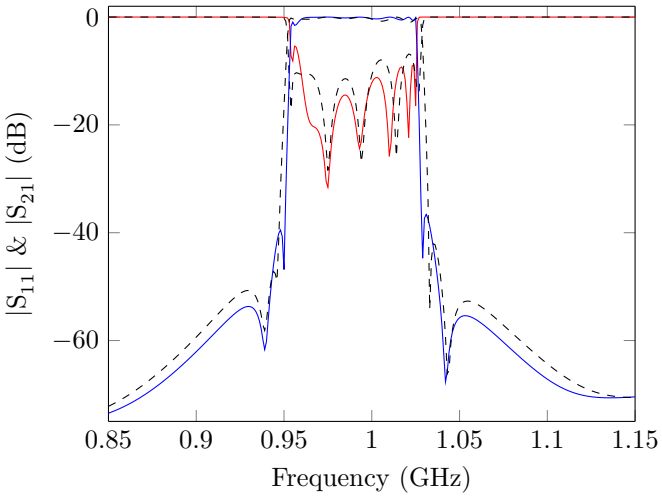


**Figure 5.3** $|S_{11}|$ (—) and $|S_{21}|$ (—) for the adjusted filter. The dashed curves show the $S$-parameters of the initial design.

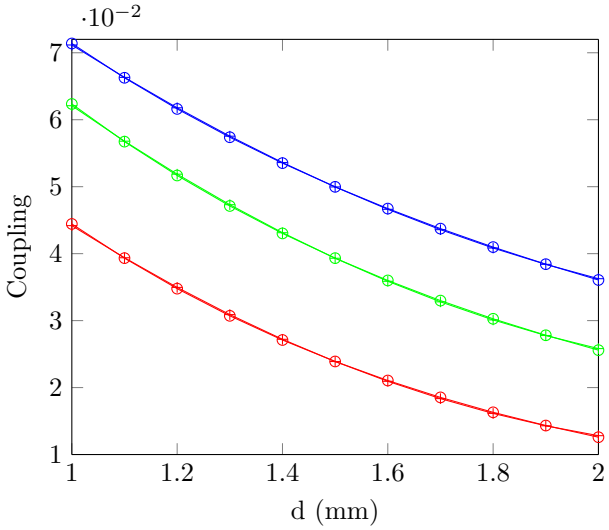


**Figure 5.4** Desgin curves relating the inter-resonator coupling to the design parameter $d$: $k_E$ for the electric coupling (o) and its quadratic approximation (+). $k_M$ for the magnetic coupling (+) and its quadratic approximation (o). $k_B$ for the mixed coupling (+) and its quadratic approximation (o).

at Figure 5.3 shows that the bandwidth of the filter is closer to the desired bandwidth, which also shows that the filter is closer to the golden goal. Note that the lengths of the resonators have not been adjusted yet during this generation

which explains why the offsets have not changed that much.

| Parameter | Initial | Iteration 1 | Target |
|---|---|---|---|
| $M_{12}$ | 0.9467 | 0.8509 | 0.8478 |
| $M_{23}$ | 0.8549 | 0.7669 | 0.6896 |
| $M_{34}$ | 0.6169 | 0.6016 | 0.5217 |
| $M_{14}$ | -0.2157 | -0.1624 | -0.1463 |
| $M_{45}$ | 0.6656 | 0.6321 | 0.5328 |
| $M_{56}$ | 0.5314 | 0.5183 | 0.4424 |
| $M_{67}$ | 0.9410 | 0.8937 | 0.8218 |
| $M_{78}$ | 0.8978 | 0.7664 | 0.7769 |
| $M_{58}$ | -0.3973 | -0.3894 | -0.3694 |
| $M_{11}$ | 0.5780 | 0.5506 | 0 |
| $M_{22}$ | 0.2656 | 0.3164 | 0 |
| $M_{33}$ | 0.4738 | 0.4514 | 0 |
| $M_{44}$ | 0.3833 | 0.3927 | 0 |
| $M_{55}$ | 0.3863 | 0.4082 | 0 |
| $M_{66}$ | 0.0267 | 0.1157 | 0 |
| $M_{77}$ | 0.4558 | 0.4796 | 0 |
| $M_{88}$ | 0.5494 | 0.5136 | 0 |

**Table 5.1** Extracted and target coupling parameters for the initial design and the adjusted design after 1 iteration of the SOLR CQ filter.

## 5.4 Tuning of a CQ filter

We now use the identification method to tune the CQ filter introduced in Section 4.8. The tuning is carried out 'manually', meaning that the filter dimensions are adjusted incrementally at each iteration based on a comparison between the extracted and the target coupling matrix. Sometimes the adjustments are too strong leading to an overshoot, sometimes they are too small leading to an undershoot. The tuning procedure required 48 iterations to tune 19 physical design parameters. The filter is implemented in a RT/duroid substrate with a $\epsilon_r = 10.2$ and a thickness of 1.27 mm. It is important to note that we have first tuned the inter-resonator couplings and next we tuned the self-couplings. During the tuning procedure, the filter is simulated for a realization with a loss-less substrate and ideal conductors. The filter was simulated using ADS Momentum [ADS 14] and 1 simulation takes around 8 min 30 s. The structure was simulated for an infinite substrate and ground plane and with 60 mesh cells per wavelength (of the shortest wavelength). Figure 5.5 shows the values for the tuned design parameters in ADS. Figure 5.6 shows the layout of the filter in ADS Momentum. Figure 5.7 shows $|S_{11}|$ and $|S_{21}|$ for the initial and final loss-less

design together with the ideal response. The TZs are not exactly falling at the correct golden goal positions due to the presence of the unavoidable parasitic couplings.

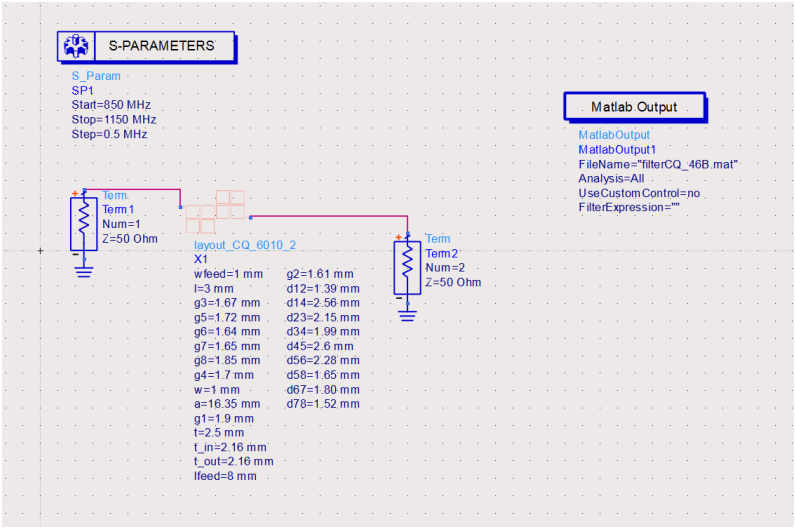


**Figure 5.5** Final design values for the tuned filter in ADS.

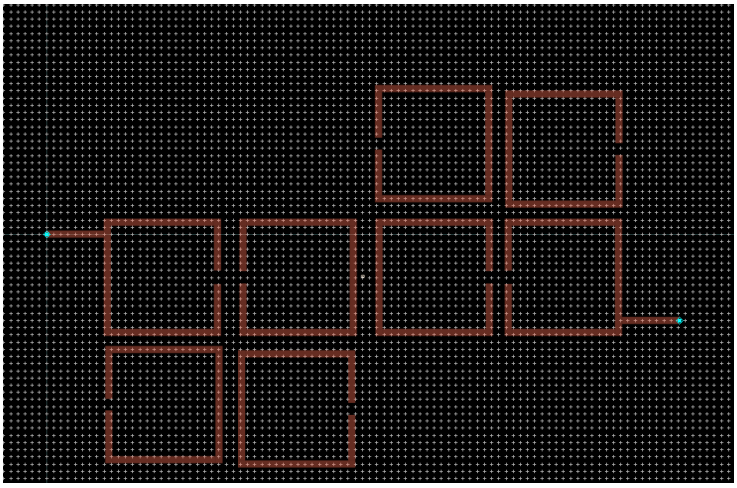

**Figure 5.6** Layout of the filter in Momentum.

The final design is also simulated for the lossy substrate ($\tan\delta = 0.0023$). Figure 5.8 shows $|S_{11}|$ and $|S_{21}|$ for the final loss-less and lossy design together with the ideal response. Inclusion of the substrate losses clearly degrades the quality factors of the TZs and the insertion loss within the passband as could be

expected. Table 5.2 contains the extracted and ideal coupling parameters. The extracted coupling parameters for the final design are very close to those of the target coupling matrix: the maximum difference between the couplings is less than 0.02 for the inter-resonator couplings. Note that there are still parasitic couplings present and that the self-couplings of the resonators are not zero. For the lossy filter, the real part of the diagonal elements is no longer negligible. Table 5.4 contains the extracted quality factors of the resonators, the quality factor of resonator $k$ is determined as $Q_k = \frac{1}{FBW\,\mathrm{Re}(M_{kk})}$ (2.40). Note that (2.40) only holds if the real parts of the non-diagonal couplings are zero.

If we take a closer look at Table 5.2, we observe that the parasitic coupling $M_{13}$ and $M_{57}$ are not negligible. To have an idea of their effect on the $S$-parameters, we have added them to the ideal (target) coupling matrix and calculated the corresponding $S$-parameters. Figure 5.9 shows that these couplings heavily deteriorate the reflection coefficient in the passband. Nevertheless the tuned filter fulfills the specifications. It must be noted that some self-couplings ($M_{33}$ and $M_{66}$) are relatively large for the tuned filter. This implies that these non-zero self-couplings compensate somehow for the presence of $M_{13}$ and $M_{57}$. In the next chapter we will use this effect to re-optimize the target coupling matrix, changing the golden goal to take into account the parasitic couplings in the physical filter.

### Measurements

The final design is fabricated and measured for verification using a Vectorial Network Analyzer. Figure 5.10 shows a picture of the fabricated filter. The measurements show that there is a frequency offset and also that there is more insertion loss than is predicted by the EM-simulator (Figure 5.11). The frequency offset is due to an underestimate of the relative dielectric constant $\varepsilon_r$ of the substrate. In the simulation a dielectric constant of 10.2 was used where the physical substrate has a $\varepsilon_r$ of 10.6. This explains the shift of the center frequency. The increase of the insertion loss is due to the presence of the conductor loss of the copper which was not included in the simulation. To take into account for these effects, the same structure was simulated using the updated substrate and conductor parameters. To take into account the loss of the copper strip, the conductivity was set to be 5.8 $\frac{\mathrm{MS}}{m}$. We have also included the effect of a finite thickness of the metal strip, because this affects the coupling between the lines. The thickness of the metal was set 17.5 $\mu$m. Figure 5.11 shows that the simulations and measurement now agree quite well. Table 5.3 contains the extracted coupling parameters of the measured and re-simulated filters. Note that these

| Parameter | Initial | Final Loss-Less | Final Lossy | Target |
|---|---|---|---|---|
| $M_{S1}$ | 0.9941 | 1.0452 | 1.0459 | 1.0416 |
| $M_{L8}$ | 0.9920 | 1.0423 | 1.0431 | 1.0416 |
| $M_{12}$ | 0.9467 | 0.8496 | 0.8493 | 0.8478 |
| $M_{23}$ | 0.8549 | 0.6796 | 0.6812 | 0.6896 |
| $M_{34}$ | 0.6169 | 0.5115 | 0.5120 | 0.5217 |
| $M_{14}$ | -0.2157 | -0.1453 | -0.1451 | -0.1463 |
| $M_{45}$ | 0.6656 | 0.5377 | 0.5385 | 0.5328 |
| $M_{56}$ | 0.5314 | 0.4332 | 0.4317 | 0.4424 |
| $M_{67}$ | 0.9410 | 0.8092 | 0.8089 | 0.8218 |
| $M_{78}$ | 0.8978 | 0.7782 | 0.7775 | 0.7769 |
| $M_{58}$ | -0.3973 | -0.3593 | -0.3615 | -0.3694 |
| $M_{11}$ | 0.5780 | -0.0115 | -0.0093 | 0 |
| $M_{22}$ | 0.2656 | -0.0565 | -0.0534 | 0 |
| $M_{33}$ | 0.4738 | 0.1780 | 0.1662 | 0 |
| $M_{44}$ | 0.3833 | -0.0176 | -0.0213 | 0 |
| $M_{55}$ | 0.3863 | -0.0070 | -0.0073 | 0 |
| $M_{66}$ | 0.0267 | -0.1896 | -0.2018 | 0 |
| $M_{77}$ | 0.4558 | 0.0659 | 0.0715 | 0 |
| $M_{88}$ | 0.5494 | -0.0039 | -0.0032 | 0 |
| $M_{24}$ | -0.0662 | -0.1046 | -0.0963 | 0 |
| $M_{57}$ | 0.1388 | 0.0853 | 0.0907 | 0 |

**Table 5.2** Extracted and target coupling parameters of the SOLR CQ filter.

are just estimation of the quality factors, since the real parts of the non-diagonal couplings are not zero. The real parts of the non-diagonal couplings are 2 orders of magnitude smaller than those of the diagonal elements. As expected the self-couplings are still quite large, which is due to the frequency shift. Table 5.4 contains the extracted quality factors, which are much lower than in the case where no metal loss was included as expected.

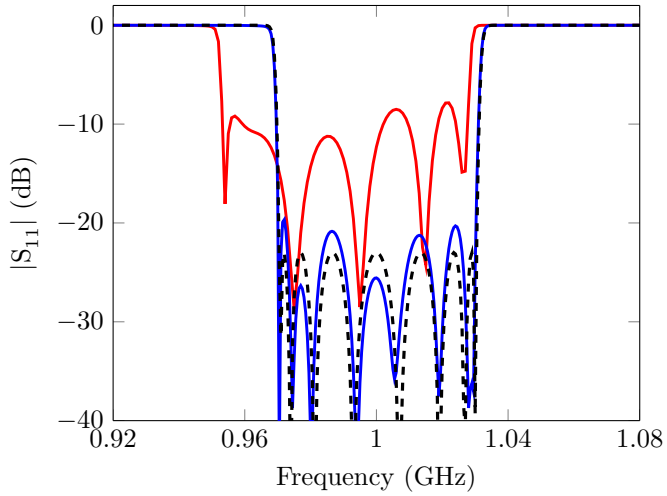


**(a)** $|S_{11}|$ for the initial design (—), the final loss-less design (—) and the ideal response (- - -)

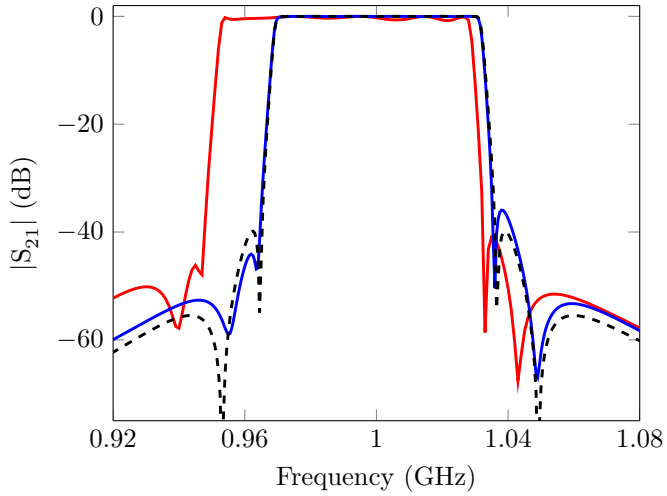


**(b)** $|S_{21}|$ for the initial design (—), the final loss-less design (—) and the ideal response (- - -)

**Figure 5.7** $|S_{11}|$ and $|S_{21}|$ for the initial design, the final loss-less design and the ideal response

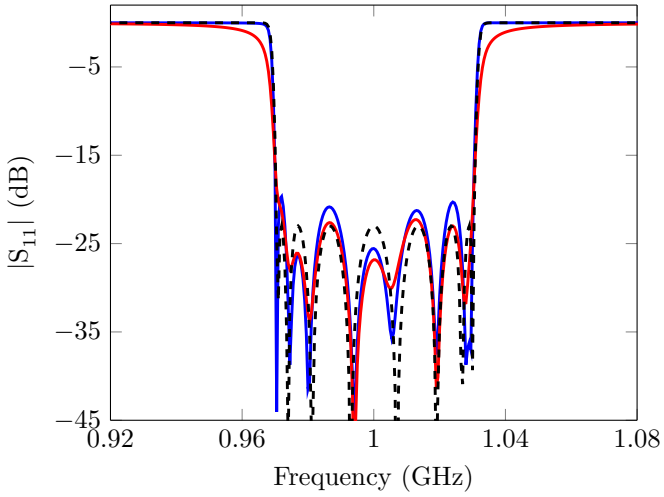


**(a)** $|S_{11}|$ for the final lossy design (—), the final loss-less design (—) and the ideal response (- - -)

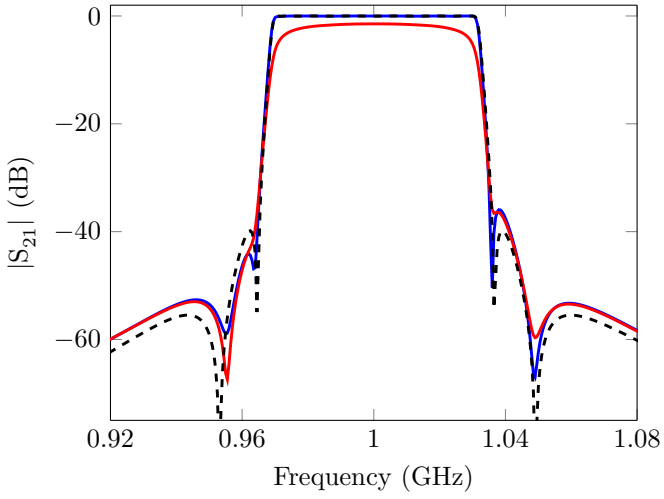


**(b)** $|S_{21}|$ for the final lossy design (—), the final loss-less design (—) and the ideal response (- - -)

**Figure 5.8** $|S_{11}|$ and $|S_{21}|$ for the final lossy and loss-less design and the ideal response.

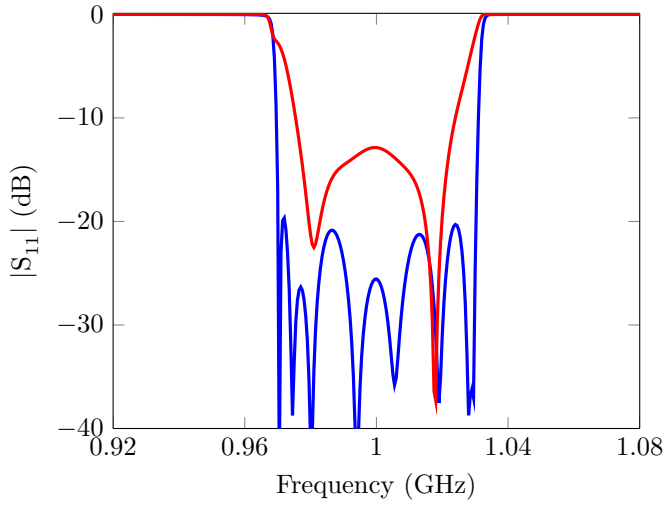


**(a)** $|S_{11}|$ for the ideal coupling matrix with extra couplings added (—), the final loss-less design (—) and the ideal response (- - -)

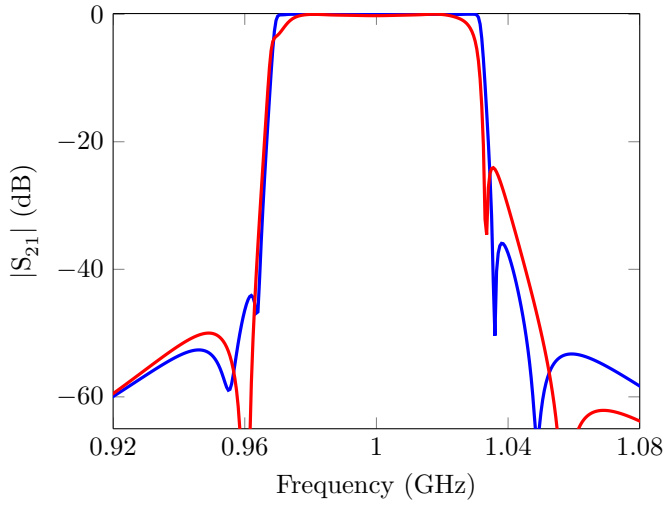


**(b)** $|S_{21}|$ for the ideal coupling matrix with extra couplings added (—), the final loss-less design (—) and the ideal response (- - -)

**Figure 5.9** $|S_{11}|$ and $|S_{21}|$ for the ideal coupling matrix with extra couplings added, the final loss-less design and the ideal response

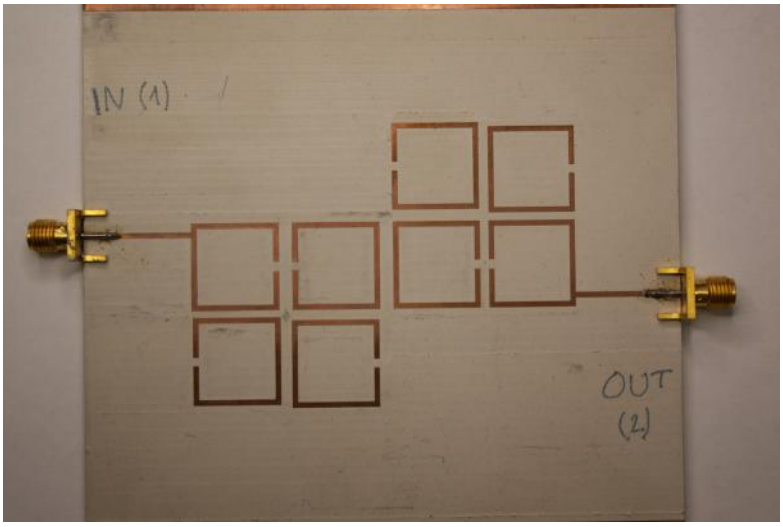


**Figure 5.10** Top-view of the manufactured filter.

| Parameter | Measured | Re-simulated | Target |
|---|---|---|---|
| $M_{S1}$ | 1.0204 | 1.0290 | 1.0416 |
| $M_{L8}$ | 1.0369 | 1.0283 | 1.0416 |
| $M_{12}$ | 0.9328 | 0.8307 | 0.8478 |
| $M_{23}$ | 0.7097 | 0.6522 | 0.6896 |
| $M_{34}$ | 0.5582 | 0.5016 | 0.5217 |
| $M_{14}$ | -0.1684 | -0.1220 | -0.1463 |
| $M_{45}$ | 0.5429 | 0.5274 | 0.5328 |
| $M_{56}$ | 0.4672 | 0.4176 | 0.4424 |
| $M_{67}$ | 0.8465 | 0.8104 | 0.8218 |
| $M_{78}$ | 0.8491 | 0.7470 | 0.7769 |
| $M_{58}$ | -0.3956 | -0.3726 | -0.3694 |
| $M_{11}$ | 0.6779 | 0.6693 | 0 |
| $M_{22}$ | 0.6110 | 0.6241 | 0 |
| $M_{33}$ | 0.9202 | 0.8580 | 0 |
| $M_{44}$ | 0.6731 | 0.6519 | 0 |
| $M_{55}$ | 0.5583 | 0.6659 | 0 |
| $M_{66}$ | 0.3623 | 0.5548 | 0 |
| $M_{77}$ | 0.7170 | 0.7113 | 0 |
| $M_{88}$ | 0.4857 | 0.6789 | 0 |
| $M_{24}$ | -0.1532 | -0.1066 | 0 |
| $M_{57}$ | 0.0939 | 0.0492 | 0 |

**Table 5.3** Extracted and target coupling parameters of the measured and re-simulated SOLR CQ filter.

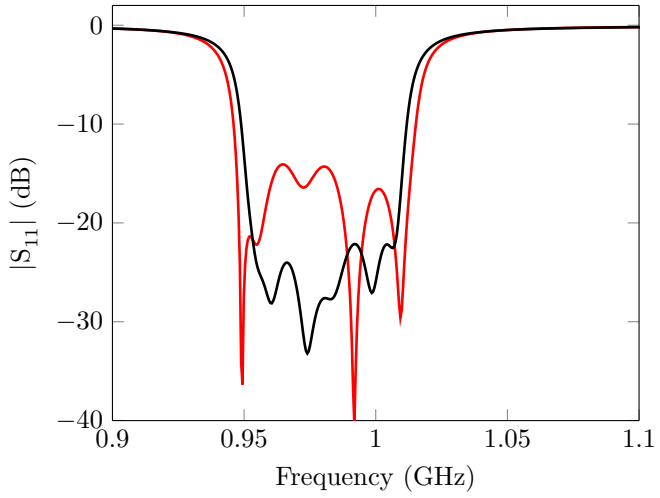


**(a)** $|S_{11}|$ for the measured filter (—) and the re-simulated filter (—).

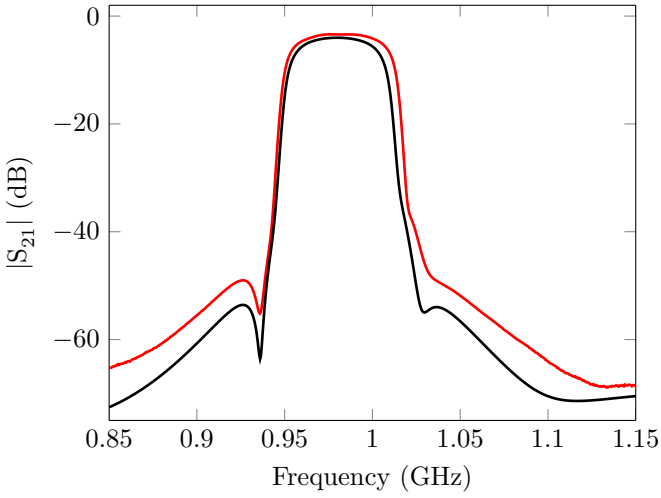


**(b)** $|S_{21}|$ for the measured filter (—) and the re-simulated filter (—).

**Figure 5.11** $|S_{11}|$ and $|S_{21}|$ for the measured filter and the re-simulated filter.

| | $Q_1$ | $Q_2$ | $Q_3$ | $Q_4$ | $Q_5$ | $Q_6$ | $Q_7$ | $Q_8$ |
|---|---|---|---|---|---|---|---|---|
| Lossy Design | 422 | 394 | 379 | 450 | 467 | 615 | 547 | 423 |
| Measured | 180 | 214 | 152 | 218 | 207 | 205 | 211 | 188 |
| Re-Simulated | 160 | 180 | 149 | 172 | 178 | 205 | 165 | 158 |

**Table 5.4** Extracted Quality Factors for the lossy final design, measured filter and re-simulated filter.

## 5.5 Conclusion

This chapter presents a novel method to identify the physically implemented coupling matrix for CT and CQ filters. The example illustrates the utility of the method during the tuning of cascaded topology filters. There are however some limitations. Since the initialization phase is based on the specific relation between the TZs and the quadruplets (or triplets), the method is limited to this kind of topologies. When dealing with other topologies having multiple solutions such as *extended box* topologies [Came 07a], the initialization procedure must be adapted. Moreover when the number of sections grows, the number of simulations to initialize the method grows as well which is disadvantageous when the simulation time is high.

Once the $\boldsymbol{M}^0_{Phys}$ has been determined, the quadratic approximation of the design curves allows to predict the variations of the inter-resonator couplings with sufficient accuracy. Note that we only track the inter-resonator coupling and thus do not take into account the effect of parasitic couplings and self-couplings. The quality of $\boldsymbol{M}_{Pred}$ thus heavily depends on the quality of the design curves and the hypothesis that the inter-resonator couplings are mainly affected by the distances between the resonators.

In order to avoid an exhaustive search among the possible solutions an alternative approach could be to impose the target topology and use an optimization-based method to extract the coupling parameters. A possible cost function in this case is the distance between the imposed target matrix and the extracted coupling parameters. To obtain an extracted coupling matrix at the beginning of the tuning procedure a criterion must be assigned such that the extracted coupling matrix has the same nature as the target matrix. If we consider for example the case of two cascaded quadruplets, we can order the imaginary parts of the extracted TZs in ascending order. As a criterion we can then assign the first and last TZs to the first quadruplet and the second and third TZs to the second quadruplet. Obviously this criterion must also hold for the target coupling matrix. The benefits of such an approach are that we avoid the necessity of multiple simulations and that the computations are faster. The main drawback is that there is no guaranteed optimization convergence.

The tuning procedure used in Section 5.4 can be improved as well. In the next chapter we present an automated tuning procedure which is based on the Jacobian of the function that maps the coupling parameters to the physical dimensions.

# 6

# Electromagnetic Optimization of Microstrip Bandpass Filters based on Adjoint Sensitivity Analysis

This chapter introduces a novel computer-aided tuning (CAT) or optimization method for coupled resonator microwave bandpass filters. The method is based on the estimation of the Jacobian of the function that relates the geometrical design parameters of the filter to the physically implemented coupling parameters. The Jacobian is estimated by combining the adjoint sensitivity of the $S$-parameters with respect to the coupling parameters on the one hand and the adjoint sensitivity of the $S$-parameters with respect to the physical filter design parameters on the other hand.

Formal expressions exist to calculate the adjoint sensitivities of the $S$-parameters with respect to the circuit parameters using the values of the extracted coupling parameters only. Lately commercial EM-simulators, such as CST Microwave Studio [CST 15], provide the adjoint sensitivities of the $S$-parameters with respect to the geometrical or substrate parameters of the filter. One EM-simulation therefore suffices to estimate the Jacobian. In the case of coupling topologies with multiple solutions, the Jacobian is estimated for each solution separately. This still requires only one EM-simulation. We present a criterion to determine the physical solution using the estimated Jacobian matrices.

The tuning procedure first calculates the difference between the physically implemented coupling matrix and the golden goal. Next it uses this difference together with the Pseudo-inverse of the Jacobian, to obtain corrections for the geometrical parameters. This process is repeated iteratively until the corrections become sufficiently small with respect to a user specified goal. The CAT method is applied to the design of a cascaded triplet (CT) and a single quadruplet (SQ) microstrip filter.

## 6.1 Introduction

Over the last years various automated CAT methods have been developed to optimize the physical dimensions (design parameters) of coupled resonator microwave bandpass filters. Some methods optimize a cost function based on the values of $S$-parameters simulated at some well-chosen frequencies [Band 94b; Arnd 04]. Other methods use a cost function based on the positions of the poles and the zeros which are estimated starting from a rational model of the $S$-parameters [Koza 02]. A third approach optimizes a cost function based on the extracted coupling matrix [Lamp 04; Koza 06]. These methods share the same time-consuming step which is the EM-simulation of the filter. Therefore one of the main challenges is to reduce the number of EM-simulations needed to tune the filter.

The coupling matrix based methods in [Lamp 04; Koza 06] correct the physical dimensions using the Jacobian of the function that maps these parameters to the extracted coupling parameters. The Jacobian matrix is estimated numerically using forward differences. This estimation requires $n_g$ EM-simulations, where $n_g$ is the number of physical design parameters of the filter. At each iteration of the tuning method, the Jacobian is updated. The updates use the Broyden method [Broy 65] to reduce the required number of EM-simulations. The methods discussed in [Lamp 04; Koza 06] all converge to a tuned design that meets the specifications with a very low number of required EM-simulations. Nevertheless the initial estimate still requires a high number of EM-simulation, especially in the case of filters having a large number of design parameters. Another shortcoming that is common to the current methods is that they do not handle coupling topologies with multiple possible solutions.

The CAT method introduced in this chapter, estimates the Jacobian differently. It combines the adjoint sensitivity of the $S$-parameters with respect to the coupling parameters on the one hand and the adjoint sensitivity of the $S$-parameters with respect to the physical filter design parameters on the other hand. Section 6.2 derives formal expressions to calculate the adjoint sensitivities of the $S$-parameters with respect to the circuit parameters using the values of the extracted coupling parameters only. Lately, commercial EM-simulators such as CST Microwave Studio [CST 15] provide the adjoint sensitivities of the $S$-parameters with respect to the geometrical or substrate parameters of the filter without drastically increasing the simulation time. One EM-simulation therefore suffices to estimate the Jacobian. Moreover, the Jacobian is re-estimated at each iteration of the tuning procedure hereby improving the accuracy of the tuning.

The method identifies the physically implemented coupling matrix whenever non-canonical topologies are considered, again using only one EM-simulation. One simulation suffices to estimate the Jacobian for each admissible solution. Jacobian-based tuning the physical parameters requires one to determine their Jacobian of the function relating the physical design parameters to the couplings in the physical realization. The idea is that in a physical design, a coupling parameter is mainly affected by a specific prior-known set of design parameters. As a consequence the partial derivatives of the coupling parameter with respect to these parameters are larger than the partial derivatives with respect to the other design parameters having a second order effect at most. This assumption allows one to predict which elements of the Jacobian are dominant in the case that the underlying relation correspond to the physical relation. Selection of the Jacobian of the physical relation boils down to finding the Jacobian for which those elements are dominant. Note however that a single EM-simulation with the determination of the Jacobian requires more time, since the adjoint sensitivities are computed as well.

Section 6.6 explains the operation of the tuning method. Basically it calculates the corrections for the geometrical parameters using the difference between the physically implemented coupling matrix and the target matrix and uses the Pseudo-inverse [Ben 03] of the Jacobian to calculate the estimation of the compensation to be applied. Thereto, the method minimizes the 2-norm of the difference between the implemented and the target coupling parameters.

The physical dimensions are adjusted iteratively until the necessary corrections become smaller than a user specified value. Section 6.7 applies the tuning method to the design of a cascaded trisection filter. Section 6.8 applies the tuning method to the design of a quadruplet filter. This design is more challenging due to the presence of parasitic couplings. The effect of the parasitics on the response is much greater here as it is in the CT case. To take this into account we re-optimize the target matrix (golden goal) during the tuning method as well. Section 6.5 explains how this re-optimization of the target matrix is performed.

## 6.2 Adjoint Sensitivity of the $S$-parameters with respect to the Coupling Parameters

In Section 2.6.2 we have derived equations to express the $S$-parameters as a function of the inverse of the matrix $\boldsymbol{A} = j\boldsymbol{M} + \boldsymbol{G} + j\omega\tilde{\boldsymbol{I}}_{\boldsymbol{N+2}}$. Here, the matrix $\boldsymbol{M}$ contains the imaginary part of the extracted coupling matrix, the matrix $\boldsymbol{G}$ contains the real part of the coupling matrix and the matrix $\tilde{\boldsymbol{I}}_{\boldsymbol{N+2}}$ is an identity

matrix of size $(N+2)\times(N+2)$ whith the first and last elements on the diagonal equal to 0. The $S$-parameters are obtained as follows:

$$\begin{aligned} S_{11} &= 2[\boldsymbol{A}^{-1}]_{11} - 1 \\ S_{12} &= 2[\boldsymbol{A}^{-1}]_{1,N+2} \\ S_{21} &= 2[\boldsymbol{A}^{-1}]_{N+2,1} \\ S_{22} &= 2[\boldsymbol{A}^{-1}]_{N+2,N+2} - 1 \end{aligned} \tag{6.1}$$

where $[\boldsymbol{A}]_{kl}$ denotes the element at position $k,l$ of the matrix $\boldsymbol{A}$. We now derive a formal expression for $\frac{\partial S_{ij}}{\partial M_{k,l}}(\omega)$. This represents the sensitivity of a scattering parameter $S_{ij}$ with respect to a coupling parameter $M_{k,l}$ taken at a certain frequency $\omega$. In Section 6.3 these sensitivities are used to estimate the Jacobian of the functional relation between the physical filter parameters and the circuit parameters. The sensitivities can be expressed as a function of $\boldsymbol{A}^{-1}$ . Remember that the partial derivative of the inverse of a matrix $\boldsymbol{A}$ can be written as:

$$\frac{\partial \boldsymbol{A}^{-1}}{\partial x} = -\boldsymbol{A}^{-1}\frac{\partial \boldsymbol{A}}{\partial x}\boldsymbol{A}^{-1} \tag{6.2}$$

Applying (6.2) to the expressions given in (6.1) yields:

$$\begin{aligned} &\text{For } l \neq k: \\ &\quad \frac{\partial S_{11}}{\partial M_{lk}} = -4j([\boldsymbol{A}^{-1}]_{1,l}[\boldsymbol{A}^{-1}]_{1,k}) \\ &\quad \frac{\partial S_{21}}{\partial M_{lk}} = -2j([\boldsymbol{A}^{-1}]_{N+2,l}[\boldsymbol{A}^{-1}]_{k,1} + [\boldsymbol{A}^{-1}]_{1,k}[\boldsymbol{A}^{-1}]_{l,N+2}) \\ &\quad \frac{\partial S_{22}}{\partial M_{lk}} = -4j([\boldsymbol{A}^{-1}]_{N+2,l}[\boldsymbol{A}^{-1}]_{N+2,k}) \\ &\text{For } l = k: \\ &\quad \frac{\partial S_{11}}{\partial M_{ll}} = -2j[\boldsymbol{A}^{-1}]^2_{1,l} \\ &\quad \frac{\partial S_{21}}{\partial M_{ll}} = -2j[\boldsymbol{A}^{-1}]_{1,l}[\boldsymbol{A}^{-1}]_{l,N+2} \\ &\quad \frac{\partial S_{22}}{\partial M_{ll}} = -2j[\boldsymbol{A}^{-1}]^2_{N+2,l} \end{aligned} \tag{6.3}$$

These expressions are the same as the ones derived in [Mart 12]. Moreover they are equivalent to those found in [Amar 00a] where the dual circuit based on impedance inverters and series inductors is used

## 6.3 Estimation of the Jacobian Matrix $\boldsymbol{J}$

The tuning procedure is based on the relation between the geometrical design parameters and the extracted coupling parameters describing the physical implementation of the filter. The coupling matrix is extracted using the extraction method described in Chapter 4. Assume that there are $n_g$ geometrical parameters $\boldsymbol{g}$ and $n_c$ coupling parameters $\boldsymbol{m}$. The relation between them is represented by:

$$f(\boldsymbol{g}) = \boldsymbol{m} \tag{6.4}$$

where $\boldsymbol{g}$ is a real vector of size $n_g \times 1$ containing the geometrical parameters and $\boldsymbol{m}$ is a pure imaginary vector of size $n_c \times 1$ containing the extracted coupling parameters. As discussed in Section 4.5 the extracted coupling matrix contains coupling parameters that are considered as first order effects (inter-resonator couplings and self-couplings) and parameters that are considered as second order effects (parasitic couplings). Since the optimization aims to tune the first order effects, the vector $\boldsymbol{m}$ does not contain these parasitic couplings. The Jacobian matrix $\boldsymbol{J}$ of $f(\boldsymbol{g})$ is estimated by combining the adjoint sensitivities of the $S$-parameters.

Commercial EM-simulators such as Computer Simulation Technology (CST) [CST 15], provide the adjoint sensitivities of the $S$-parameters with respect to the geometrical parameters as a function of the frequency. Combining this information with the adjoint sensitivity of the $S$-parameters with respect to the extracted coupling parameters parameters (calculated using (6.3)) results in an estimate of the Jacobian of $f(\boldsymbol{g})$.

The sensitivity of $S_{ij}$ with respect to a single geometrical parameter $g_s$ can be written as

$$\frac{\partial S_{ij}}{\partial g_s}(\omega) = \sum_{k=1}^{n_c} \frac{\partial S_{ij}(\omega)}{\partial m_k} \frac{\partial m_k}{\partial g_s} \tag{6.5}$$

where $\frac{\partial S_{ij}}{\partial m_k}$ is the adjoint sensitivity of $S_{ij}$ with respect to the $k^{th}$ circuital

parameter of $\boldsymbol{m}$ and $\frac{\partial m_k}{\partial g_s}$ is element $[\boldsymbol{J}]_{k,s}$ of the Jacobian $\boldsymbol{J}$. Using (6.3) it is possible to calculate the sensitivity of $S_{ij}$ with respect to each extracted circuit parameter at each frequency used in the simulation. The frequencies are transformed to the normalized low-pass domain and grouped in increasing order in a vector $\boldsymbol{\omega} = [\omega_1, ..., \omega_{n_F}]^t$, where $n_F$ is the number of frequencies. The column wise ordering these frequency dependent sensitivities yields a complex matrix of size $4n_F \times n_c$ :

$$\boldsymbol{S_{dM}} = \begin{bmatrix} \frac{\partial S_{11}}{\partial m_1}(\omega_1) & \dots & \frac{\partial S_{11}}{\partial m_k}(\omega_1) & \dots & \frac{\partial S_{11}}{\partial m_{n_c}}(\omega_1) \\ \vdots & & \vdots & & \vdots \\ \frac{\partial S_{11}}{\partial m_1}(\omega_{n_F}) & \dots & \frac{\partial S_{11}}{\partial m_k}(\omega_{n_F}) & \dots & \frac{\partial S_{11}}{\partial m_{n_c}}(\omega_{n_F}) \\ \frac{\partial S_{12}}{\partial m_1}(\omega_1) & \dots & \frac{\partial S_{12}}{\partial m_k}(\omega_1) & \dots & \frac{\partial S_{12}}{\partial m_{n_c}}(\omega_1) \\ \vdots & & \vdots & & \vdots \\ \frac{\partial S_{12}}{\partial m_1}(\omega_{n_F}) & \dots & \frac{\partial S_{12}}{\partial m_k}(\omega_{n_F}) & \dots & \frac{\partial S_{12}}{\partial m_{n_c}}(\omega_{n_F}) \\ \frac{\partial S_{21}}{\partial m_1}(\omega_1) & \dots & \frac{\partial S_{21}}{\partial m_k}(\omega_1) & \dots & \frac{\partial S_{21}}{\partial m_{n_c}}(\omega_1) \\ \vdots & & \vdots & & \vdots \\ \frac{\partial S_{21}}{\partial m_1}(\omega_{n_F}) & \dots & \frac{\partial S_{21}}{\partial m_k}(\omega_{n_F}) & \dots & \frac{\partial S_{21}}{\partial m_{n_c}}(\omega_{n_F}) \\ \frac{\partial S_{22}}{\partial m_1}(\omega_1) & \dots & \frac{\partial S_{22}}{\partial m_k}(\omega_1) & \dots & \frac{\partial S_{22}}{\partial m_{n_c}}(\omega_1) \\ \vdots & & \vdots & & \vdots \\ \frac{\partial S_{22}}{\partial m_1}(\omega_{n_F}) & \dots & \frac{\partial S_{22}}{\partial m_k}(\omega_{n_F}) & \dots & \frac{\partial S_{22}}{\partial m_{n_c}}(\omega_{n_F}) \end{bmatrix} \tag{6.6}$$

Similarly, the sensitivities of $S_{ij}$ with respect to the geometrical parameters as a function of the frequency as is provided by the simulator are ordered column wise in a complex matrix of size $4n_F \times N_g$

$$\mathbf{S_{dG}} = \begin{bmatrix} \frac{\partial S_{11}}{\partial g_1}(\omega_1) & \dots & \frac{\partial S_{11}}{\partial g_k}(\omega_1) & \dots & \frac{\partial S_{11}}{\partial g_{N_g}}(\omega_1) \\ \vdots & & \vdots & & \vdots \\ \frac{\partial S_{11}}{\partial g_1}(\omega_{n_F}) & \dots & \frac{\partial S_{11}}{\partial g_k}(\omega_{n_F}) & \dots & \frac{\partial S_{11}}{\partial g_{N_g}}(\omega_{n_F}) \\ \frac{\partial S_{12}}{\partial g_1}(\omega_1) & \dots & \frac{\partial S_{12}}{\partial g_k}(\omega_1) & \dots & \frac{\partial S_{12}}{\partial g_{N_g}}(\omega_1) \\ \vdots & & \vdots & & \vdots \\ \frac{\partial S_{12}}{\partial g_1}(\omega_{n_F}) & \dots & \frac{\partial S_{12}}{\partial g_k}(\omega_{n_F}) & \dots & \frac{\partial S_{12}}{\partial g_{N_g}}(\omega_{n_F}) \\ \frac{\partial S_{21}}{\partial g_1}(\omega_1) & \dots & \frac{\partial S_{21}}{\partial g_k}(\omega_1) & \dots & \frac{\partial S_{21}}{\partial g_{N_g}}(\omega_1) \\ \vdots & & \vdots & & \vdots \\ \frac{\partial S_{21}}{\partial g_1}(\omega_{n_F}) & \dots & \frac{\partial S_{21}}{\partial g_k}(\omega_{n_F}) & \dots & \frac{\partial S_{21}}{\partial g_{N_g}}(\omega_{n_F}) \\ \frac{\partial S_{22}}{\partial g_1}(\omega_1) & \dots & \frac{\partial S_{22}}{\partial g_k}(\omega_1) & \dots & \frac{\partial S_{22}}{\partial g_{N_g}}(\omega_1) \\ \vdots & & \vdots & & \vdots \\ \frac{\partial S_{22}}{\partial g_1}(\omega_{n_F}) & \dots & \frac{\partial S_{22}}{\partial g_k}(\omega_{n_F}) & \dots & \frac{\partial S_{22}}{\partial g_{N_g}}(\omega_{n_F}) \end{bmatrix} \tag{6.7}$$

$\boldsymbol{S_{dG}}$ can be written as a function of $\boldsymbol{S_{dM}}$ using the Jacobian:

$$\boldsymbol{S_{dG}} = \boldsymbol{S_{dM}}\boldsymbol{J} \tag{6.8}$$

The Jacobian $\boldsymbol{J}$ is estimated in least squares sense:

$$\boldsymbol{J} = (\boldsymbol{S_{dM}^*}\boldsymbol{S_{dM}})^{-1}\boldsymbol{S_{dM}^*}\boldsymbol{S_{dG}} \tag{6.9}$$

where $\boldsymbol{S_{dM}^*}$ is the conjugate transpose of $\boldsymbol{S_{dM}}$.

Note that in the ideal case the Jacobian matrix is a purely imaginary matrix. There is however a small real part, due to the fact that the extracted coupling matrix also has a small real part (Chapter 4). In the case of a loss-less filter, the real part will be a few orders of magnitude lower than the imaginary part in the extracted coupling matrix. Therefore the real part of the complex Jacobian matrix is also a few orders of magnitude lower. In what follows we therefore only consider the imaginary part of the Jacobian matrix and thus the Jacobian is purely imaginary.

Another important remark is that, since we are working in the lowpass domain, the adjoint sensitivities given by CST ($\frac{\partial S_{ij}^{CST}}{\partial g_k}$) must be compensated for the delays and frequency shifts as is explained in Section 4.3. At a frequency $\omega_l$, the adjoint sensitivity of $\boldsymbol{S}$ with respect to a geometrical parameter $g_k$ therefore is:

$$\begin{bmatrix} \frac{\partial S_{11}}{\partial g_k}(\omega_l) & \frac{\partial S_{12}}{\partial g_k}(\omega_l) \\ \frac{\partial S_{21}}{\partial g_k}(\omega_l) & \frac{\partial S_{22}}{\partial g_k}(\omega_l) \end{bmatrix} = \\ \begin{bmatrix} e^{j(\omega_l \alpha_{11}+\beta_{11})} \frac{\partial S_{11}^{CST}}{\partial g_k}(\omega_l) & e^{j(\omega_l \frac{\alpha_{11}+\alpha_{22}}{2}+\frac{beta_{11}+\beta_{22}}{2})} \frac{\partial S_{12}^{CST}}{\partial g_k}(\omega_l) \\ e^{j(\omega_l \alpha_{22}+\beta_{22})} \frac{\partial S_{22}^{CST}}{\partial g_k}(\omega_l) & e^{j(\omega_l \frac{\alpha_{11}+\alpha_{22}}{2}+\frac{beta_{11}+\beta_{22}}{2})} \frac{\partial S_{21}^{CST}}{\partial g_k}(\omega_l) \end{bmatrix} \tag{6.10}$$

## 6.4 Determination of the Physically Implemented Coupling Matrix

In the case of coupling topologies supporting $n_S$ different possible solutions, the extraction procedure yields $n_S$ different vectors $\boldsymbol{m}_p$ ($p \in \{1, \ldots, n_S\}$). This means $n_S$ equivalent functions $f_p$ relate the design parameters $\boldsymbol{g}$ to the coupling parameters $\boldsymbol{m}_p$. Among them only one function $f_{Phys}$ relates $\boldsymbol{g}$ to the physically implemented coupling parameters $\boldsymbol{m}_{Phys}$.

To identify $f_{Phys}$ among all others, we assume that in a physical design a specific coupling is mainly determined by a specific set of physical parameters and that it is possible to determine which physical parameters influence the couplings most. This assumption is also implicitly made during the initial dimensioning of the filter. Remember that second order effects, such as loading of the resonators, are also neglected there (Chapter 3). One can therefore predict which partial derivatives $\frac{\partial m_k}{\partial g_s}$ are dominant for the physical design. These derivatives correspond to the dominant elements of the Jacobian matrix $\boldsymbol{J_{Phys}}$ of $f_{Phys}$. Let $V$ denote the set of indexes corresponding to these elements. For each estimated $\boldsymbol{J}_p$, the relative influence of these predicted elements is calculated:

$$c_p = \frac{\sum_{k,l \in V} [\boldsymbol{J}_p]_{l,k}^2}{\sum_{m=1}^{n_c} \sum_{n=1}^{n_g} [\boldsymbol{J}_p]_{m,n}^2} \tag{6.11}$$

Here $[\boldsymbol{J}_p]_{l,k}$ denotes the imaginary part of the element at position $(l, k)$ of the matrix $\boldsymbol{J}_p$. In the set of equivalent Jacobian matrices one selects the matrix for which $c_p$ is maximal. This matrix corresponds to the solution for which the design parameters have the expected dominant main effects on the coupling parameters. This solution can then safely be assumed to be the physical one. In what follows we denote the physical function $f_{Phys}$, the associated implemented parameters $\boldsymbol{m}_{Phys}$ and Jacobian $\boldsymbol{J}_{Phys}$ as $f$, $\boldsymbol{m}$ and $\boldsymbol{J}$ respectively to make the notation more readable.

## 6.5 Re-optimization of the Target Coupling Matrix

The presence of parasitic couplings can heavily deteriorate the performance of the filter, even when the other inter-resonator and self-couplings correspond to the requested target values. For the example discussed in Section 5.4, the presence of the parasitic couplings $M_{13}$ and $M_{57}$ ruins the behavior of $S_{11}$ in the passband (Figure 5.9). It is however possible to compensate for this effect when using the presence of non-zero diagonal elements. This can result in a final filter, that meets the specification. In this section we propose to re-optimize the target coupling matrix taking into account the presence of the observed parasitic effects. We minimize the difference between reflection and transmission coefficients created by the coupling matrix containing the parasitic elements and the target values of reflection and transmission coefficients evaluated at a finite number of frequencies.

We choose these frequencies in the passband for the reflection coefficient and around the TZs for the transmission coefficient. We denote the target coupling matrix with the observed coupling parameters added as $\boldsymbol{M}_{par,0}$ and the target coupling matrix as $\boldsymbol{M}_{id}$. We denote the response created by $\boldsymbol{M}_{par,0}$ as $S_{kl}^{par,0}$ and the target response as $S_{kl}^{id}$ $(k,l \in \{1,2\})$. We now optimize the diagonal elements of the matrix $\boldsymbol{M}_{par,i}$ to compensate the effect of the parasitic couplings. The index $i$ denotes the iteration and $S_{kl}^{par,i}$ is the response created by $\boldsymbol{M}_{par,i}^{tar}$. The least squares cost function that is minimized is:

$$c_{par,i} = \sqrt{\sum_{f_{11}=1}^{n_{f_{11}}} |S_{11}^{par,i}(\omega_{f_{11}}) - S_{11}^{id}(\omega_{f_{11}})|^2 + \sum_{f_{21}=1}^{n_{f_{21}}} |S_{21}^{par,i}(\omega_{f_{21}}) - S_{21}^{id}(\omega_{f_{21}})|^2} \tag{6.12}$$

where $\omega_{f_{11}}$ $(f_{11} \in \{1,\ldots,n_{f_{11}}\})$ are the lowpass frequencies chosen in the passband and $\omega_{f_{21}}$ $(f_{21} \in \{1,\ldots,n_{f_{21}}\})$ are the lowpass frequencies chosen in the vicinity of the TZs at finite frequencies. Similarly to Section 4.6 , the minimizer of (6.12) is calculated using the Matlab function *fminunc*, which calculates the minimum for an unconstrained multi-variable scalar function. Note that only the diagonal elements of $\boldsymbol{M}_{par,i}$ are varied during the optimization. We denote the re-optimized target matrix as $\boldsymbol{M}_{re}$

In the examples considered in this work, the inter-resonator couplings are mainly affected by the distances between the resonators and the self-couplings by the distances between the ends of the resonators. We assume that the parasitic cou-

plings are mainly affected by the inter-resonator distances. In the case of strong parasitic couplings, we first tune the filter until the inter-resonator distances yield the target inter-resonator couplings. Next we re-optimize the target matrix diagonal by taking into account the observed parasitic couplings by minimizing $c_{par,i}$ (6.12). We continue to tune the filters towards the newly found target matrix $\boldsymbol{M}_{re}$.

## 6.6 Tuning Method

### 6.6.1 CORRECTION OF THE DESIGN PARAMETERS

The optimization method calculates the update for the design parameters $\boldsymbol{g}$ such that the corresponding circuital parameters $f(\boldsymbol{g}) = \boldsymbol{m}$ coincide maximally with the target coupling parameters $\tilde{\boldsymbol{m}}$ of the golden goal. Evaluating the function $f$ for the initial design parameters $\boldsymbol{g_0}$ yields the difference between the circuital parameters of the initial design $\boldsymbol{m_0}$ and the target parameters $\tilde{\boldsymbol{m}}$ which allows to evaluate the design error:

$$\Delta \boldsymbol{m_0} = \tilde{\boldsymbol{m}} - f(\boldsymbol{g_0}) \tag{6.13}$$

The corrections of $\boldsymbol{g_0}$ necessary to improve the filter response are therefore readily obtained as:

$$\Delta \boldsymbol{g_0} = \boldsymbol{g_1} - \boldsymbol{g_0} = f^{-1}(\boldsymbol{m_o} + \Delta \boldsymbol{m_0}) - \boldsymbol{g_0} \tag{6.14}$$

where $\boldsymbol{g_1}$ are the design parameters of the improved filter. A linear approximation of $f$ using the estimated Jacobian $\boldsymbol{J_0}$ evaluated at $\boldsymbol{g_0}$ yields:

$$\boldsymbol{m_1} = f(\boldsymbol{g_1}) \approx \boldsymbol{J_0} \Delta \boldsymbol{g_0} + \boldsymbol{m_0} \tag{6.15}$$

Expression (6.15) approximates the correction of the design parameters using the pseudo-inverse of the Jacobian $\boldsymbol{J_0^{-1}}$ :

$$\Delta \boldsymbol{g_0} \approx \boldsymbol{J_0^{-1}} \Delta \boldsymbol{m_0} \tag{6.16}$$

A simulation of the updated filter response yields the coupling parameters $\boldsymbol{m_1}$

and the Jacobian $\boldsymbol{J_1}$ in the same way as above. Repeating the process above then allows to refine the correction until the necessary corrections become sufficiently small:

$$\| \Delta \boldsymbol{g_k} \|_\infty = \max_l [\Delta \boldsymbol{g_k}]_l < \delta_{corr} \tag{6.17}$$

where $\delta_{corr}$ is a user-defined value. Since there is no point in calculating geometrical parameters more precisely than the limits imposed by the fabrication tolerance, a valid choice for $\delta_{corr}$ is readily found to be the accuracy of the fabrication process. For all considered examples, the optimization method converges after a number of iterations smaller than the number of design parameters to be tuned.

When the parasitic couplings heavily influence the response, we tune the filter until the corrections for the inter-resonator distances become smaller than $\delta_{corr}$. To this end, we order the inter-resonator couplings in a vector $\boldsymbol{g_k^d}$. Next we re-optimize the target coupling matrix as discussed in Section 6.5 and order them into a vector $\tilde{\boldsymbol{m}}_{\boldsymbol{re}}$.

### 6.6.2 OPTIMIZATION ALGORITHM

1. Approximation of a frequency template to obtain the ideal rational scattering matrix that fulfills the specifications (Chapter 2)
2. Synthesis of the target coupling matrix $\tilde{\boldsymbol{M}}$ (the couplings are ordered in a vector $\tilde{\boldsymbol{m}}$). In the case of multiple solutions, one solution is chosen as the target matrix
3. Computation of the initial design parameters $\boldsymbol{g_k}$ of the filters' physical implementation, where $k = 0$ (Chapter 3)
4. Full-wave EM-simulation of the filters $S$-parameters in the frequency band of interest and the adjoint sensitivities of the $S$-parameters with respect to the design parameters $\boldsymbol{g_k}$
5. Extraction of the coupling parameters (Chapter 4):
   (a) Rational approximation of the simulated $S$-parameters.
   (b) Coupling matrix synthesis
   (c) Determination of all the possible solutions corresponding to the implemented coupling topology

6. Estimation of the Jacobian of the couplings with respect to the physical parameters for each solution and determination of the physically implemented coupling matrix using expression (6.11) (Section 6.3)

7. Computation of the error of the circuit parameters $\Delta \boldsymbol{m_k}$ (Section 6.6.1)

8. Estimation of the correction for the design parameters $\Delta \boldsymbol{g_k} \approx \boldsymbol{J_k^{-1}} \Delta \boldsymbol{m_k}$

9. Case of strong parasitics: re-optimize the target to obtain $\tilde{\boldsymbol{m}}_{\boldsymbol{re}}$ if $\| \Delta \boldsymbol{g_k^d} \|_\infty < \delta_{corr}$

10. Termination of the optimization process if $\| \Delta \boldsymbol{g_k} \|_\infty < \delta_{corr}$

11. Update of the design parameters: $\boldsymbol{g_{k+1}} = \boldsymbol{g_k} + \Delta \boldsymbol{g_k}$ and return to step 4

## 6.7 Tuning of a CT filter

In this section the tuning method is applied to the design of a $6^{th}$ order CT filter. The filter is designed to have center frequency $f_c = 1.2$ GHz, a fractional bandwidth $FBW = 0.04$, a minimum return loss $RL$ of 22 dB and 2 finite transmission zeros (TZs) at $\omega = 1.15$ and $\omega = 2.1$. The target coupling matrix is synthesized using Dededale-HF [Seyf 00]. There are 2 solutions to the reduction problem of which one is chosen (arbitrarily). The chosen target coupling matrix is:

$$\begin{bmatrix} 0 & 1.0422 & 0 & 0 & 0 & 0 & 0 & 0 \\ 1.0422 & 0.0394 & 0.8355 & 0.2745 & 0 & 0 & 0 & 0 \\ 0 & 0.8355 & -0.3377 & 0.5789 & 0 & 0 & 0 & 0 \\ 0 & 0.2745 & 0.5789 & 0.1138 & -0.5986 & 0 & 0 & 0 \\ 0 & 0 & 0 & -0.5986 & 0.1349 & 0.3544 & 0.6483 & 0 \\ 0 & 0 & 0 & 0 & 0.3544 & -0.8252 & 0.5942 & 0 \\ 0 & 0 & 0 & 0 & 0.6483 & 0.5942 & 0.0394 & 1.0422 \\ 0 & 0 & 0 & 0 & 0 & 0 & 1.0422 & 0 \end{bmatrix} \tag{6.18}$$

In the chosen solution, the first triplet realizes the TZ at $\omega_1 = 2.1$ and the second one the TZ at $\omega_2 = 1.15$

The filter is implemented on a RO4360 substrate with a thickness of 1.016 mm and $\varepsilon_r = 6.15$. To implement the $\frac{\lambda}{2}$-resonators we use a variation of the SOLR resonator, which is not square but rectangular. Figure 6.1 shows the top-view

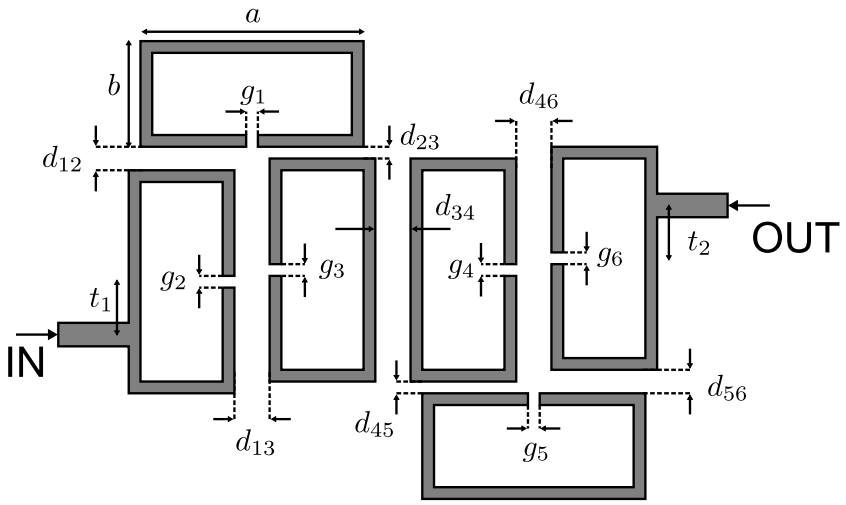


**Figure 6.1** Top-view of the layout of a sixth order cascaded triplet filter.

of the layout of the CT filter. Table 6.1 contains the initial dimensions of the filter. There are 15 design parameters which are the spacing $d_{kl}$ between the resonators $k$ and $l$ and the distance between the ends $g_i$ of the resonator $i$. Note that the positions of the feeding lines $t_i$ are also design parameters. They are however not included in the optimization method, since CST is not capable to calculate the adjoint sensitivity with respect to a parameter that influences the position of a port. Therefore these parameters have to be tuned manually.

Figure 6.2 shows the $S$-parameters of the initial design. Note that the initial design is far away from the target design. We did not use design curves to obtain initial values for the mixed couplings $M_{12}$, $M_{23}$, $M_{45}$ and $M_{56}$ but we have chosen values within the range of values found for the other spacings using visual inspection.

The coupling matrices are extracted using the method described in Chapter 4. There are 2 solutions to the reconfiguration problem and thus there are 2 possible Jacobian matrices too. The parameters are ordered such that dominant elements should be positioned on the main diagonal of the matrix. When we calculate the relative influence of these dominant elements over the others for the first iteration, we find the following values for $c_p$ as defined in (6.11):

$$c_p = \begin{bmatrix} 0.9104 & 0.2024 \end{bmatrix} \tag{6.19}$$

| Physical parameter | Initial Value (mm) | Final Value (mm) |
|---|---|---|
| $a$ | 16.7 | 16.7 |
| $b$ | 16.5 | 16.5 |
| $w$ | 1 | 1 |
| $t_1$ | 4.6 | 4.6 |
| $t_2$ | 4.6 | 4.6 |
| $d_{12}$ | 0.6 | 0.74 |
| $d_{23}$ | 1.4 | 1.16 |
| $d_{13}$ | 2.1 | 1.9 |
| $d_{34}$ | 2.2 | 2.74 |
| $d_{45}$ | 1.5 | 1.71 |
| $d_{56}$ | 1.4 | 1.05 |
| $d_{46}$ | 1.3 | 1.37 |
| $g_1$ | 0.75 | 0.61 |
| $g_2$ | 1.1 | 0.8 |
| $g_3$ | 0.65 | 0.47 |
| $g_4$ | 0.6 | 0.48 |
| $g_5$ | 1.3 | 1.22 |
| $g_6$ | 0.75 | 0.55 |

**Table 6.1** Initial and final values for the physical design parameters of the CT filter.

This indicates that the first solution corresponds to the physically implemented coupling matrix. Table 6.2 contains the coupling parameters associated to the initial design parameters.

Figure 6.3a compares the magnitude of the adjoint sensitivity $\frac{\partial S_{11}}{\partial M_{12}}(\omega)$ obtained using (6.3) to $\frac{\partial S_{11}}{\partial d_{12}}(\omega)$ obtained using CST. Similarly, Figure 6.3b compares the magnitude of the $\frac{\partial S_{21}}{\partial M_{12}}(\omega)$ to $\frac{\partial S_{21}}{\partial d_{12}}(\omega)$. We observe that the trend of the sensitivity as a function of $\omega$ is very similar. This indicates that the $S$-parameters vary similarly to a change of $d_{12}$ and $M_{12}$. There is however a difference since the other geometrical parameters also act on $M_{12}$. Figure 6.4 compares the adjoint sensitivity of $S_{11}$ with respect to $d_{12}$ and $M_{12}$ respectively in the complex plane. Besides the difference in amplitude, we also observe a phase shift of $-\pi$ rad. This phase shift is due to the fact that in (6.3) the $S$-parameters are derived with respect to $M_{kl}$ instead of $jM_{kl}$. If we compensate for this by multiplying $\frac{\partial S_{mn}}{\partial M_{lk}}$ by $-j$, we observe a similar phase behavior for both adjoint sensitivities.

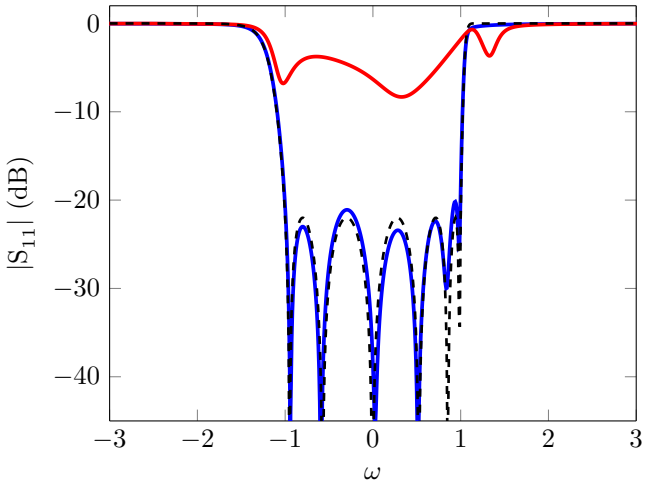


**(a)** $|S_{11}|$ for the initial design (—), the final loss-less design (—) and the ideal response (- - -)

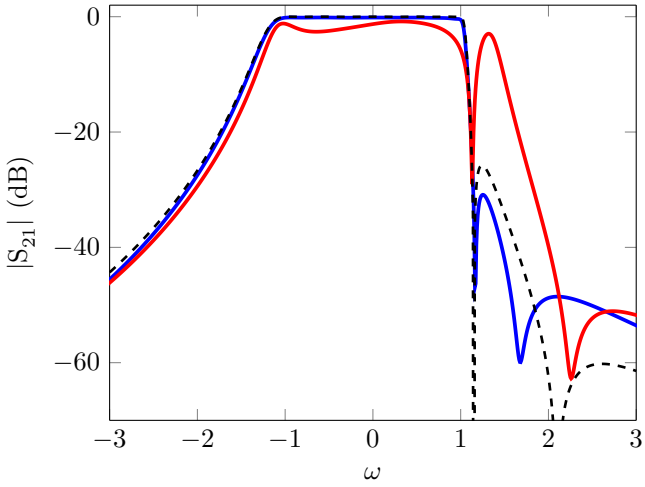


**(b)** $|S_{21}|$ for the initial design (—), the final loss-less design (—) and the ideal response (- - -)

**Figure 6.2** $|S_{11}|$ and $|S_{21}|$ for the initial design, the final loss-less design and the ideal response of the CT filter.

The elements of $\boldsymbol{m}$ and $\boldsymbol{g}$ are ordered such that the first row of the Jacobian corresponds to the partial derivatives $\frac{\partial M_{21}}{\partial g_s}$, $s \in \{1, \ldots, 13\}$, where $g_s$ is one of the 13 geometrical design parameters. The first 7 elements of this row correspond to the partial derivatives with respect to the spacing between the resonators:

$$\begin{bmatrix} \frac{\partial M_{21}}{\partial d_{12}} & \frac{\partial M_{21}}{\partial d_{23}} & \frac{\partial M_{21}}{\partial d_{13}} & \frac{\partial M_{21}}{\partial d_{34}} & \frac{\partial M_{21}}{\partial d_{45}} & \frac{\partial M_{21}}{\partial d_{56}} & \frac{\partial M_{21}}{\partial d_{46}} \end{bmatrix} = \\ \begin{bmatrix} -0.7061 & -0.0086 & -0.1677 & 0.0529 & -0.0050 & -0.0121 & 0.0012 \end{bmatrix} \tag{6.20}$$

It is clear that $M_{12}$ mainly depends on $d_{12}$ as expected. The negative sign of $\frac{\partial M_{21}}{\partial d_{12}}$ also corresponds to what we physically expect: if the distance increases, the coupling decreases and vice versa. The other parameter that mainly influences $M_{12}$ is $d_{13}$. This is logical since, $d_{13}$ determines the offset of resonator 1 with respect to resonator 2. As expected $M_{12}$ is mainly determined by design parameters in the first triplet. The 6 last elements of this row in the Jacobian correspond to the partial derivatives with respect to the spacing between the ends of each resonator:

$$\begin{bmatrix} \frac{\partial M_{21}}{\partial g_1} & \frac{\partial M_{21}}{\partial g_2} & \frac{\partial M_{21}}{\partial g_3} & \frac{\partial M_{21}}{\partial g_4} & \frac{\partial M_{21}}{\partial g_5} & \frac{\partial M_{21}}{\partial d_{56}} \end{bmatrix} = \\ \begin{bmatrix} 0.0912 & -0.0503 & 0.0058 & -0.0191 & 0.0058 & 0.0012 \end{bmatrix} \tag{6.21}$$

It is clear that $M_{12}$ is mainly influenced by $g_1$ and $g_2$, which is consistent with what we expect.

The value of $\delta_{corr}$ was set to 0.01 mm and after 4 iterations (5 EM-simulations) we found a $\| \Delta \boldsymbol{g_k} \|_\infty = 0.01$. On average, an EM-simulation takes 2 hours 30 min (with adjoint sensitivities included). Note that the adaptive meshing is included in this time and this already takes 1 hour. An EM-simulation without adjoint sensitivities takes 2 hours 10 min on average, indicating that the extra time that is needed to calculate the adjoint sensitivities is acceptable. Figure 6.5 shows the evolution of the inter-resonator couplings and of the self-coupling during the tuning process. The figure shows that after 2 iterations, the coupling parameters are already very close to the target values. The last 2 iterations can be seen as fine tuning. Note that for clarity of the figure, we have not taken into account the sign of the inter-resonator couplings. Figure 6.6a shows the evolution of the 2-norm and the $\infty$-norm of the design error $\Delta \boldsymbol{m}$. Note

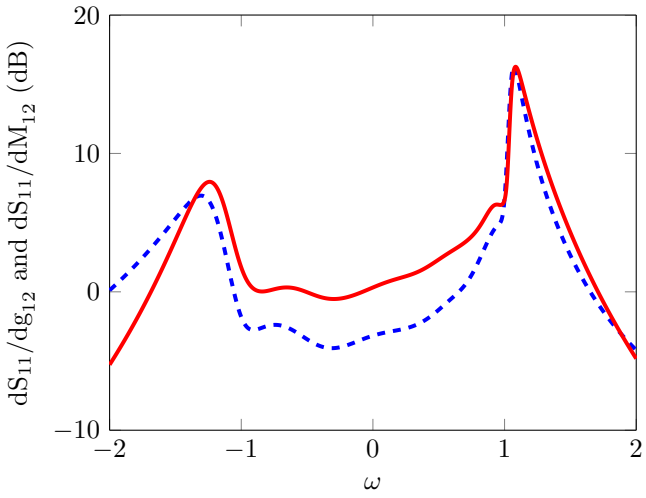


**(a)** Comparison between the adjoint sensitivities $|\frac{\partial S_{11}}{\partial M_{12}}|$ (—) and $|\frac{\partial S_{11}}{\partial d_{12}}|$ (- - -).

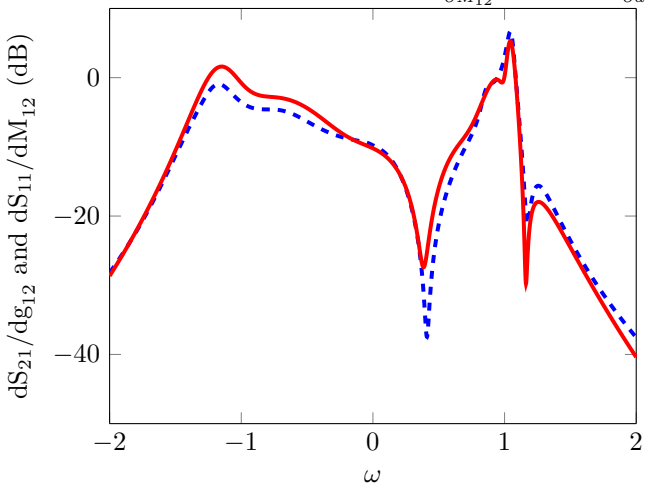


**(b)** Comparison between the adjoint sensitivities $|\frac{\partial S_{21}}{\partial M_{12}}|$ (—) and $|\frac{\partial S_{21}}{\partial d_{12}}|$ (- - -).

**Figure 6.3** Comparison between the adjoint sensitivities of the $S$-parameters with respect to the geometrical (- - -) and circuit or coupling parameters (—).

that $\infty$-norm is the smallest after iteration 2 (at simulation 3), meaning that the maximum difference with respect to the target value is the lowest at that iteration. However the 2-norm of the vector $\Delta \boldsymbol{m}$ is clearly minimal after the $4^{th}$ iteration. Figure 6.6b shows the evolution of the 2-norm and the $\infty$-norm of the correction vector $\Delta \boldsymbol{g}$ during the tuning process. The maximum correction proposed for the second iteration is larger than for the first, for the following

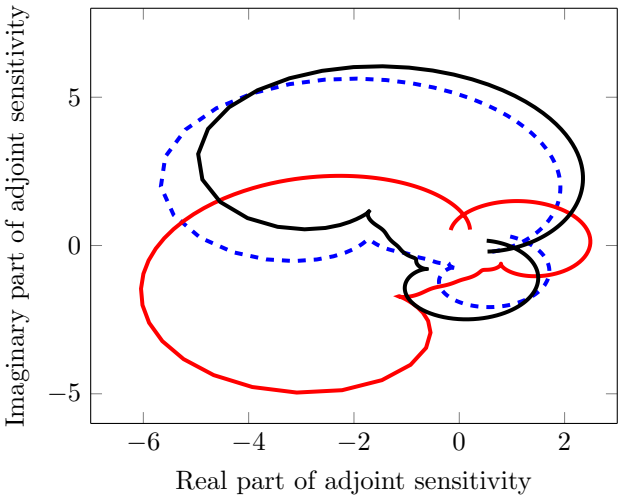


**Figure 6.4** Comparison between the adjoint sensitivities $\frac{\partial S_{11}}{\partial M_{12}}$ (—), $-j\frac{\partial S_{11}}{\partial M_{12}}$ (—) and $\frac{\partial S_{11}}{\partial d_{12}}$ (- - -).

iteration it clearly decreases. Note that these corrections are in mm. Finally remark that the TZs do not perfectly coincide. This is due to the presence of the unwanted parasitic couplings $M_{16}, M_{26}$ and $M_{36}$ (shown in Table 6.2). We have not re-distributed the parasitic couplings, so note that they are not necessarily physically located at those positions. Figure 6.7 shows the response that is obtained from the ideal coupling matrix when the parasitic couplings are added. It is clear that then the TZs now coincide. Note however that the parasitic couplings are small, we therefore choose not to re-optimize the target matrix.

| Parameter | Initial | Final | Target |
|---|---|---|---|
| $M_{S1}$ | 1.0605 | 1.0485 | 1.0422 |
| $M_{L8}$ | 1.0490 | 1.0407 | 1.0422 |
| $M_{12}$ | 0.9199 | 0.8342 | 0.8355 |
| $M_{23}$ | 0.4751 | 0.5800 | 0.5789 |
| $M_{13}$ | 0.2146 | 0.2768 | 0.2745 |
| $M_{34}$ | -0.1227 | -0.5993 | -0.5986 |
| $M_{45}$ | 0.4434 | 0.3552 | 0.3544 |
| $M_{56}$ | 0.4594 | 0.5944 | 0.5942 |
| $M_{46}$ | 0.7212 | 0.6449 | 0.6483 |
| $M_{11}$ | -0.0758 | 0.0385 | 0.0394 |
| $M_{22}$ | -0.7571 | -0.3351 | -0.3377 |
| $M_{33}$ | -0.1227 | 0.1066 | 0.1138 |
| $M_{44}$ | -0.0357 | 0.1411 | 0.1349 |
| $M_{55}$ | -0.8558 | -0.8155 | -0.8252 |
| $M_{66}$ | -0.3068 | 0.0349 | 0.0394 |
| $M_{SL}$ | 0 | -0.0001 | 0 |
| $M_{S6}$ | 0 | -0.0001 | 0 |
| $M_{L1}$ | 0 | -0.0001 | 0 |
| $M_{16}$ | -0.0010 | -0.0007 | 0 |
| $M_{26}$ | 0.0155 | 0.0133 | 0 |
| $M_{36}$ | 0.0036 | 0.0044 | 0 |

**Table 6.2** Extracted and target coupling parameters of the SOLR CT filter.

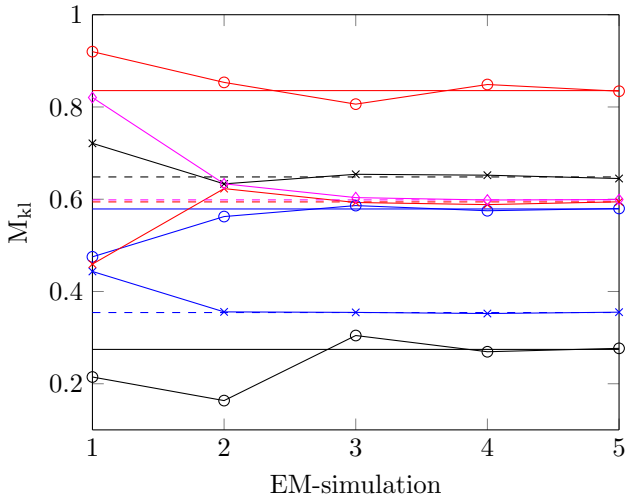


**(a)** Evolution of the inter-resonator couplings during the tuning process.

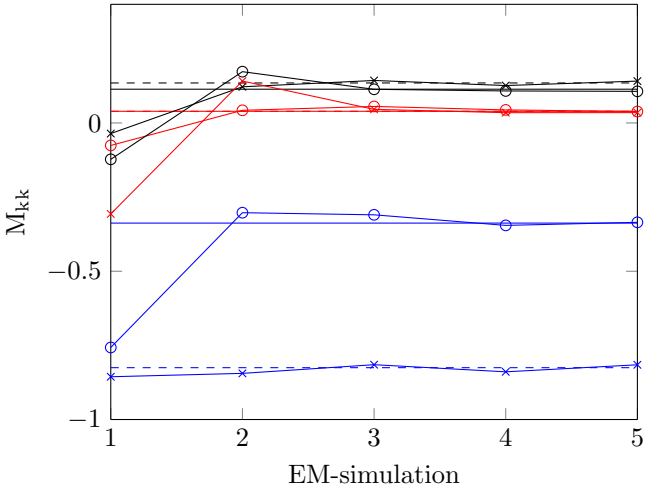


**(b)** Evolution of the self-couplings during the tuning process.

**Figure 6.5** Evolution of the coupling parameters during the tuning process. The full lines mark the target values of the first triplet and the dashed lines mark the target values of the second triplet.

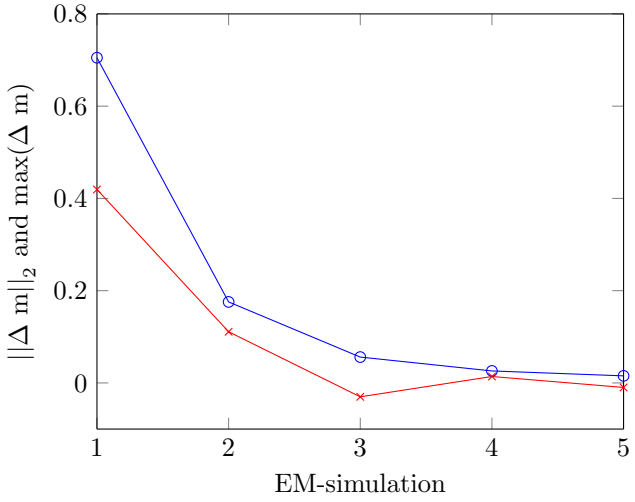


**(a)** The 2-norm of the error vector $\| \Delta \boldsymbol{m} \|_2$ (-o) and the maximal error $\| \Delta \boldsymbol{m} \|_\infty$ (-x).

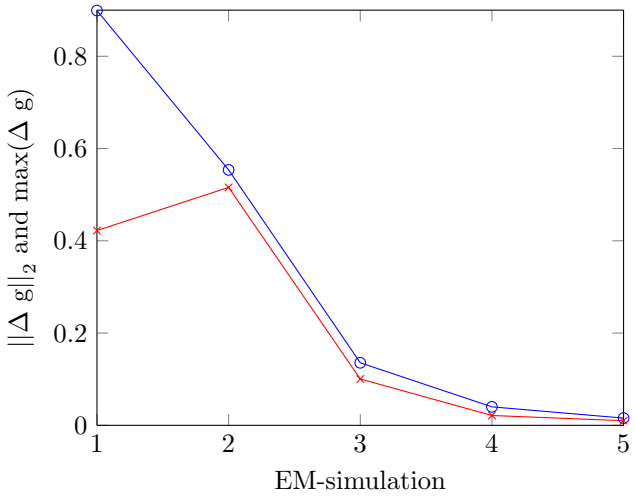


**(b)** The 2-norm of the correction vector $\| \Delta \boldsymbol{g} \|_2$ (-o) and the maximal correction $\| \Delta \boldsymbol{g} \|_\infty$ (-x) (mm).

**Figure 6.6** Evolution of the 2-norm and $\infty$-norm of the error vector $\Delta \boldsymbol{m}$ and the correction vector $\Delta \boldsymbol{g}$.

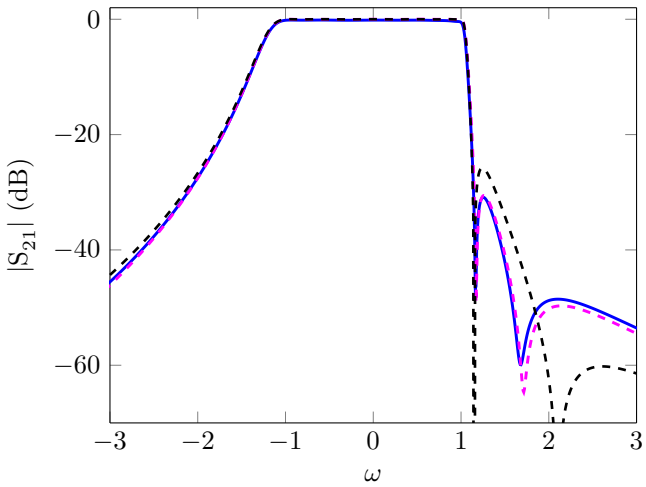


**Figure 6.7** $|S_{21}|$ (dB) of the final (—) design and response obtained from the ideal coupling matrix (- - -) when the parasitic couplings are added versus the ideal response (- - -).

## 6.8 Tuning of a SQ filter

In this section the tuning method is applied to the design of a SQ filter. In this type of filter the parasitics affects the response more than in the case of the CT filter. Therefore we will re-optimize the target matrix during the tuning procedure. The filter is designed to have center frequency $f_c = 1.2$ GHz, a fractional bandwidth $FBW = 0.04$, a return loss of 22 dB and 1 symmetric TZ pair at $\omega = \pm 1.5$. The filter is implemented on a RO4360 substrate with a thickness of 1.016 mm and $\varepsilon_r = 6.15$. To implement the $\frac{\lambda}{2}$-resonators we use SOLR structures. The filter has the same lay-out as the example discussed in Section 3.6 (Figure 3.14). The target coupling matrix is given in Table 6.3. The initial values for the filter are generated using the design curves (Section 3.6) and are given in Table 6.4.

| Parameter | Initial | Iteration 1 | Target |
|---|---|---|---|
| $M_{S1}$ | 1.0654 | 1.0702 | 1.0580 |
| $M_{L4}$ | 1.0651 | 1.0337 | 1.0580 |
| $M_{12}$ | 0.8683 | 0.8352 | 0.8365 |
| $M_{23}$ | 0.9111 | 0.8766 | 0.8713 |
| $M_{34}$ | 0.8522 | 0.8393 | 0.8365 |
| $M_{14}$ | -0.4301 | -0.4058 | -0.4089 |
| $M_{11}$ | 0.1731 | 0.0033 | 0 |
| $M_{22}$ | 0.2837 | -0.0177 | 0 |
| $M_{33}$ | -0.0708 | 0.0232 | 0 |
| $M_{44}$ | 0.1733 | -0.0092 | 0 |
| $M_{SL}$ | 0.0081 | 0.0076 | 0 |
| $M_{S4}$ | 0.0118 | 0.0113 | 0 |
| $M_{L1}$ | 0.0118 | 0.0113 | 0 |
| $M_{24}$ | 0.1665 | 0.1471 | 0 |

**Table 6.3** Extracted and target coupling parameters of the SOLR SQ filter.

### 6.8.1 TUNING TO THE ORIGINAL TARGET MATRIX

In the first part of the tuning procedure, we tune the filter such that all of the coupling parameters are as close as possible to the target coupling matrix. Similarly as for the CT filter, we set the value of the minimal correction $\delta_{corr}$ to 0.01 mm. After one iteration, all of the inter-resonator couplings are very close to the target values (maximal difference is -0.0053) and $\| \Delta \boldsymbol{g}_{\boldsymbol{k}}^{d} \|_{\infty} = -0.0067$ mm. Moreover the values of the diagonal elements are also very close to target values (maximal difference is 0.0232). Table 6.3 shows however that the parasitic coupling $M_{34}$ has the same order of magnitude as the other inter-resonator

| Physical parameter | Initial Value (mm) | Iteration 1 (mm) |
|---|---|---|
| $a$ | 16.7 | 16.7 |
| $w$ | 1 | 1 |
| $t_1$ | 5 | 5 |
| $t_2$ | 5 | 5 |
| $d_{12}$ | 1.6 | 1.64 |
| $d_{23}$ | 2 | 2.13 |
| $d_{34}$ | 1.6 | 1.65 |
| $d_{14}$ | 1.7 | 1.75 |
| $g_1$ | 1.5 | 1.68 |
| $g_2$ | 1.5 | 1.83 |
| $g_3$ | 1.5 | 1.44 |
| $g_4$ | 1.5 | 1.69 |

**Table 6.4** Initial and final values for the physical design parameters of the SQ filter.

couplings present in the filter. Figure 6.8 shows $|S_{11}|$ and $|S_{21}|$ for the ideal response, the initial values and for the first iteration. One would say that the adjustments of the filter deteriorated the response of the filter. Note however that we have only tuned for the couplings present in the target coupling matrix, without taking into account the parasitic coupling $M_{24}$. If we add the observed value of $M_{24}$ to the ideal target matrix and look at the corresponding result, we observe that the response is very close to the observed response after iteration 1. There is however still an offset since the diagonal elements $M_{22}$ and $M_{33}$ are not sufficiently close to 0. Therefore it has no use to further tune towards the initial target coupling matrix that does not take into account the parasitic couplings. We thus re-optimize the target coupling matrix, taking into account the value of $M_{24}$ at iteration 1.

### 6.8.2 RE-OPTIMIZATION OF THE TARGET COUPLING MATRIX

The target coupling matrix is re-optimized using the method discussed in Section 6.5. This means that we only re-optimize the diagonal values of the target coupling matrix. The values of the re-optimized target matrix are given in Table 6.5. Figure 6.9 shows the response of iteration 2 and the re-optimized ideal response. The filter is now much closer to the ideal response as was the case both for the initial design and after iteration 1. Table 6.5 compares the extracted coupling parameters for iteration 2 to the re-optimized coupling parameters. The table shows that the implemented coupling parameters are very close to the re-optimized target values: the maximal difference is -0.0106. Figure 6.9 shows however that the implemented response does not match the re-optimized re-

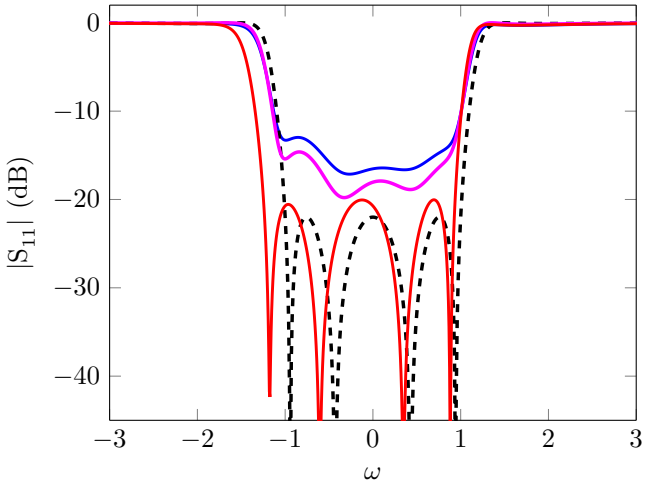


**(a)** $|S_{11}|$ for the initial design (—), after iteration 1 (—) and the ideal response without (- - -) and with parasitic couplings (—)

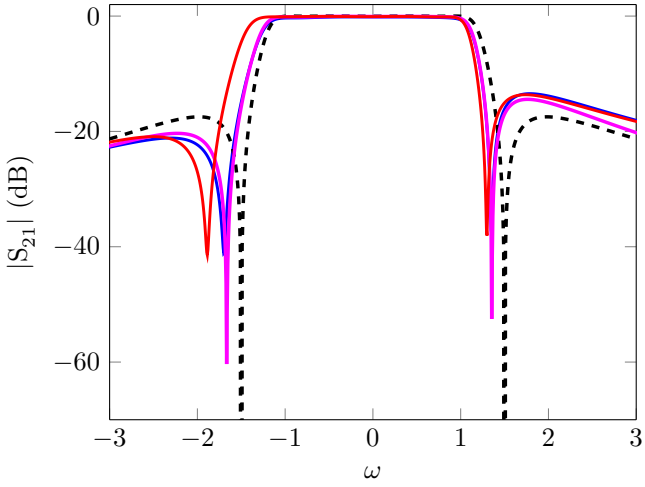


**(b)** $|S_{21}|$ for the initial design (—), after iteration 1 (—) and the ideal response without (- - -) and with parasitic couplings (—)

**Figure 6.8** $|S_{11}|$ and $|S_{21}|$ for the initial design, after iteration 1 and the ideal response with and without parasitic couplings.

sponse perfectly. This is due to the parasitic couplings, especially $M_{24}$ that also change due to the geometric adjustments. The maximum value of the proposed corrections is $\| \Delta \boldsymbol{g_k} \|_\infty = 0.0111$ mm, which is slightly higher than the value of $\delta_{corr} = 0.01$ mm. In this case we have terminated the tuning procedure since we can not predict how the parasitics will evolve after new adjustments. Moreover

we are very close to the target values. Finally note that $S_{21}$ of the re-optimized response attenuates less in the upper stopband when compared to the original ideal response.

| Parameter | Iteration 2 | Re-optimized Target | Target |
|---|---|---|---|
| $M_{S1}$ | 1.0703 | 1.0580 | 1.0580 |
| $M_{L4}$ | 1.0725 | 1.0337 | 1.0580 |
| $M_{12}$ | 0.8329 | 0.8365 | 0.8365 |
| $M_{23}$ | 0.8687 | 0.8713 | 0.8713 |
| $M_{34}$ | 0.8338 | 0.8365 | 0.8365 |
| $M_{14}$ | -0.4107 | -0.4089 | -0.4089 |
| $M_{11}$ | -0.0090 | -0.0069 | 0 |
| $M_{22}$ | 0.0501 | 0.0396 | 0 |
| $M_{33}$ | -0.2169 | -0.2119 | 0 |
| $M_{44}$ | -0.0521 | -0.0491 | 0 |
| $M_{SL}$ | 0.0077 | 0.0076 | 0 |
| $M_{S4}$ | 0.0114 | 0.0113 | 0 |
| $M_{L1}$ | 0.0114 | 0.0113 | 0 |
| $M_{24}$ | 0.1514 | 0.1471 | 0 |

**Table 6.5** The extracted coupling parameters for iteration 2, the original target and the re-optimized target matrix.

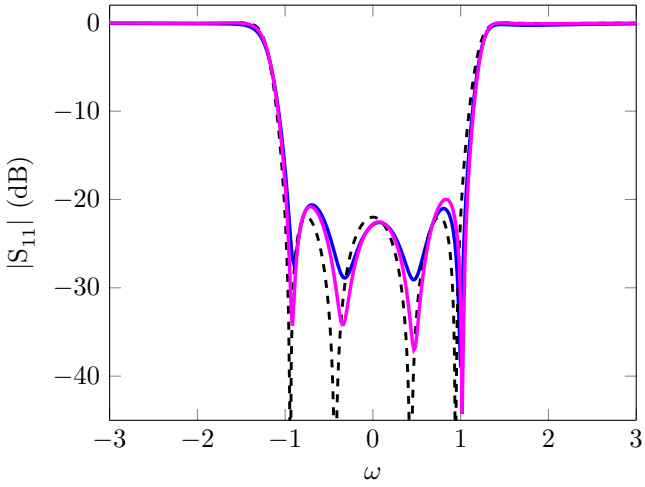


**(a)** $|S_{11}|$ for iteration 2 (—), the ideal response (- - -) and the target re-optimized for the parasitic couplings (—).

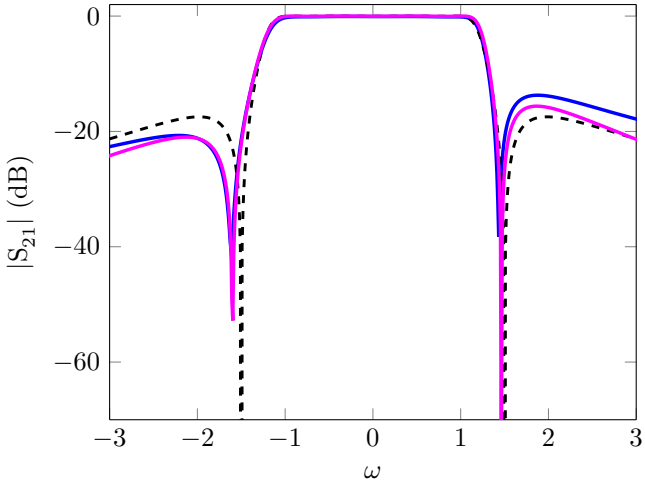


**(b)** $|S_{21}|$ for iteration 2 (—), the ideal response (- - -) and the target re-optimized for the parasitic couplings (—).

**Figure 6.9** $|S_{11}|$ and $|S_{21}|$ iteration 2, the ideal response and the target re-optimized for the parasitic couplings.

## 6.9 Discussion

The major benefit of using a coupling matrix based cost function is that in the vicinity of the solution the Jacobian matrix of the function relating the design parameters to the coupling parameters is almost diagonal. This makes that a certain coupling parameter mainly depends of one design parameter and is

practically independent of the other design parameters. Moreover it is known that coupling parameter behaves more or less quadratic as a function of the design parameters [Amar 06]. Therefore the tuning algorithm requires only a few iterations. Moreover there are no local minima in the region where the extracted coupling matrix models the filter behavior well. This is a major advantage with respect to other tuning methods based on pole-zero matching [Koza 02], which optimize a cost function based on the position of the poles and the zeros. The relation between the poles and zeros and the design parameters is more complex than the relation between physically implemented couplings and the design parameters. Thus there is no guarantee that there are no local minima in the vicinity of the solution.

## 6.10 Remarks

The first remark is related to the implementation of the tuning procedure in Matlab. Due to a bug in CST [CST 15], it was necessary to divide the adjoint sensitivity of the $S$-parameters with respect to the geometrical parameters (provided by CST) by 2. CST has guaranteed that in the future version this error will be resolved. We must remark that in the case the *Fast reduced order model* simulation setting is used, the adjoint sensitivities are correct.

The second remark has to do with the simulation time. At the moment it is rather high. This is mainly due to the adaptive meshing which takes almost half of the simulation time. We plan to investigate how we can decrease the required simulation time without loosing accuracy.

As a final remark, we point out that at the moment the method can not be used to tune the input-to-first-resonator and output-to-$N^{th}$-resonator coupling. The reason for that is that it is not possible to obtain the adjoint sensitivity with respect to parameters that touch the ports.

## 6.11 Conclusion

This chapter presents a novel CAT method based on the estimation of the Jacobian matrix relating the physical design parameters to the physically implemented coupling matrix. The main novelty of the method is the estimation of the Jacobian matrix of the coupling parameters with respect to the physical design parameters using adjoint sensitivities. To estimate the Jacobian one EM-simulation suffices. This is a vast improvement over the finite difference evaluation where an extra EM-simulation is needed for each physical design

parameter. Note that an EM-simulation with adjoint sensitivities requires more time than a simulation without. Nevertheless this does not drastically increase the simulation time. Another benefit of the Jacobian estimation method is that it offers a criterion to determine the physically implemented coupling matrix in the case of non-canonical topologies. The novel CAT method is used to tune a $6^{th}$ order CT and $4^{th}$ order SQ filter. Both examples shows that knowledge of the Jacobian matrix drastically decreases the number of EM-simulations required to tune the filter. For the CT filter 4 iterations (5 EM-simulation) suffice, where the filter has 13 design parameters. Note that an estimation of the Jacobian using finite differences would already take 13 extra EM-simulations. In the example of SQ filter, the target coupling matrix had to be re-optimized due to the presence of strong parasitic couplings. Nevertheless the tuning only required 2 iterations (3 EM-simulations). Note that the proposed strategy to handle parasitic couplings must be further improved in the future, since it does not take into account the fact that parasitic couplings also change due to adjustments of the physical parameters. We may conclude that this method is an ideal candidate for EM-based fine-tuning of coupled resonator bandpass filters.

# PART II

## Metamodel Approach

# 7

# Efficient and Automated Generation of Multidimensional Design Curves using Metamodels

This chapter introduces a method to automatically generate multidimensional design curves for the initial dimensioning of coupled-resonator filters. As we have seen in Chapter 3, these curves are look-up tables that relate the inter-resonator couplings and the input and output couplings (or external quality factors) to the physical design parameters of the filters. To minimize the number of EM simulations required for the generation of the curves, these curves often consider only a single design parameter. In reality, several design parameters simultaneously influence the inter-resonator coupling and external quality factors. In this chapter, a metamodeling method is used to generate multidimensional design curves with a reasonable number of EM simulations, while maintaining a good accuracy. The generation process only requires one to provide ranges of the design parameters over which the curves are generated. This information is readily available based on geometric and process related arguments. The remainder of the generation process requires no further user interaction. To show the applicability of the method, we generate design curves for the design of a coupled hairpin resonator filter. We use the extracted curves to generate initial values for a $5^{th}$ order filter for 3 different design scenarios.

## 7.1 Introduction

In Chapter 3 a method to generate initial values for coupled-resonator bandpass filters was introduced. The method first divides the filter into building blocks. Next, it dimensions these blocks separately and finally merges them together. The dimensioning of each individual block relies on design curves to relate the physical parameters to the coupling parameters [Pugl 00; Pugl 01]. The classical generation procedure of design curves (discussed in Section 3.5), first computes the frequency response function (FRF) of a building block (section of coupled

resonators or single input/output resonator) at a discrete set of frequency samples for some "well-chosen" values of a design parameter. For each value of the design parameter, the corresponding coupling parameter and external quality factor are extracted from the FRFs (the frequency-domain scattering parameters). This process yields sampled design curves (or look-up tables) on some kind of regular grid in the geometric parameters. As the FRFs are usually obtained using electromagnetic (EM) field solvers [Swan 07b], the design curve generation procedure often becomes very time-consuming.

To our knowledge, no real guidelines/techniques exist to determine the set of frequencies and the values of the design parameters the EM simulations that have to be selected to obtain design curves with a minimal number of the EM simulations and frequencies while the desired accuracy is preserved. Preferably, multiple design parameters should be considered in the design curves generation process. As a consequence, the number of EM simulations and therefore the design curves generation time grow very rapidly if some kind of regular grid is chosen for the geometrical parameters, even though many grid points bring only a limited amount of information.

Here, we propose an efficient and automated metamodel-based design curves generation procedure. It overcomes the limitations of the classical design curve generation procedure. A metamodel [Klei 08] is a very efficient representation of a multi-dimensional function that provides a functional relationship between input and output variables. In our case, these correspond to physical design parameters and the coupling parameters and external quality factors, respectively. Metamodels can have different basis functions: e.g. polynomial functions, radial basis functions, or splines [Klei 08]. Adaptive sampling methods [Wang 07] limit the amount of computationally expensive numerical simulations needed for the generation of metamodels while maintaining the coverage of the input space.

This chapter presents a metamodeling approach that automates and drastically speeds-up the generation of multidimensional design curves for microwave filters. The coupling parameter and the external quality factors of coupled-resonator filters are modeled as a function of multiple geometrical design parameter. To obtain it, a system identification approach is combined with an adaptive frequency sampling. This allows to efficiently and accurately extract the values of the coupling parameter and external quality factors over the complete design space using a set of design parameter values automatically chosen by the metamodeling adaptive sampling and starting from frequency-domain scattering parameters. The values of the coupling parameters extracted from the simulated

data are used for the generation of the metamodels. The user interaction is limited to providing the frequency range of interest, the design parameters of interest and their corresponding ranges. If the design parameters ranges are chosen wide enough to allow the modeling of all physically significant variations of the coupling parameter and external quality factor, then the design curves can be used for multiple design cases. Multidimensional design curves that depend on multiple design parameters can be generated in a reduced amount of time. This offers a significant flexibility to the designer while generating initial values for the filter design. The proposed metamodeling method is validated by the generation of the design curves of a coupled hairpin resonator filter. These curves are then used for multiple initial designs.

## 7.2 Generation of the Design Curves using Metamodels

This section describes the generation of metamodels linking the coupling parameters and the external quality factors to the geometrical parameters of the filter. In Section 3.5.1 we have seen how to extract the inter-resonator coupling from the magnitude of $|S_{21}|$. Equation (3.10) relates the peak frequencies $f_{p1}$ and $f_{p2}$ to the inter-resonator coupling $k_X$ (in the bandpass domain):

$$k_X = \pm \frac{f_{p2}^2 - f_{p1}^2}{f_{p2}^2 + f_{p1}^2} \tag{7.1}$$

Similarly we have derived an equation in Section 3.5.2 to determine the input/output coupling $M_{S1}^{'}$ (3.20) or external quality factor $Q_e$ (3.23) from the group delay of $S_{11}$ when looking at the resonant frequency $\tau_{S_{11}}(f_0)$. In this chapter we illustrate the method for the design of a coupled hairpin resonator filter.

In the literature it is common to use the external quality factor rather than the input/output coupling for such a filter. Therefore we will model $Q_e$ rather than $M_{S1}^{'}$. Figure 7.1 shows the building blocks of the considered hairpin resonator filter. We model the inter-resonator coupling $k_X$, the peak frequencies $f_{p1}$ and $f_{p2}$, the external quality factor $Q_e$ and the resonant frequency $f_0$. The values of $(k_X, f_{p1}, f_{p2}, Q_e, f_0)$ change if the geometrical design parameters, $t_1, l_1, l_2, w_1, w_2, h_1, h_2$ and $d_{12}$ as introduced in Figure 7.1 vary.

A metamodel $\boldsymbol{F}(\boldsymbol{x})$ is a model that describes the relationship between the inputs $\boldsymbol{x}$ (in our case the geometrical parameters of the filter) and outputs (response) $\boldsymbol{y}$ (in our case $(k_X, f_{p1}, f_{p2}, Q_e, f_0)$). Therefore, we derive a model $\boldsymbol{y} = \boldsymbol{F}(\boldsymbol{x})$.

A number of input-output data samples $[\boldsymbol{x}_k, \boldsymbol{y}_k]$, $k = 1, ..., K$ is needed to estimate and validate a metamodel. Two data grids can be used for this purpose in the modeling process, namely an *estimation* grid to build the metamodel and a *validation* grid to validate the it. The samples distribution in the estimation and validation grid are automated using adaptive sampling approaches for metamodels [Wang 07].

We generate two metamodels to describe the relationship between $(k_X, f_{p1}, f_{p2})$ and $(Q_e, f_0)$ (response variables) and the corresponding geometrical parameters (input variables). The response variables $(k_X, f_{p1}, f_{p2}, Q_e, f_0)$ taken at a generic design space sample $\boldsymbol{x}_k$ are extracted starting from the corresponding frequency-domain scattering parameters. The appropriate selection of the frequency-domain sampling grid is very important to obtain an accurate response in a small amount of time. When the frequency resolution is chosen too coarse to save computational resources (EM simulations are computationally expensive), the evaluation of the response variables is inaccurate. When a too dense frequency sampling is used the computational cost will increase without any gain in accuracy.

We propose to use a system identification approach to model the FRF data

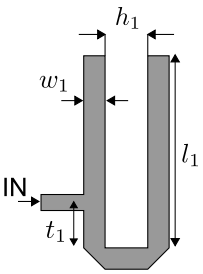


**(a)** Input/output hairpin resonator.

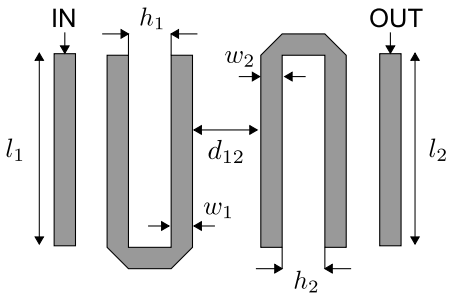


**(b)** Coupled hairpin resonator structure.

**Figure 7.1** Building blocks of a typical coupled hairpin resonator filter.

($S_{21}(j2\pi f_n)$ of two coupled resonators, $S_{11}(j2\pi f_n)$ of a singly loaded resonator) at each selected value of the design parameter vector $\boldsymbol{x}_k$. The design parameter vector $\boldsymbol{x}_k$ is chosen by the adaptive sampling method. Here, $f_n$ denotes a simulation frequency. This allows to obtain an efficient and accurate estimation of response variable. System identification methods [Pint 12] generate FRF models $\boldsymbol{H}_{model}(s)$ in different representations (e.g. pole-residue, pole-zero forms and state-space forms) to describe the frequency domain response of systems. Here, $s$ represents the Laplace variable. The sampling in the frequency-domain, used to provide FRF data samples to the system identification method at the selected frequencies, can be automated using adaptive sampling approaches to optimize the frequency grid density. Once the rational models are computed, they can efficiently be evaluated over a dense frequency grid to achieve an accurate estimation of the response variables $(k_X, f_{p1}, f_{p2}, Q_e, f_0)$.

Note that the metamodel adaptive sampling in the design parameters space (input space of a metamodel) allows to reduce the number of EM simulations, while the adaptive sampling in the frequency-domain allows to reduce the number of frequency samples at which the response is simulated in each EM simulation. The combination of these adaptive sampling schemes drastically reduces the required computational cost for the generation of multidimensional design curves.

Next, we recast the main steps of the proposed metamodeling technique: Once the value of the design parameter vector $\boldsymbol{x}_k$ is chosen by the adaptive sampling method. The corresponding structure is simulated yielding the response $\boldsymbol{H}_{data}(j2\pi f_n, \boldsymbol{x}_k)$. Next a pole-residue form is identified for this data $\boldsymbol{H}_{model}(s, \boldsymbol{x}_k)$ using the well known Vector Fitting identification technique [Gust 99; Gust 06]. Next the response variables of interest (e.g. the coupling coefficient $k_X$) are extracted from the identified model $\boldsymbol{H}_{model}(s, \boldsymbol{x}_k)$. This process is repeated iteratively until the desired accuracy is met. These main steps are listed below:

$$\boldsymbol{H}_{data}(j2\pi f_n, \boldsymbol{x}_k) \xrightarrow{system\ identification} \boldsymbol{H}_{model}(s, \boldsymbol{x}_k)$$

$$\boldsymbol{H}_{model}(s, \boldsymbol{x}_k) = \sum_{p=1}^{P(\boldsymbol{x}_k)} \frac{\boldsymbol{C}_p(\boldsymbol{x}_k)}{s - a_p(\boldsymbol{x}_k)} + \boldsymbol{D}(\boldsymbol{x}_k)$$

$$\boldsymbol{H}_{model}(s, \boldsymbol{x}_k) \xrightarrow{extraction} \boldsymbol{y}_k = \boldsymbol{y}(\boldsymbol{x}_k)$$

$$(\boldsymbol{x}_k, \boldsymbol{y}_k) \xrightarrow{metamodel} \boldsymbol{F}(\boldsymbol{x})$$

$$f_n(\text{chosen by adaptive frequency sampling})$$

$$\boldsymbol{x}_k(\text{chosen by metamodel adaptive sampling})$$

Note that $\boldsymbol{H}_{data}$ denotes the FRF data $S_{21}$ of two coupled resonators and $S_{11}$ of a singled loaded resonator. The matrix $\boldsymbol{C}_p$ is $2 \times 2$ matrix that contains the residues of the pole $a_p$ and the matrix $\boldsymbol{D}$ is $2 \times 2$ matrix that contains the direct terms.

## 7.3 Example: Hairpin Resonator Filter

This section validates the proposed metamodeling technique for the generation of multidimensional design curves of a 5-th order coupled hairpin resonator filter (Figure 7.2). The extracted design curves are then used for the design of multiple $5^{th}$ order Chebyshev filters with the center frequency $f_c$ in the range $[1.8 - 2.2]$ GHz and a fractional bandwidth $FBW = \frac{f_2 - f_1}{f_c}$ (where $f_1$ and $f_2$ are the equiripple cutoff frequencies) in the range $[0.08 - 0.12]$.

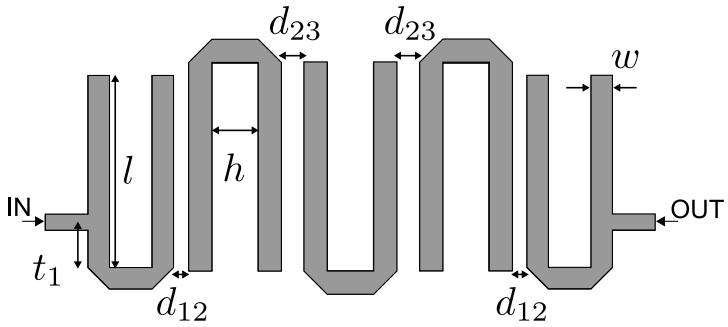


**Figure 7.2** Top-view of the layout of a $5^{th}$ order hairpin resonator filter.

The single resonator structure (Figure 7.1a) is used in order to model $Q_e$ and $f_0$ as a function of the position of the feed line $t$, the length of the legs of the

hairpin $l_1$, and the spacing between the legs $h_1$. Since the tapping position $t_1$ mainly affects $Q_e$, its range is chosen wide enough to have variations of $Q_e$ that enable the use of the corresponding design curve in multiple design scenarios. The range is set equal to $t_1 = [2 - 7]$ mm. The resonant frequency $f_0$ is mainly affected by the total length of the hairpin. Since we want $f_c$ to vary in the range $[1.8 - 2.2]$ GHz, the ranges for $h_1$ and $l_1$ are chosen equal to $h_1 = [1.5 - 3]$ mm and $l_1 = [15 - 20]$ mm in order to keep $f_0$ within the $f_c$ range. The width $w_1$ is equal to 1 mm. Figure 7.3 shows the variations of $Q_e$ as a function of $t$ and $l_1$ for two different values of $h_1$.

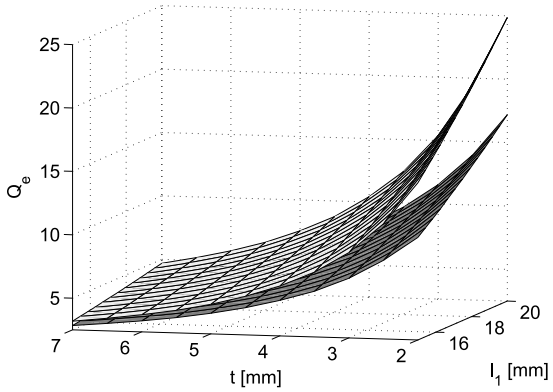


**Figure 7.3** Design curve: $Q_e$ as a function of $t$ and $l_1$ for $h_1 = 1.5$ mm (light gray) and $h_1 = 3$ mm (dark gray).

The coupled resonator pair (Figure 7.1b) is used in order to model $(k_X, f_{p1}, f_{p2})$ as a function of the distance between the resonators $d_{12}$, the line width $w_1 = w_2$, the length of the legs of the hairpin $l_1 = l_2$, and the spacing between the legs $h_1 = h_2$. Since the coupling parameter $k_X$ is mainly affected by $d_{12}$, its range is chosen wide enough $d_{12} = [0.1{-}1.5]$ mm to handle multiple design scenarios. The design parameter $w_1$ also affects the coupling. To increase our design freedom, we also include a width range $w_1 = w_2 = [0.8 - 1.2]$ mm that is chosen to have a trade-off between a change of the characteristic impedance (50 Ω) and the effect on the coupling. For the ranges of $h_1 = h_2$ and $l_1 = l_2$ the reasoning of the single resonator case is reused. The ranges are set equal to $h_1 = [1.5 - 3]$ mm and $l_1 = [16 - 21]$ mm. The single resonator is more heavily loaded (due to the feed line) and this loading effect reduces the resonant frequency slightly. Figure 7.4 shows the variations of $k_X$ as a function of $d_{12}$ and $h_1$ for a value of $l_1$ and two different values of $w_1$.

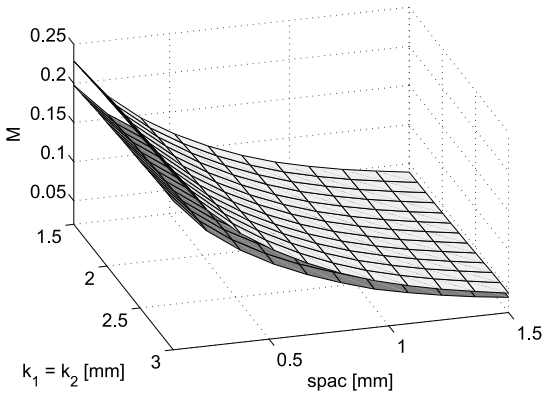


**Figure 7.4** Design curve: $k_X$ as a function of $h_1$ and $d_{12}$ for $l_1 = 19.75$ mm and $w_1 = 0.8$ mm (light gray) and $w_1 = 1.2$ mm (dark gray).

All numerical experiments use Matlab R2014A and ADS Momentum EM solver [ADS 14] and run on a Windows platform equipped with Intel Core $i7 - 4770$ 3.40GHz CPU and 8 GB RAM.

The metamodels for this example describe the output variables $(M, f_{p1}, f_{p2})$ and $(Q_e, f_0)$ as a function of the corresponding input variables (geometrical design parameters) defined above. The metamodels are generated using the sparse grid interpolation schemes with adaptive sampling proposed in [Klim 05; Klim 07]. The quality of the metamodels is judged based on an error measure. It is defined as the absolute error of the modeled quantity (e.g. $M$) divided by the difference between the maximum and minimum value of this quantity over the range for which the quantity is modeled. A maximum error equal to 0.01 is desired. We have used the built-in adaptive frequency sampling of the ADS Momentum [ADS 14] to efficiently sample the scattering parameters response of the coupled resonator and single loaded resonator structures in the frequency-domain. The Vector Fitting system identification method [Gust 99] has been used to build pole-residue rational models of $S_{21}(j2\pi f)$ and $S_{11}(j2\pi f)$ of these two structures. These rational models have been evaluated over a dense frequency grid of 1001 samples to extract the response variables data samples of $(M, f_{p1}, f_{p2})$ and $(Q_e, f_0)$. This is repeated at each value of the design parameters chosen by the adaptive sampling process [Klim 05; Klim 07] in the design space.

The adaptive sampling method [Klim 05; Klim 07] has required 157 samples to generate the metamodels of $(M, f_{p1}, f_{p2})$ and 121 samples for the model of $(Q_e, f_0)$ with a maximum error equal to 0.01. The average CPU time needed to

extract the data samples of $(M, f_{p1}, f_{p2})$ and $(Q_e, f_0)$ in a design space point from EM simulations (with adaptive frequency sampling and Vector Fitting models) is equal to 7.4 s and 3.8 s respectively. The overall CPU time needed to build the metamodels of $(M, f_{p1}, f_{p2})$ and $(Q_e, f_0)$ is equal to 20 m 4 s and 6 m 47 s, respectively.

The average CPU time needed to evaluate the built metamodels of $(M, f_{p1}, f_{p2})$ and $(Q_e, f_0)$ in a design space point is equal to 0.64 ms and 0.28 ms. When we compare this to the classical design curves generation method to generate 4-D design curves on regular grid for $(M, f_{p1}, f_{p2})$ taking 5 samples for each design parameter in the design space $(d_{12}, w_1 = w_2, l_1 = l_2, h_1 = h_2)$, this would already require $5^4 = 625$ samples (therefore 625 EM simulations). This is more than two times the amount of samples needed to generate the metamodels of $(M, f_{p1}, f_{p2})$ and $(Q_e, f_0)$ with the proposed approach. Moreover, in the classical approach the user has no idea whether the frequency axis and the design space are over- or under-sampled and has no clue about the level of accuracy achieved.

The 4-D and 3-D metamodel-based design curves of $(M, f_{p1}, f_{p2})$ and $(Q_e, f_0)$ are finally used to obtain design parameters values for three different design scenarios with the following specifications:

1. *Design 1*: $f_c = 1.9$ GHz, $FBW = 0.12$, passband ripple = 0.1 dB ($RL =$ 16.43 dB)
2. *Design 2*: $f_c = 2$ GHz, $FBW = 0.8$, passband ripple = 0.1 dB ($RL =$ 16.43 dB)
3. *Design 3*: $f_c = 2.1$ GHz, $FBW = 0.1$, passband ripple = 0.1 dB ($RL =$ 16.43 dB)

Figure 7.5 shows the scattering parameters of the 5-th order filter after an initial dimensioning based on the metamodel-based design curves for each design scenario. In the three design scenarios, the difference between the desired and actual $FBW$ is less than 0.005 and there is a small shift of the center frequency $f_c$. When we compare these results to other initial designs found in the literature [Hong 01], we observe a similar quality of the initial designs. In order to have an idea of the difference between the implemented and ideal coupling parameters in the bandpass domain we extract the coupling matrices using the method discussed in Chapter 4. Table 7.1 compares the extracted and ideal couplings for the 3 designs. For *Design 1* we observe an maximum relative error of 0.0428. The relative error on $Q_e$ is 0.0033. The frequency shift with respect

to $f_c$ explains the presence of non-zero self-couplings, which are relatively small. For *Design 2* we observe a similar relative error for the inter-resonator couplings of 0.0169. The error on the external quality factor is 0.0362. There is also a frequency shift, but this shift is smaller. Note that the inter-resonator couplings are smaller for this example, because of the narrower bandwidth. This results in larger distances between the resonators. Therefore the loading on the resonators is smaller and thus the frequency shift is expected to be smaller. This is what we observe. For *Design 3* we find a relative error of 0.0313 for the inter-resonator couplings and relative error 0.12 for the external quality factor. Nevertheless this error is still acceptably small for an initial design value.

The fact that the curves are multi-dimensional allows the designer to use them for several designs. An important parameter that is different for the three cases is the length of the legs $l_1$ and the distance between the legs $h_1$ of the hairpin resonator . These parameters also have an important effect on the coupling and thus on the inter-resonator spacings. In the classical approach the inter-resonator coupling curves would have to be re-extracted for every new value of $l_1$ and $h_1$.

| | *Design 1* | | *Design 2* | | *Design 3* | |
|---|---|---|---|---|---|---|
| Parameter | Extracted | Ideal | Extracted | Ideal | Extracted | Ideal |
| $Q_{e1}$ | 9.5251 | 9.5568 | 14.3352 | 13.8349 | 11.4681 | 13.0950 |
| $Q_{e2}$ | 9.5251 | 9.5568 | 14.3352 | 13.8347 | 11.4681 | 13.0947 |
| $M'_{12}$ | 0.0998 | 0.0957 | 0.0638 | 0.0649 | 0.0797 | 0.0823 |
| $M'_{23}$ | 0.0737 | 0.0729 | 0.0486 | 0.0492 | 0.0608 | 0.0627 |
| $M'_{34}$ | 0.0732 | 0.0729 | 0.0486 | 0.0492 | 0.0608 | 0.0627 |
| $M'_{45}$ | 0.0997 | 0.0957 | 0.0638 | 0.0649 | 0.0797 | 0.0823 |
| $M'_{11}$ | 0.0285 | 0 | 0 | 0.0197 | 0 | 0.0299 |
| $M'_{22}$ | 0.0269 | 0 | 0 | 0.0049 | 0 | 0.0130 |
| $M'_{33}$ | 0.0222 | 0 | 0 | 0.0113 | 0 | 0.0050 |
| $M'_{44}$ | 0.0335 | 0 | 0 | 0.0034 | 0 | 0.0152 |
| $M'_{55}$ | 0.0285 | 0 | 0 | 0.0197 | 0 | 0.0299 |

**Table 7.1** Extracted and ideal coupling parameters in the bandpass domain for the three designs.

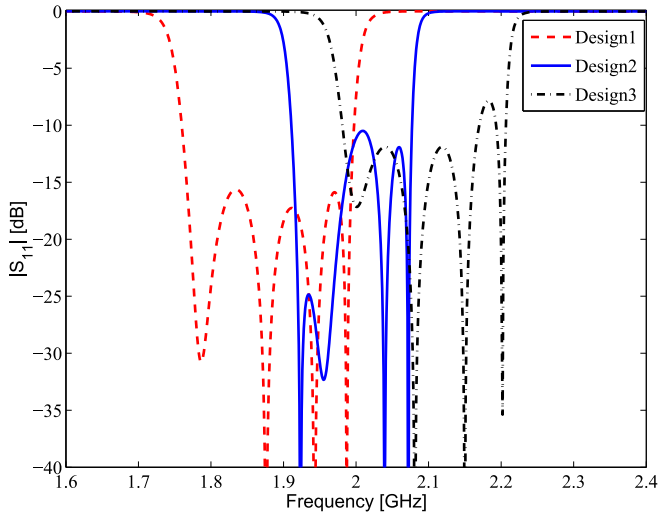


**(a)** $|S_{11}|$ for the different initial designs.

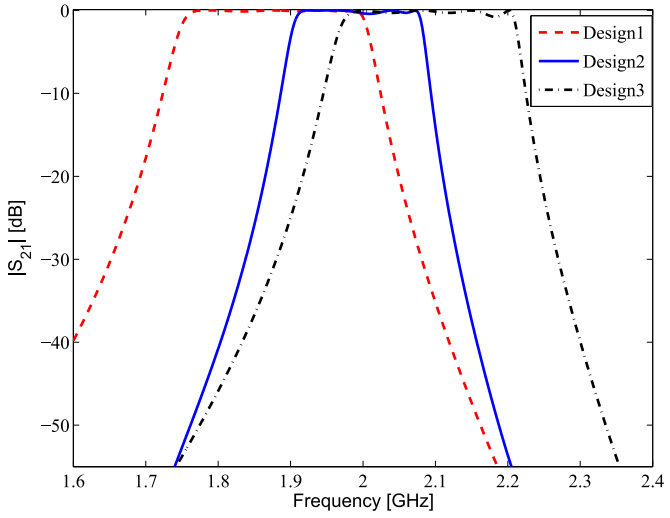


**(b)** $|S_{21}|$ for the different initial designs.

**Figure 7.5** $|S_{11}|$ and $|S_{21}|$ for the initial values of the different design scenarios.

## 7.4 Conclusion

This chapter introduces a metamodeling approach for an efficient and automated generation of multidimensional design curves for coupled-resonator bandpass filters. Adaptive sampling approaches are used to minimize the number of EM-simulations and the number of frequency samples per EM-simulation needed to generate the metamodels that represent the design curves. The only required user interaction is the choice of the ranges of the frequency and of the design parameters. Large variations of multiple design parameters can be taken into account, which allows one to use the design curves in multiple design scenarios. These large variations come at a cost of a higher time to generate the curves. Also when the number of design parameters grows, the time needed to generate the curves increases very fast as well. This is known as the curse of dimensionality. In this application however the number of design parameters is typically low, since the filter is divided into its individual building blocks and each block is modeled separately.

The numerical results have confirmed the efficiency, accuracy and flexibility of the proposed methodology. Multidimensional design curves based on efficient metamodels whose generation is fully automated are a powerful design tool that allows designers to efficiently explore multiple design scenarios and significantly save computational resources during the design flow.

# 8

# A Scalable Macromodeling Methodology for the Efficient Design of Microwave Filters

This chapter introduces a novel computer-aided design (CAD) methodology for microwave filters. The methodology uses scalable macromodels to model the behavior of the $S$-parameters as a function of the physical design parameters of the filter. The physical parameters are varied over a well chosen range of values. The benefit of a scalable macromodel is that they are numerically cheap to evaluate. Once the model is generated, it can thus be used to optimize the filter design parameters to meet the specifications. If the ranges of the design parameters are chosen sufficiently broad, the model can be reused in multiple design scenarios. So far the inclusion of scalable macromodels in the design cycle of microwave filters has not been studied and discussed in the literature.

In this chapter, we show that scalable macromodels can be included in the design cycle of microwave filters and can be reused in multiple designs at a low computational cost. We give guidelines to properly generate and use these scalable macromodels in a filter design context. We illustrate the approach on a state-of-the-art design example: a microstrip dual-band bandpass filter with closely spaced passbands and a complex geometrical structure. The results confirm that scalable macromodels can indeed be used as proper design tools and represent an efficient and accurate alternative to the mainstream, but computationally expensive EM simulator-based design flow. The work discussed in this chapter has been published in [Caen 16].

## 8.1 Introduction

Over the last years several methods have been developed to improve the design of microwave filters [Levy 02; Swan 07a]. Design techniques based on design curves are shown to yield relatively good initial designs. However most de-

sign curve based filters, require post-processing and fine-tuning to meet the desired frequency template specifications. The fine-tuning process involves numerical optimization and is based on multiple accurate electromagnetic (EM) simulations. Accuracy comes at a price however, these solvers are known to be computationally expensive and hence time consuming. Even though most optimization methods [Band 94b; Arnd 04; Koza 02; Lamp 04; Koza 06] yield accurate designs, their design time grows linearly with the number of filters to be designed. Even though the layout if similar. This is a consequence of the optimization towards a single set of specifications. If the specifications change, the complete process must be redone.

To speed up the design process, we propose to replace the EM solver by a computationally efficient scalable frequency response macromodel. In this chapter, scalable (or parametric) macromodels are used as a compromise between model accuracy and complexity. Generating scalable macromodels to represent the parameterized response of microwave systems as a function of frequency and additional design parameters such as geometrical variables and material properties, is an active field of research [Peik 98; Lame 03; Cuyt 06; Deva 03; Lame 09; Basl 10; Lehm 01; Triv 09; Ferr 09; Ferr 10; Triv 10; Ferr 11; Ferr 12]. The two main advantages of using scalable macromodels in the design process are:

1. The scalable macromodels replace the expensive EM solver to evaluate the filter response as a function of the frequency and the design parameters of interest (e.g. geometrical parameters) over certain predefined ranges. Therefore, these scalable macromodels can be used in different optimization scenarios where changes in the specifications of the filter (e.g. the bandwidth of interest, the selectivity, etc.) need to be examined.

2. The scalable macromodels can also be used to speed up other computationally expensive design activities, such as design exploration and design variability analysis. Design space exploration leads to an understanding of the filter behavior with respect to design parameters. Design variability analysis evaluates the system reliability. Since macromodels are quite cheap to evaluate and also accurate enough to properly capture the effects of the design parameter variations on the filter frequency response, they increase the time-efficiency of these design tasks.

Even though the extraction of scalable macromodels can easily be automated using sequential sampling approaches [Chem 14b], it still requires the designer to specify additional information. For example, the designer must select ranges

for the design parameters, for which the model is then built to be accurate over these ranges. For a first design the model must thus be extracted during the design process itself. Note that once it is extracted it can be used to optimize filters having the same physical structure for different design specifications.

In this chapter, we show how to include scalable macromodels in the design cycle of microwave filters. We give guidelines to properly generate and use scalable macromodels in a filter design context. The focus is put on the practical use of scalable macromodels for design purposes. We show that scalable macromodels can be reused to optimize the design of different filters to meet multiple sets of specifications. This distinguishes the proposed method from existing model-based optimization methods and breaks the linear growth of the extraction time with respect to the number of designs. This is a major difference with respect to the approach used in [Kozi 06; Kozi 10b; Kozi 10a; Couc 10; Couc 12] that aims at optimizing a particular performance measure for a particular design. This leads to restart the modeling step for optimization each time the specifications are changed. To summarize, this chapter explains how scalable macromodels can effectively and practically be used by designers to speed-up the design flow, while still achieving accurate results.

We have chosen a state-of-the-art design example: a microstrip dual-band band-pass filter described as it is described in [Hsu 13] is used to illustrate our approach. In [Hsu 13], a design method is presented to adjust the center frequency, the bandwidth, the position of the transmission zeros and the desired ratio of the resonant frequency of the two passbands. This filter consists of two coupled unequal length shunted-line stepped impedance resonators. The example nicely illustrates the proposed macromodel-based design approach, since the design parameters are all coupled and optimization of the design is therefore necessary on all parameters simultaneously.

Section 8.2 describes a state-of-the-art scalable macromodeling method for an automated model generation. To speed-up the generation process, a sampling algorithm [Chem 14b] is used to gather data samples located at spots in the design space where the response changes rapidly.

## 8.2 Scalable Macromodels for Microwave Filters

This section introduces a state-of-the-art scalable macromodeling technique that is coupled to a sequential sampling algorithm to obtain an automated model generation framework for microwave filters.

### 8.2.1 BUILDING A SCALABLE MACROMODEL FROM DATA SAMPLES GENERATED BY EM SOLVERS

The first step needed for the scalable macromodeling process is to generate data samples used to train the model. A set of multivariate data samples $\{(s_n, \boldsymbol{g_k}), \boldsymbol{H}(s_n, \boldsymbol{g_k})\}$ $(n \in \{1, \ldots, n_F\},\ k \in \{1, \ldots, n_g\})$ represents a set of parameter-dependent frequency-domain responses. This data set depends on the Laplace variable or complex frequency $s = j\Omega = j2\pi f$ and also on an additional set of $n_g$ physical design variables $\boldsymbol{g} = (g_1, \ldots, g_{n_g})$. Note that $f$ is the physical frequency in the bandpass domain. The region in the parameter space that contains the selected parameters $\boldsymbol{g}$ is called the design space.

For filter structures, these design variables describe the geometry of the system that a designer varies during the design. The data samples $\{(s_n, \boldsymbol{g_k}), \boldsymbol{H}(s_n, \boldsymbol{g_k})\}$ are used to generate a scalable macromodel. The model needs to be able to efficiently and accurately describe the parameterized behavior of the system under study.

Similarly to what was done in Chapter 7 the data samples are divided into two datasets: an estimation set and a validation set. The estimation set is utilized to build a scalable macromodel. The validation set is used to validate the model accuracy in design space points that were not used for the model generation. An efficient sampling algorithm [Chem 14b] is used to gather data samples located at maximally informative design space positions automatically. Spots in the design space where the response changes rapidly are sampled more densely, while the total number of data samples is minimized as much as possible. The algorithm is briefly described in Section 8.2.2. In [Chem 14b], the sequential sampling algorithm is used to automatically gather the data for the generation of scalable macromodels [Ferr 11; Ferr 12]. These modeling methods [Ferr 11; Ferr 12] are based on the use of interpolation of transfer functions and the use of scaling coefficients. Recently, a scalable macromodeling approach has been proposed in [Chem 14a] to enhance the modeling capability of [Ferr 11; Ferr 12] by using multiple frequency scaling coefficients.

In this work, we use the scalable macromodeling technique [Chem 14a] and combine it with the sequential sampling method [Chem 14b]. This is an important step to allow automating the generation of scalable macromodels and reducing the effort and prior knowledge needed by designers to use scalable macromodels as a design tool. The corresponding main modeling steps are recalled briefly in what follows. The reader can refer to [Ferr 11; Ferr 12; Chem 14a] for a more detailed explanation. The idea is to use $n_g$ dimensional hyper-rectangular

($n_g$-box) regions as a building block for the design space. The design space is decomposed in a concatenation of several hyper-rectangular regions. These are denoted as $\Psi_l$, $l \in \{1, \ldots, L\}$.

Each $\Psi_l$ regions contain $2^{n_g}$ frequency-dependent rational models, called *root macromodels* at the corresponding corner points. Note that the Laplace variable $s$ is not considered to be part of the design space. It is modeled separately as the *root macromodels* are rational pole-residue models of the Laplace variable, representing the frequency response functions (FRFs).

These *root macromodels* are identified given the estimation data samples $\{(s_n, \boldsymbol{g}_k), \boldsymbol{H}(s_n, \boldsymbol{g}_k)\}$ using the well known Vector Fitting identification technique [Gust 99; Gust 06]. The *root macromodels* $\boldsymbol{R}^{\Psi_l}(s, \boldsymbol{g}_i{}^{\Psi_l})$, $i \in \{1, \ldots, 2^{n_g}\}$ contained in an $n_g$-box region $\Psi_l$ are represented next in a pole-residue form as

$$\boldsymbol{R}^{\Psi_l}(s, \boldsymbol{g}_i{}^{\Psi_l}) = \sum_{p=1}^{P_i^{\Psi_l}} \frac{\boldsymbol{C}_{p,i}^{\Psi_l}}{s - a_{p,i}^{\Psi_l}} + \boldsymbol{D}_i^{\Psi_l} \tag{8.1}$$

where $\boldsymbol{C}_{p,i}^{\Psi_l}$ represents the residue matrices, $a_{p,i}^{\Psi_l}$ denotes the poles and $\boldsymbol{D}_i^{\Psi_l}$ is the direct-term matrix, where $\boldsymbol{C}_{p,i}^{\Psi_l}, \boldsymbol{D}_i^{\Psi_l} \in \mathbb{R}^(2 \times 2)$.

For each $n_g$-box region $\Psi_l$ a set of amplitude and frequency scaling coefficients is computed. An interpolation of the FRFs and the scaling coefficients is used to generate a scalable macromodel $\boldsymbol{R}^{\Psi_l}(s, \boldsymbol{g})$ [Ferr 11; Ferr 12; Chem 14a] that preserves the passivity and the stability. To evaluate the accuracy of the model in every $n_g$-box region of the design space at the corresponding validation points, we use The Mean Absolute Error (MAE) $E^{MAE}$:

$$E^{MAE}(\boldsymbol{g}) = \max_{u \in \{1,\ldots,P\}, v \in \{1,\ldots,P\}} \frac{1}{N_F} \left( \sum_{n=1}^{N_F} |R_{u,v}(s_n, \boldsymbol{g}) - H_{u,v}(s_n, \boldsymbol{g})| \right) \tag{8.2}$$

where $H_{u,v}(s, \boldsymbol{g})$ denotes the EM-simulation response and $R_{u,v}(s, \boldsymbol{g})$ the scalable macromodel response, respectively. The MAE is thus the maximum of the L1-norm between the scalable macromodel response and the EM-simulation, over the different $S$-parameters. $P$ is the number of system ports, which is 2 in this filter case.

The MAE error gives a global view on the norm of the difference between the EM data and the model frequency responses. We note that a user can decide to

utilize another error measure that is more suitable to his modeling needs. If a fixed set of estimation and validation data samples is available, each region $\Psi_l$ in the design space is modeled and the corresponding model is validated. The complete design space is covered cell by cell. In the next section, we briefly describe the sequential sampling method [Chem 14b; Chem 14a] that is used to automate the generation of scalable macromodels.

### 8.2.2 AUTOMATED DESIGN SPACE SAMPLING USING SEQUENTIAL SAMPLING

The sequential sampling algorithm [Chem 14b] used in this work simultaneously automates the generation of scalable macromodels [Chem 14a] and reduces the computational effort needed to gather estimation and validation data samples. Figure 8.1 shows the flowchart of the algorithm. The different steps are discussed below:

1. *Initialization*: defines the design space. The $n_g$ dimensional vector design parameters is labeled $\boldsymbol{g} = (g_1, \ldots, g_{n_g})$. The initial design space is a hyper rectangle bound by $2^{n_g}$ corner points. It forms one single $n_g$-box region $\Psi_l$ with $l = L = 1$, where $L$ is the number of hyper rectangles that divide the complete design space.

2. *Scalable macromodel extraction* : A scalable macromodel $\boldsymbol{R}^{\Psi_l}(s, \boldsymbol{g})$ is built for each elementary region $\Psi_l$ ($l \in \{1, \ldots, L\}$) (see Section 8.2.1).

3. *Model validation*: The model response in the selected region $\Psi_l$ is validated with respect to the actual EM-solver response. This requires a set of validation data points, with corresponding EM simulations that are not used for the model estimation. This is done in two steps: first the response of the EM solver is compared with the macromodel response evaluating using the MAE measure (8.2) at the center of the maximal dynamic edge. The maximal dynamic edge is the edge for which the difference between the response in the corresponding corner points is the greatest. If the model is accurate enough, a second level of accuracy check is performed at the geometric center of the hyper rectangle (similarly to [Chem 14b]).

4. *Refinement*: If the accuracy of the model in the region $\Psi_l$ is below the threshold $\Delta_\Psi$, the region $\Psi_l$ is not divided further. Otherwise, the region is split into two subregions along the maximally sensitive edge [Chem 14b]. The accuracy threshold $\Delta_\Psi$ can be decided based on the design specifications set by the user. The threshold $\Delta_\Psi$ must thus be specified by the

user. For example, if a minimal stopband attenuation of 30 dB is required for the optimal design, the scalable macromodel should reach an accuracy of at least −30 dB.

After updating the total number of regions $L$ the algorithm is repeated from Step 2 on until all regions $\Psi_l$ are covered with the required accuracy level, i.e. $l = L$. Figure 8.1 shows a schematic overview of the sequential sampling algorithm.

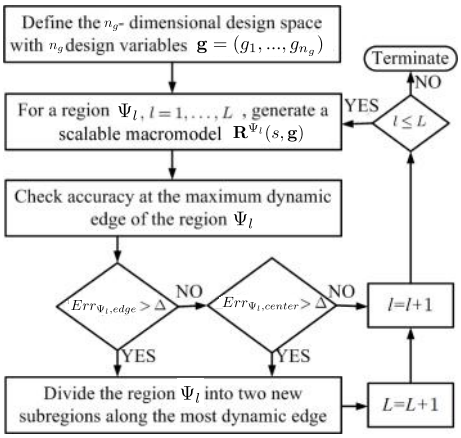


**Figure 8.1** Flowchart of the sequential sampling algorithm.

## 8.3 Including the Scalable Macromodel in the Design Process

As we have seen in Chapter 3, design curves are often used to obtain initial values for the physical design parameters of the filter. Due to second order effects most initial designs require post-processing and fine-tuning to meet the desired specification. This process involves numerical optimization and is classically based on multiple, accurate EM-simulations. In Chapter 5 and Chapter 6, we have introduced novel tuning methods for coupled resonator based bandpass filters. Although the methods yield accurate designs, they still require several EM-simulations. The alternative that is explained here starts from the following idea: Rather than investing time in the tuning or optimization, we may invest that time to extract a scalable macromodel. Although the model generation process is automated, some judicious user choices are still required:

- The frequency range of interest has to be chosen.
- The physical parameters of the filter have to be chosen (the choice of $\boldsymbol{g}$). Typically $n_g$ parameters are chosen in order to maximally influence the

properties of the filter response that do not meet the specifications. For example, when the center frequency of the filter is too high, the physical length of the resonators is certainly included.

- The ranges of variation of the design parameters must also be set. These ranges depend on practical and/or physical considerations. To make this less abstract, let us consider the spacing between two microstrip lines in a coupled line pair. When the spacing is too small, the design cannot be realized physically due to fabrication tolerances. When the spacing becomes too large, there is no more coupling between the lines.

- Another important choice is the desired accuracy of the macromodel. This choice depends on the filter specifications. For example, when the required minimal attenuation is equal to $-20$ dB, the scalable macromodel should be able to describe the filter characteristics up to an accuracy of at least $-20$ dB. The user may decide to increase the model accuracy to include some safety margin (e.g. from 5 to 10 dB of margin).

As their name suggests, user choices depend on the design and must thus be made by the user after the initial design step. Once the model is generated it is used to optimize the initial design. On top of that, the model can also be used to gain insights about the behavior of the filter with respect to the design parameters or used to optimize a new filter for a different set of specifications. The macromodel based optimization is explained in the next section.

## 8.4 Macromodel based Optimization

The scalable macromodel $\boldsymbol{R}(s, \boldsymbol{g})$ of a microwave filter can be used to optimize the initial design such that it fulfills the desired specifications. The global optimization function *MultiStart* in Matlab is used in this chapter to perform global optimization of the filter to satisfy the desired performances. The geometrical values obtained during the initial dimensioning of the filter are used as starting point for the optimization. In order to avoid local minima, the *MultiStart* routine also generates uniformly distributed starting points in the design space from which several local optimizer runs are performed, generating multiple solutions. This routine then ranks the solutions in terms of their cost function values in ascending order. It is important to highlight that a global optimization usually requires a high number of function evaluations (and then simulations of the system behavior). This is not computationally expensive if scalable macromodels

are used for it. Global optimization is interesting since it searches for design solutions over the complete design space of interest.

First we choose a frequency grid for which the scalable macromodel $\boldsymbol{R}(s_m, \boldsymbol{g})$ is evaluated during the optimization. A frequency in this grid is denoted as $s_m$, where $m \in \{1, 2, \ldots, n_F^{Opt}\}$ and $n_F^{Opt}$ is the number of frequencies in the grid. These frequencies are chosen in the stop and passbands of the filter. The frequency template specifies a lower frequency response threshold $R_L^m$ and a upper frequency response threshold $R_U^m$ at frequency samples $s_m$. The scalable macromodel allows to calculate whether the filter satisfies or violates the given specification by calculating:

$$F(s_m, \boldsymbol{g}) = R_L^m - R(s_m, \boldsymbol{g}) \quad \text{or} \quad R(s_m, \boldsymbol{g}) - R_U^m. \tag{8.3}$$

A negative value in (8.3) indicates that the corresponding specification is satisfied, while a positive value denotes that the specification is violated. Note that the evaluation of the macromodel in (8.3) is numerically cheap. The cost function that the optimization minimizes in this chapter is the worst-case violation over all the S-parameters matrix entries and the $s_m$ samples

$$F(\boldsymbol{g}) = \max_{i,j} \max_{s_m} F_{i,j}(s_m, \boldsymbol{g}). \tag{8.4}$$

where $F_{i,j}$ represents the cost function for the $(i, j) - th$ S-parameter matrix entry. Note that this is the same cost function as the one used in [Band 94b]. The cost function (8.4) is then supplied to the *MultiStart* optimization routine, resulting in multiple optimal design space points that satisfy the specifications. The application to a filter case is illustrated in Section 8.5. Note that in the literature several more suitable cost functions exist [Came 07b; Band 88] and that the scalable macromodel can also be used to optimize other cost functions.

## 8.5 Example: Microstrip Dual-Band Bandpass Filter

We have chosen the dual-band bandpass microstrip filter described in [Hsu 13] to illustrate and validate the proposed approach. The filter consists of two coupled unequal length shunted-line stepped impedance resonators (Figure 8.2). We use the design method presented in [Hsu 13] to obtain initial values of the design parameters for the initial design.

The filter is fabricated on a RO4003 substrate with a relative permittivity $\varepsilon_r$

equal to 3.55, a dielectric height of 1.542 mm and a loss tangent $\delta$ equal to 0.0022. The EM solver used to calculate the filter response is ADS Momentum [ADS 14]. All numerical experiments are performed using Matlab R2012A running on a Windows platform equipped with an Intel Core2 Extreme CPU Q9300 running at 2.53 GHz and with 8 GB RAM. The steps to obtain the initial design are discussed in what follows.

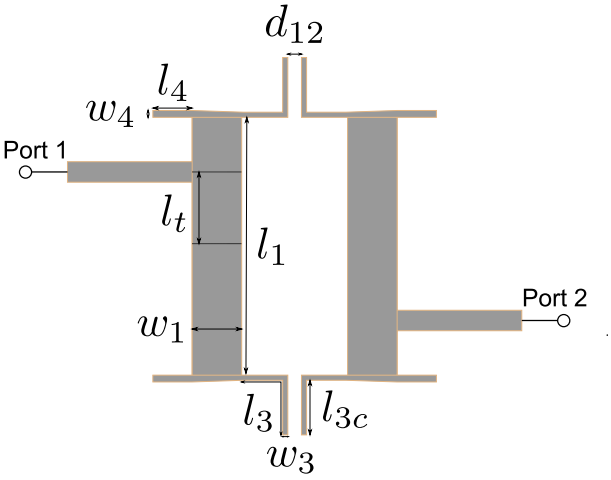


**Figure 8.2** Top-view of the layout of the filter.

### 8.5.1 FILTER SPECIFICATIONS AND FILTER FUNCTION

The specifications of the filter are summarized in Table 8.1. The design method in [Hsu 13] proposes to approximate each band separately with a Chebyshev response of order 2. For Chebyshev filter functions formulas exist to determine the low-pass prototype (Figure 8.3) parameters $g_i$ of the equivalent lumped circuit [Matt 64]. The corresponding coupling coefficients and external quality factors are determined as follows:

$$Q_{ei} = \frac{g_0 g_1}{FBW} \tag{8.5}$$

$$Q_{eo} = \frac{g_n g_{n+1}}{FBW} \tag{8.6}$$

$$M_{i,i+1} = \frac{FBW}{\sqrt{g_i g_{i+1}}}, \text{ for } i = 1 \text{ to } n-1 \tag{8.7}$$

**Table 8.1** Specifications of the Dual-Band Filter

| | $f_{c1}$ | $f_{c2}$ |
|---|---|---|
| Center frequency | 2 GHz | 2.65 GHz |
| Bandwidth | 50 MHz | 50 MHz |
| In-band insertion loss | $\leq$-3 dB | $\leq$-3 dB |
| In-band return loss | $\geq$-10 dB | $\geq$-10 dB |

Table 8.2 contains the coupling coefficients for each band where the center frequency of the lower and upper band are denoted as $f_{c1}$ and $f_{c2}$ respectively.

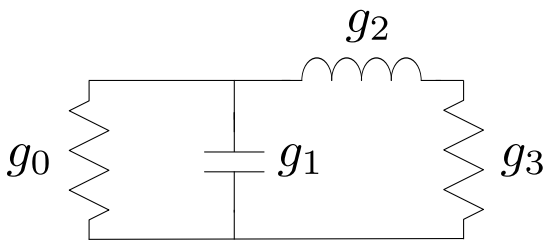


**Figure 8.3** Equivalent low-pass prototype for $N = 2$.

**Table 8.2** Coupling Coefficients and External Quality Factors

| | $f_{c1}$ | $f_{c2}$ |
|---|---|---|
| $M_{1,2}$ | 0.0345 | 0.026 |
| $Q_{ei}$ | 33.7 | 44.8 |
| $Q_{eo}$ | 33.7 | 44.8 |

### 8.5.2 PHYSICAL IMPLEMENTATION: INITIAL DESIGN

The initial values for the design parameters are obtained by applying the procedure described in [Hsu 13]. In this section, we briefly summarize this procedure focusing on the effect of the physical parameters on the center frequency of the bands, the coupling coefficients and the external quality factors.

The lengths $l_1, l_3, l_{3c}$ and $l_4$ are chosen to result in a half-wavelength resonator that resonates at $f_{c1}$. The impedance ratios $\frac{Z_{01}}{Z_{03}}$ and $\frac{Z_{01}}{Z_{04}}$ determine the ratio $\frac{f_{c2}}{f_{c1}}$ . Decreasing the values of $\frac{Z_{01}}{Z_{03}}$ and $\frac{Z_{01}}{Z_{04}}$ leads to decrease the value of $\frac{f_{c2}}{f_{c1}}$. The widths $w_1$, $w_3$ and $w_4$ mainly determine the value of $Z_{01}$, $Z_{03}$ and $Z_{04}$ respectively. The values of $w_1$, $w_3$ and $w_4$ are chosen to obtain $\frac{f_{c2}}{f_{c1}} = 1.325$.

The tapping position $l_t$ and the lengths $l_{3c}$ and $l_4$ mainly affect the external quality factors $Q_{ei}$ and $Q_{eo}$. They are chosen to match the physical external

quality factors approximately to the ones found during the realization step. Initial values for these parameters are difficult to determine, as they affect the response of both bands. The physical $Q_{ei}$ and $Q_{eo}$ are shown in Table 8.3. Note that these quality factors are extracted using (3.19) at $\omega_{c1} = 2\pi f_{c1}$ and $\omega_{c2} = 2\pi f_{c2}$ separately, neglecting the influence of the bands on each other.

The spacing parameter $d_{12}$ between the resonators mainly affects the coupling coefficient $M_{12}$. $w_3$ and $w_4$ also affect the coupling coefficient, but their effect is smaller. The values of $d_{12}$, $w_3$ and $w_4$ are chosen such that the physical coupling coefficient $M_{12}$ is approximately equal to the value found during the realization step. The physical $M_{12}$ for both bands is shown in Table 8.3. These parameters are extracted using (3.11) for each band separately.

**Table 8.3** Coupling Coefficients and External Quality Factors (EM simulations)

| | $f_{c1}$ | $f_{c2}$ |
|---|---|---|
| $M_{1,2}$ | 0.0373 | 0.0327 |
| $Q_{ei}$ | 25 | 33.5 |
| $Q_{eo}$ | 25 | 33.5 |

The initial value of the design parameters given by this design method are summarized in Table 8.4. Figure 8.4 shows the magnitude of $S_{21}$ and $S_{11}$ for the initial design, respectively. It is clear that the specifications are not met and therefore optimization is needed.

**Table 8.4** Initial Values of the Design Parameters

| | |
|---|---|
| $l_1$ | 24.5 mm |
| $l_3$ | 17 mm |
| $l_{3c}$ | 10 mm |
| $l_4$ | 1.5 mm |
| $l_t$ | 8.8 mm |
| $w_1$ | 9.5 mm |
| $w_3$ | 1 mm |
| $w_4$ | 1 mm |
| $d_{12}$ | 1.62 mm |

### 8.5.3 DESIGN SPACE

In this section, we describe how to select the physical parameters that become design parameters. Figure 8.4b shows that the ratio $\frac{f_{c2}}{f_{c1}}$ is not equal to 1.325. But $f_1 = 2$ GHz is indeed properly realized. As the ratio $\frac{f_{c2}}{f_{c1}}$ is mainly affected by $\frac{Z_{01}}{Z_{03}}$ and $\frac{Z_{01}}{Z_{04}}$, $w_1$ and $w_3 = w_4$ are chosen as design parameters. The ranges are

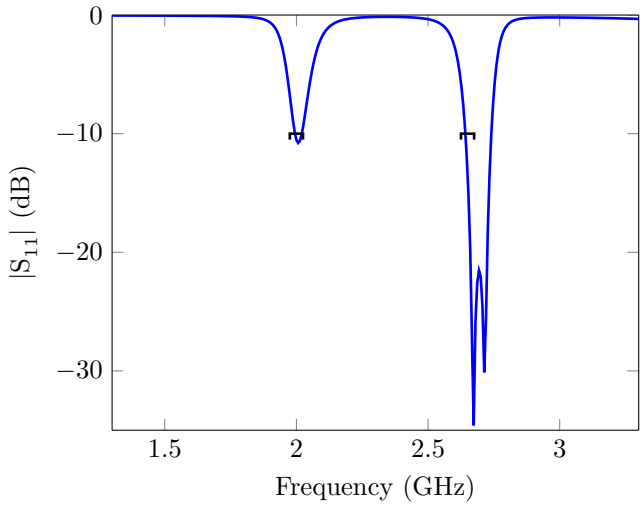


**(a)** $|S_{11}|$ for the initial design (—) and specifications (—).

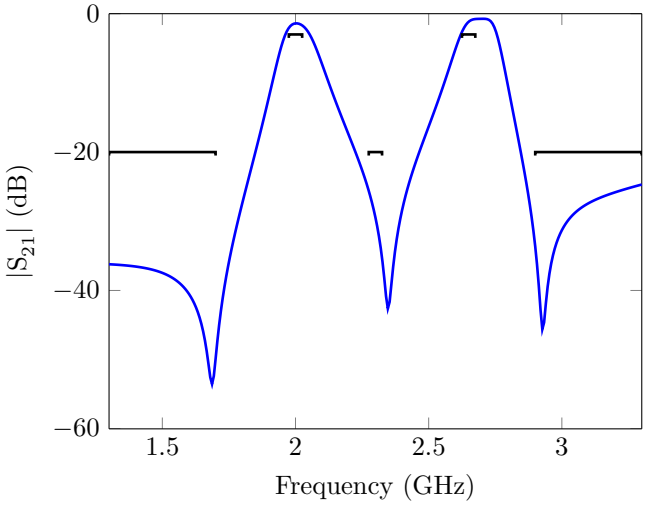


**(b)** $|S_{21}|$ for the initial design (—) and specifications (—).

**Figure 8.4** $|S_{11}|$ and $|S_{21}|$ for the initial design and the specifications.

determined as follows: $w_1$ must not become too large, because for large values of $w_1$ the characteristic impedance $Z_{01}$ does not decrease anymore. Hence, it is not relevant to model the filter behavior for those values. The value of $w_1$ must not become too small either, because then the ratio $\frac{Z_{01}}{Z_{03}}$ then becomes too large and $\frac{f_{c2}}{f_{c1}}$ becomes too large. The value of $w_3$ must not become too small, because then it is not physically realizable. It must also not become too large,

because then the ratio $\frac{Z_{01}}{Z_{03}}$ becomes too large and $\frac{f_{c2}}{f_{c1}}$ becomes too large. Since the coupling coefficient between the resonators is too large in the design, $d_{12}$ is also chosen as a design parameter. The upper bound of the range of $d_{12}$ (= 2 mm) is chosen to ensure that there is still electromagnetic coupling between the resonators and the lower bound (=0.5 mm) is chosen such that it is physically realizable. Table 8.5 contains the ranges of the design parameters.

**Table 8.5** Ranges of the design parameters.

| Parameter | Range |
|---|---|
| $w_1$ | 8.5-10.5 mm |
| $w_3$ | 0.5-2 mm |
| $d_{12}$ | 0.5-2 mm |

### 8.5.4 GENERATION OF THE SCALABLE MACROMODEL

Section 8.2.1 and Section 8.2.2 show that the generation of scalable macromodels is an automated process. Nevertheless, the user has to specify the design space, the frequency span and the accuracy for the model. The choice of the design space $\boldsymbol{g} = [w_1, w_2, d_{12}]$ has been previously discussed. The frequency span is chosen equal to $f \in [1.3 - 3.3]$ GHz to be wide enough to contain the filter behavior of interest within it. The choice of the model accuracy is based on the minimal attenuation desired in the stopband that is set equal to 30 dB in this numerical example. The accuracy of the scalable macromodel has been set to $-30$ dB based on the MAE measure (8.2).

The scalable macromodeling method of [Chem 14a] discussed in Section 8.2.2 has been implemented in Matlab R2012a and used to drive the Momentum software with Adaptive Frequency Sampling (AFS) [ADS 14] to generate the S-parameters at selected design space samples. AFS is a technique included in ADS2011 Momentum that adaptively samples the frequency range and can be used to efficiently provide the system response for a specified number of samples, that are chosen freely in the band. The number of simulated frequency samples $n_F$ obtained by AFS over the range $f \in [1.3 - 3.3]$ GHz has been chosen equal to 301 to build the scalable macromodel. The steep changes in the behavior of the $S$-parameters of the microwave filter with respect to frequency are hence well captured.

The MAE (8.2) is used to asses the accuracy of the scalable macromodel. Table 8.6 reports the total number of design space samples (estimation and validation), the worst case MAE (8.2) over the estimation and validation data, the

**Table 8.6** Scalable macromodeling

| # Samples | | CPU Time | | Accuracy |
|---|---|---|---|---|
| Generation | Validation | Modeling | Data Gen. | [dB] |
| 72 | 45 | 36 min 35 s | 1 h 55 min 21 s | −30.48 |
| Average CPU Time for one ADS frequency sweep = 50 s<br>Average CPU Time for one macromodel frequency sweep = 19.5 ms<br>Speed-up = 2564× | | | | |

CPU time needed to run all the ADS Momentum estimation and validation simulations and the CPU time needed to obtain the scalable macromodel using the sequential scheme coupled with the scalable macromodeling method [Chem 14a]. The average CPU time needed by ADS Momentum (using AFS) and the scalable macromodel for one frequency sweep over 301 frequency points is also shown in Table 8.6. This measure is crucial to judge the potential advantage of the proposed approach for efficient design optimizations when compared to the direct use of EM-based optimization schemes.

### 8.5.5 FILTER OPTIMIZATION

The scalable macromodel is used to perform multiple optimizations for this filter. The optimization specifications on the $S$-parameters of the filter under study are:

$$|S_{21}| < -L_{A1}\,\text{dB} \qquad f_{s1} \le f \le f_{s2}, \tag{8.8a}$$
$$|S_{21}| > -L_{IL}\,\text{dB} \qquad f_{p1} \le f \le f_{p2}, \tag{8.8b}$$
$$|S_{11}| < -L_{RL}\,\text{dB} \qquad f_{p1} \le f \le f_{p2}, \tag{8.8c}$$
$$|S_{21}| < -L_{A2}\,\text{dB} \qquad f_{s3} \le f \le f_{s4}, \tag{8.8d}$$
$$|S_{21}| > -L_{IL}\,\text{dB} \qquad f_{p3} \le f \le f_{p4}, \tag{8.8e}$$
$$|S_{11}| < -L_{RL}\,\text{dB} \qquad f_{p3} \le f \le f_{p4}, \tag{8.8f}$$
$$|S_{21}| < -L_{A3}\,\text{dB} \qquad f_{s5} \le f \le f_{s6}. \tag{8.8g}$$

with three optimization cases:

**Table 8.7** Dual-band bandpass filter: global optimization results using the macromodel.

| Case | Initial design $(w_1, w_2, d_{12})$ (mm) | Best optimal design $(w_1^*, w_2^*, d_{12}^*)$ (mm) | # Function evaluations | Optimization time |
|---|---|---|---|---|
| I | $[9.5, 1, 1.62]$ | $[9.66, 1, 1.44]$ | 6557 | 5 min, 40 s |
| II | $[9.5, 1, 1.62]$ | $[10.4, 1.17, 1.38]$ | 5456 | 5 min, 47 s |
| III | $[9.5, 1, 1.62]$ | $[10.3, 1.43, 1.25]$ | 6675 | 5 min, 43 s |

$$
\begin{aligned}
&I.(f_{s1}, f_{s2}, f_{p1}, f_{p2}, f_{s3}, f_{s4}, f_{p3}, f_{p4}, f_{s5}, f_{s6}) = \\
&(1.3, 1.7, 1.975, 2.025, 2.275, 2.325, 2.625, 2.675, 2.9, 3.3) \text{ GHz}, \\
&(L_{A1}, L_{IL}, L_{RL}, L_{A2}, L_{A3}) = (-20, -3, -10, -20, -20) \text{ dB} \qquad (8.9a) \\
&II.\ (f_{s1}, f_{s2}, f_{p1}, f_{p2}, f_{s3}, f_{s4}, f_{p3}, f_{p4}, f_{s5}, f_{s6}) = \\
&(1.3, 1.7, 1.975, 2.025, 2.275, 2.325, 2.625, 2.675, 2.9, 3.3) \text{ GHz}, \\
&(L_{A1}, L_{IL}, L_{RL}, L_{A2}, L_{A3}) = (-20, -3, -10, -30, -20) \text{ dB} \qquad (8.9b) \\
&III.\ (f_{s1}, f_{s2}, f_{p1}, f_{p2}, f_{s3}, f_{s4}, f_{p3}, f_{p4}, f_{s5}, f_{s6}) = \\
&(1.3, 1.6, 1.9, 1.95, 2.175, 2.25, 2.625, 2.675, 2.9, 3.3) \text{ GHz}, \\
&(L_{A1}, L_{IL}, L_{RL}, L_{A2}, L_{A3}) = (-20, -3, -10, -20, -20) \text{ dB} \qquad (8.9c)
\end{aligned}
$$

As explained in Section 8.4, the global optimization function *MultiStart* in Matlab R2012a is used to perform a global optimization with a cost function defined in (8.4) using the previous specifications. 30 starting points are used for each optimization case. For each optimization case, the function *MultiStart* found multiple possible optimization solutions $[w_1^*, w_3^*, d_{12}^*]$ that satisfy the corresponding specifications. The results of the three optimization cases are tabulated in Table 8.7, where the best optimization solutions, the total number of function evaluations and CPU time needed for the three global optimizations are shown.

Considering the average CPU time that is needed for one frequency sweep using the EM solver and the scalable macromodel (see Table 8.6) and the number of functions evaluations needed to perform the global optimizations in Table 8.7,

clearly shows that using the scalable macromodel allows a very efficient multiple global optimization. The initial computational effort needed to generate the scalable macromodel (see Table 8.6) becomes small compared to the CPU time that is saved to perform the multiple global optimizations is considered.

Figure 8.5 shows the optimization results for *Case I*: The $S$-parameters are shown before and after the optimization. The solid black lines show the specifications. From the two figures it is clearly seen that all the specifications are satisfied. Similar results are for *Case II* and *Case III* as shown in Figure 8.6 and Figure 8.7. The green response curves denote the Momentum simulations performed at the optimal solution points to verify that the model prediction (red curves) is accurate. Note that there is a difference between the evaluation of the macromodel and the EM-simulation for the optimized design. This difference is however smaller than -30 dB, which is the error limit that was specified during the the macromodel generation.

## 8.6 Discussion

Generating scalable macromodels becomes more computationally expensive with an increasing number of design parameters. The so called "curse of dimensionality" pops up in high-dimensional modeling problems. This affects two main aspects of the modeling:

- the number of data samples needed to build and validate a model (and then the CPU time to collect these data samples)
- The complexity (and then the CPU time) of the model generation when the data samples are available

Working on fully regular design space grids to collect estimation and validation data will make the complexity of the data to gathering increase in an exponential way with respect to the number of design parameter. This issue can be mitigated by using sequential sampling strategies that optimize the samples location in the design space.
The modeling step for the technique [Chem 14a] will mainly suffer from an increasing number of design parameters in the computation of the amplitude and frequency scaling coefficients for each region of the design space. This issue can be mitigated by exploiting parallelization strategies, since the scaling coefficients computation for a design space region can be performed independently from the other regions.

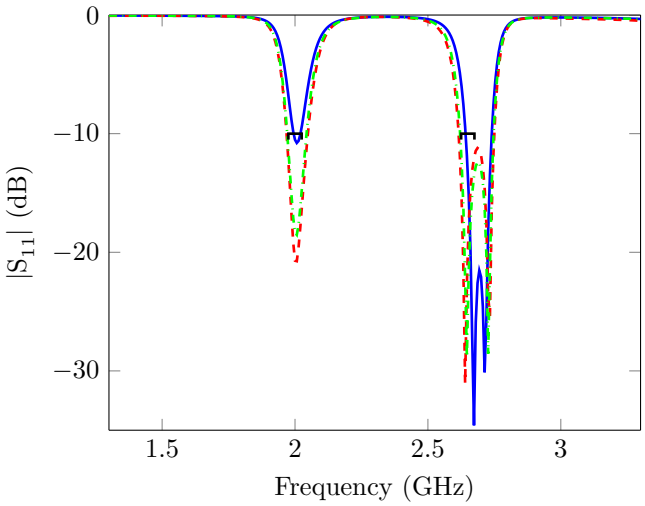


**(a)** $|S_{11}|$ for the initial design (—), optimized design evaluated using the macromodel (- - -), EM-simulation (- - -) and specifications (—).

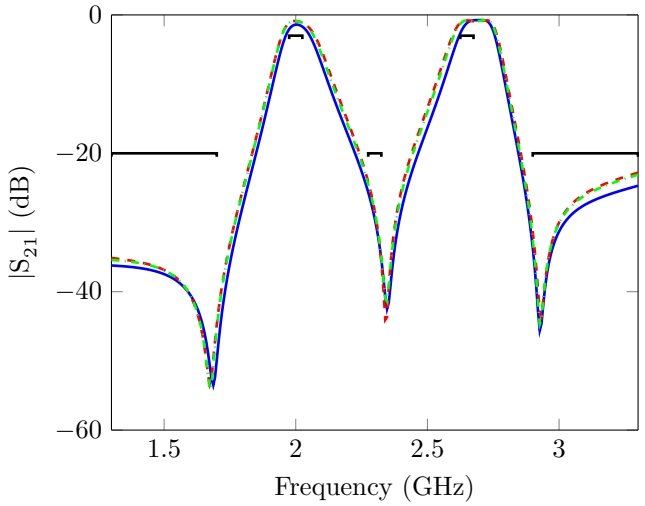


**(b)** $|S_{21}|$ for the initial design (—), optimized design evaluated using the macromodel (- - -), EM-simulation (- - -) and specifications (—).

**Figure 8.5** $|S_{11}|$ and $|S_{21}|$ for the initial design, the optimized design evaluated using the macromodel and EM-simulation for *Case I* .

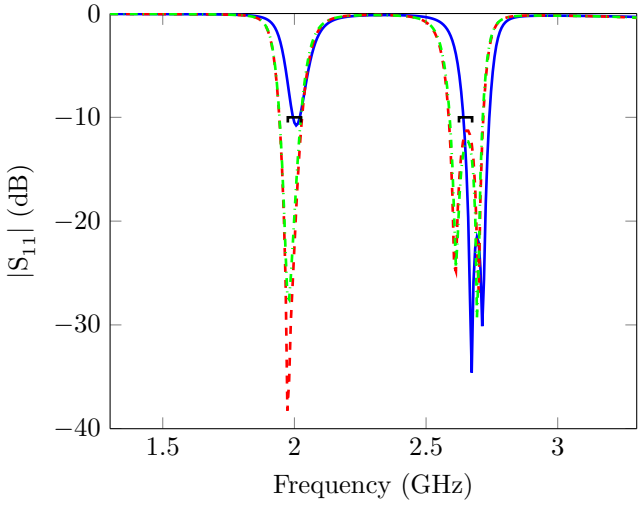


**(a)** $|S_{11}|$ for the initial design (—), optimized design evaluated using the macromodel (- - -), EM-simulation (- - -) and specifications (—).

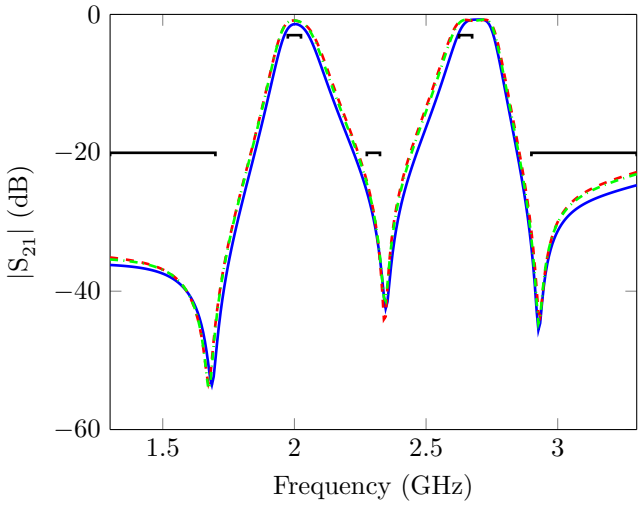


**(b)** $|S_{21}|$ for the initial design (—), optimized design evaluated using the macromodel (- - -), EM-simulation (- - -) and specifications (—).

**Figure 8.6** $|S_{11}|$ and $|S_{21}|$ for the initial design, the optimized design evaluated using the macromodel and EM-simulation for Case II.

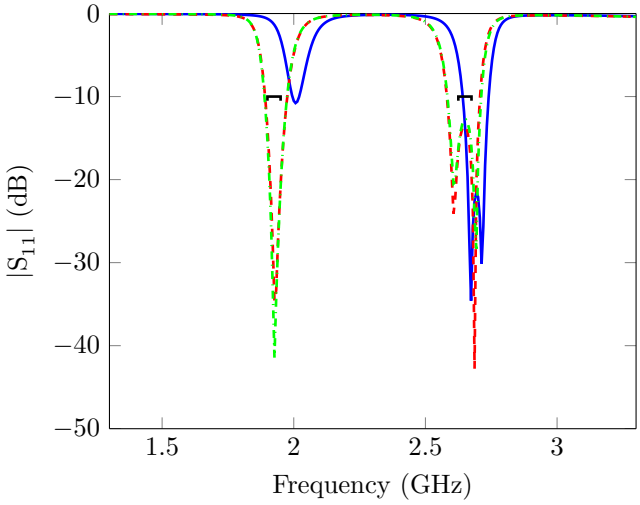


**(a)** $|S_{11}|$ for the initial design (—), optimized design evaluated using the macromodel (- - -), EM-simulation (- - -) and specifications (—).

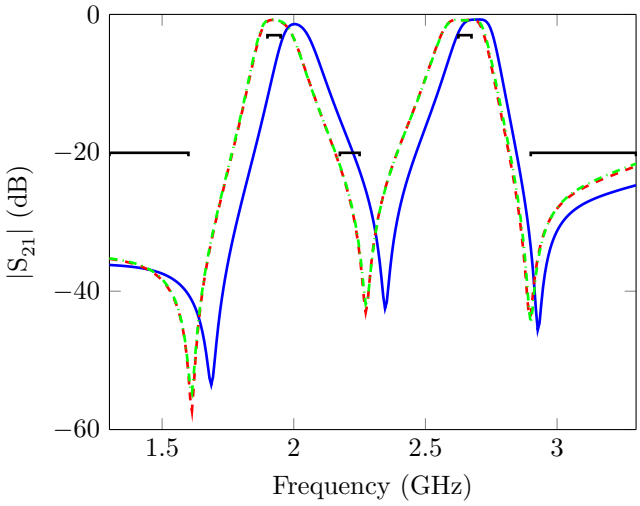


**(b)** $|S_{21}|$ for the initial design (—), optimized design evaluated using the macromodel (- - -), EM-simulation (- - -) and specifications (—).

**Figure 8.7** $|S_{11}|$ and $|S_{21}|$ for the initial design, the optimized design evaluated using the macromodel and EM-simulation for Case III.

## 8.7 Conclusion

In this chapter, we have introduced scalable macromodels in the design cycle of microwave filters. We have discussed how to generate and use scalable macromodels as a design tool for filters. The main advantage of these macromodels is that they are cheap to evaluate with a suitable accuracy. Hence, the scalable macromodels can replace the expensive EM solver during multiple optimizations of the filter and then make these steps much less CPU time intensive. It is to be noted that it also takes an initial computational effort to generate the macromodel and that this must be done during the design cycle. However, this initial computational effort that is needed to generate the scalable macromodel becomes a little effort when the CPU time saved to perform multiple global optimizations with respect to EM-based optimizations is considered. We have illustrated this macromodeling-based design approach by applying it to the design of a state-of-the-art microstrip dual-band bandpass filter. Although the generation of the scalable macromodels is an automated process, it still requires some information from a designer, namely the frequency span, the ranges of the design parameters and the desired model accuracy. How a designer can hand this information to the macromodel generation process has been explained in detail. We have finally shown how the scalable macromodel can be used for multiple optimizations. The corresponding numerical results confirm that the macromodeling-based design approach works very well.

# Conclusions

# 9 Conclusions

In this work we investigate different model driven assisted design approaches for the time-efficient design of microwave bandpass filters. We apply model assisted design approaches not only to post-optimize the physical dimensions of the filter but also to generate initial values for them.

In the first part of the thesis, we use a coupling matrix based approach. The idea is to adjust the physical design parameters based on a comparison between an extracted coupling matrix and the golden goal.

It is well known that coupling topologies may have multiple equivalent solutions to the reconfiguration problem (Chapter 2). One of the main challenges is to extract the physical solution starting from the simulated $S$-parameters of the obtained design.

In Chapter 4 we develop a method that systematically extracts all possible solutions corresponding to the implemented topology. We also propose a strategy to model the second order effects (which are not included in the coupling topology of the golden goal) by adding coupling parameters to the last row and column of the extracted coupling matrix. The extraction of the coupling matrix of a measured SQ filter shows indeed that taking these second order effects into account is indispensable to properly model the filter frequency response of the filter. We also extract all the possible solutions for a CQ filter. This extraction shows that from a mathematical point of view these solutions are equivalent. This means that more information is required to identify the physically implemented coupling matrix.

Chapter 5 shows that in the case of CQ and CT filters it is possible to identify the physically implemented coupling matrix by applying some well chosen variations to the physical structure of the filter. The main drawback of this approach is that it requires several EM-simulations to determine the physical solution. We derive

an expression to predict how many EM-simulations (experiments) are required. Once the physical solution is determined, we show that this knowledge allows one to tune the filter. The extraction procedure only tells the user how far the implemented coupling parameters are from the target values and not how far the physical parameters are from their target values. As a consequence the tuning procedure can still require a relatively high number of iterations for an unexperienced designer to tune a filter.

Chapter 6 estimates the Jacobian matrix of the functional dependence of the physically implemented coupling parameters to the design parameters using the adjoint sensitivity of the $S$-parameters. Using the adjoint sensitivity provided by the EM-simulator allows to estimate the Jacobian using only one EM-simulation. Although including the adjoint sensitivity in such a simulation is numerically more expensive, the method is more time-efficient in comparison to other techniques based on finite difference extraction of the Jacobian matrix. A good estimate of the Jacobian drastically reduces the number of iterations needed to tune relatively complex filter structures. Another benefit of using the Jacobian matrix is that it allows to determine the physically implemented coupling matrix using only 1 EM-simulation.

In the second part of the thesis, we follow a metamodel based approach. The main benefit of this kind of approach is that it generates accurate models for the $S$-parameters or features of the $S$-parameters with an acceptably low number of EM-simulations. These models are then used for 2 different kind of design activities: the generation of initial values for the design parameters and the post-optimization of the filter structures.

Chapter 7 automatically generates multidimensional design curves for the initial dimensioning of coupled-resonator filters. The benefit of using a metamodel approach with respect to the classical approach described in Chapter 3 is that it requires a lower number of EM-simulations to cover a relatively wide range of physical parameters. The multidimensional description allows to use the model to generate initial values for multiple design scenarios.

Chapter 8 generates a scalable macromodel for a complex dual-band bandpass filter. The benefit of a numerically much cheaper model when compared to the EM-solver, is the speed of the optimization of the filter. The approach is slightly different to what is normally done in filter optimization in the sense that the time is invested in the model generation rather than in the post-optimization. The model generation is automated, yet it still requires user-specified ranges over which the design parameters can vary. Another benefit of the macromodel

is that it can be used for several design scenarios if these ranges are chosen to be wide enough. There is an important trade-off here: the larger the ranges are chosen, the longer the generation will take, but the more useful the macromodel will be for different design scenarios.

## 9.1 Comparison of the proposed approaches

The coupling matrix based approach allows one to tune coupled-resonator bandpass filters having a high number of design parameters with a relatively small number of EM-simulations. The number of EM-simulations decreases drastically, if the Jacobian of the function relating the design parameters to the physically implemented coupling parameters is well estimated. Similar techniques available in the literature [Garc 04; Koza 06] estimate the Jacobian using finite differences, such that the number of required EM-simulations increases. In this case, at least one extra EM-simulation is required per design parameter. In this work, no extra EM-simulations are required to estimate the Jacobian. Moreover the Jacobian also offers a criterion to determine the physically implemented coupling matrix in the case of multiple solutions. Note however that if the Jacobian is not available, extra EM-simulations are required to determine the physical couplings in the case of multiple solutions.

Due to the curse of dimensionality, the metamodel approach requires too many EM-simulations if the number of design parameters exceeds 4. In the case of a low number of design parameters, the number of EM-simulation required to generate the metamodel depends on the desired accuracy and how smooth the $S$-parameters behave as a function of the design parameters. This approach has not been applied to the CQ and CT filters, because of the high number of design parameters.

Both approaches offer physical insight in the filter, be it in a different way. The coupling matrix relates the coupling parameters to the design parameters. The coupling matrix however does not model all off the effects: frequency dependent coupling, higher order mode resonances, etc. are not included in this model. Moreover the model is only valid in a narrow-band around the center frequency. Also the parasitic couplings are not uniquely identified. The extraction procedure proposed in Chapter 4 however proposes a strategy to handle the presence of these parasitic couplings. Including the Jacobian offers even more insight, since it locally predicts the coupling parameters variation as a function of the design parameter variations. A metamodel on the other hand covers an entire region in the design space. Since such a model is numerically cheap to evaluate, it allows

the user to explore the design space by for example sweeping a design parameter and plotting the corresponding $S$-parameters (or features of the $S$-parameters). This makes the metamodel an ideal candidate for generating design curves.

As discussed in Chapter 6 coupling matrix based optimization does not suffer of the presence of local minima. This can however not be guaranteed for methods that optimize $S$-parameter based cost functions [Band 94a] or the position of the poles and the zeros [Koza 02].

If the region in the design space is sufficiently large, the metamodel is able to handle multiple design scenarios as illustrated in Chapter 8. The coupling matrix based approach does not have this property.

Finally the coupling matrix based approach only handles narrow-band coupled-resonator bandpass filters. Thus this approach is not applied to the dual-band filter discussed in Chapter 8. The metamodel approach can be applied for different kind of filters, which do not necessarily have to fulfill the coupling matrix hypotheses. The metamodel is even capable of modeling sub-blocks of the filter, such as individual resonators or resonator pairs. Therefore the metamodel approach is more general.

If the filter fulfills the coupling matrix hypotheses, we advise to use the coupling matrix approach. If in addition the EM-simulator provides the adjoint sensitivities, we advise to estimate the Jacobian. For other filter structures with a low number of design parameters, we advise to use the metamodel approach.

| | Coupling Matrix | Jacobian | Metamodel |
|---|---|---|---|
| EM-simulations | + | ++ | - |
| Design parameters | ++ | ++ | - - |
| Physical insight | + | ++ | + |
| Local minima | + | + | - |
| Multiple design scenarios | + | + | - |
| Generality | - - | - - | ++ |

**Table 9.1** Comparison of the different properties of the proposed approaches.

## 9.2 Main contributions

In this section we briefly highlight the main contributions of this work.

Coupling Matrix Approach:

- Coupling matrix extraction method that systematically extracts all possible solutions.
- Novel strategy to determine the physically implemented coupling matrix in the case of cascaded topologies.
- Novel method to estimate the Jacobian of the function relating design parameters to the coupling parameters. The main advantage is that estimation only requires one EM-simulation.
- Development of Jacobian based criterion to determine the physically implemented coupling matrix.

Metamodel Approach:

- Development of a metamodel for the efficient generation of the design curves. The metamodels models the couplings between 2 resonators and external quality factors, rather than the $S$-parameters.
- Inclusion of the metamodel in the design cycle of filters. We show that the metamodel can be re-used for multiple design scenarios.

# 10 Preliminary Results and Future Work

This chapter briefly summarizes some preliminary results and ideas for future work. Section 10.1 proposes to generate a parametric model of the physically implemented coupling matrix. This work has led to some preliminary results which were presented at *European Microwave Conference 2015 (EuMC)* [Caen 15b]. For convenience of the reader the article has been added in Appendix A. The method did already yield some interesting results, but they are however not mature enough to be included fully in the thesis.

## 10.1 Preliminary Results: Parametric Modeling of the Coupling Parameters

The idea of the method proposed in [Caen 15b] is to model each physically implemented coupling parameter separately as a function of a set of well chosen design parameters. As a model structure we propose to use multi-variable polynomials of order 2. This model is inspired by the fact that in the region of interest the behavior of an inter-resonator coupling as a function of the inter-resonator spacing can be well approximated by a quadratic function [Amar 06]. In Chapter 6 we have however seen that coupling parameters also depend on other design parameters, albeit to a lesser extent. We model their effect on the coupling using a linear term instead of a quadratic term in the multi-variable polynomial.

The eventual model for the entire filter is thus a set of $n_c$ multi-variable polynomials of order 2. Here $n_c$ is the number of coupling parameters to be modeled. This corresponds to 1 polynomial for each modeled coupling parameter. In order to keep the complexity and the generation time of the model relatively low, we do not take into account all of the design parameters to model the behavior of a single coupling parameter, but we pre-select those that are known to have a relevant effect. Consider for example a cascaded quadruplet filter: a coupling in

the first quadruplet is only modeled as a function of geometrical parameters in the first quadruplet, since the effect of design parameters in the second quadruplet is negligible. This assumption allows to break the *curse of dimensionality* which can be a serious problem in the case of high number of design parameters, as is discussed in Chapter 8.

The minimum number of EM-simulations required to generate the model for the entire filter corresponds to the maximal number of coefficients in one of the $n_c$ polynomial models. The maximum number of coefficients is denoted as $n_a$. The generation of the model is summarized next: the geometrical design parameters are varied in a random way over the region of interest, which is chosen as is discussed in Chapter 8. For each random set of geometrical parameters, the corresponding filter structure is simulated. Starting from the simulated $S$-parameters, the corresponding coupling matrix is extracted for each geometry using the techniques described in Chapter 4 and Chapter 5. This yields $n_a$ simulated filters and $n_a$ corresponding coupling matrices. Finally the multivariable polynomials are estimated for each coupling matrix separately in least-squares sense.

The aim of the model is to tune the filter by solving the non-linear set of equations for the target values of the coupling matrix. So far this has not yielded the desired results, since the effect of parasitic couplings was not included. As future work we propose to model the parasitic effects too to take them into account during the tuning. Another potential benefit to be investigated is to re-use the model for multiple design scenarios. This implies however that the ranges of the varied geometrical parameters must be enlarged, which can possibly deteriorate the quality of the quadratic model.

## 10.2 Future Work

### 10.2.1 RE-OPTIMIZATION OF THE TARGET MATRIX

In Chapter 5 and Chapter 6 we have seen that some filter structures suffer heavily from the presence of parasitic coupling. In order to tune the filters taking into account these effects, we re-optimize the diagonal elements of the target matrix. Next, the filter is tuned to the re-optimized target matrix. This strategy assumes that parasitic coupling do not change due to further adjustments of the filter structure. This is however not the case: when the filter is adjusted this affects

the parasitic couplings as well, which requires a new adjustment of the target matrix. This is not done at the moment. To properly handle the variation of the parasitic couplings during the tuning procedure, a new strategy based on re-optimization of the target coupling matrix must be further developed.

### 10.2.2 EXTENSION TO OTHER COUPLING TOPOLOGIES

Throughout this thesis, we have applied our modeling strategies mainly to cascaded triplet and quadruplet topologies. Since these topologies have multiple solutions to the reduction problem, they are interesting to show the utility of the proposed methods in the case of non-canonical topologies. There are however other non-canonical topologies such as *extended box topologies*. For this kind of topologies the relations between the TZs and the coupling matrix is less straightforward. The identification of the physical solution is therefore harder to obtain. We believe that the use of Jacobian criterion introduced in Chapter 6 is the best strategy. Remark however that the number of admissible solutions grows rapidly for such topologies and thus many Jacobians must be checked. Another contribution could be to test the methods for filters implemented in other technologies such as waveguide and dielectric resonator filters.

### 10.2.3 FABRICATION AND MEASUREMENTS

So far only one of the designed filters has been fabricated and measured. The measured response showed some differences with respect to the simulated response, which were due to the fact that the substrate parameters in the simulator did not perfectly match with the one of the substrate used for fabrication. In the future we plan to measure the other designs as well.

# List of scientific publications

## JOURNAL PAPERS

**Caenepeel, M.**, Chemmangat, K., Ferranti, F., Rolain, Y., Dhaene, T. and Knockaert, L. (2016). Scalable macromodelling methodology for the efficient design of microwave filters. *IET Microwaves, Antennas & Propagation*, Vol. 10, No. 5, pp. 579–586

## PEER REVIEWED CONFERENCE PAPERS (IN WEB OF SCIENCE)

**Caenepeel, M.** and Rolain, Y. (2014). Macromodeling of narrow-band band-pass filters based on interpolation of coupling matrices, In *Proceedings of the 2014 IEEE 18th Workshop on Signal and Power Integrity (SPI)*, pp. 1–4, Ghent, Belgium, 11–14 May 2014.

**Caenepeel, M.**, Seyfert, F., Rolain, Y. and Olivi, M. (2015). Microwave filter design based on coupling topologies with multiple solutions, In *Proceedings of the 2015 IEEE MTT-S International Microwave Symposium (IMS)*, pp. 1–4, Phoenix, AZ, USA, 17–22 May 2015.

**Caenepeel, M.**, Seyfert, F., Rolain, Y. and Olivi, M. (2015). Parametric modeling of the coupling parameters of planar coupled-resonator microwave filters, In *Proceedings of the 2015 European Microwave Conference (EuMC)*, pp. 538–541, Paris, France, 7–10 Sept. 2015.

**Caenepeel, M.**, Ferranti, F. and Rolain, Y. (2016). Efficient and Automated Generation of Multidimensional Design Curves for Coupled-Resonator Filters using System Identification and Metamodels, In *Proceedings of the 2016 International Conference on Synthesis, Modeling, Analysis and Simulation Methods and Applications to Circuit Design (SMACD)*, Lisbon, Portugal, 27–30 June, Accepted For Publication

Gevers, M., **Caenepeel, M.** and Schoukens, J.(2012). Experiment design for

the identification of a simple Wiener system, In *2012 IEEE 51st IEEE Conference on Decision and Control (CDC)*, pp. 7333–7338, Maui, USA, 10–13 Dec.

Barachart, L., **Caenepeel, M.** and Rolain, Y.(2015). Wiener-Hammerstein systems and harmonic identification, In *2015 IEEE International Instrumentation and Measurement Technology Conference (I2MTC) Proceedings*, pp. 612–617 , Pisa, Italy, 11–14 May 2015.

# Appendices

# A

# Appendix A

This appendix contains the paper entitled *Parametric Modeling of the Coupling Parameters of Planar Coupled-Resonator Microwave Filters* as it appeared in the Proceedings of *European Microwave Conference 2015 (EuMC)*.

# Parametric Modeling of the Coupling Parameters of Planar Coupled-Resonator Microwave Filters

Matthias Caenepeel*†, Fabien Seyfert†, Yves Rolain* and Martine Olivi†
*ELEC, Vrije Universiteit Brussel
Pleinlaan 2, 1050 Elsene, Belgium Email: mcaenepe@vub.ac.be
†APICS, INRIA Sophia Antipolis
2004 Route des Lucioles, 06902 Valbonne, France Email: fabien.seyfert@inria.fr

***Abstract*—The design of planar coupled-resonator microwave filters is widely based on coupling matrix theory. In this framework a coupling matrix is first obtained during the synthesis step. Next this coupling matrix is physically implemented by correctly dimensioning the geometrical parameters of the filter. The implementation step is carried out using simplified empirical design curves relating the coupling coefficients and geometrical parameters. The curves typically only provide initial values and EM optimization is often needed such that the filter response meets the specifications. This paper proposes to extract parametric models that relate the filters design parameters directly to the coupling parameters. The advantage of such models is that they allow to tune the filter in a numerically cheap way and that they provide physical insight in the filters behavior. This paper explains how such models can be extracted from EM simulations and illustrates the technique for the design of an 8 pole cascaded quadruplet filter in a microstrip technology.**

## I. Introduction

Coupling matrix theory is widely used to design narrowband bandpass microwave filters [1], [2] in which the filter is modeled as a low-pass coupled resonator circuit (Fig. 1) [3]. The design process begins therefore by the derivation of a filtering characteristic meeting the filtering specifications. In a second step this characteristic is realized by a circuit. Next the circuit elements (coupling parameters) must be implemented physically by correctly dimensioning the geometrical parameters of the filter. An initial dimensioning of the filter is carried out by means of simplified empirical design curves relating the coupling parameters and geometrical parameters of the filter [4]. These curves however typically do not take into account more complex interactions, such as loading effects of the resonators by the couplings, which require that the initial values must be optimized to meet the filter specifications.
Several electomagnetic (EM) optimization techniques exist in the literature [2]. Although these techniques prove to be successful, there are still some disadvantages. The computation time grows rapidly with the complexity of the design (number of geometrical parameters). When the filter specifications change even slightly, the whole optimization process must be relaunched. Moreover the optimization process does not provide any physical insight in the filters behavior.
Literature shows that the coupling parameters are smooth functions of the controlling geometrical parameters [4], [5]. Therefore we propose to approximate this relation as a quadratic multivariate polynomial. The multivariate character stems from the fact that we also take into account several parameters to model second order effects such as the loading of the resonators. The main advantage is that these models are numerically cheap to evaluate and provide physical insight in the filters behavior. Moreover they can be re-used in various design scenarios. This paper explains how such parametric models can be extracted from EM simulations.
A crucial step in the modeling process, is the extraction of the coupling parameters from the simulated scattering data ($S$-parameters).

State-of-the-art gradient-based parameter extraction methods optimize the generalized low-pass network such that the networks frequency response meets the measured or simulated response [6], [7]. In the case where multiple solutions are possible, these methods do not necessarily converge to the implemented circuit. Section II shortly describes a three stage extraction process that overcomes this drawback. The $S$-parameters and network parameters are related as follows [8] $S(s) = I + C(sI - A)^{-1}C^t$ with

$$C = \begin{bmatrix} i\sqrt{2R_{in}} & 0 & \dots & 0 \\ 0 & \dots & 0 & i\sqrt{2R_{out}} \end{bmatrix}, \quad (1)$$

$$A = -R - iM. \quad (2)$$

The first step identifies a rational matrix from the simulated $S$-parameters [8]. The second step finds all possible circuital realizations of the previously computed rational approximation with a specified coupling topology. The third step finally deciphers the physically implemented matrix.
Section III describes how, given the physical coupling parameters, the quadratic multivariate polynomials are estimated in a least-squares sense. Eventually the modeling technique is illustrated for a design of an 8 pole cascaded quadruplet filter in microstrip technology (Fig.2). The design example shows that the models can be used to improve the filter response drastically.

## II. Coupling Parameter Extraction

This section describes the three stage parameter extraction procedure. First a canonical solution is extracted. Next all possible solutions corresponding to the desired topology are identified. Finally the physically implemented coupling matrix is identified among these solutions using prior knowledge. A more detailed explanation can be found in [9].
The first step identifies a rational matrix from the simulated

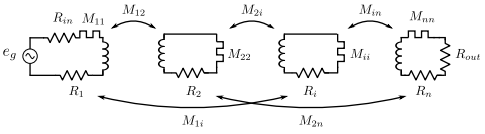


Fig. 1: Low-pass prototype network model for a general cross-coupled resonator filter.

$S$-parameters. The scattering data is first transformed to the low-pass domain. Next a rational common denominator matrix is identified using the toolbox PRESTO-HF [10] . The order of the common denominator $n$ is chosen to be equal to the number of resonators. The rational matrix is then transformed into the canonical arrow form of the coupling matrix.
The second step finds all possible realizations for the given rational matrix corresponding to a given topology. This topology corresponds to the topology used during the synthesis step. It is however possible that for certain geometrical values, the corresponding $S$-parameters can not be realized with the ideal topology. E.g. the response is asymmetric while the topology is only able to realize symmetric responses. Such a situation might occur when frequency offsets and/or extra couplings are present in the physical structure. To handle these situations the allowable topology is extended to a topology that is close to the original topology but still allows to capture these effects. This corresponds to expanding the class of realizable responses of the filter. Next the arrow form obtained during step one is transformed to the new topology using the toolbox DEDALE-HF [11]. The only drawback of this extended topology is that it concentrates the extra couplings at fixed positions in the matrix, while physically they might occur somewhere else. To compensate for this unwanted effect, the solutions found by DEDALE-HF are optimized by means of similarity transformations on the coupling matrix. This optimization process minimizes the influence of the extra couplings by redistributing them over the whole matrix. The influence of the extra couplings is expressed by a relative measure $c$:

$$c = \frac{\Sigma(M^{extra})^2}{\Sigma(M^{all})^2} \tag{3}$$

which is the sum of squares of the extra couplings ($M^{extra}$) over the sum of the squares of all the couplings ($M^{all}$).
During the last step of the process, the physically implemented coupling matrix is estimated among the solutions found during step 2. The choice of this matrix is based on some physical assumptions. First of all we assume that the couplings present in the original topology are dominant in the implemented filter. Therefore only those solutions for which $c$ is sufficiently small are considered. Since we use the extraction method in a design context, we assume that the implemented couplings are close to the ideal ones found during the synthesis step. Therefore the solutions for which the 2-norm of the difference to the ideal coupling matrix is minimal is chosen. To model the couplings as a function of the geometrical parameters, the filter is simulated for several geometrical values. This information allows to check whether the choice of the physical matrix is consistent with the geometry. E.g. when the spacing between resonator $i$ and $k$ is varied, this should mainly affect the coupling $M_{ik}$. If this is not the case, the solution that is coherent with the geometric variation, is chosen instead.

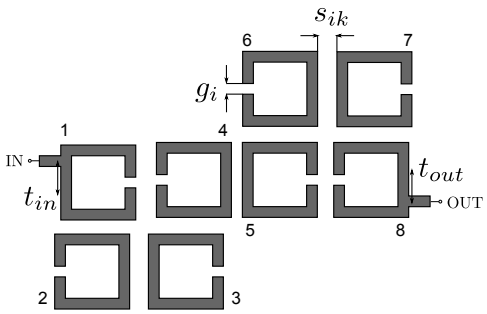


Fig. 2: Top-view of a square open-loop resonator cascaded quadruplet filter and the design parameters $s_{ik}$, $g_i$, $t_{in}$ and $t_{out}$.

## III. Multivariate Quadratic Approximation

The design curves that are available in the literature show that the behavior of coupling parameters as a function of the geometrical parameters is smooth [4], [5]. Therefore we propose to model the coupling parameters using multivariate polynomials of a maximal degree of 2. Since the process described in section II, extracts the physical coupling matrix, it is possible to relate a coupling parameter directly to a set of geometrical parameters.
We illustrate this with the example of 2 coupled resonators. It is known that the coupling between 2 resonators depends strongly on the spacing between the resonators, but is also affected by a possible offset introduced by spacings between other adjacent resonators (Fig.3). In this case we propose to use the following model:

$$M_{ik} = a_1 s_{ik}^2 + b_1 s_{ik} + b_2 d + c_1 \tag{4}$$

where $s_{ik}$ is the spacing between the resonators and $d$ represents the offset. In this case 4 coefficients $a_1, b_1, b_2$ and $c_1$ must be estimated. This requires at least 4 different EM simulations. The mesh that is used for the different simulations however might differ slightly since it depends on the geometry. This difference together with the error norm between the rational model and the EM simulation used during the extraction step, introduce an error on the extracted coupling matrices. To avoid that the parametric model of the coupling parameter would model these effects as well, we propose to use at least 2 times more simulations than what is minimally needed to estimate the coefficients.
The geometrical values for which the filter must be simulated are selected as follows. First the initial values for the geometrical parameters are determined using the design curves. Next the physical coupling matrix for this structure is extracted. This coupling matrix gives an idea of the distance between the initial design and the ideal design. This allows to determine a validity interval around each design parameter. Values for each geometrical parameter are then randomly generated

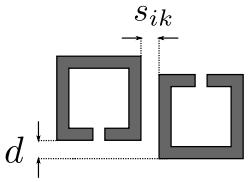


Fig. 3: Top-view of 2 coupled resonators, where $s_{ik}$ is the spacing between them and $d$ is a possible offset.

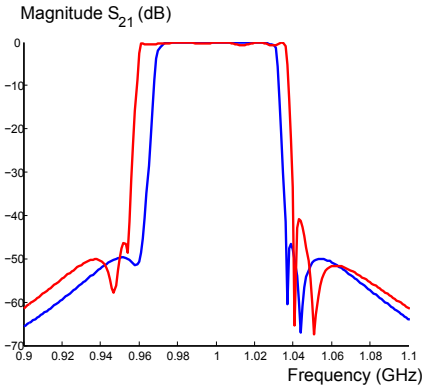


Fig. 4: Magnitude of $S_{21}$ for the initial (red) and final (blue) design.

within this interval. The number of values corresponds to the proposed number of simulations needed to estimate the parametric models. The filter is simulated for all these sets of values. Once the EM simulations are gathered, the coupling parameters are extracted using the method described in section II. The couplings together with the geometrical parameters are then used to estimate a parametric model for each coupling parameter in least-squares sense.

## IV. Example

The design of an 8-pole cascaded quadruplet microstrip filter consisting of square open-loop resonators (Fig.2) is used to illustrate the proposed method. The filter is designed for a center frequency $f_c$ of 1 GHz and fractional bandwidth $FBW$ of 0.06. The ideal coupling matrix is synthesized using DEDALE-HF. The synthesis step yields 2 possible solutions among which one is chosen. The filter is implemented in a RT/duroid substrate with a relative permittivity 10.2. The initial dimensions of the filter are obtained using empirical formulae derived for the coupling coefficients between square open-loop resonators [12]. The filter is simulated using ADS Momentum 2014 [13]. Fig. 4 and 5 show that the responses can clearly be improved with respect to center frequency, insertion loss and bandwidth.

There are three types of coupling parameters that potentially need to be tuned and thus modeled:

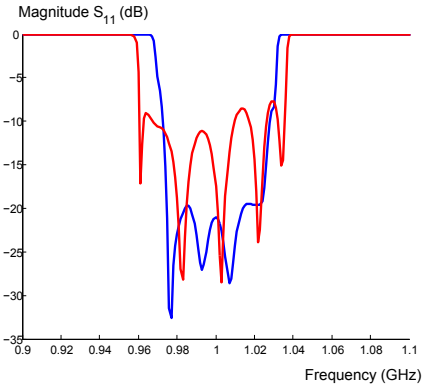


Fig. 5: Magnitude of $S_{11}$ for the initial (red) and final (blue) design.

- Inter-resonator couplings $M_{ik}$ where $i \neq k$
- Center frequency offsets $M_{kk}$
- Normalized input/output impedances $R_1$ and $R_2$ respectively

It is well known that inter-resonator couplings mainly depend on the spacing between the resonators. Spacings between other resonators can introduce an extra offset (Fig.3). E.g. the coupling between resonator 1 and 2 mainly depends on the distance $s_{12}$. The spacing between resonator 1 and 4, labeled $s_{14}$ and the spacing between 2 and 3, labeled $s_{23}$ introduce an offset $\frac{|s_{14}-s_{23}|}{2}$. Thus we can model this coupling as:

$$M_{12} = a_1 s_{12}^2 + b_1 s_{12} + b_2\left(\frac{|s_{14} - s_{23}|}{2}\right) + c_1 \qquad (5)$$

The same reasoning can be repeated for the other inter-resonator couplings.

The diagonal elements $M_{kk}$ express the difference between the center frequency of the filter and the resonance frequency $f_k$ of resonator $k$. $f_k$ is directly related to the length of the resonator and thus to $g_k$, but also depends on the loading of the resonator influences $f_k$. This loading is modeled by means of the distances between the neighboring resonators. Therefore we propose as a model:

$$M_{kk} = a_1 g_k^2 + b_1 g_k + b_2 s_{k-1,k} + b_3 s_{k,k+1} + b_1 \qquad (6)$$

if $k \neq 1, n$ and

$$M_{kk} = a_1 g_k^2 + b_1 g_k + b_2 s_{k-1,k} + b_3 s_{k,k+1} + b_4 t_{in/out} + c_1 \quad (7)$$

if $k = 1$ or n. The normalized input and output impedances mainly depend on the position of the input and output feeding lines. The length of the lines however also has an effect. Therefore we propose a model:

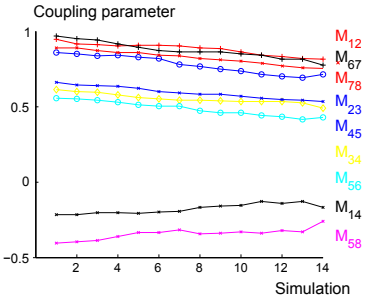


Fig. 6: The extracted inter-resonator couplings for each simulation.

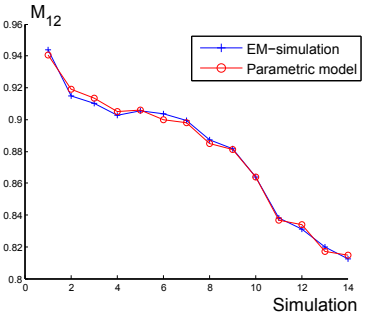


Fig. 7: Comparison between the coupling parameters extracted from the EM simulations (+- blue) and result of the parametric model (o- red).

$$R_1 = a_1 t_{in}^2 + b_1 t_{in} + b_2 g_1 + c_1 \tag{8}$$

$$R_2 = a_1 t_{out}^2 + b_1 t_{out} + b_2 g_n + c_1 \tag{9}$$

This reasoning shows that the most complicated model requires the estimation of 6 coefficients. We propose to perform 14 EM simulations to estimate them. Since the coupling parameters are not too far from the ideal ones, we propose to simulate the filters for values in an intervals varying from 0.3 up to 0.5 mm for the design parameters $s_{ik}$, since the offset from $f_c$ are also not too large we use the same intervals for $g_k$. For $t_{in}$ and $t_{out}$ we take an interval of 0.5 mm.

After the EM simulations are gathered, the coupling matrices are extracted using the method described in section II. Fig. 6 shows the extracted inter-resonator couplings for each simulation. Eventually the simulations are used to extract the parametric models given in equations 5-9. Fig. 7 shows the result of the model for $M_{12}$ for all of the simulations. It shows that there is model error, which is expected due to simulation meshing and parameter extraction errors.

Once the parametric models are extracted they can be used to fine-tune the filter. The models form a set of non-linear equations. This set is solved in Matlab using the function $fminunc$. The filter is next re-simulated for the found geometrical parameters. The result is shown in Fig. 4 and 5. The response can still be improved, but remark that only 14 EM simulations were required to tune a filter with 19 design parameters.

## V. Conclusion

This paper introduces parametric models that relate the coupling matrix parameters to the design parameters of the filter. The advantage of the models is that they are cheap to evaluate and allow to improve the filters response in a numerically cheap way. We explain how the models can be extracted using EM simulations. Moreover we illustrate the utility of the models with a design example. The design example shows that the models allow to improve the filters response drastically using only 14 EM simulations.

## References


[1] R. J. Cameron, "General coupling matrix synthesis methods for chebyshev filtering functions," *IEEE Transaction on Microwave Theory and Techniques*, vol. 47, no. 4, pp. 433–442, 1999.

[2] R. J. Cameron, C. M. Kudsia, and R. R. Mansour, *Microwave filters for communication systems*. Wiley-Interscience, 2007.

[3] A. Atia and A. Williams, "New types of waveguide bandpass filters for satellite transponders," *Comsat Tech. Review*, vol. 1, no. 1, pp. 20–43, 1971.

[4] J.-S. G. Hong and M. J. Lancaster, *Microstrip filters for RF/microwave applications*. Wiley-interscience, 2001, vol. 126.

[5] S. Amari, C. LeDrew, and W. Menzel, "Space-mapping optimization of planar coupled-resonator microwave filters," *Microwave Theory and Techniques, IEEE Transactions on*, vol. 54, no. 5, pp. 2153–2159, 2006.

[6] P. Harscher, R. Vahldieck, and S. Amari, "Automated filter tuning using generalized low-pass prototype networks and gradient-based parameter extraction," *Microwave Theory and Techniques, IEEE Transactions on*, vol. 49, no. 12, pp. 2532–2538, 2001.

[7] P. Harscher, E. Ofli, R. Vahldieck, and S. Arnari, "Em-simulator based parameter extraction and optimization technique for microwave and millimeter wave filters," in *Microwave Symposium Digest, 2002 IEEE MTT-S International*, vol. 2. IEEE, 2002, pp. 1113–1116.

[8] M. Olivi, F. Seyfert, and J.-P. Marmorat, "Identification of microwave filters by analytic and rational h2 approximation," *Automatica*, vol. 49, no. 2, pp. 317–325, 2013.

[9] M. Caenepeel, F. Seyfert, Y. Rolain, and M. Olivi, "Microwave filter design based on coupling topologies with multiple solutions," *Accepted for publication on IMS 2015*.

[10] "PRESTO-HF : a matlab toolbox dedicated to the identification problem of low pass coupling parameters of band pass microwave filters." [Online]. Available: https://project.inria.fr/presto-hf/

[11] "DEDALE-HF : a matlab toolbox dedicated to the equivalent network synthesis for microwave filters." [Online]. Available: http://www-sop.inria.fr/apics/Dedale/

[12] J.-S. Hong and M. J. Lancaster, "Couplings of microstrip square open-loop resonators for cross-coupled planar microwave filters," *IEEE Transactions on Microwave Theory and Techniques*, vol. 44, no. 11, pp. 2099–2109, 1996.

[13] Agilent Technologies, "Advanced design system," 2014, santa Rosa, CA.

## Bibliography


[ADS 14] "ADS Momentum". www.keysight.com, 2014.

[Amar 00a] S. Amari. "Sensitivity analysis of coupled resonator filters". *IEEE Transactions on Circuits and Systems II: Analog and Digital Signal Processing*, Vol. 47, No. 10, pp. 1017–1022, 2000.

[Amar 00b] S. Amari. "Synthesis of cross-coupled resonator filters using an analytical gradient-based optimization technique". *IEEE Transactions on Microwave Theory and Techniques*, Vol. 48, No. 9, pp. 1559–1564, 2000.

[Amar 06] S. Amari, C. LeDrew, and W. Menzel. "Space-mapping optimization of planar coupled-resonator microwave filters". *IEEE Transactions on Microwave Theory and Techniques*, Vol. 54, No. 5, pp. 2153–2159, 2006.

[Amar 99] S. Amari. "On the maximum number of finite transmission zeros of coupled resonator filters with a given topology". *IEEE Microwave and Guided Wave Letters*, Vol. 9, No. 9, pp. 354–356, 1999.

[Ande 73] B. Anderson and S. Vongpanitlerd. *Network analysis and synthesis*. NJ, Prentice-Hall, 1973.

[Arnd 04] F. Arndt, J. Brandt, V. Catina, J. Ritter, I. Rullhusen, J. Dauelsberg, U. Hilgefort, and W. Wessel. "Fast CAD and optimization of waveguide components and aperture antennas by hybrid MM/FE/MoM/FD methods-state-of-the-art and recent advances". *IEEE Transactions on Microwave Theory and Techniques*, Vol. 52, No. 1, pp. 292–305, 2004.

[Atia 71] A. E. Atia and A. E. Williams. "New types of waveguide bandpass filters for satellite transponders". *Comsat Tech. Review*, Vol. 1, No. 1, pp. 20–43, 1971.

[Atia 72] A. E. Atia and A. E. Williams. "Narrow-bandpass waveguide filters". *EEE Transactions on Microwave Theory and Techniques*, Vol. 20, No. 4, pp. 258–265, 1972.

[Atia 74] A. E. Atia, A. E. Williams, and R. Newcomb. "Narrow-band multiple-coupled cavity synthesis". *IEEE Transactions on Circuits and Systems*, Vol. 21, No. 5, pp. 649–655, 1974.

[Atia 98] W. A. Atia, K. A. Zaki, and A. E. Atia. "Synthesis of general topology multiple coupled resonator filters by optimization". In: *Microwave Symposium Digest, 1998 IEEE MTT-S International*, pp. 821–824, IEEE, Baltimore, MD, USA, 7-12 June 1998.

[Bahl 77] I. Bahl and R. Garg. "Simple and accurate formulas for a microstrip with finite strip thickness". *Proceedings of the IEEE*, Vol. 65, No. 11, pp. 1611–1612, 1977.

[Band 88] J. W. Bandler and S. H. Chen. "Circuit optimization: the state of the art". *IEEE transactions on Microwave Theory and Techniques*, Vol. 36, No. 2, pp. 424–443, 1988.

[Band 94a] J. W. Bandler, R. M. Biernacki, S. H. Chen, D. Swanson, and S. Ye. "Microstrip filter design using direct EM field simulation". *IEEE Transactions on Microwave Theory and Techniques*, Vol. 42, No. 7, pp. 1353–1359, 1994.

[Band 94b] J. W. Bandler, R. M. Biernacki, S. H. Chen, D. G. Swanson Jr, and S. Ye. "Microstrip filter design using direct EM field simulation". *Microwave Theory and Techniques, IEEE Transactions on*, Vol. 42, No. 7, pp. 1353–1359, 1994.

[Basl 10] P. Basl, R. Gohary, M. Bakr, and R. Mansour. "Modelling of electromagnetic responses using a robust multi-dimensional Cauchy interpolation technique". *IET Microwaves, Antennas Propagation,*, Vol. 4, No. 11, pp. 1955 –1964, Nov. 2010.

[Bele 68] V. Belevitch. *Classical network theory.* Holden-Day, 1968.

[Bell 82] H. C. Bell Jr. "Canonical asymmetric coupled-resonator filters". *IEEE Transactions on Microwave Theory and Techniques*, Vol. 30, No. 9, pp. 1335–1340, 1982.

[Belo 75] E. Belohoubek and E. Denlinger. "Loss considerations for microstrip resonators (short papers)". *IEEE Transactions on Microwave Theory and Techniques*, Vol. 23, No. 6, pp. 522–526, 1975.

[Ben 03] A. Ben-Israel and T. N. Greville. *Generalized inverses: theory and applications*. Vol. 15, Springer Science & Business Media, 2003.

[Bila 99] S. Bila, D. Baillargeat, M. Aubourg, S. Verdeyme, P. Guillon, C. Zanchi, J. Sombrin, J. Grimm, and L. Baratchart. "Direct electromagnetic optimisation method for microwave filter design". *Electronics Letters*, Vol. 35, No. 5, pp. 400–401, 1999.

[Broy 65] C. G. Broyden. "A class of methods for solving nonlinear simultaneous equations". *Mathematics of Computation*, Vol. 19, No. 92, pp. 577–593, 1965.

[Caen 15a] M. Caenepeel, F. Seyfert, Y. Rolain, and M. Olivi. "Microwave filter design based on coupling topologies with multiple solutions". In: *Microwave Symposium (IMS), 2015 IEEE MTT-S International*, pp. 1–4, IEEE, Phoenix, AZ, USA, 17-22 May 2015.

[Caen 15b] M. Caenepeel, F. Seyfert, Y. Rolain, and M. Olivi. "Parametric modeling of the coupling parameters of planar coupled-resonator microwave filters". In: *Microwave Conference (EuMC), 2015 European*, pp. 538–541, IEEE, Paris, France, 7-10 Sept 2015.

[Caen 16] M. Caenepeel, K. Chemmangat, F. Ferranti, Y. Rolain, T. Dhaene, and L. Knockaert. "Scalable macromodelling methodology for the efficient design of microwave filters". *IET Microwaves, Antennas & Propagation*, Vol. 10, No. 5, pp. 579–586, 2016.

[Came 03] R. J. Cameron. "Advanced coupling matrix synthesis techniques for microwave filters". *IEEE Transactions on Microwave Theory and Techniques*, Vol. 51, No. 1, pp. 1–10, 2003.

[Came 05] R. J. Cameron, J.-C. Faugere, and F. Seyfert. "Coupling matrix synthesis for a new class of microwave filter configuration". In: *Microwave Symposium Digest, 2005 IEEE MTT-S International*, p. 4, Long Beach, CA, USA, 12-17 June 2005.

[Came 07a] R. J. Cameron, J.-C. Faugere, F. Rouillier, and F. Seyfert. "Exhaustive approach to the coupling matrix synthesis problem and application to the design of high degree asymmetric filters". *International Journal of RF and Microwave Computer-Aided Engineering*, Vol. 17, No. 1, pp. 4–12, 2007.

[Came 07b] R. J. Cameron, C. M. Kudsia, and R. R. Mansour. *Microwave filters for communication systems.* Wiley-Interscience, 2007.

[Came 82] R. J. Cameron. "Fast generation of Chebyshev filter prototypes with asymmetrically-prescribed transmission zeros". *ESA Journal*, Vol. 6, pp. 83–95, 1982.

[Came 99] R. J. Cameron. "General coupling matrix synthesis methods for Chebyshev filtering functions". *Microwave Theory and Techniques, IEEE Transactions on*, Vol. 47, No. 4, pp. 433–442, 1999.

[Chem 14a] K. Chemmangat, F. Ferranti, T. Dhaene, and L. Knockaert. "Parametric macromodelling of linear high-frequency systems using multiple frequency scaling and sequential sampling". *Electronics Letters*, Vol. 50, No. 6, pp. 475–476, 2014.

[Chem 14b] K. Chemmangat, F. Ferranti, T. Dhaene, and L. Knockaert. "Scalable models of microwave system responses using sequential sampling on unstructured grids". *International Journal of Numerical Modelling: Electronic Networks, Devices and Fields*, Vol. 27, No. 1, pp. 122–137, 2014.

[Cohn 58] S. B. Cohn. "Parallel-coupled transmission-line-resonator filters". *IRE Transactions on Microwave Theory and Techniques*, Vol. 6, No. 2, pp. 223–231, 1958.

[Couc 10] I. Couckuyt, F. Declercq, T. Dhaene, H. Rogier, and L. Knockaert. "Surrogate-based infill optimization applied to electromagnetic problems". *International Journal of RF and Microwave Computer-Aided Engineering*, Vol. 20, No. 5, pp. 492–501, 2010.

[Couc 12] I. Couckuyt, D. Deschrijver, and T. Dhaene. "Towards efficient multiobjective optimization: multiobjective statistical criterions". In: *2012 IEEE Congress on Evolutionary Computation*, pp. 1–8, IEEE, Brisbane, QLD, Australia, 10-15 June 2012.

[Cris 72] E. Cristal and S. Frankel. "Hairpin-line and hybrid hairpin-line/half-wave parallel-coupled-line filters". *IEEE Transactions on Microwave Theory and Techniques*, Vol. 20, No. 11, pp. 719–728, 1972.

[CST 15] "CST Microwave Studio". www.cst.com, 2015.

[Cuyt 06] A. Cuyt, R. Lenin, S. Becuwe, and B. Verdonk. "Adaptive multivariate rational data fitting with applications in electromagnetics". *IEEE Transactions on Microwave Theory and Techniques,*, Vol. 54, No. 5, pp. 2265 – 2274, May 2006.

[Denl 80] E. J. Denlinger. "Losses of microstrip lines". *IEEE Transactions on Microwave Theory Techniques*, Vol. 28, pp. 513–522, 1980.

[Deva 03] V. Devabhaktuni, B. Chattaraj, M. Yagoub, and Q.-J. Zhang. "Advanced microwave modeling framework exploiting automatic model generation, knowledge neural networks, and space mapping". *IEEE Transactions on Microwave Theory and Techniques,*, Vol. 51, No. 7, pp. 1822 – 1833, July 2003.

[Ferr 09] F. Ferranti, L. Knockaert, and T. Dhaene. "Parameterized S-Parameter Based Macromodeling With Guaranteed Passivity". *IEEE Microwave and Wireless Component Letters*, Vol. 19, No. 10, pp. 608–610, Oct. 2009.

[Ferr 10] F. Ferranti, L. Knockaert, and T. Dhaene. "Guaranteed Passive Parameterized Admittance-Based Macromodeling". *IEEE Transactions on Advanced Packaging*, Vol. 33, No. 3, pp. 623–629, Aug. 2010.

[Ferr 11] F. Ferranti, L. Knockaert, and T. Dhaene. "Passivity-Preserving Parametric Macromodeling by Means of Scaled and Shifted State-Space Systems". *IEEE Transactions on Microwave Theory and Techniques*, Vol. 59, No. 10, pp. 2394 –2403, Oct. 2011.

[Ferr 12] F. Ferranti, L. Knockaert, T. Dhaene, and G. Antonini. "Parametric macromodeling based on amplitude and frequency scaled systems with guaranteed passivity". *International Journal of Numerical Modelling: Electronic Networks, Devices and Fields*, Vol. 25, No. 2, pp. 139 –151, March/April 2012.

[Fook 90] E. H. Fooks and R. A. Zakarevicius. *Microwave engineering using microstrip circuits*. Prentice-Hall, Inc., 1990.

[Garc 04] A. García-Lampérez, S. Llorente-Romano, M. Salazar-Palma, and T. K. Sarkar. "Efficient electromagnetic optimization of microwave filters and multiplexers using rational models". *IEEE Transactions on Microwave Theory and Techniques*, Vol. 52, No. 2, pp. 508–521, 2004.

[Garg 79] R. Garg and I. Bahl. "Characteristics of coupled microstriplines". *IEEE Transactions on Microwave Theory and Techniques*, Vol. 27, No. 7, pp. 700–705, 1979.

[Gilb 63] E. G. Gilbert. "Controllability and observability in multivariable control systems". *Journal of the Society for Industrial and Applied Mathematics, Series A: Control*, Vol. 1, No. 2, pp. 128–151, 1963.

[Gopi 81] A. Gopinath. "Maximum Q-factor of microstrip resonators". *IEEE Transactions on Microwave Theory and Techniques*, Vol. 29, No. 2, pp. 128–131, 1981.

[Gupt 79] K. Gupta, R. Garg, I. Bahl, and P. Bhartia. *Microstrip lines and slotlines*. Vol. 2, Artech house Dedham, Massachusetts, 1979.

[Gust 06] B. Gustavsen. "Improving the pole relocating properties of vector fitting". *IEEE Transactions on Power Delivery*, Vol. 21, No. 3, pp. 1587–1592, July 2006.

[Gust 99] B. Gustavsen and A. Semlyen. "Rational approximation of frequency domain responses by Vector Fitting". *IEEE Transactions on Power Delivery*, Vol. 14, No. 3, pp. 1052–1061, July 1999.

[Hamm 80] E. Hammerstad and O. Jensen. "Accurate models for microstrip computer-aided design". In: *1980 IEEE MTT-S International Microwave Symposium Digest*, pp. 407–409, Washington, DC, USA, 28-30 May 1980.

[Harr 96] R. F. Harrington and J. L. Harrington. *Field computation by moment methods*. Oxford University Press, 1996.

[Hars 01] P. Harscher, R. Vahldieck, and S. Amari. "Automated filter tuning using generalized low-pass prototype networks and gradient-based parameter extraction". *IEEE Transactions on Microwave Theory and Techniques*, Vol. 49, No. 12, pp. 2532–2538, 2001.

[Hars 02] P. Harscher, E. Ofli, R. Vahldieck, and S. Arnari. "EM-simulator based parameter extraction and optimization technique for microwave and millimeter wave filters". In: *Microwave Symposium Digest, 2002 IEEE MTT-S International*, pp. 1113–1116, IEEE, Seattle, WA, USA, 2-7 June 2002.

[Hong 00] J.-S. Hong. "Couplings of asynchronously tuned coupled microwave resonators". *IEE Proceedings: Microwaves, Antennas and Propagation*, Vol. 147, No. 5, pp. 354–358, 2000.

[Hong 01] J.-S. Hong and M. J. Lancaster. *Microstrip filters for RF/microwave applications*. Vol. 126, Wiley-interscience, 2001.

[Hong 96] J.-S. Hong and M. J. Lancaster. "Couplings of microstrip square open-loop resonators for cross-coupled planar microwave filters". *IEEE Transactions on Microwave Theory and Techniques*, Vol. 44, No. 11, pp. 2099–2109, 1996.

[Hong 99] J.-S. Hong and M. Lancaster. "Microstrip cross-coupled trisection bandpass filters with asymmetric frequency characteristics". *IEE Proceedings: Microwaves, Antennas and Propagation*, Vol. 146, No. 1, pp. 84–90, 1999.

[Hsu 13] C.-Y. Hsu, C.-Y. Chen, and H.-R. Chuang. "Microstrip dual-band bandpass filter design with closely specified passbands". *Microwave Theory and Techniques, IEEE Transactions on*, Vol. 61, No. 1, pp. 98–106, 2013.

[Hu 13] H. Hu and K.-L. Wu. "An adaptive computer-aided design-and-tuning scheme for a predistorted filter with uneven-Q effect". In: *Microwave Symposium Digest (IMS), 2013 IEEE MTT-S International*, pp. 1–3, IEEE, Seattle, WA, USA, 2-7 June 2013.

[Hu 14] H. Hu and K.-L. Wu. "A Generalized Coupling Matrix Extraction Technique for Bandpass Filters With Uneven-Qs". *IEEE Transactions on Microwave Theory and Techniques*, Vol. 62, No. 2, pp. 244–251, Feb 2014.

[Kail 80] T. Kailath. *Linear systems*. Vol. 156, Prentice-Hall Englewood Cliffs, NJ, 1980.

[Kirs 84] M. Kirschning and R. H. Jansen. "Accurate wide-range design equations for the frequency-dependent characteristic of parallel coupled

microstrip lines". *IEEE Transactions on Microwave Theory and Techniques*, Vol. 32, No. 1, pp. 83–90, 1984.

[Klei 08] J. P. C. Kleijnen. *Design and Analysis of Simulation Experiments*. Springer, 2008.

[Klim 05] A. Klimke and B. Wohlmuth. "Algorithm 847: spinterp: Piecewise Multilinear Hierarchical Sparse Grid Interpolation in MATLAB". *ACM Transactions on Mathematical Software*, Vol. 31, No. 4, 2005.

[Klim 07] A. Klimke. "Sparse Grid Interpolation Toolbox – User's Guide". Tech. Rep. IANS report 2007/017, University of Stuttgart, 2007.

[Koza 02] P. Kozakowski and M. Mrozowski. "Automated CAD of coupled resonator filters". *IEEE Microwave and Wireless Components Letters*, Vol. 12, No. 12, pp. 470–472, 2002.

[Koza 06] P. Kozakowski and M. Mrozowski. "Quadratic programming approach to coupled resonator filter CAD". *IEEE Transactions on Microwave Theory and Techniques*, Vol. 54, No. 11, pp. 3906–3913, 2006.

[Kozi 06] S. Koziel, J. Bandler, and K. Madsen. "A Space-Mapping Framework for Engineering Optimization; Theory and Implementation". *IEEE Transactions on Microwave Theory and Techniques,*, Vol. 54, No. 10, pp. 3721 –3730, Oct. 2006.

[Kozi 10a] S. Koziel. "Shape-Preserving Response Prediction for Microwave Design Optimization". *IEEE Transactions on Microwave Theory and Techniques,*, Vol. 58, No. 11, pp. 2829 –2837, Nov. 2010.

[Kozi 10b] S. Koziel, J. Bandler, and Q. Cheng. "Robust Trust-Region Space-Mapping Algorithms for Microwave Design Optimization". *IEEE Transactions on Microwave Theory and Techniques,*, Vol. 58, No. 8, pp. 2166 –2174, Aug. 2010.

[Kuds 92] C. Kudsia, R. Cameron, and T. Wai-Cheung. "Innovations in microwave filters and multiplexing networks for communications satellite systems". *IEEE Transactions on Microwave Theory and Techniques*, Vol. 40, No. 6, pp. 1133–1149, 1992.

[Kuro 65] K. Kurokawa. "Power waves and the scattering matrix". *IEEE Transactions on Microwave Theory and Techniques*, Vol. 13, No. 2, pp. 194–202, 1965.

[Lame 03] A. Lamecki, P. Kozakowski, and M. Mrozowski. "Efficient implementation of the Cauchy method for automated CAD-model construction". *IEEE Microwave and Wireless Components Letters,*, Vol. 13, No. 7, pp. 268 –270, July 2003.

[Lame 09] A. Lamecki, L. Balewski, and M. Mrozowski. "Adaptive CAD-Model Construction Schemes". *IEEE Transactions on Magnetics,*, Vol. 45, No. 3, pp. 1538 –1541, March 2009.

[Lamp 04] A. G. Lampérez, T. K. Sarkar, and M. S. Palma. "Generation of accurate rational models of lossy systems using the Cauchy method". *IEEE Microwave and Wireless Components Letters*, Vol. 14, No. 10, pp. 490–492, 2004.

[Lehm 01] R. Lehmensiek and P. Meyer. "Creating accurate multivariate rational interpolation models of microwave circuits by using efficient adaptive sampling to minimize the number of computational electromagnetic analyses". *IEEE Transactions on Microwave Theory and Techniques*, Vol. 49, No. 8, pp. 1419 –1430, Aug. 2001.

[Levy 02] R. Levy, R. V. Snyder, and G. Matthaei. "Design of microwave filters". *IEEE Transactions on Microwave Theory and Techniques*, Vol. 50, No. 3, pp. 783–793, 2002.

[Levy 84] R. Levy and S. B. Cohn. "A history of microwave filter research, design, and development". *IEEE Transactions on Microwave Theory and Techniques*, Vol. 32, No. 9, pp. 1055–1067, 1984.

[Macc 08] G. Macchiarella. "Generalized coupling coefficient for filters with nonresonant nodes". *IEEE Microwave and Wireless Components Letters*, Vol. 18, No. 12, pp. 773–775, 2008.

[Macc 10] G. Macchiarella. "Extraction of unloaded Q and coupling matrix from measurements on filters with large losses". *Microwave and Wireless Components Letters, IEEE*, Vol. 20, No. 6, pp. 307–309, 2010.

[Mark 92] R. B. Marks and D. F. Williams. "A general waveguide circuit theory". *Journal of Research-National Institute of Standards and Technology*, Vol. 97, pp. 533–533, 1992.

[Marm 02] J.-P. Marmorat, M. Olivi, B. Hanzon, and R. L. Peeters. "Matrix rational H 2 approximation: a state-space approach using Schur

parameters". In: *Proceedings of the 41st IEEE Conference on Decision and Control*, pp. 4244–4249, IEEE, Las Vegas, NV, USA, 10-13 Dec. 2002.

[Mart 12] M. Martinez-Mendoza, F. Seyfert, C. Ernst, and A. Alvarez-Melcon. "Formal Expression of Sensitivity and Energy Relationship in the Context of the Coupling Matrix". *IEEE Transactions on Microwave Theory and Techniques*, Vol. 60, No. 11, pp. 3369–3375, 2012.

[Matt 64] G. L. Matthaei, L. Young, and E. Jones. *Microwave filters, impedance-matching networks, and coupling structures.* Vol. 5, McGraw-Hill New York, 1964.

[Mira 08] V. Miraftab and M. Yu. "Generalized lossy microwave filter coupling matrix synthesis and design using mixed technologies". *IEEE Transactions on Microwave Theory and Techniques*, Vol. 56, No. 12, pp. 3016–3027, 2008.

[Mont 48] C. G. Montgomery, R. H. Dicke, and E. M. Purcell. *Principles of microwave circuits.* Iet, 1948.

[Oliv 13] M. Olivi, F. Seyfert, and J.-P. Marmorat. "Identification of microwave filters by analytic and rational H2 approximation". *Automatica*, Vol. 49, No. 2, pp. 317–325, 2013.

[Part 97] J. R. Partington. *Interpolation, identification, and sampling.* Oxford University Press, 1997.

[Peik 98] S. Peik, R. Mansour, and Y. Chow. "Multidimensional Cauchy method and adaptive sampling for an accurate microwave circuit modeling". *IEEE Transactions on Microwave Theory and Techniques,*, Vol. 46, No. 12, pp. 2364 –2371, Dec. 1998.

[Pint 12] R. Pintelon and J. Schoukens. *System Identification: A Frequency Domain Approach.* Wiley-IEEE Press, 2012.

[Poza 98] D. Pozar. *Microwave engineering.* John Wiley & Sons, 1998.

[Puce 68] R. A. Pucel, D. J. Masse, and C. P. Hartwig. "Losses in microstrip". *IEEE Transactions on Microwave Theory and Techniques*, Vol. 16, No. 6, pp. 342–350, 1968.

[Pugl 00] K. Puglia. “A General Design Procedure for Bandpass Filters Derived from Lowpass Prototype Elements: Part I”. *Microwave Journal -Euroglobal Edition-*, Vol. 43, No. 12, pp. 22–38, 2000.

[Pugl 01] K. Puglia. “A general design procedure for bandpass filters derived from low pass prototype elements: Part II”. *Microwave Journal -Euroglobal Edition-*, Vol. 44, No. 1, pp. 114–137, 2001.

[RARL] “RARL2: a Matlab toolbox dedicated to the computation of a stable rational L2-approximation of specified order to a given L2-stable matrix-valued function”. http://www-sop.inria.fr/apics/RARL2/rarl2.html.

[Seyf 00] F. Seyfert. “DEDALE-HF: a Matlab toolbox dedicated to the equivalent network synthesis for microwave filters”. http://www-sop.inria.fr/apics/Dedale/, 2000.

[Seyf 03] F. Seyfert, L. Baratchart, J.-P. Marmorat, S. Bila, J. Sombrin, *et al.* “Extraction of coupling parameters for microwave filters: Determination of a stable rational model from scattering data”. In: *IEEE MTT-S International Microwave Symposium Digest*, pp. 25–30, Citeseer, 2003.

[Seyf 04] F. Seyfert. “PRESTO-HF: a Matlab toolbox dedicated to the identification problem of low pass coupling parameters of band pass microwave filters”. https://project.inria.fr/presto-hf/, 2004.

[Seyf 07] F. Seyfert and S. Bila. “General synthesis techniques for coupled resonator networks”. *IEEE Microwave Magazine*, Vol. 8, No. 5, pp. 98–104, Oct 2007.

[Seyf 98] F. Seyfert. *Problèmes extrémaux dans les espaces de Hardy.* PhD thesis, Ecole Nationale Supérieure des Mines de Paris, 1998.

[Snyd 07] R. V. Snyder. “Practical aspects of microwave filter development”. *IEEE Microwave Magazine*, Vol. 8, No. 2, pp. 42–54, 2007.

[Swan 07a] D. Swanson and G. Macchiarella. “Microwave filter design by synthesis and optimization”. *IEEE Microwave Magazine*, Vol. 8, No. 2, pp. 55–69, 2007.

[Swan 07b] D. Swanson. “Narrow-band microwave filter design”. *IEEE Microwave Magazine*, Vol. 8, No. 5, pp. 105–114, 2007.

[Tami 05] S. Tamiazzo and G. Macchiarella. “An analytical technique for the synthesis of cascaded N-tuplets cross-coupled resonators microwave filters using matrix rotations”. *IEEE Transactions on Microwave Theory and Techniques*, Vol. 53, No. 5, pp. 1693–1698, 2005.

[Triv 09] P. Triverio, S. Grivet-Talocia, and M. Nakhla. “A Parameterized Macromodeling Strategy With Uniform Stability Test”. *IEEE Transactions on Advanced Packaging*, Vol. 32, No. 1, pp. 205 –215, Feb. 2009.

[Triv 10] P. Triverio, M. Nakhla, and S. Grivet-Talocia. “Passive parametric macromodeling from sampled frequency data”. In: *2010 IEEE 14th Workshop on Signal Propagation on Interconnects (SPI)*, pp. 117–120, IEEE, Hildesheim, The Netherlands, 9-12 May 2010.

[Wang 07] G. G. Wang and S. Shan. “Review of Metamodeling Techniques in Support of Engineering Design Optimization”. *Journal of Mechanical Design*, Vol. 129, No. 4, pp. 370–380, 2007.

[Wong 79] J. S. Wong. “Microstrip tapped-line filter design”. *IEEE Transactions on Microwave Theory Techniques*, Vol. 27, pp. 44–50, 1979.

[Yang 99] C.-C. Yang and C.-Y. Chang. “Microstrip cascade trisection filter”. *IEEE Microwave and Guided Wave Letters*, Vol. 9, No. 7, pp. 271–273, 1999.